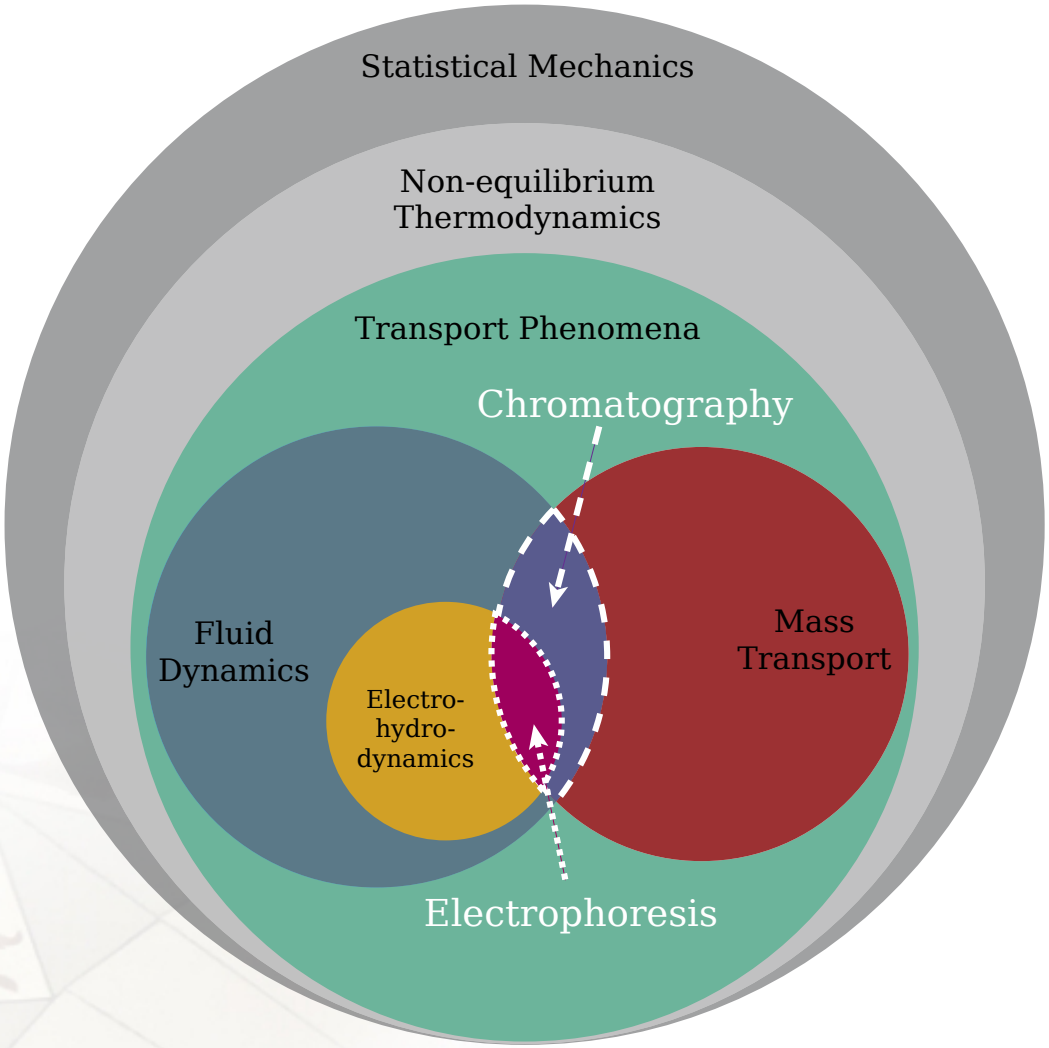

Figure : Chromatographic separation science is a subset of mass transport and fluid dynamics. In the case of electrophoresis, electro-hydrodynamics are necessary to describe electrophoresis of polyelectrolytes. Both mass transport and fluid dynamics can be described as a field of transport phenomena, which is a branch of non-equilibrium thermodynamics.

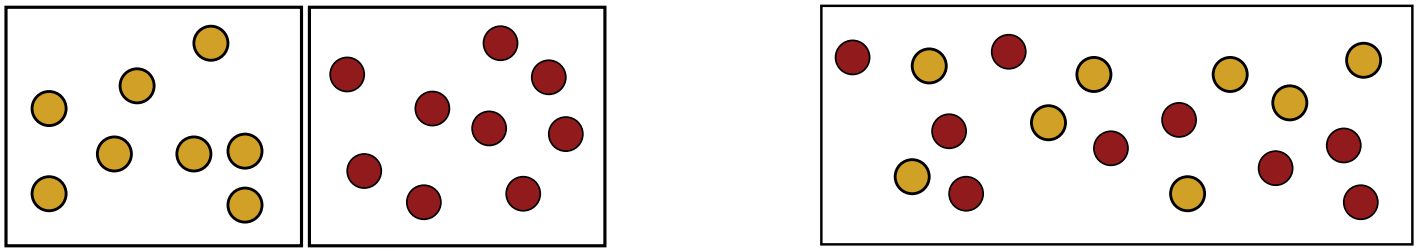

Figure : Mixed states possess higher entropy then when different species are ordered into well-resolved separated volumes.

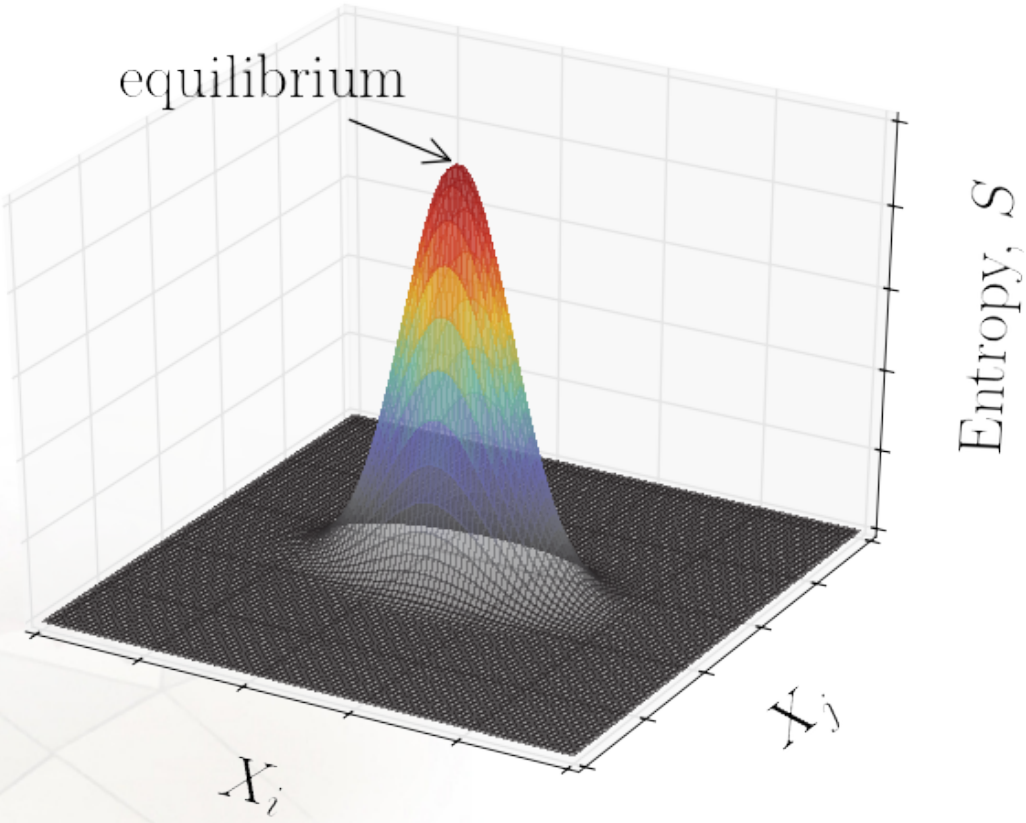

Figure : Equilibrium occurs at the point of maximum entropy. An example system that depends on only two generalized coordinates is shown.

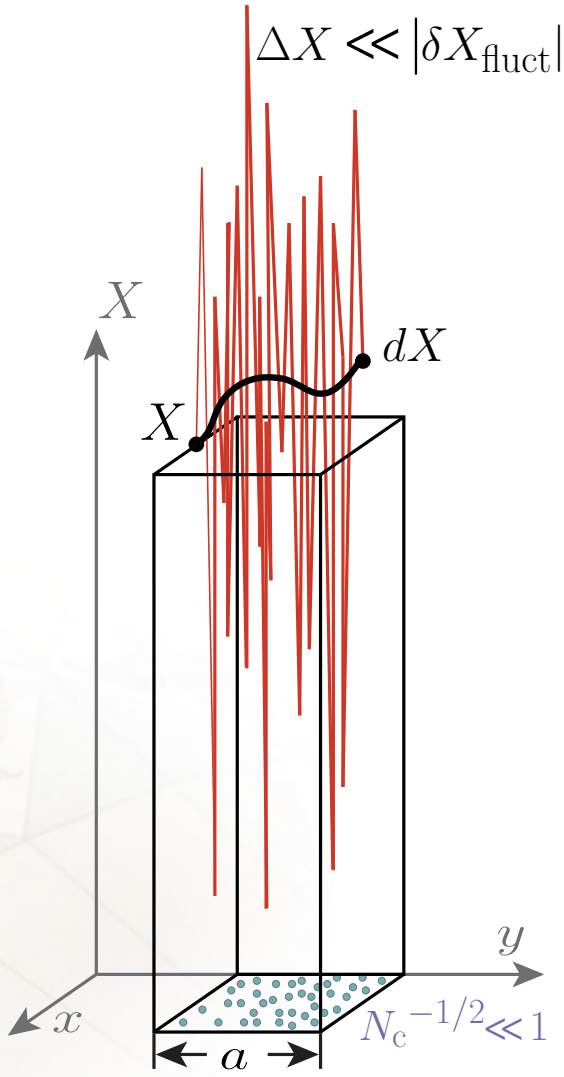

Figure : Postulate I of non-equilibrium thermodynamics is the quasi-equilibrium assumption that changes in generalized coordinates are small relative to fluctuations, while remaining in the thermodynamic limit.

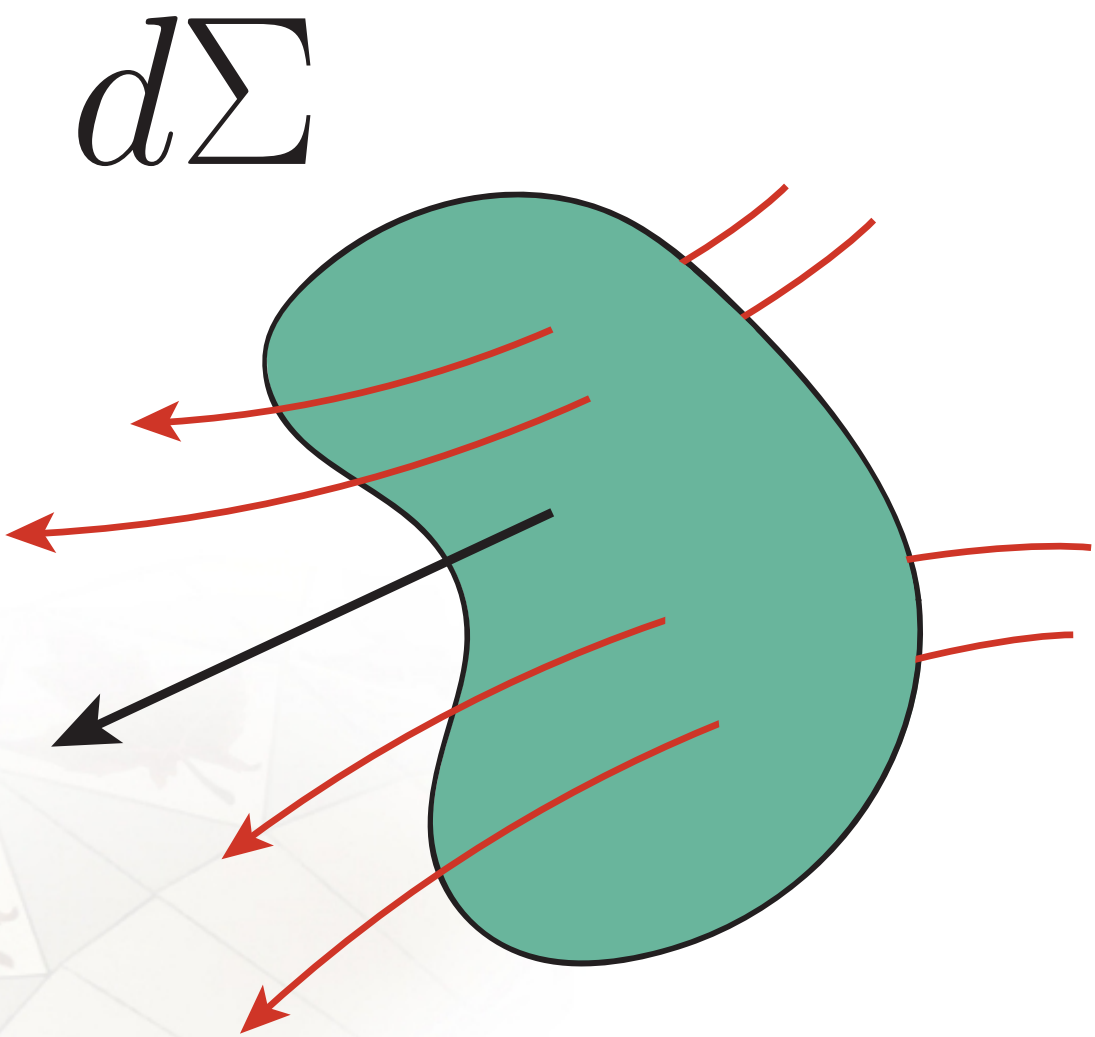

Figure : Flux of X is the flow per unit time through a unit area $d\Sigma$ or equivalently the amount of X transported across the surface is the flux normal to that surface.

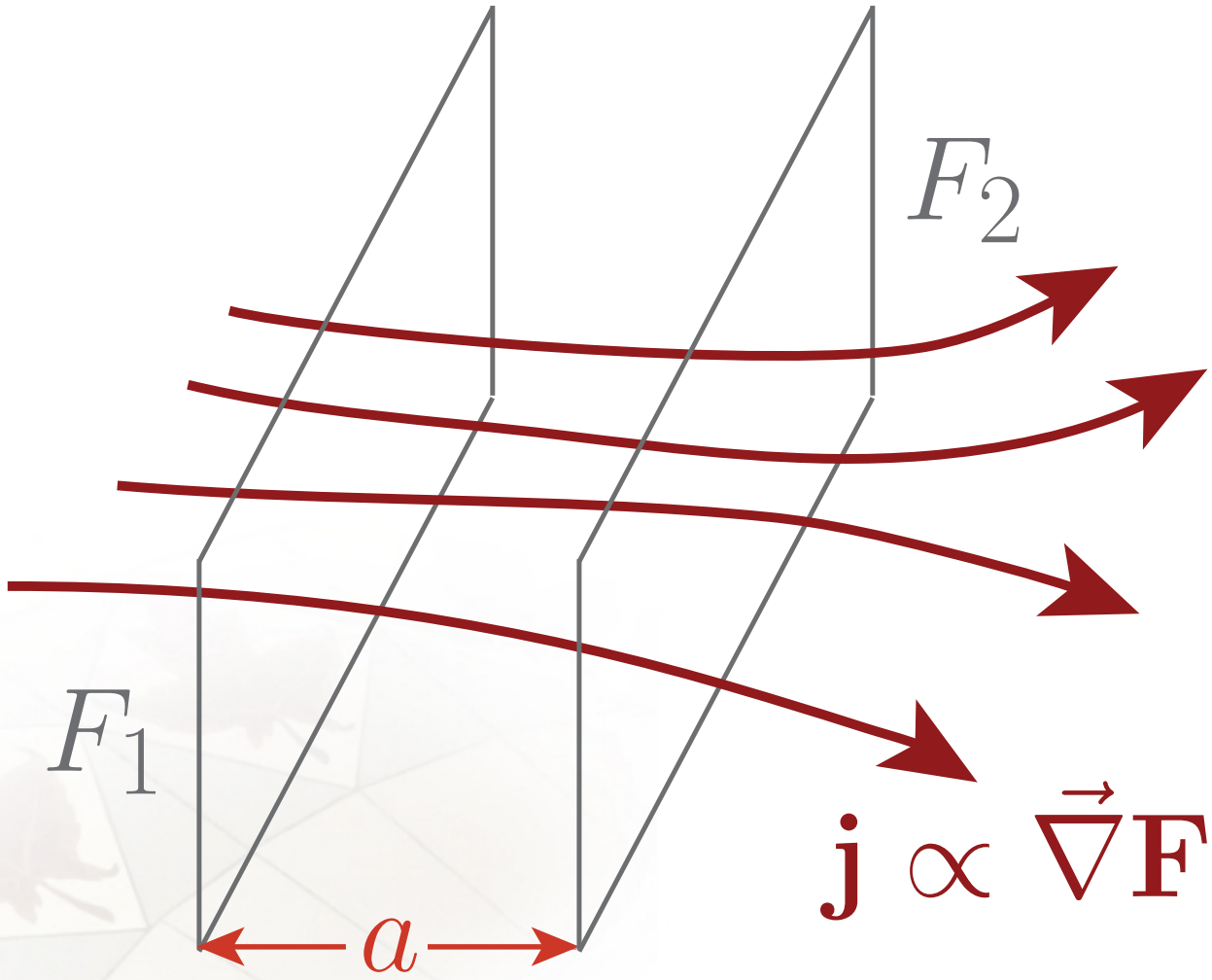

Figure : Postulate II of non-equilibrium thermodynamics is the linear transport assumption that fluxes are linearly proportional to affinities.

Figure : Fourier's law of heat flux. Thermal energy flows from a hot surface (red) through a medium defined by a thermal conductivity κ. Thermal conductivity is an example of a linear kinetic coefficient.

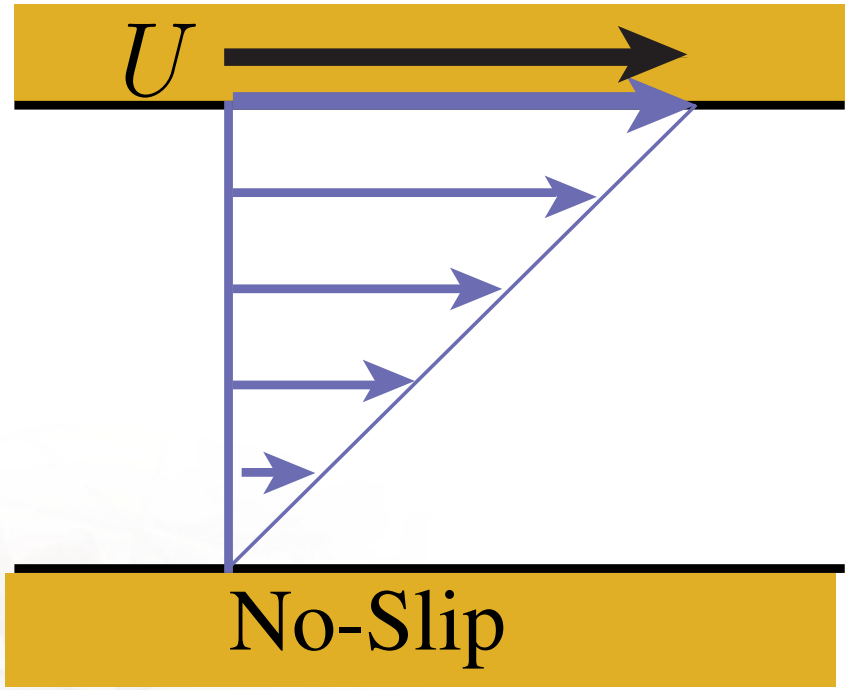

Figure : Shear flow between two plates. No-flip boundary conditions at each plate result in a velocity gradient within the fluid Newtonian fluid. The velocity variation results in internal, viscous stress. Newton's law of viscous dissipation describes the case when viscous stress is linearly related to the velocity gradient.

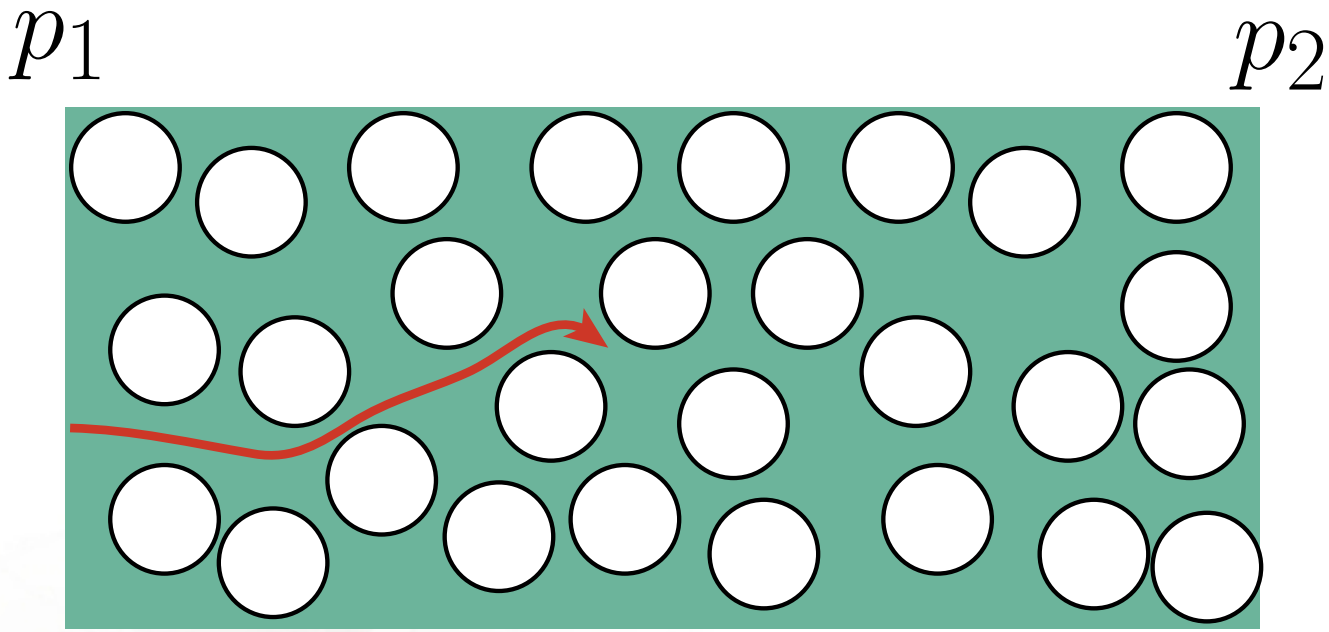

Figure : An illustration of a system for which the volumetric flow rate would be described by Darcy's law. A system of packed beads creates a series of effective channels, through which fluid flows. Darcy's law describes when the volumetric flow rate of the fluid is linearly proportional to the pressure drop per unit length.

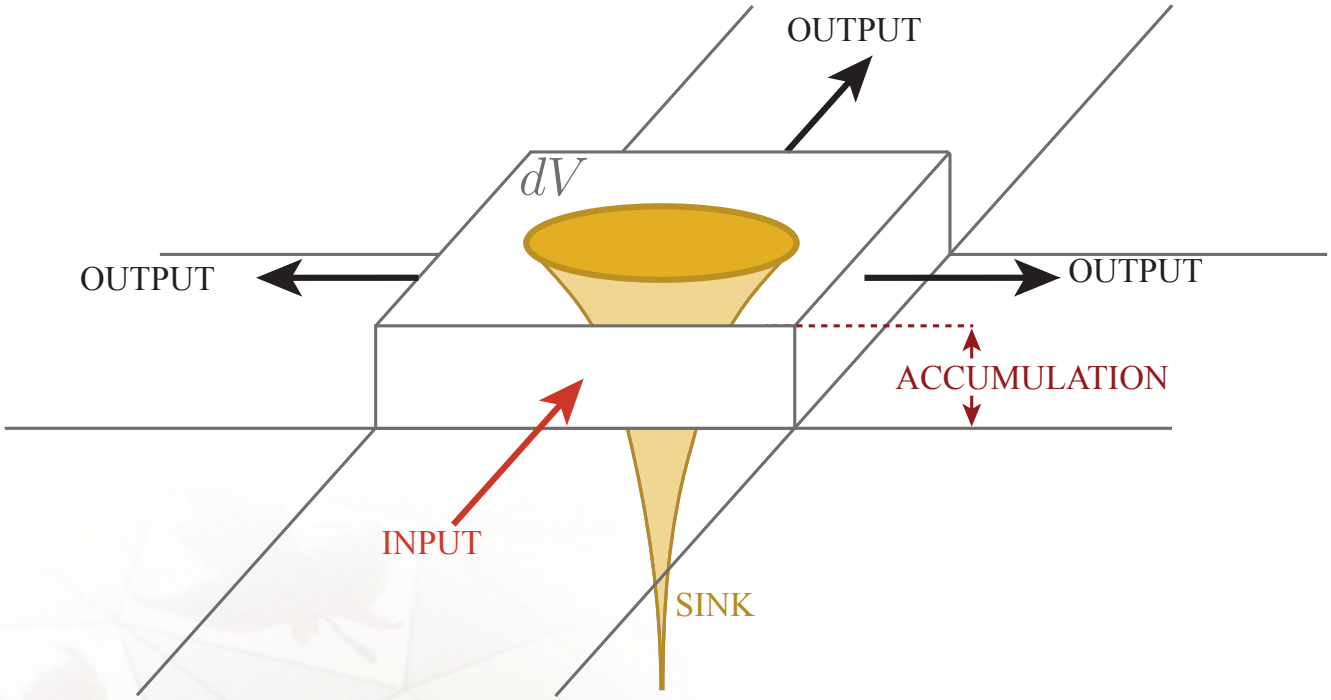

Figure : Schematic representation of the balance equation. Whatever comes enters (less what exits) plus any sources (less sinks) accumulates within the local volume dV.

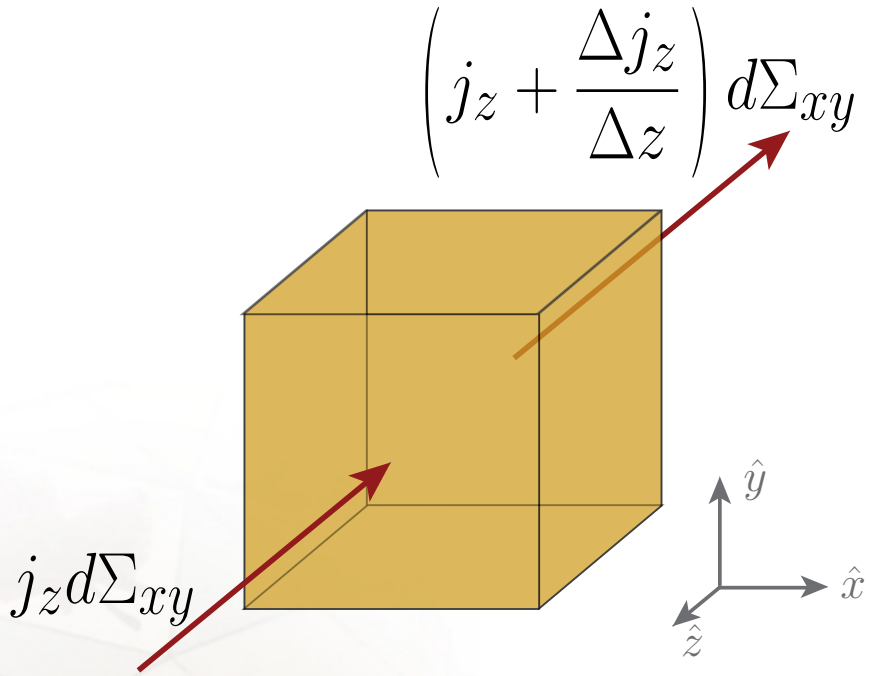

Figure : Input and output through the *xy*-planes of a cubic control volume.

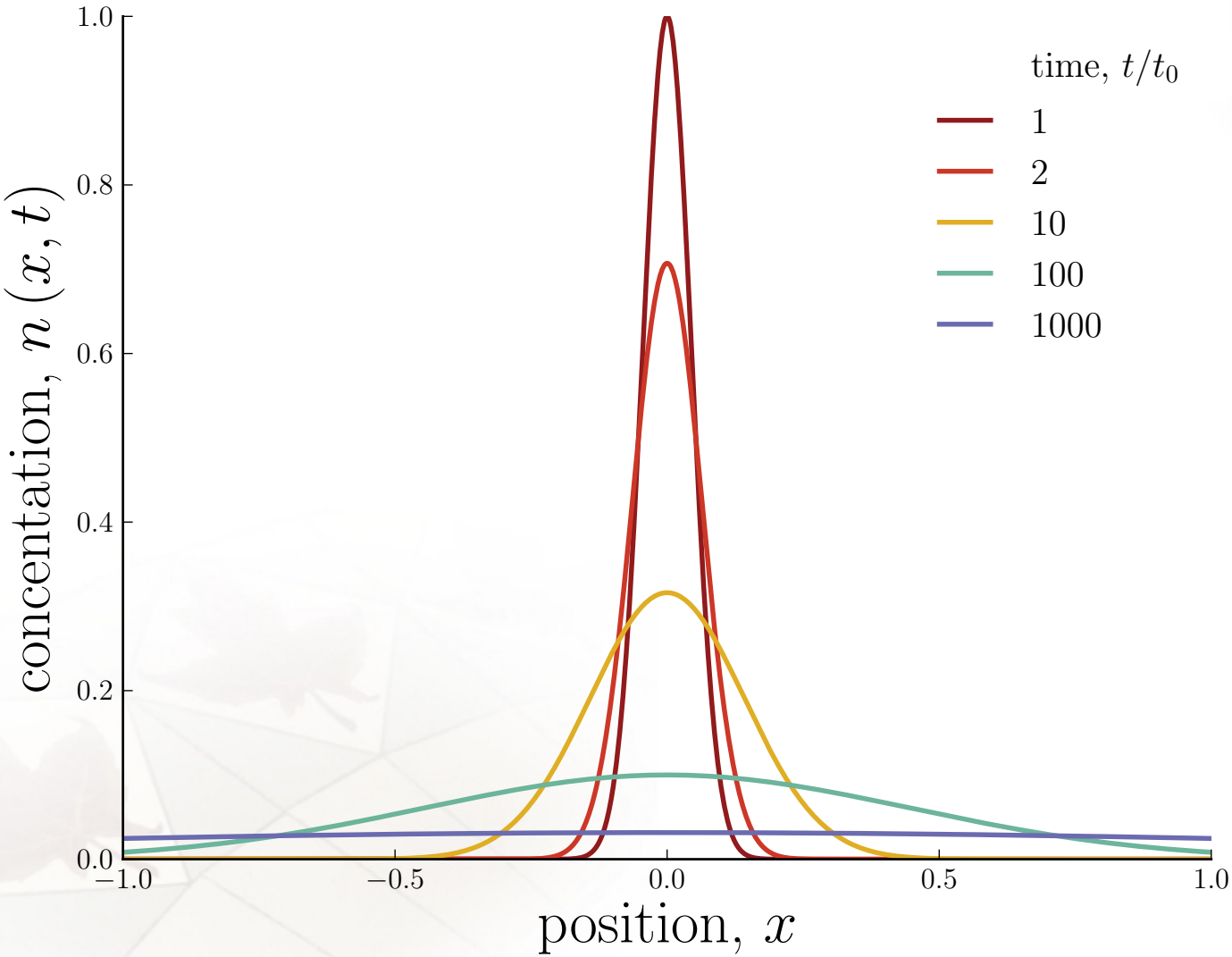

Figure : The 1D solution of Fick's second law, for an initial distribution of $n\,(x,t) = \exp\left[-x^2/4\mathcal{D}t_o\right]$ in a closed system of size $2x_o$.

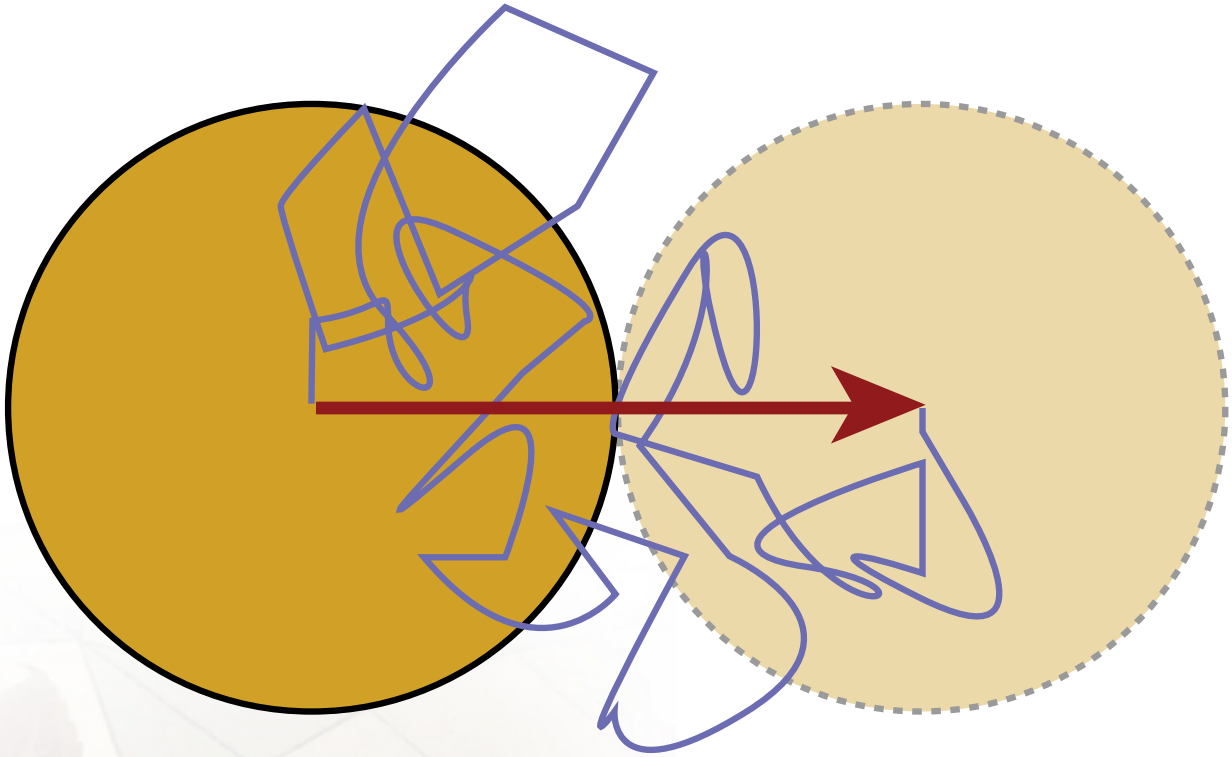

Figure : A convecting particle requires a time $[\tau]_{\text{conv}}$ to convectively translate its own body length. It would diffuse that same distance in a time $[\tau]_{\text{diff}}$.

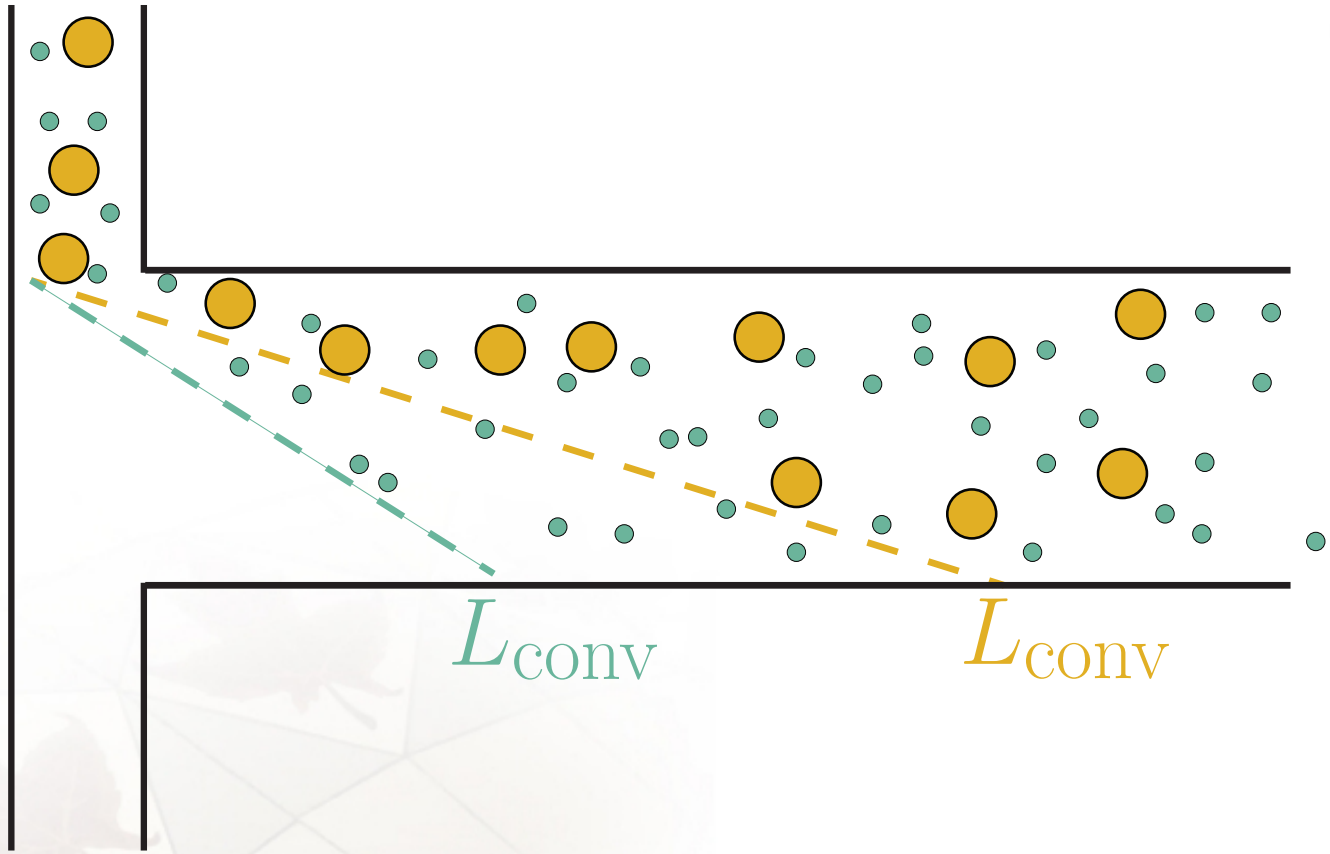

Figure : Smaller red particles diffuse across the channel after they have convected a distance $[L]_{\text{conv}}$. In the same flow, the larger blue particles must elute a greater distance.

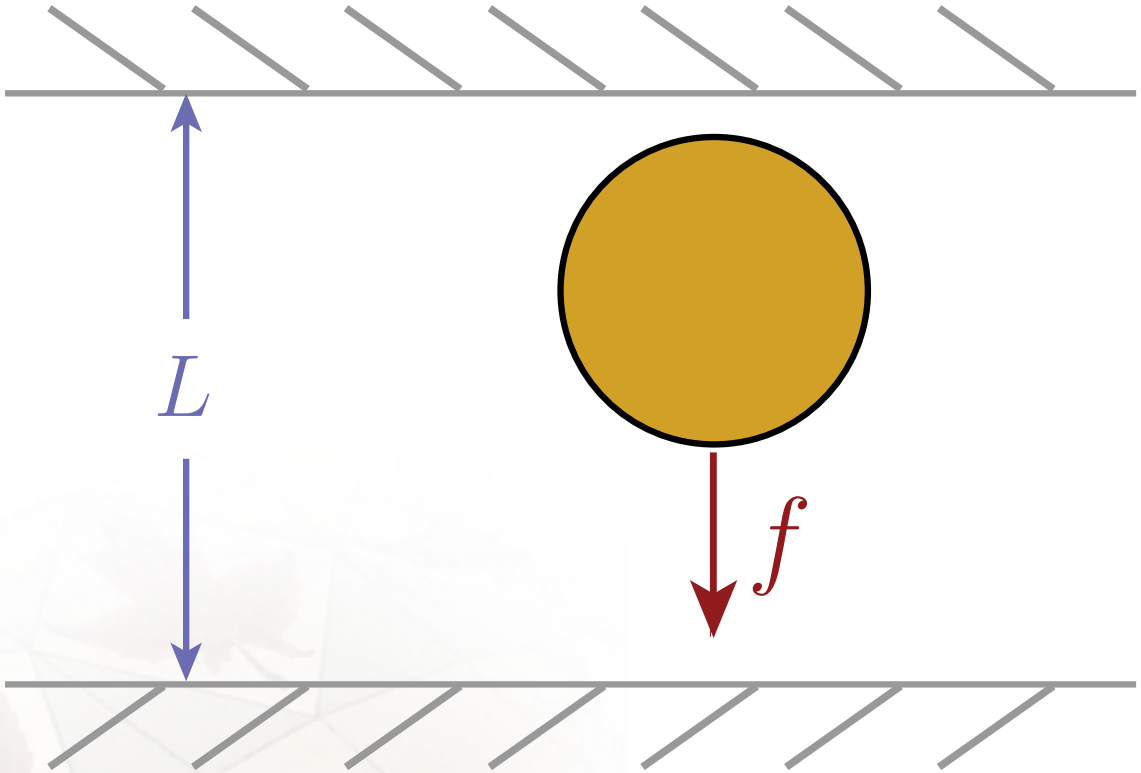

Figure : The probability distribution of finding a particle at a given position results from the competition between randomizing thermal energy and the potential energy landscape.

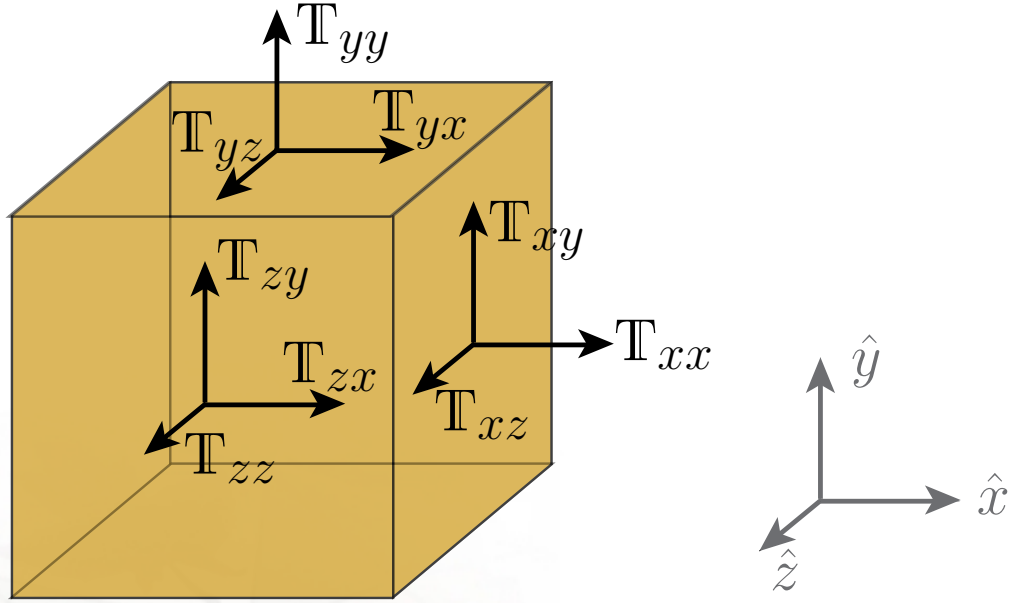

Figure : Stress elements (momentum flux) on each surface of a Cartesian volume.

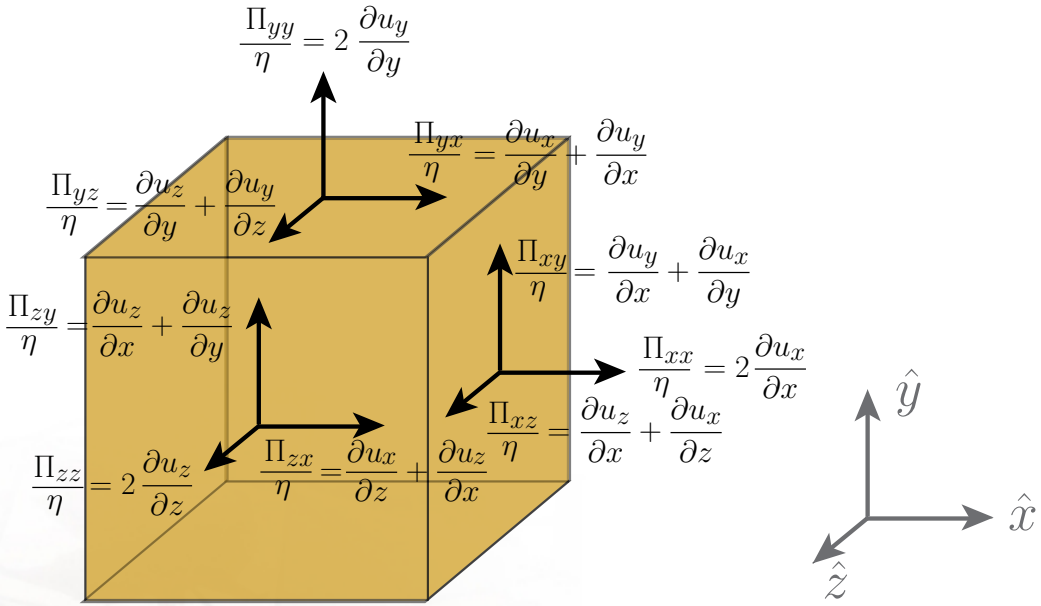

Figure : Viscous stress elements on each surface of a Cartesian volume for an incompressible, Newtonian fluid.

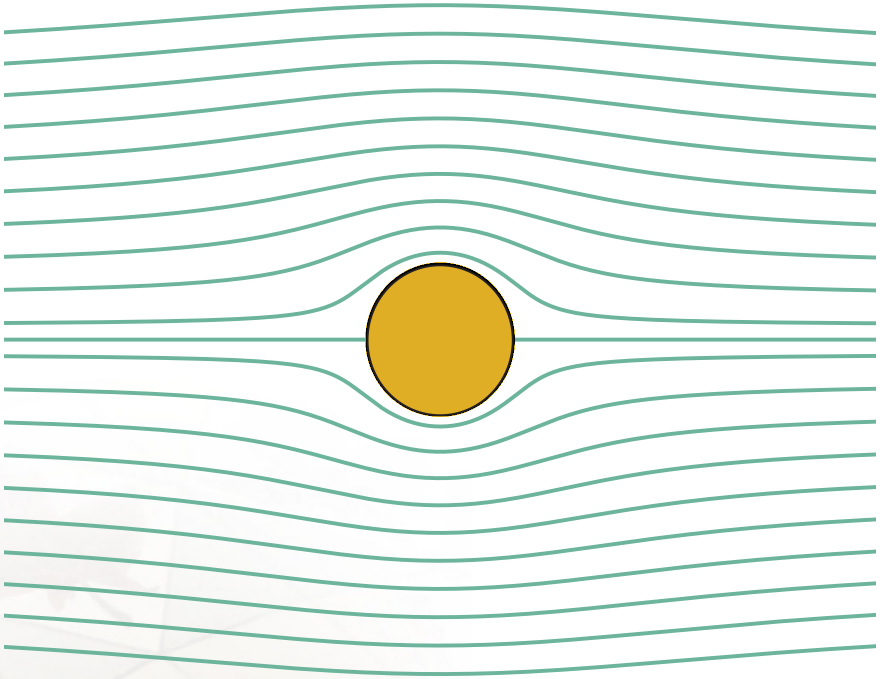

Figure : Laminar streamlines of flow past a fixed spherical body.

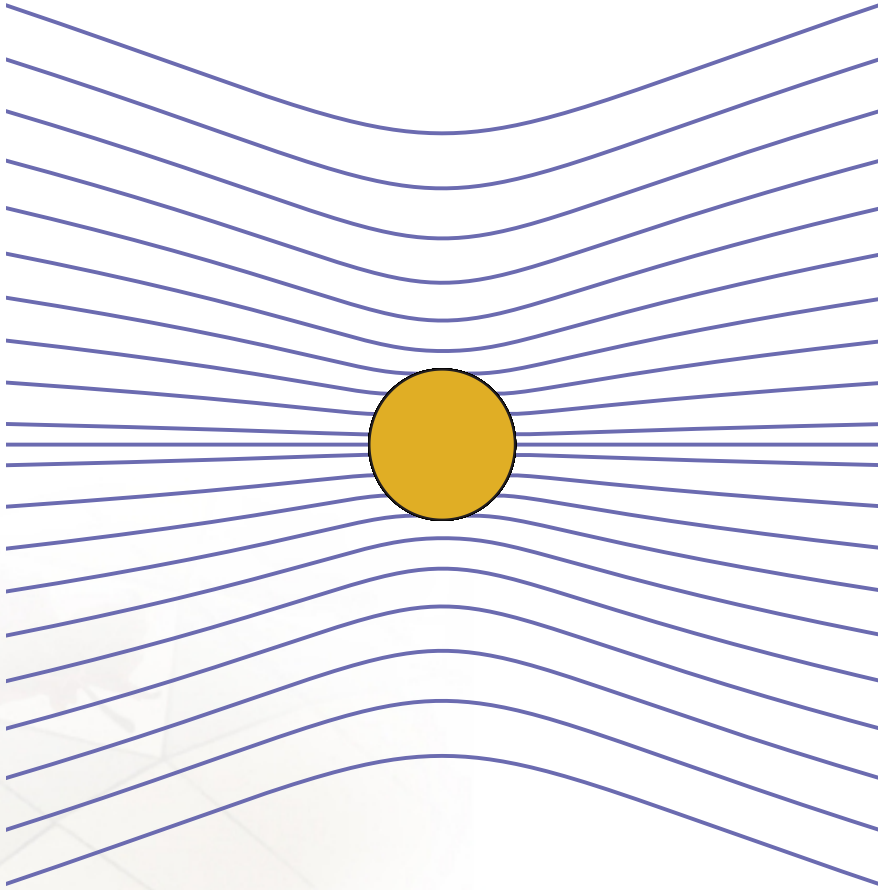

Figure : Laminar streamlines of flow due to a translating spherical body.

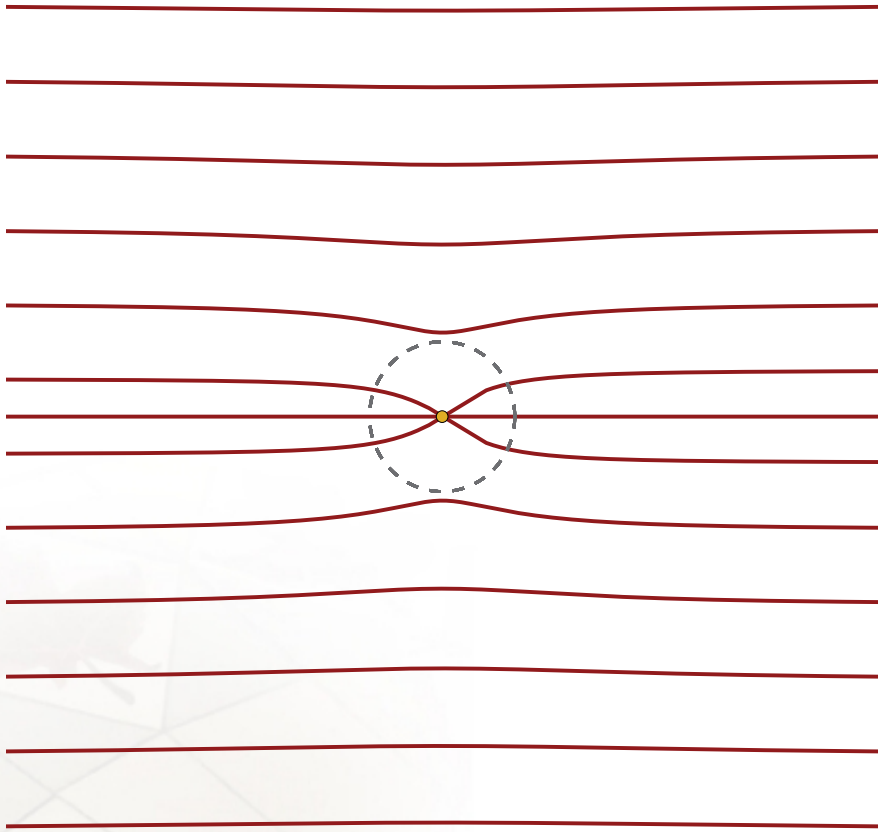

Figure : Stokeslet due to the Oseen-Burgers hydrodynamic interaction tensor.

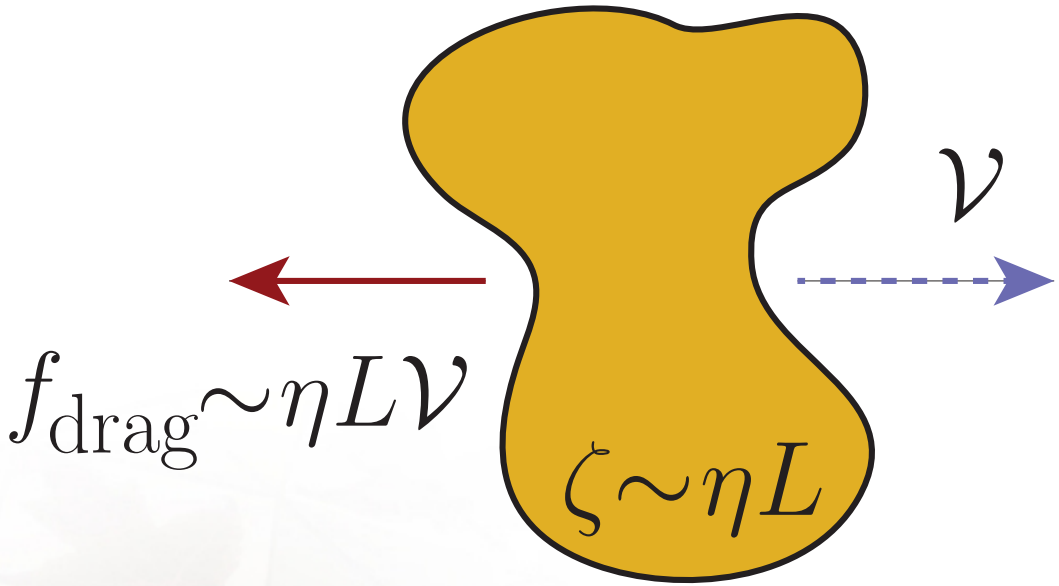

Figure : The drag on any body scales as the velocity $\mathcal{V}$ times the friction coefficient ζ at low Reynolds number. For an arbitrarily shaped body the friction coefficient must scale as the viscosity of the fluid medium η times the characteristic size of the body $[L]$.

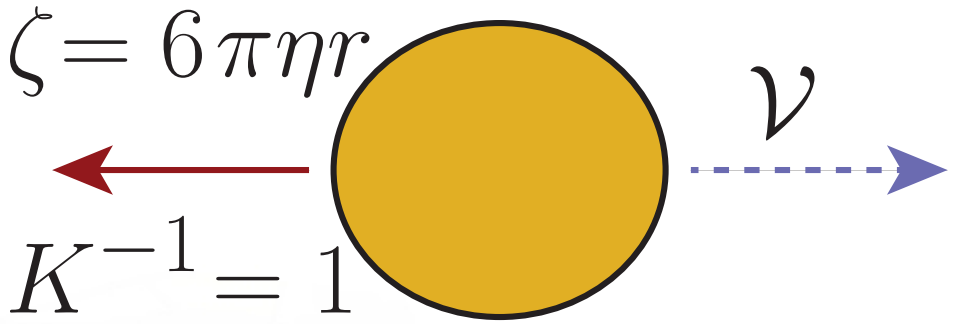

Figure : The drag on a spherical body of radius r moving through a fluid of viscosity η at low Reynolds numbers (small speed $\mathcal{V}$) has a friction coefficient that obeys Stokes' law $\zeta = 6\pi\eta r$.

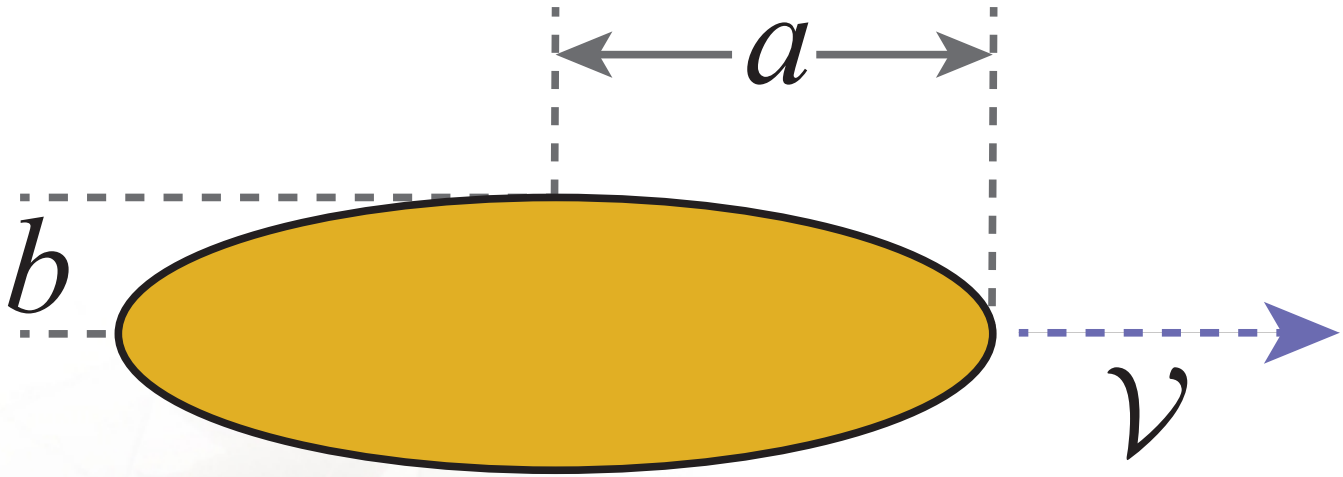

Figure : Ellipsoid oriented with the major axis (of length a) oriented parallel to the direction of motion.

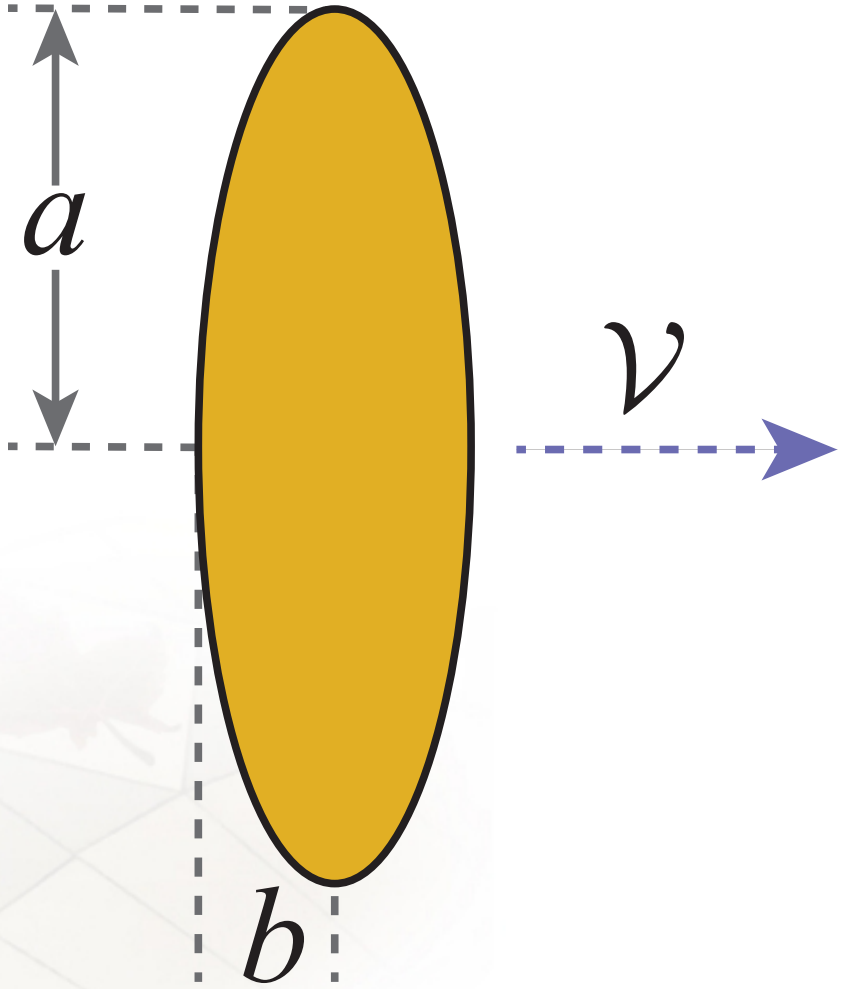

Figure : Ellipsoid oriented with the major axis oriented perpendicular to the direction of motion.

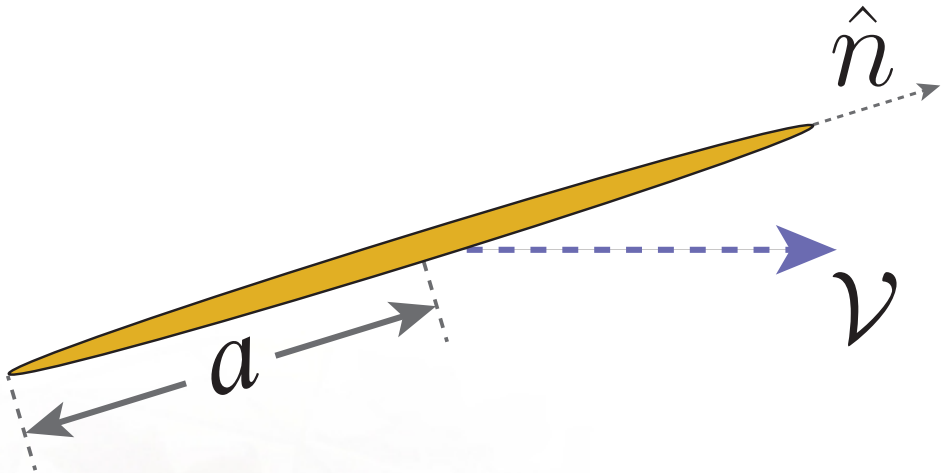

Figure : The friction coefficient of a rod-like body is orientation dependent. A rod oriented perpendicular to its direction of motion has a friction coefficient that is roughly double that of a rod oriented along its direction of motion.

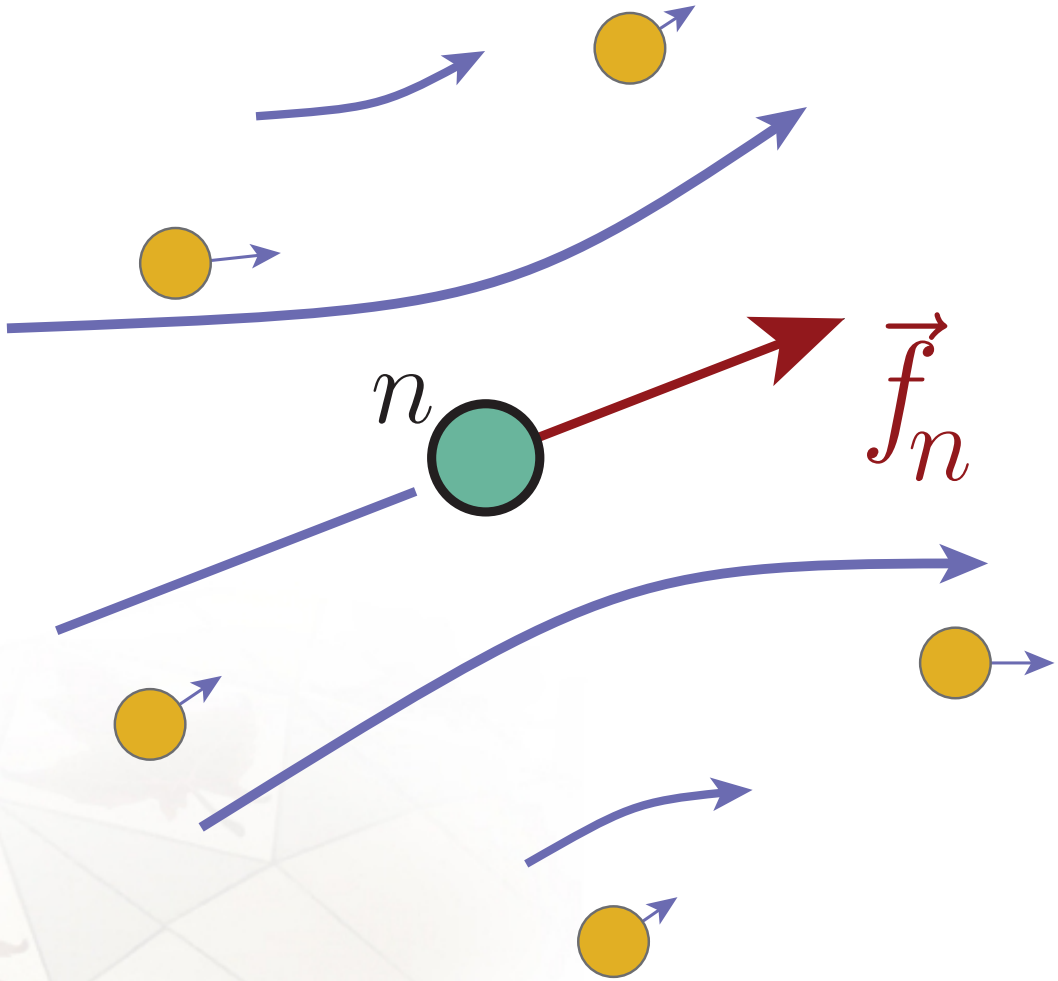

Figure : The motion of a solute n subject to a force perturbs the surrounding fluid. The resulting flow enacts a hydrodynamic-mediated force on neighbouring solutes. Likewise, the motion of all the neighbouring solutes enact a net force on the n^{th} monomer. This is the idea of long-ranged hydrodynamic interactions.

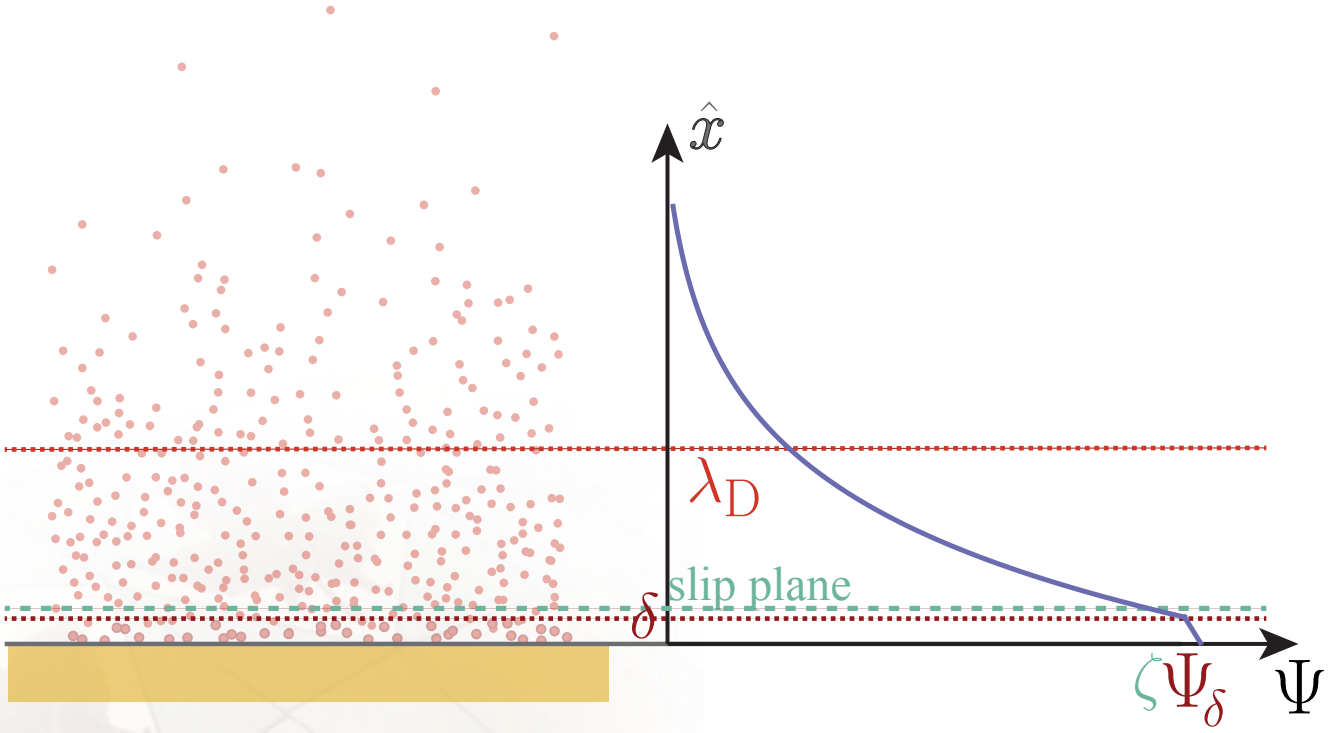

Figure : Schematic of electric double layer.

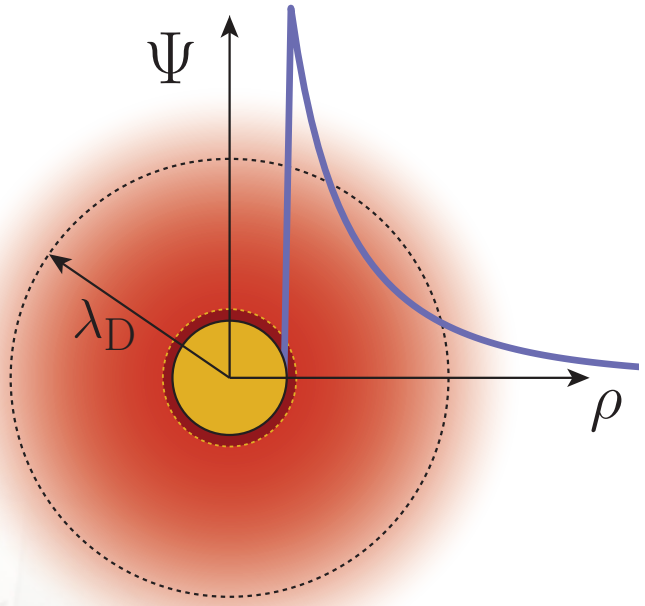

Figure : The Debye-Hückel approximation around a spherical, charged particle.

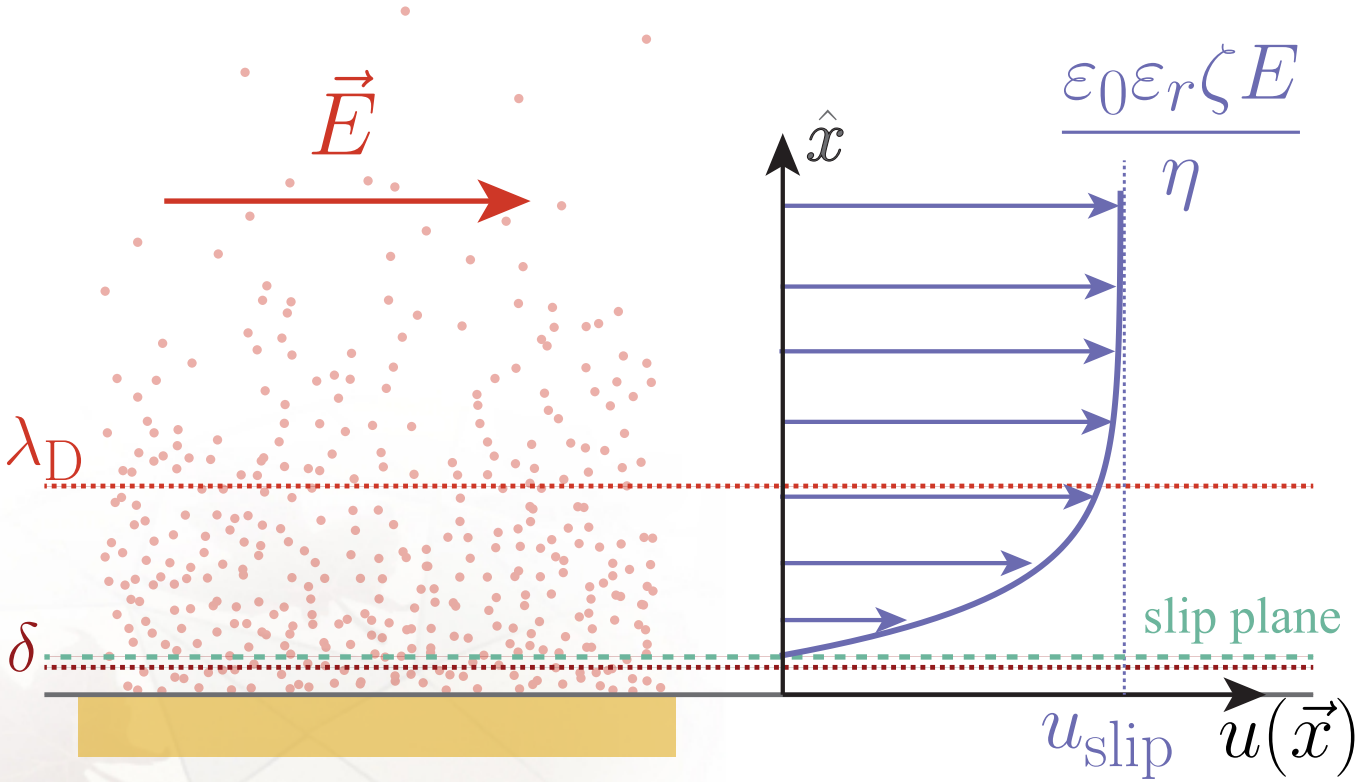

Figure : Schematic electro-osmotic flow parallel to a planar wall.

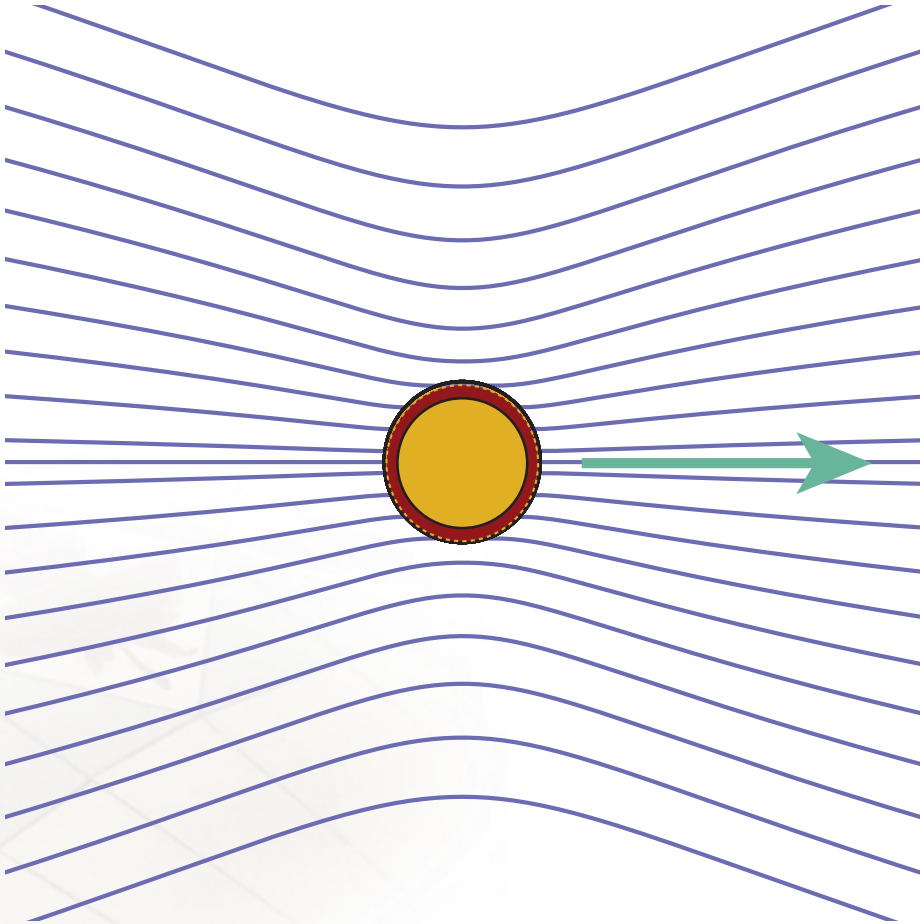

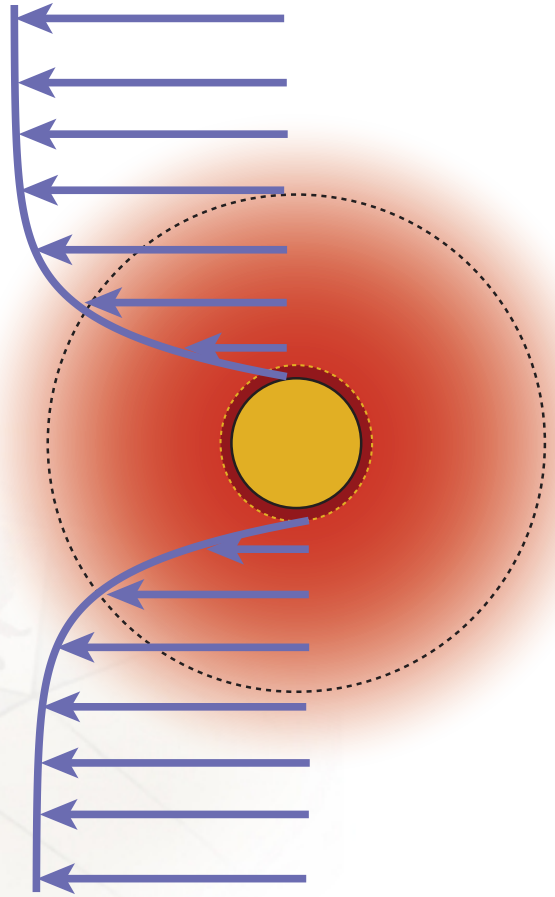

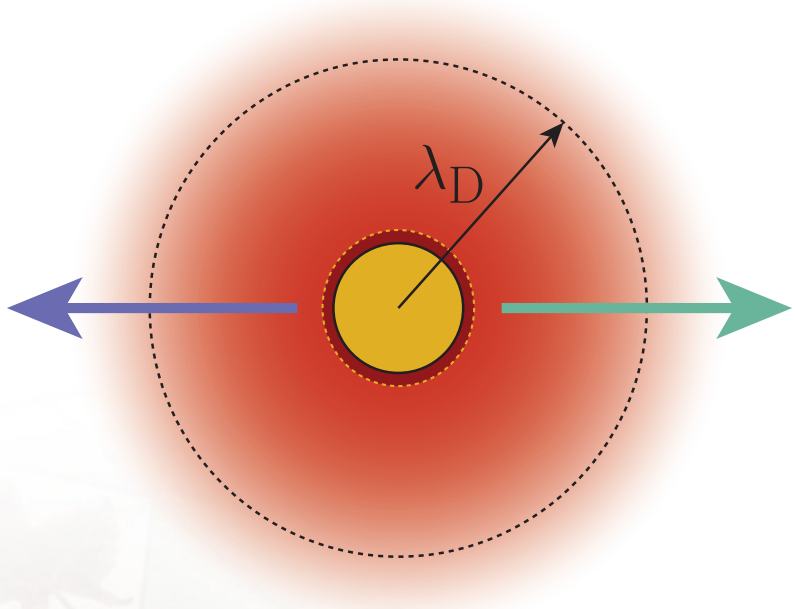

Figure : Schematic representation of hydrodynamic interaction screening due to the diffuse layer. The electric field pulls on the monomer and its ion sheath with equal and opposite force. To first order, the perturbation of the fluid due to the shear from the monomer is cancelled by the shear due to the counter-ions. Hydrodynamic interactions can only exist on length scales shorter than λ_D.

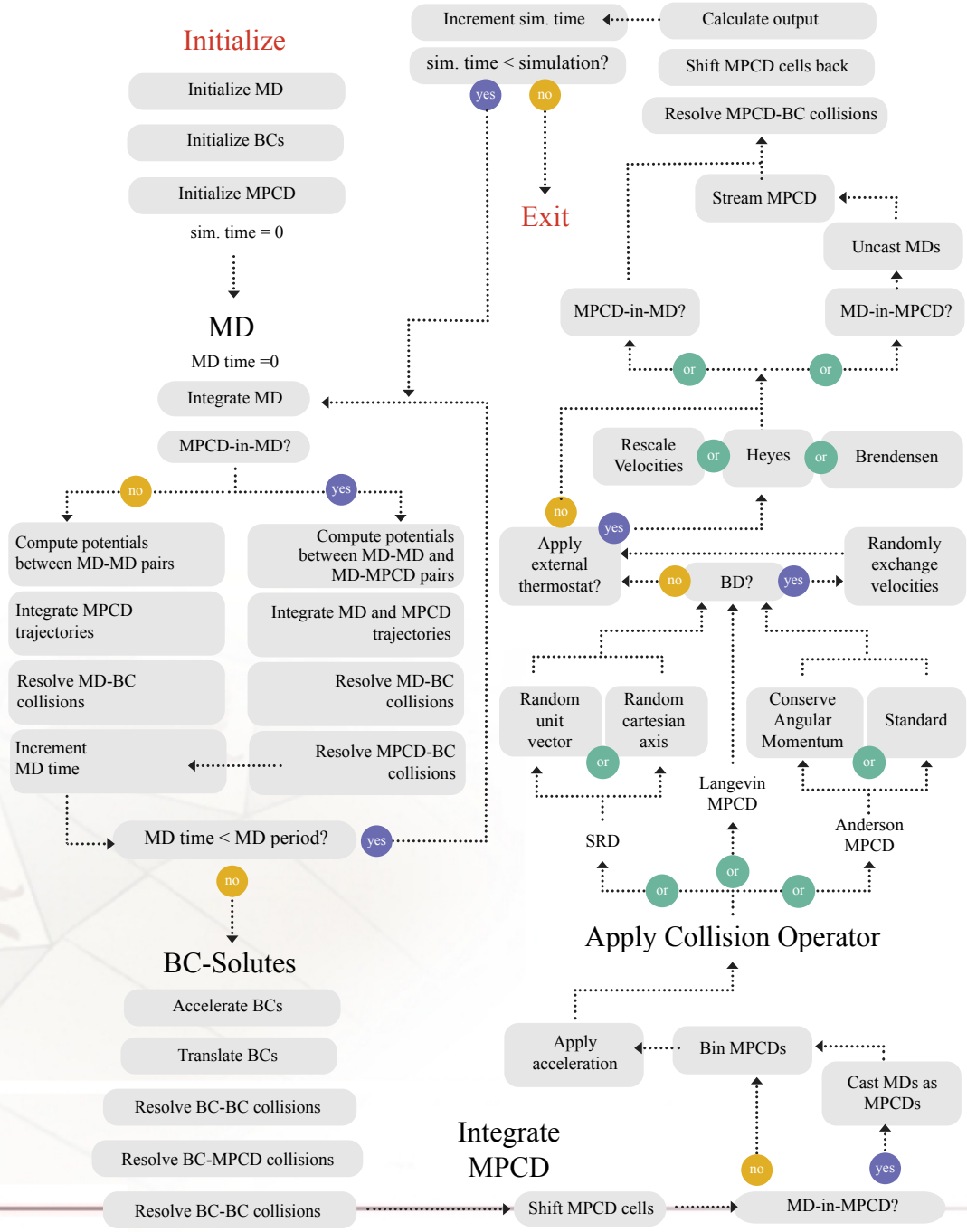
Initialize
Initialize MD
Initialize BCs
Initialize MPCD
sim. time = 0
MD
MD time =0
Integrate MD
MPCD-in-MD?
no
yes
Compute potentials between MD-MD pairs
Integrate MPCD trajectories
Resolve MD-BC collisions
Increment MD time
Compute potentials between MD-MD and MD-MPCD pairs
Integrate MD and MPCD trajectories
Resolve MD-BC collisions
Resolve MPCD-BC collisions
MD time < MD period?
yes
no
BC-Solutes
Accelerate BCs
Translate BCs
Resolve BC-BC collisions
Resolve BC-MPCD collisions
Resolve BC-BC collisions
Integrate MPCD
Shift MPCD cells
MD-in-MPCD?
no
yes
Apply acceleration
Bin MPCDs
Cast MDs as MPCDs
Apply Collision Operator
Random unit vector
Random cartesian axis
or
SRD
Langevin MPCD
Conserve Angular Momentum
Standard
or
Anderson MPCD
or
or
or
Apply external thermostat?
no
yes
BD?
no
yes
Randomly exchange velocities
Rescale Velocities
or
Heyes
or
Brendensen
MPCD-in-MD?
MD-in-MPCD?
or
or
Stream MPCD
Uncast MDs
Resolve MPCD-BC collisions
Shift MPCD cells back
Calculate output
Increment sim. time
sim. time < simulation?
yes
no
Exit

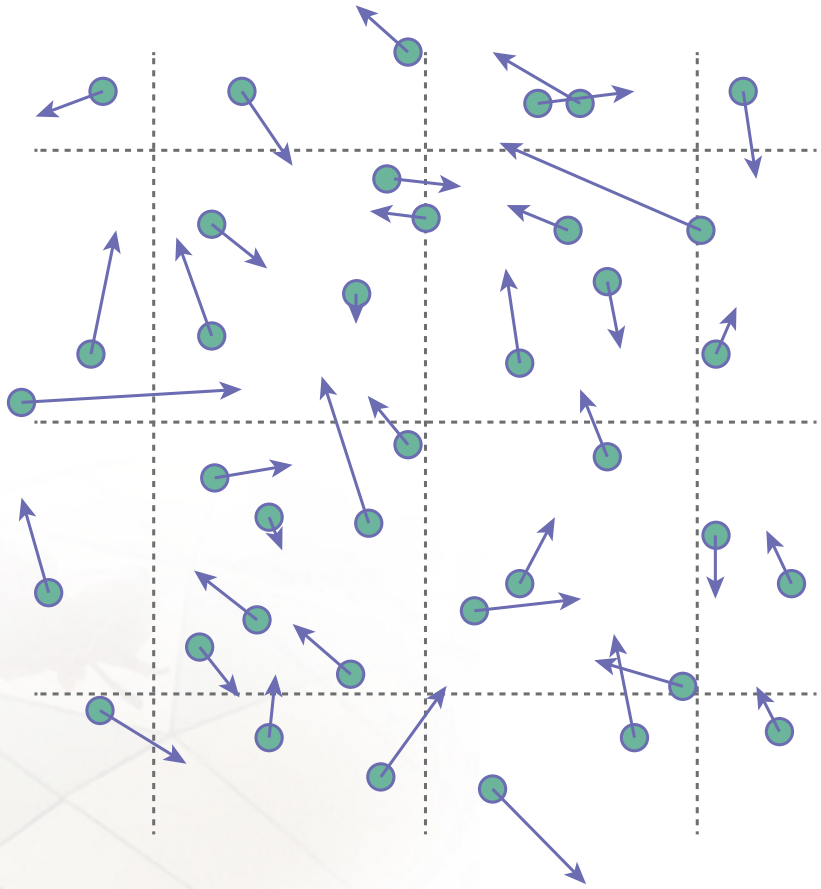

Figure : The streaming step.

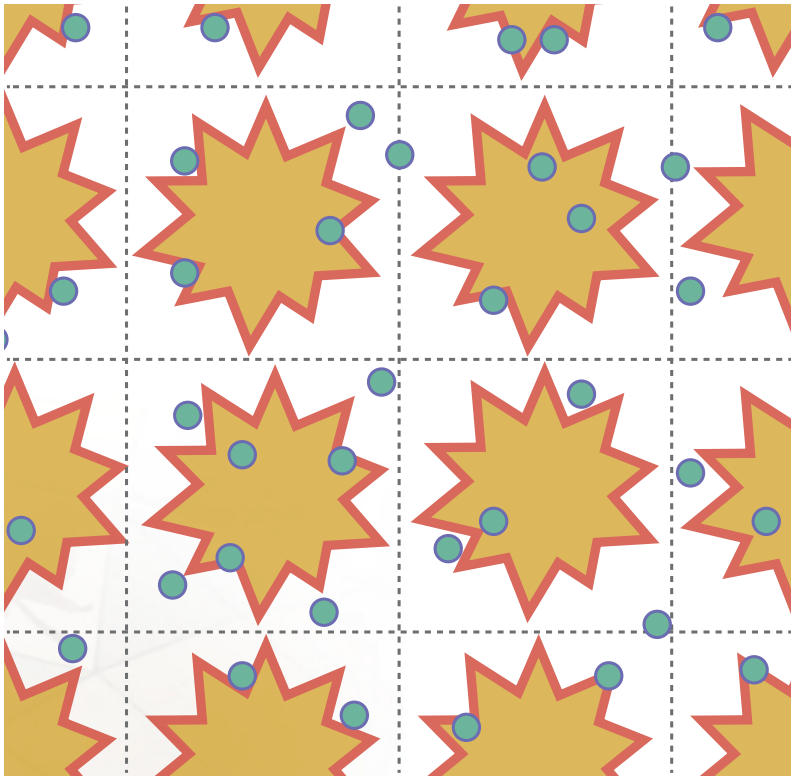

Figure : The collision step.

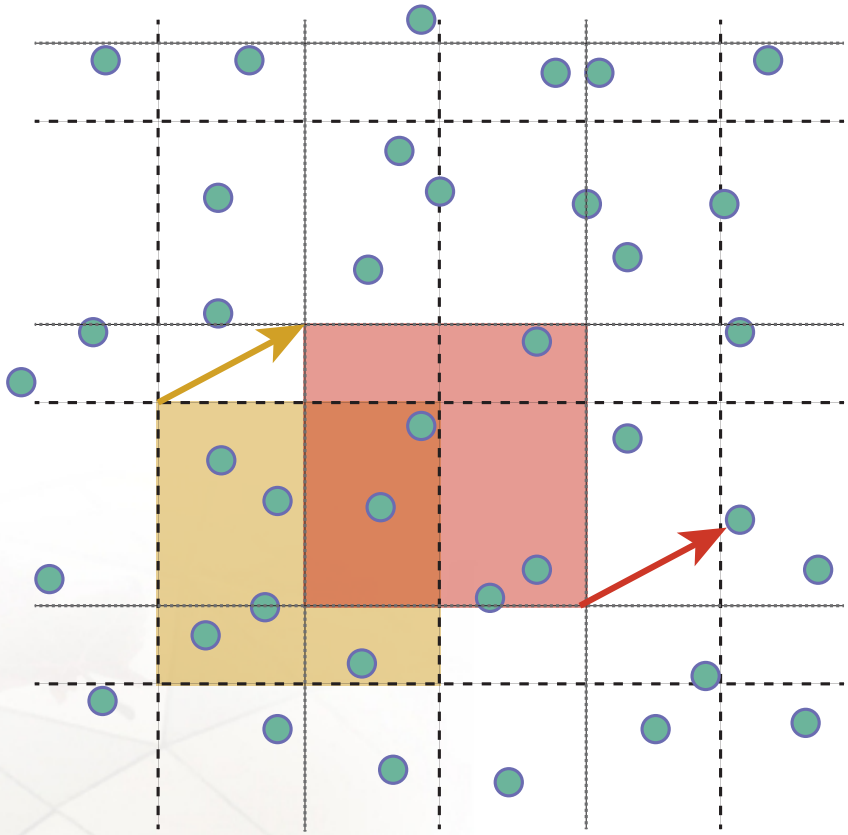

Figure : The structure of the MPCD cells breaks Galilean invariance. The MPCD fluid properties depend on the frame of reference because at low temperatures, a given particle may collide with a different set of neighbours depending on the frame of reference.

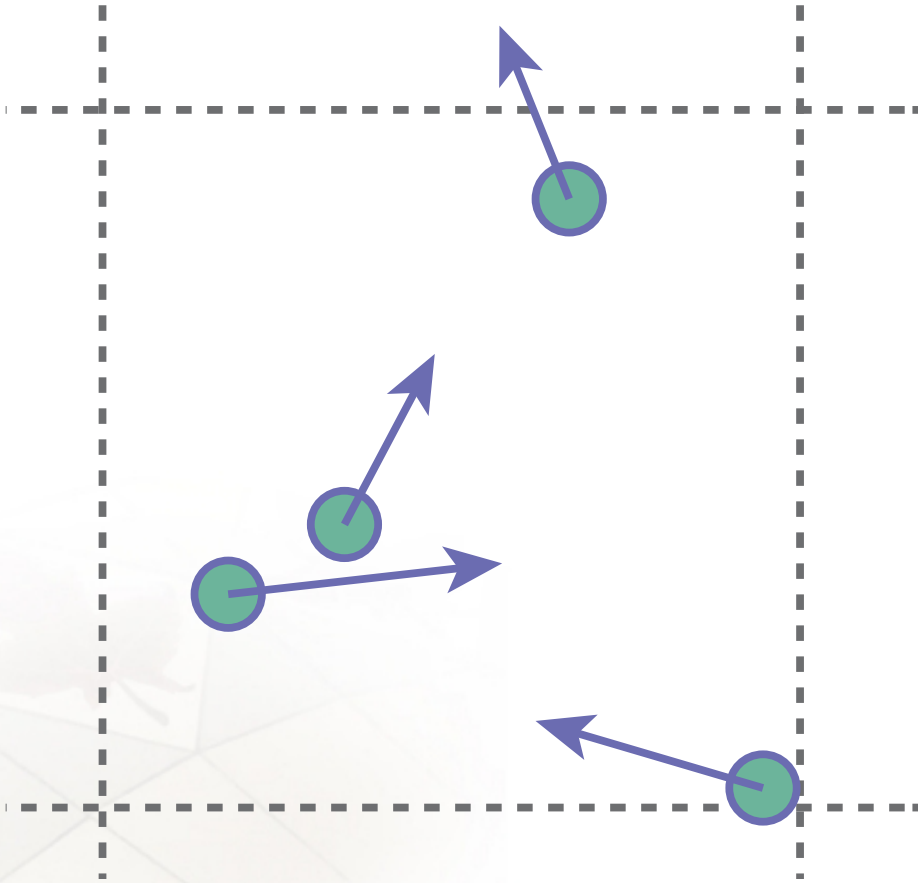

Figure : Bin MPCD particles into cells.

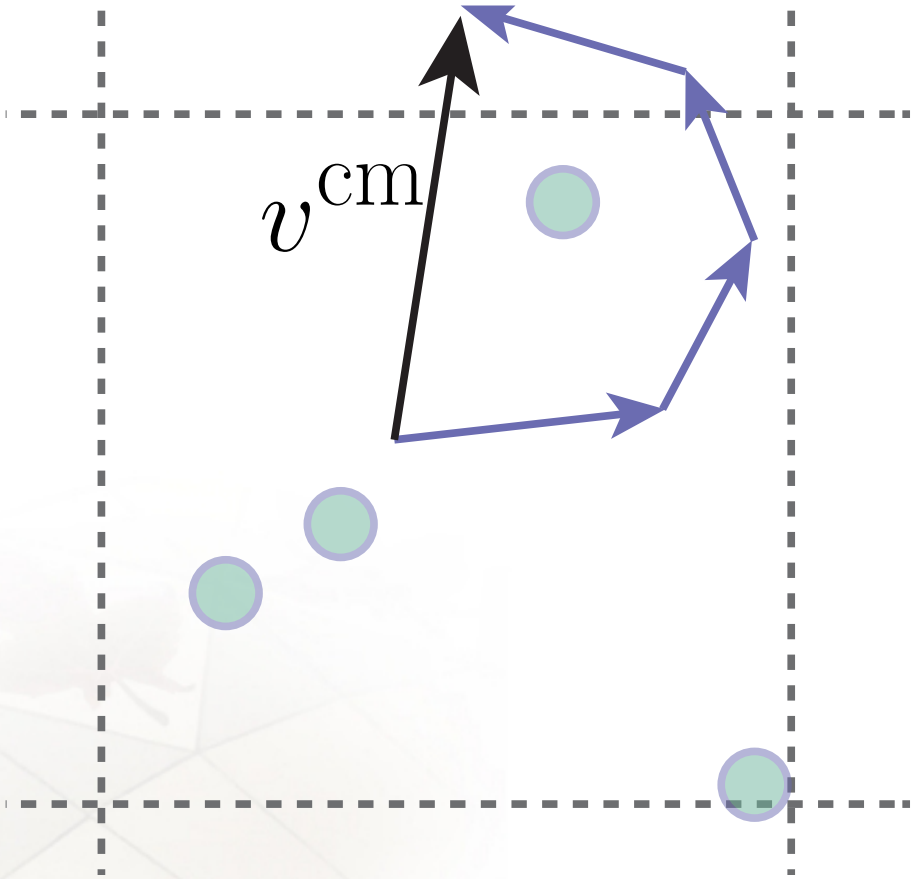

Figure : Calculate centre of mass velocity v^{cm}.

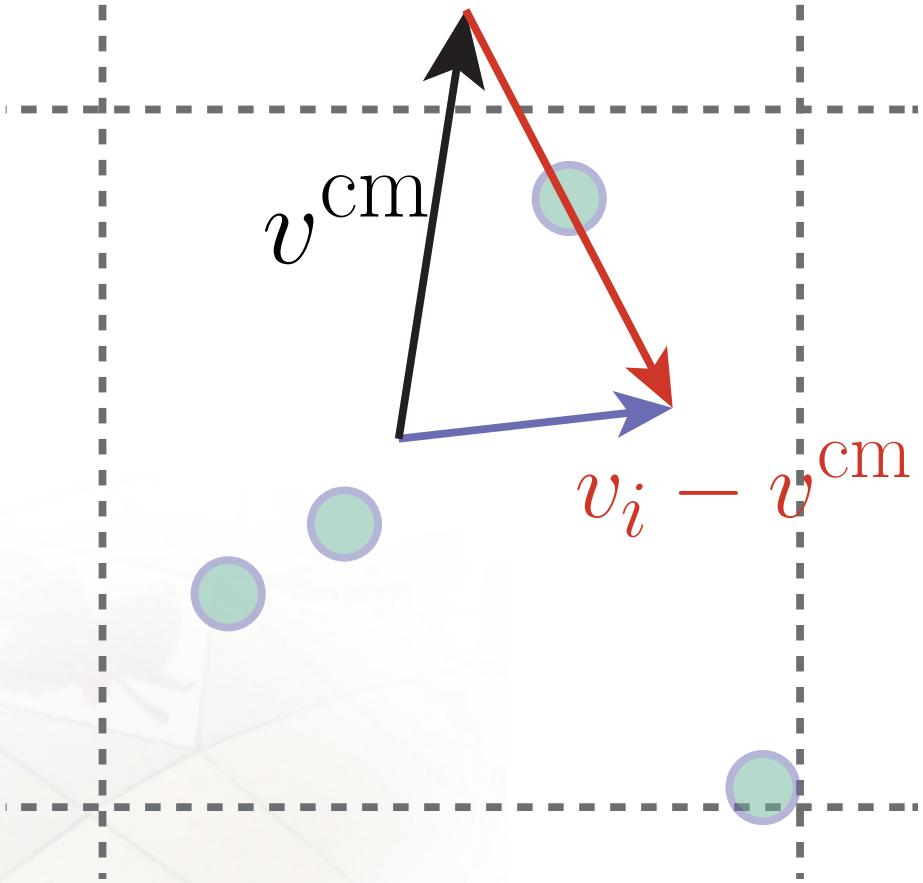

Figure : For each MPCD particle calculate the difference from v^{cm}.

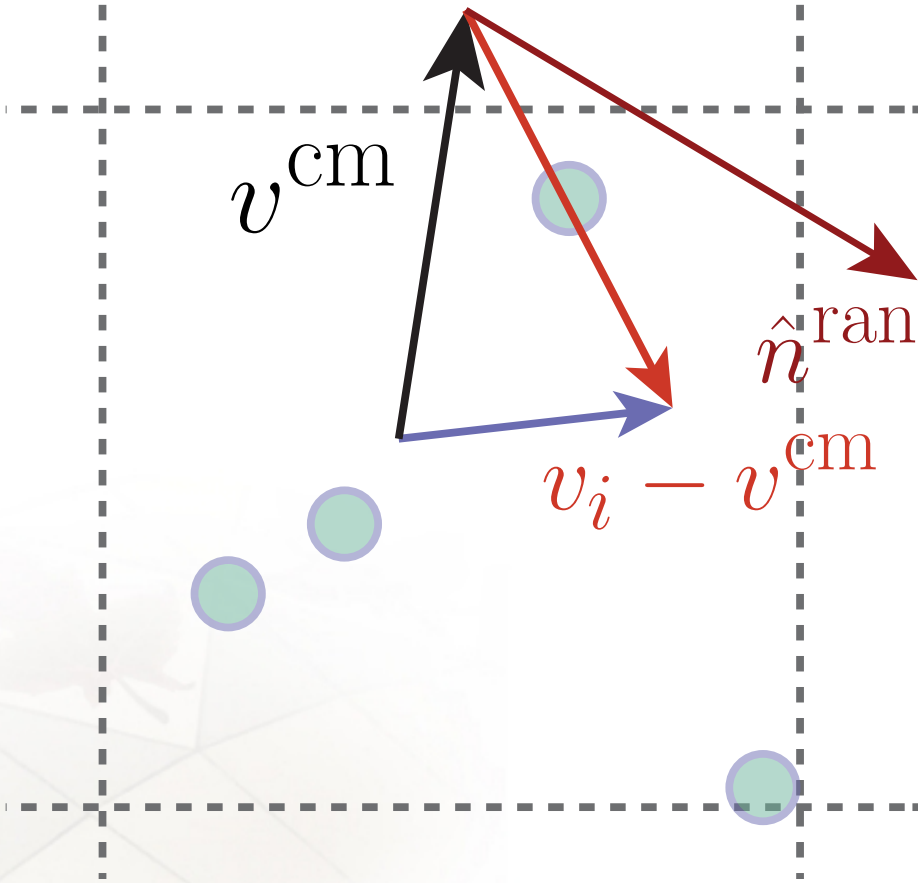

Figure : For each cell generate a random unit vector $\hat{n}^{\mathrm{ran}}$.

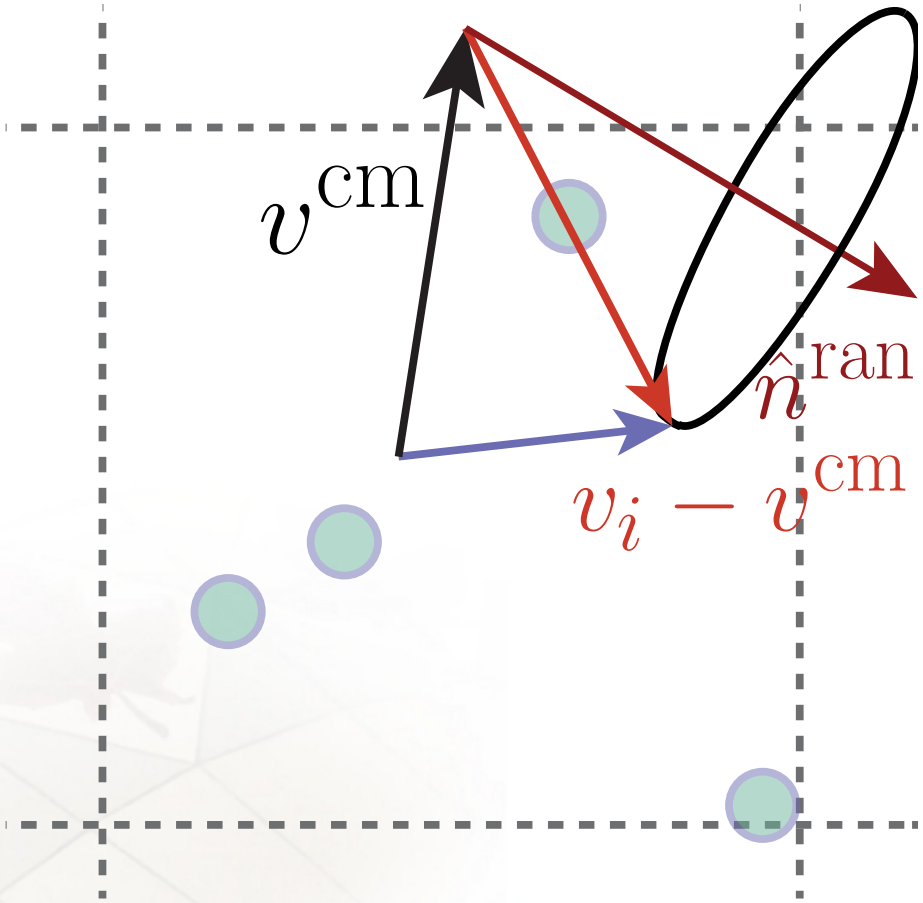

Figure : Rotate each difference about $\hat{n}^{\mathrm{ran}}$ by ϑ.

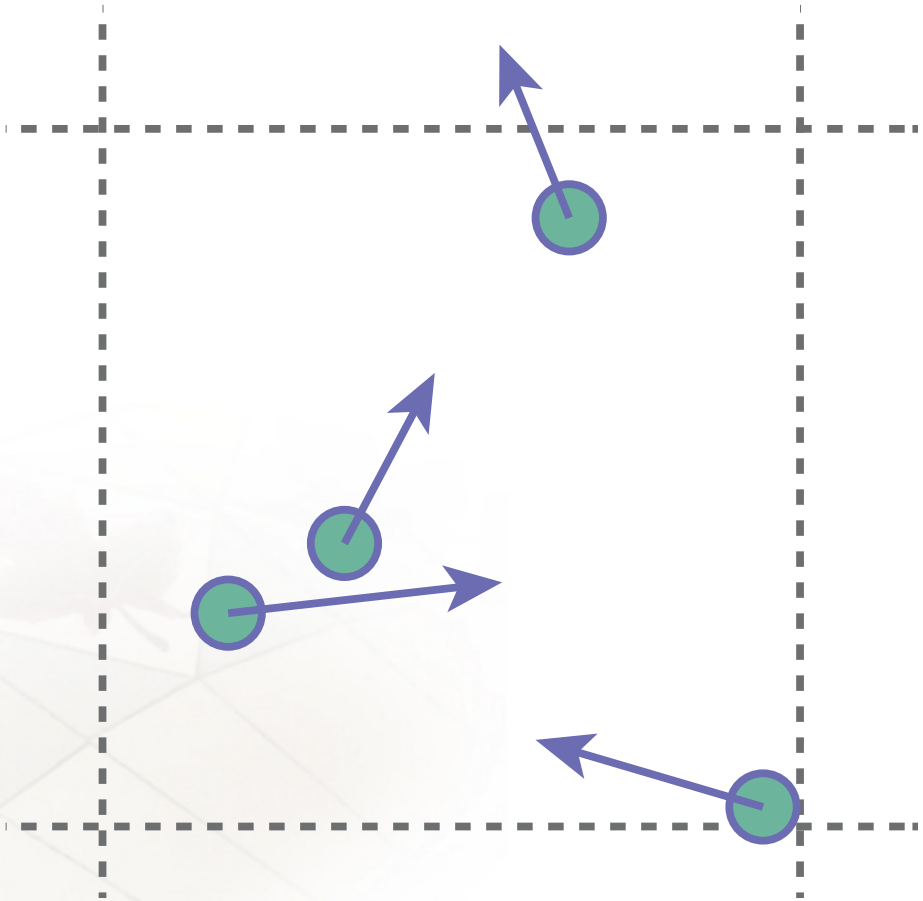

Figure : Bin MPCD particles into cells.

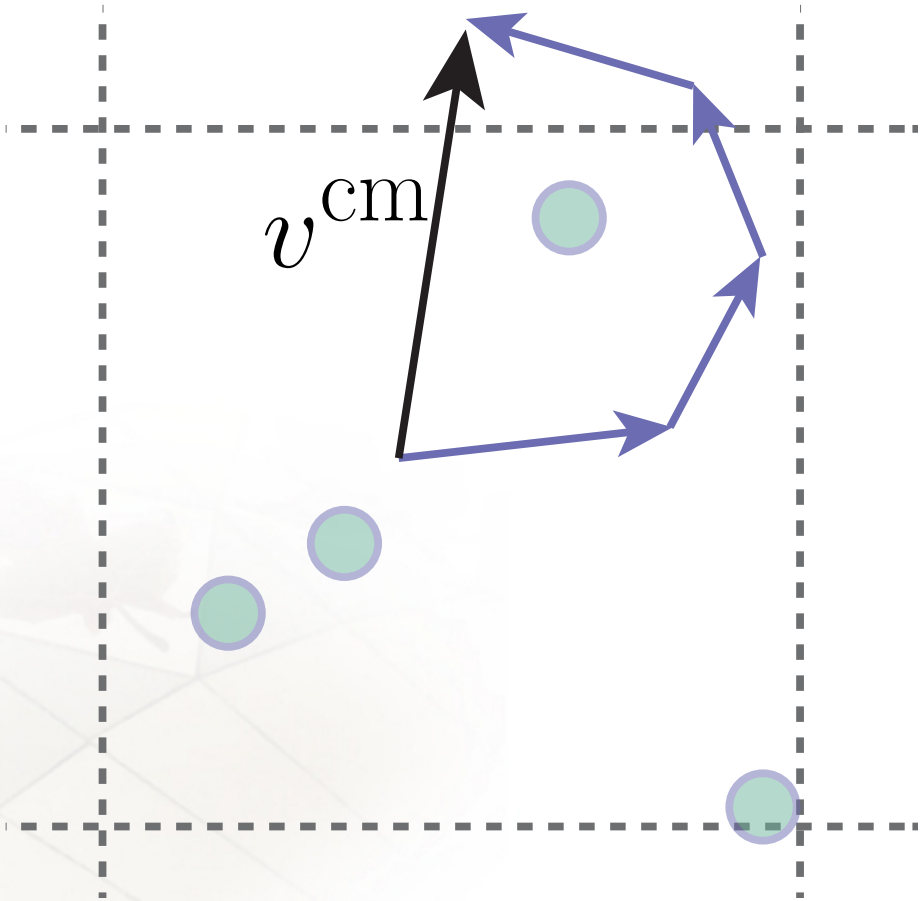

Figure : Calculate centre of mass velocity v^{cm}.

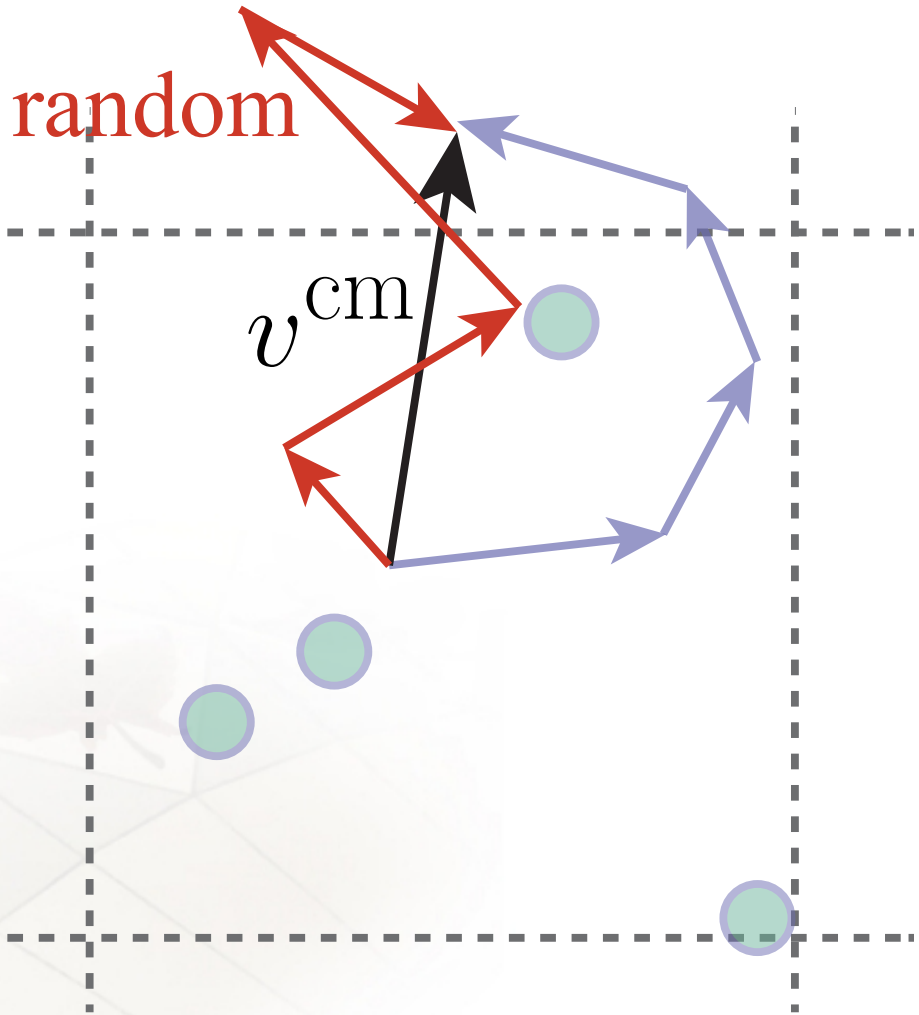

Figure : For each MPCD particle generate a random velocity that all sum to v^{cm}.

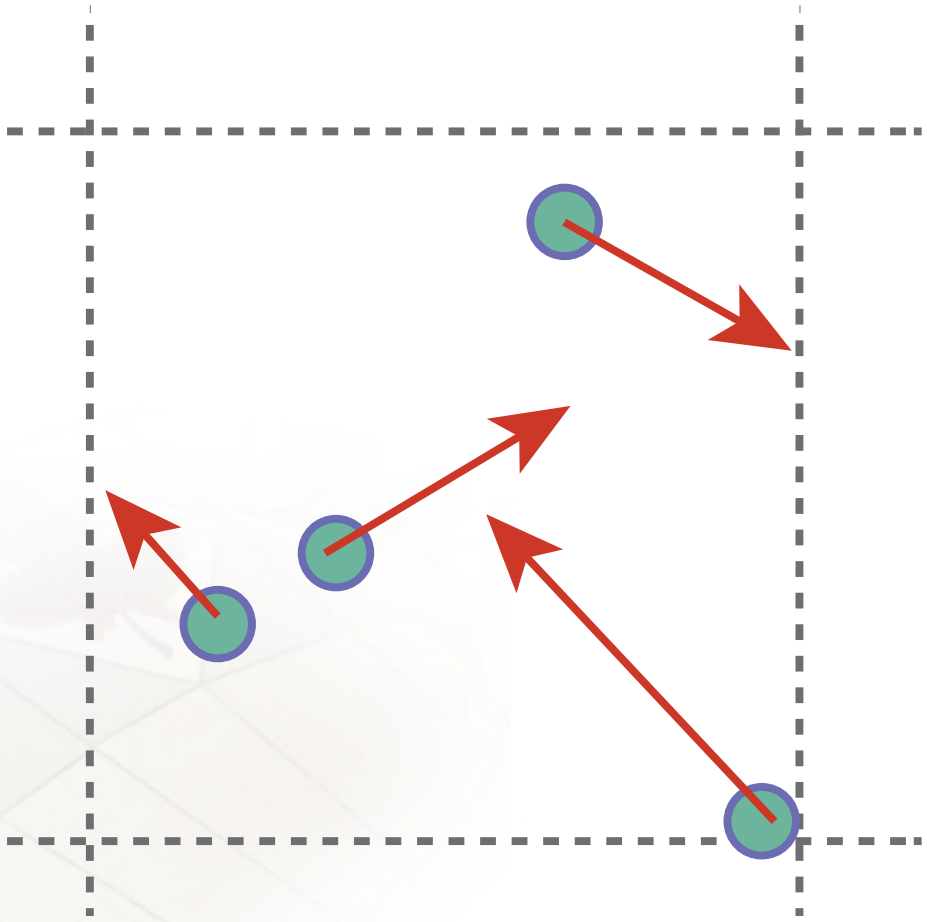

Figure : Apply to each MPCD particle.

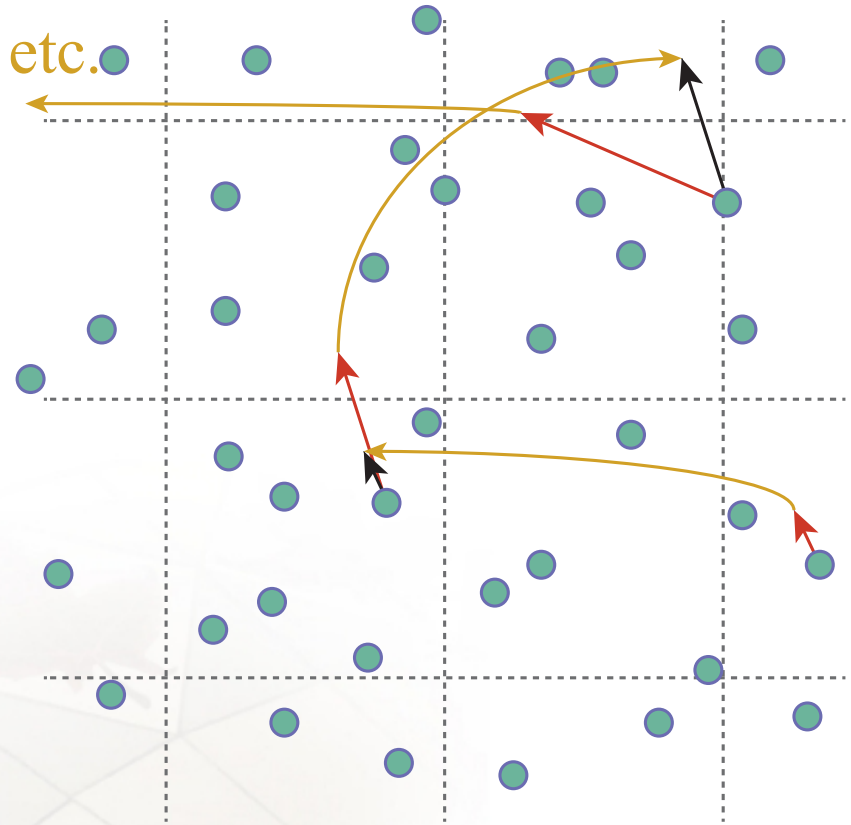

Figure : In order to produce a Brownian fluid with the same properties as an MPCD fluid but with no hydrodynamic interactions, the velocities of all the particles are randomly interchanged.

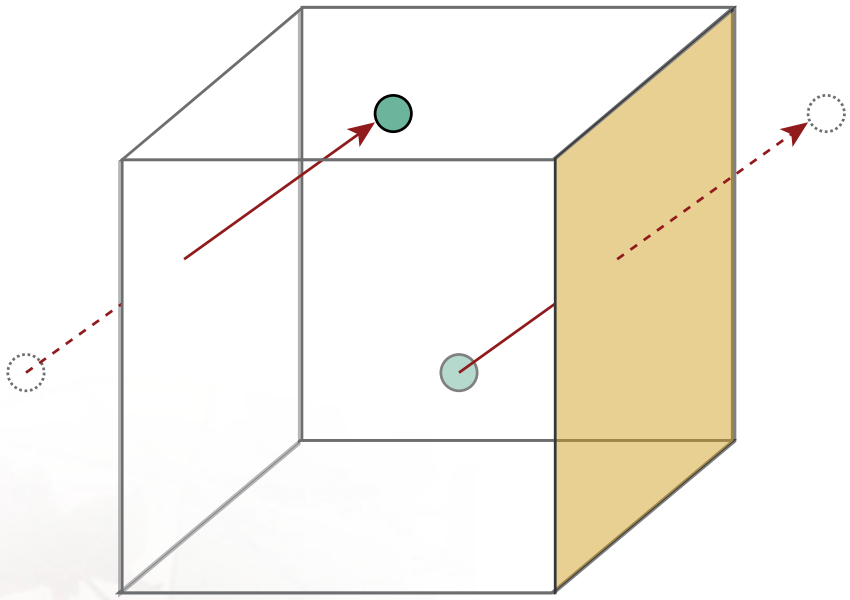

Figure : Periodic boundary conditions wrap the system and the positions of particles that pass the planar surface are shifted to the opposite end of the control volume.

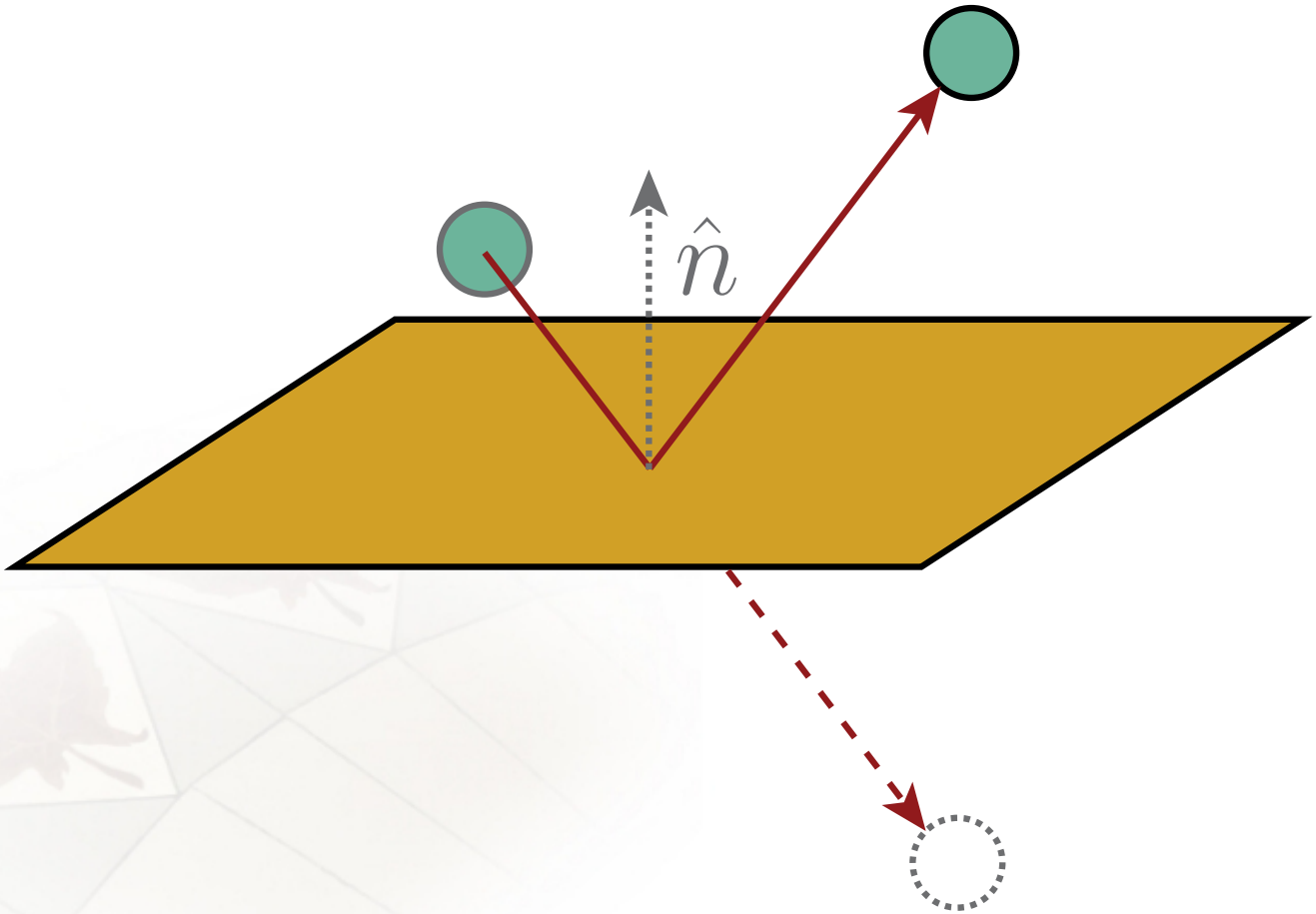

Figure : Reflective boundary conditions invert the normal component of a colliding particle's velocity.

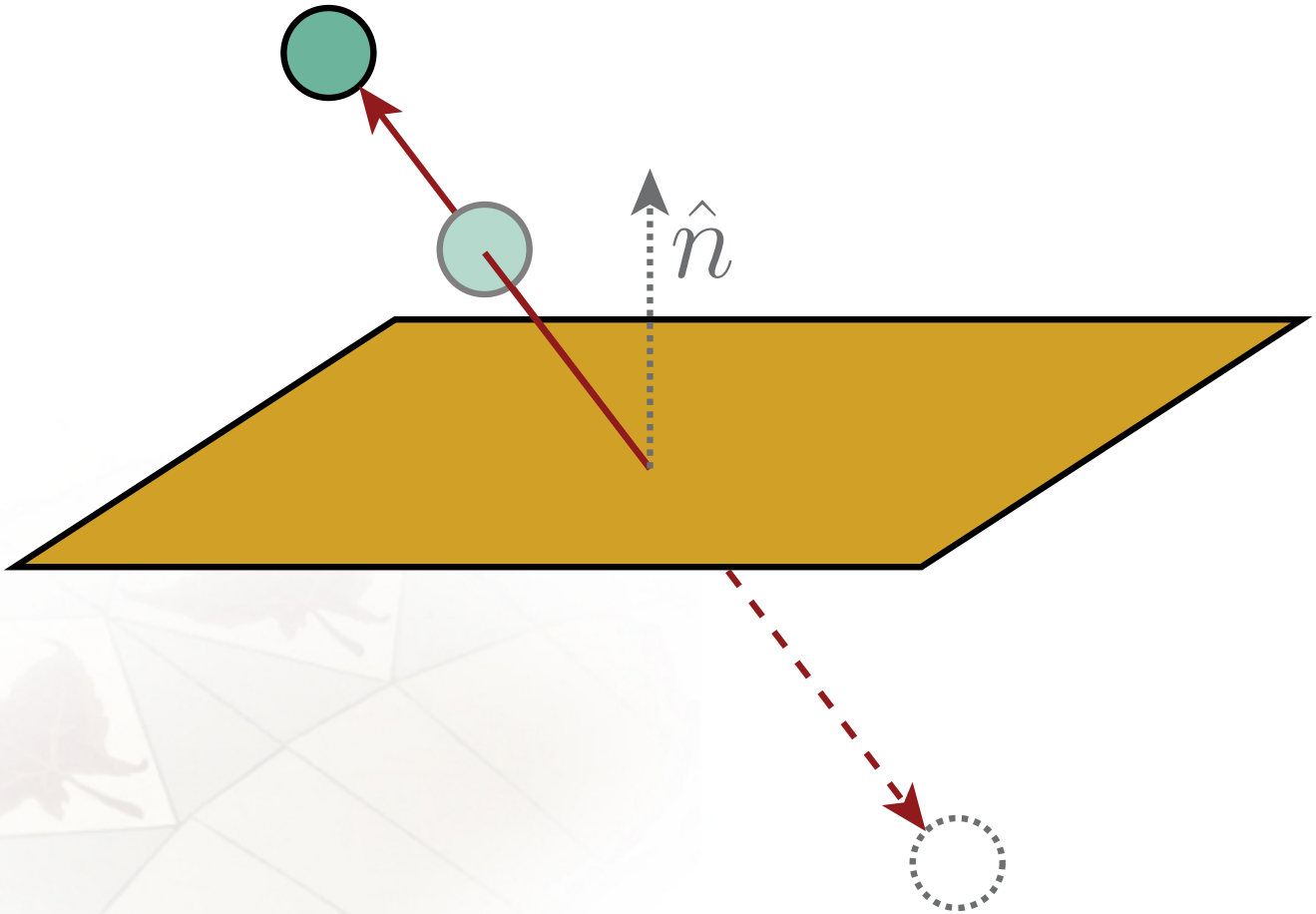

Figure : Bounce-back boundary conditions invert both the normal and tangential components of a colliding particle's velocity.

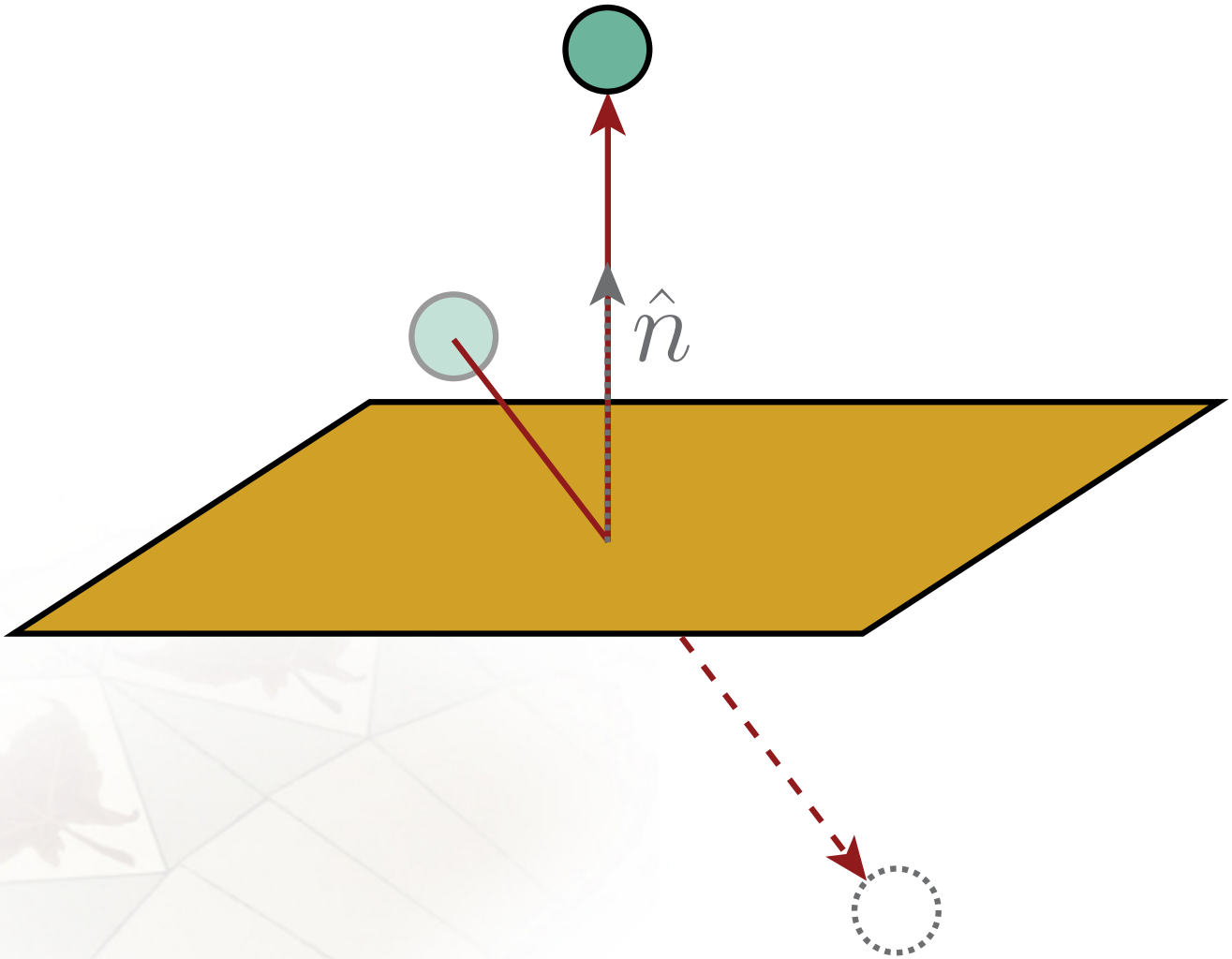

Figure : Stick boundary conditions invert the normal component of a colliding particle's velocity and set the tangential component to zero.

$$\langle N_c \rangle = 5$$

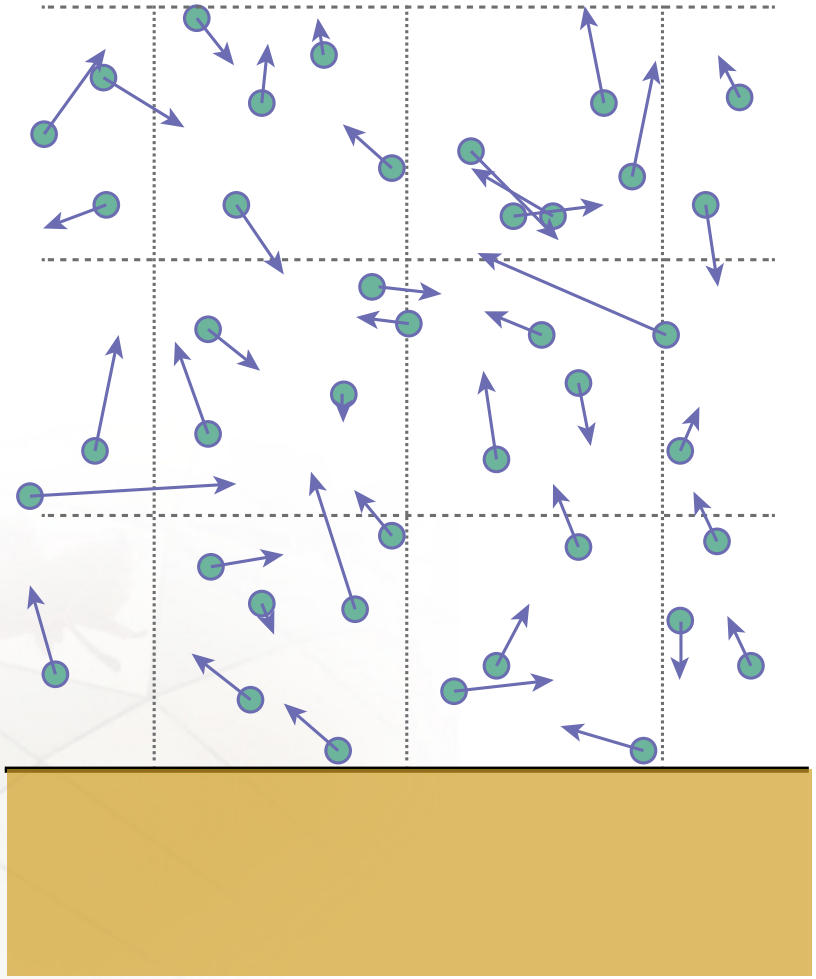

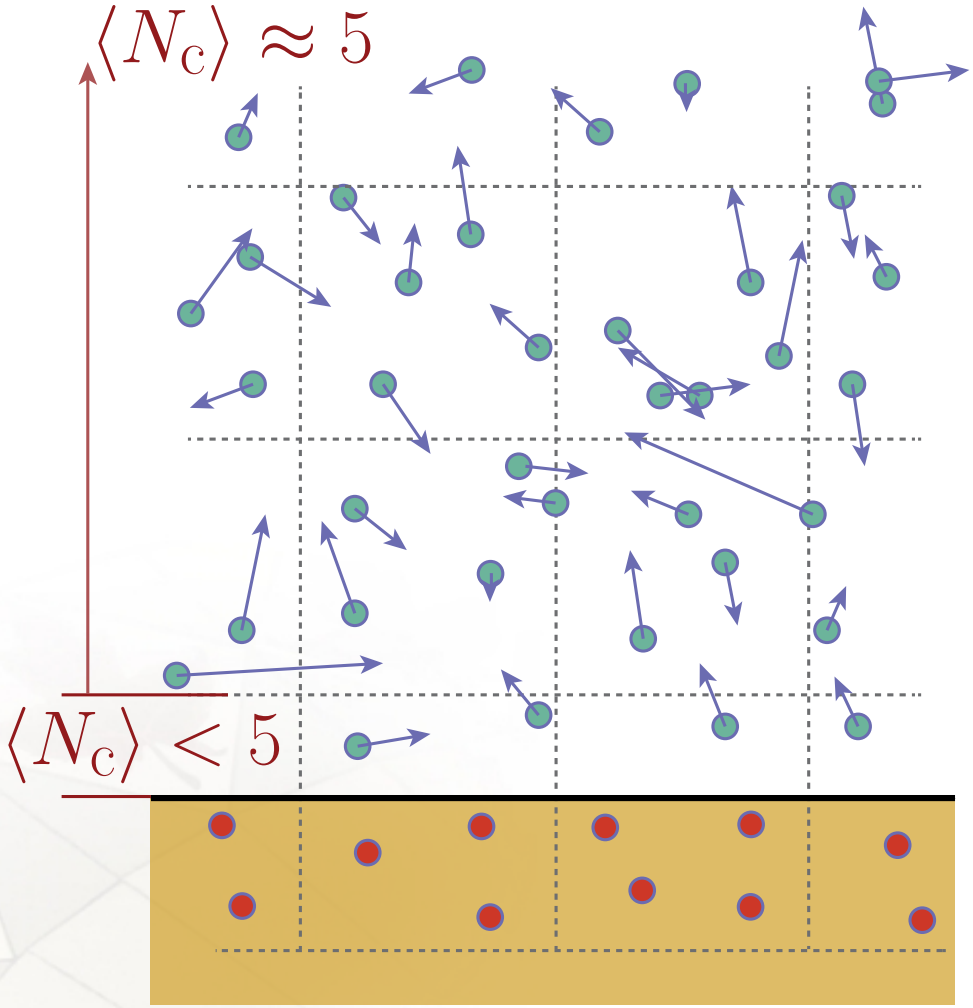

Figure : When a planar, bounce-back wall is flush to the neighbouring MPCD cells, no-slip boundary conditions are respected. However, if the boundary surface excludes a portion of the MPCD cells, the local average number of MPCD fluid particles is less than typical in the bulk, which reduces the local viscosity.

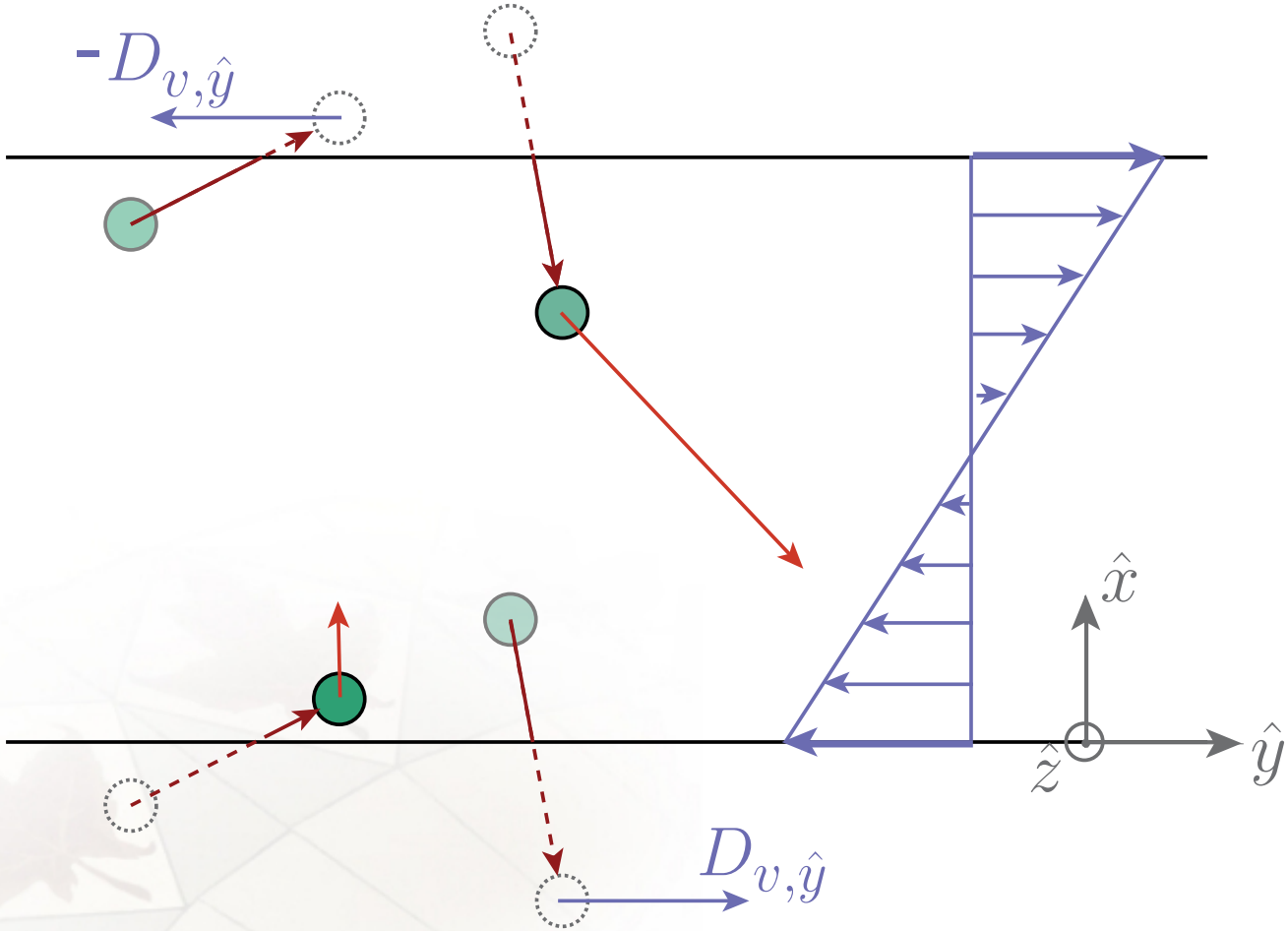

Figure : Lees-Edwards boundary conditions for simple shear.

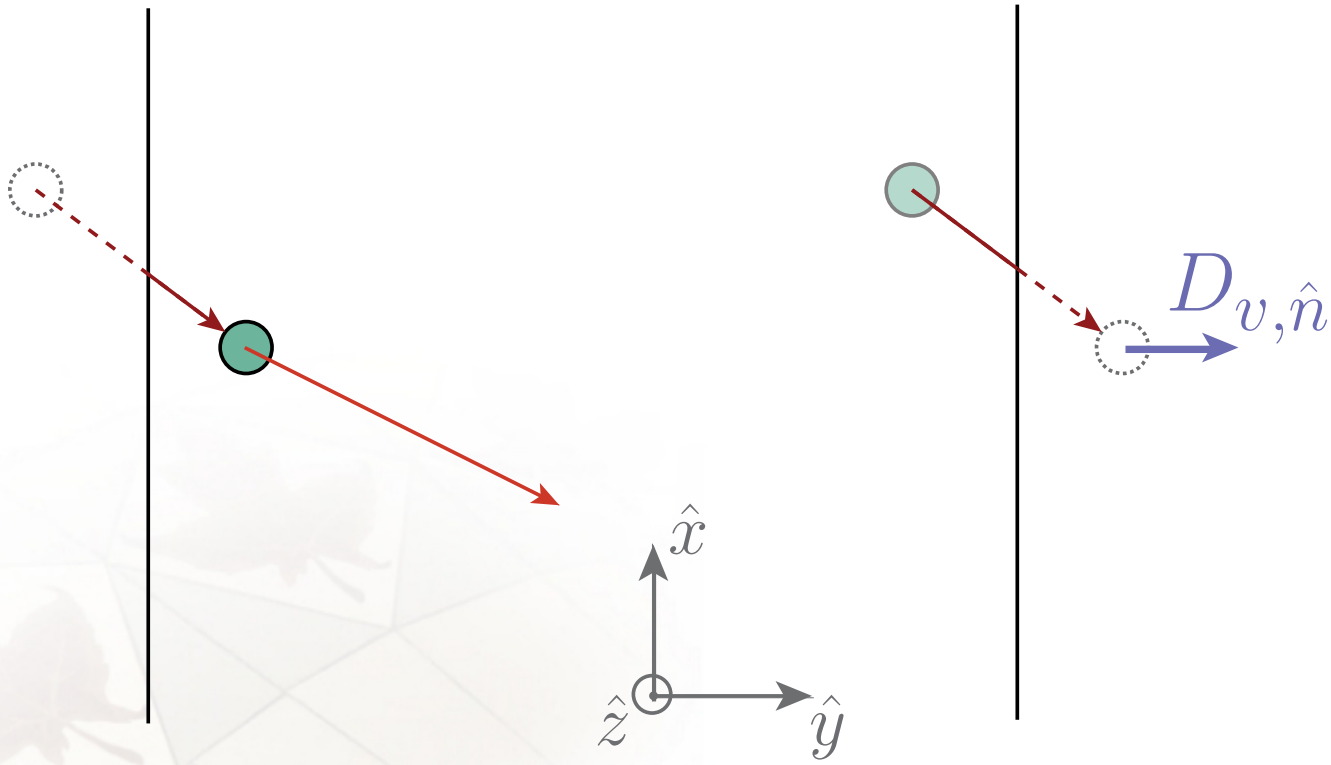

Figure : Pump periodic boundary conditions for homogeneous (or plug) flows.

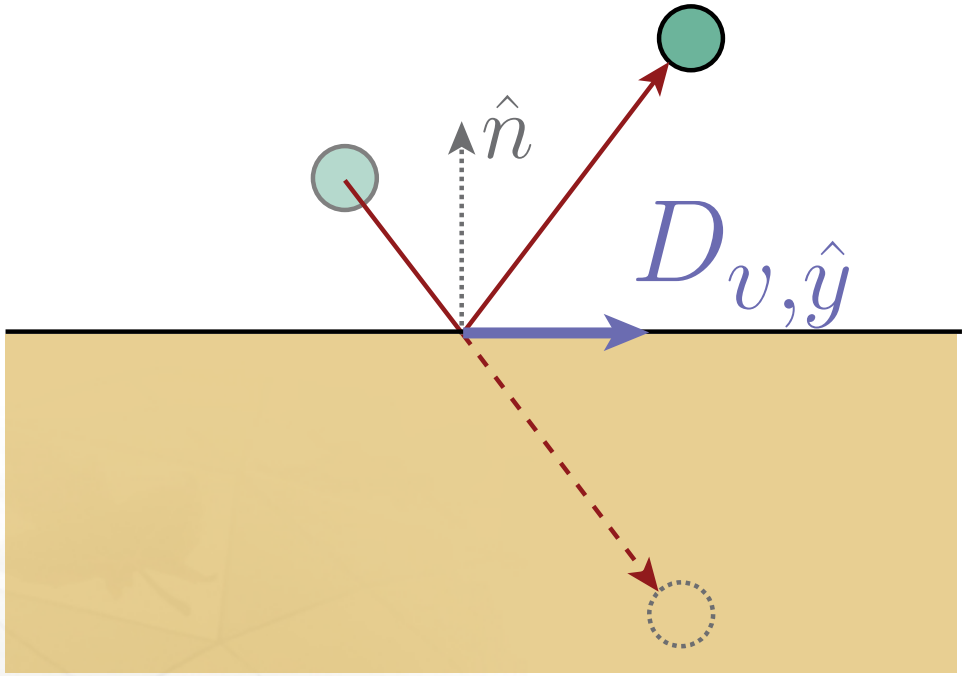

Figure : Translating no-slip boundary conditions simulating a moving wall.

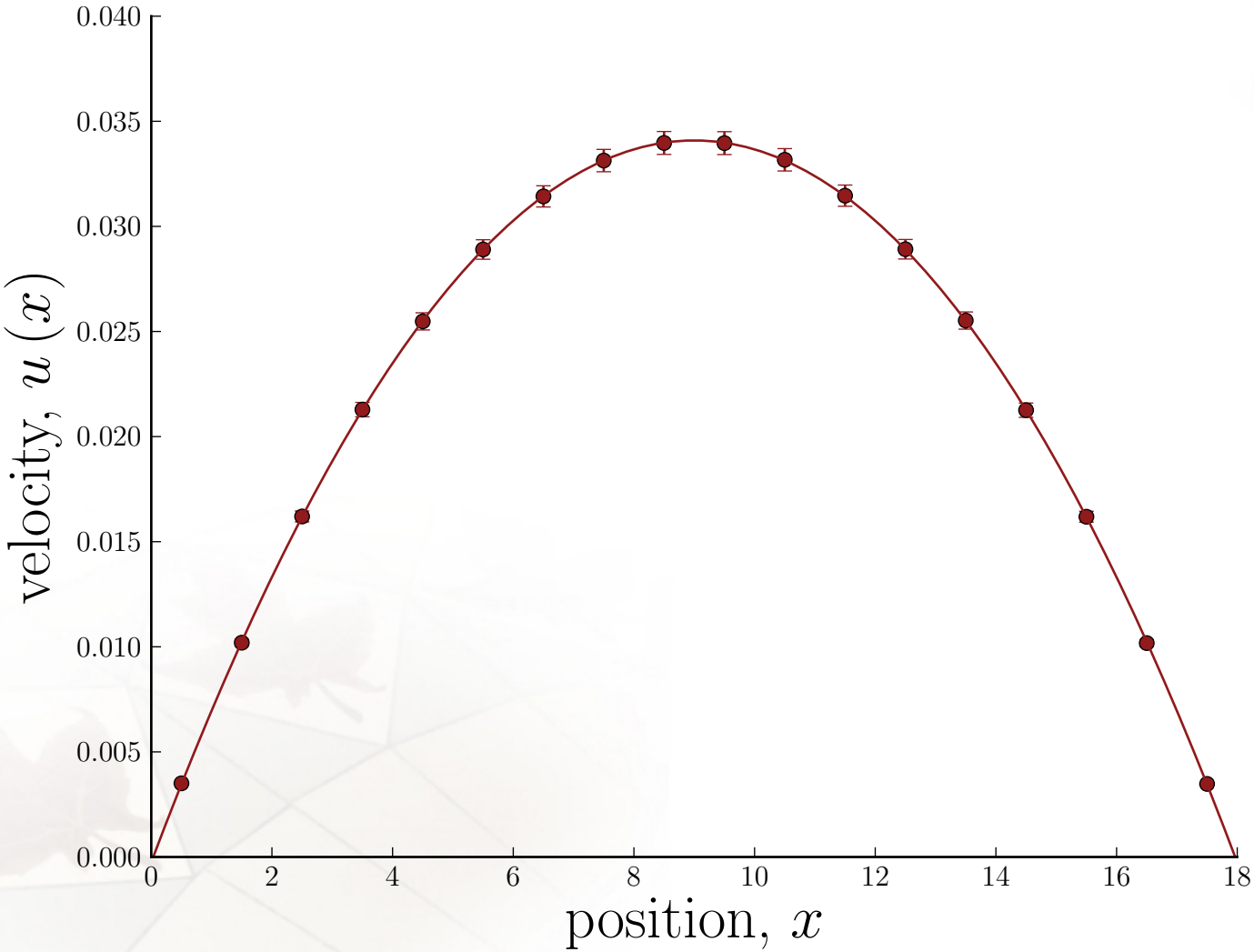

Figure : 2D simulation.

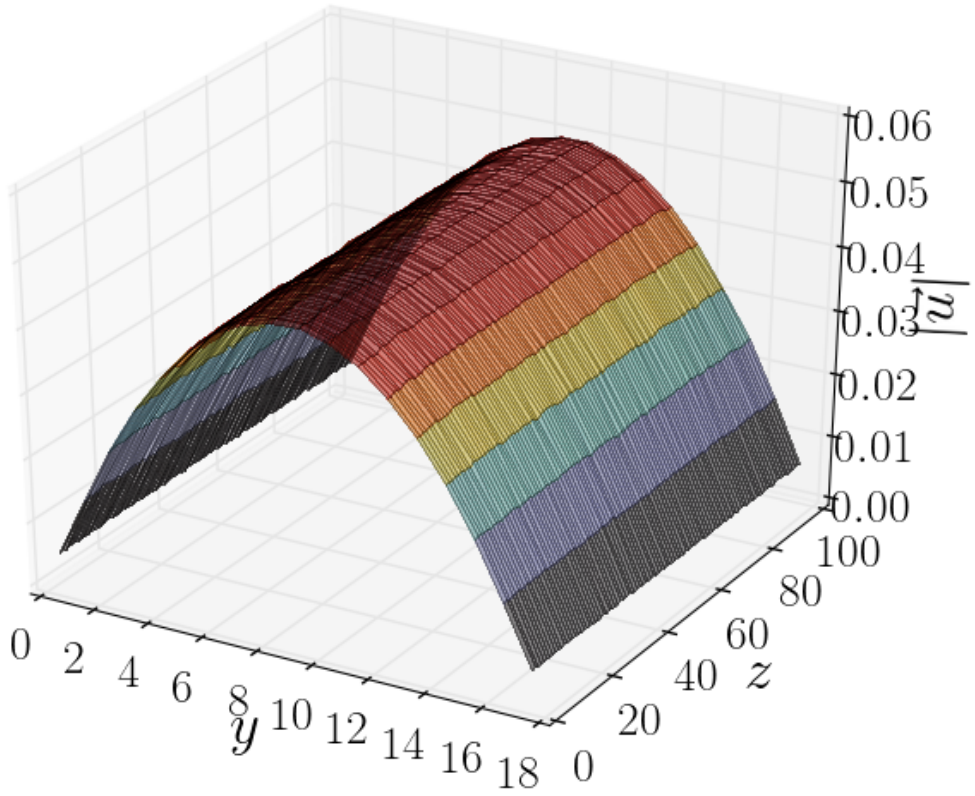

Figure : 3D simulation.

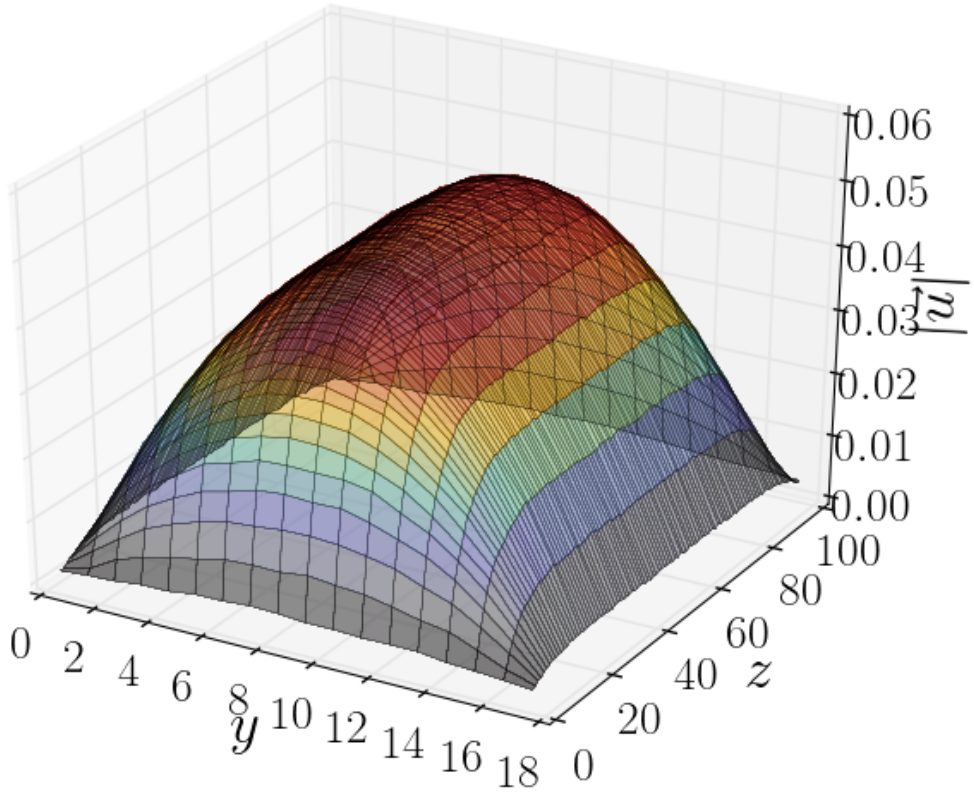

Figure : Flow profile produced by 3D Anderson-MPCD simulation of flow through a rectangular channel of aspect ratio $\tilde{w} = 9/50$.

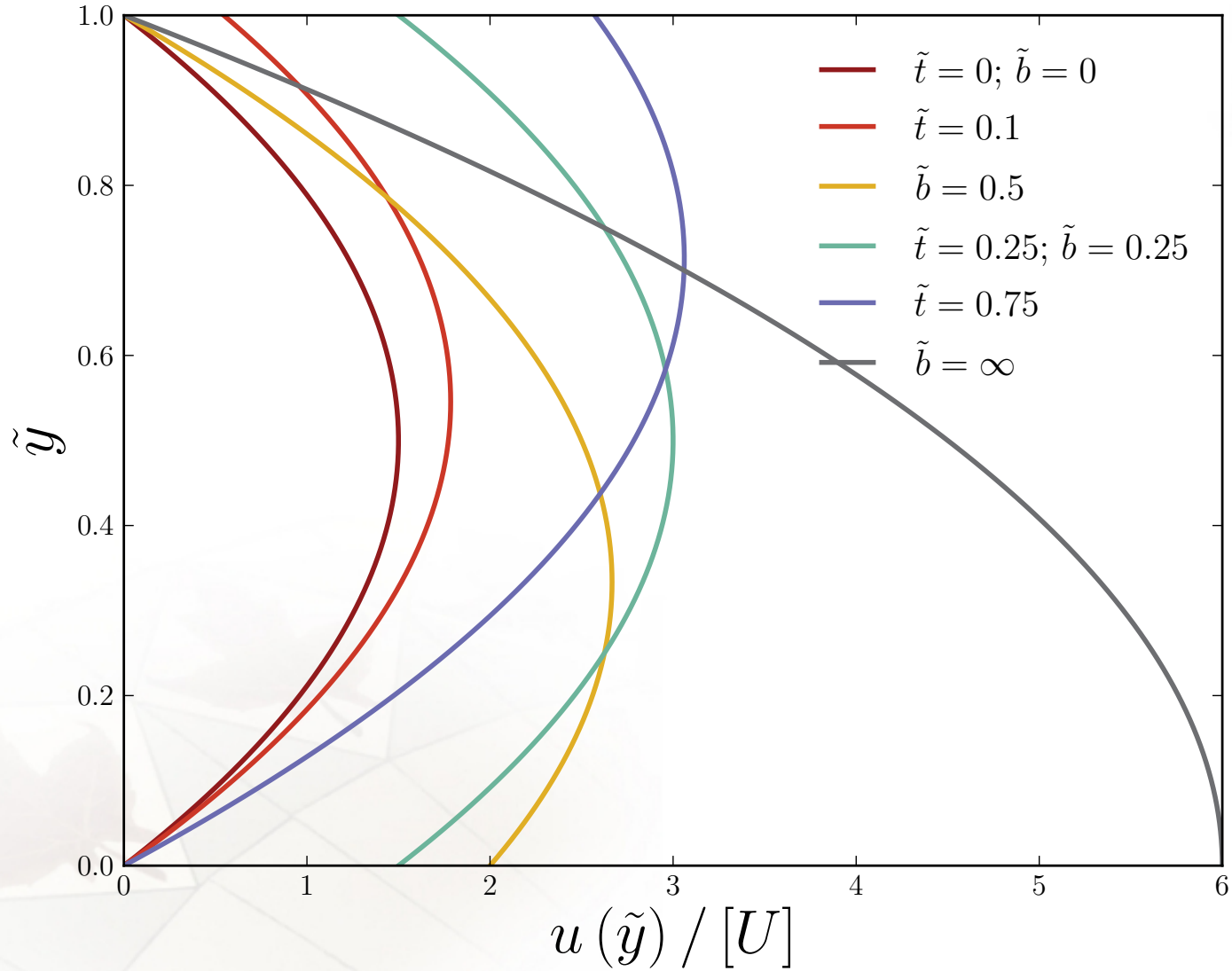

Figure : Fluid flow profiles for a variety of slip lengths $\tilde{b}$ and $\tilde{t}$, for the accumulation (or bottom) and depletion (or top) wall respectively. Fluid velocity normalized by no slip $[U] = h^2 (\partial P/\partial y) /12\eta$.

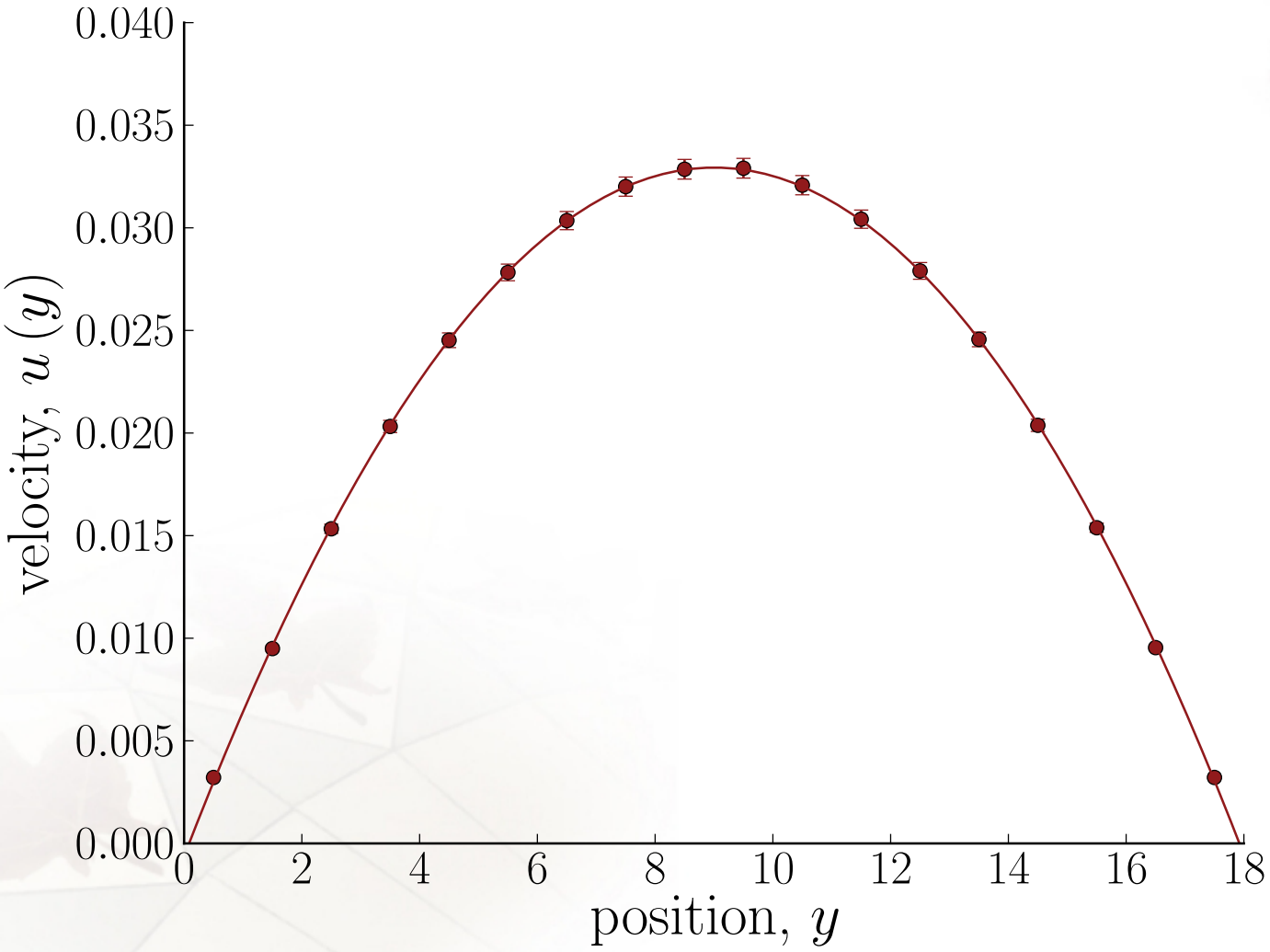

Figure : Without including phantom MPCD particles. Minute slip is observable at the limits.

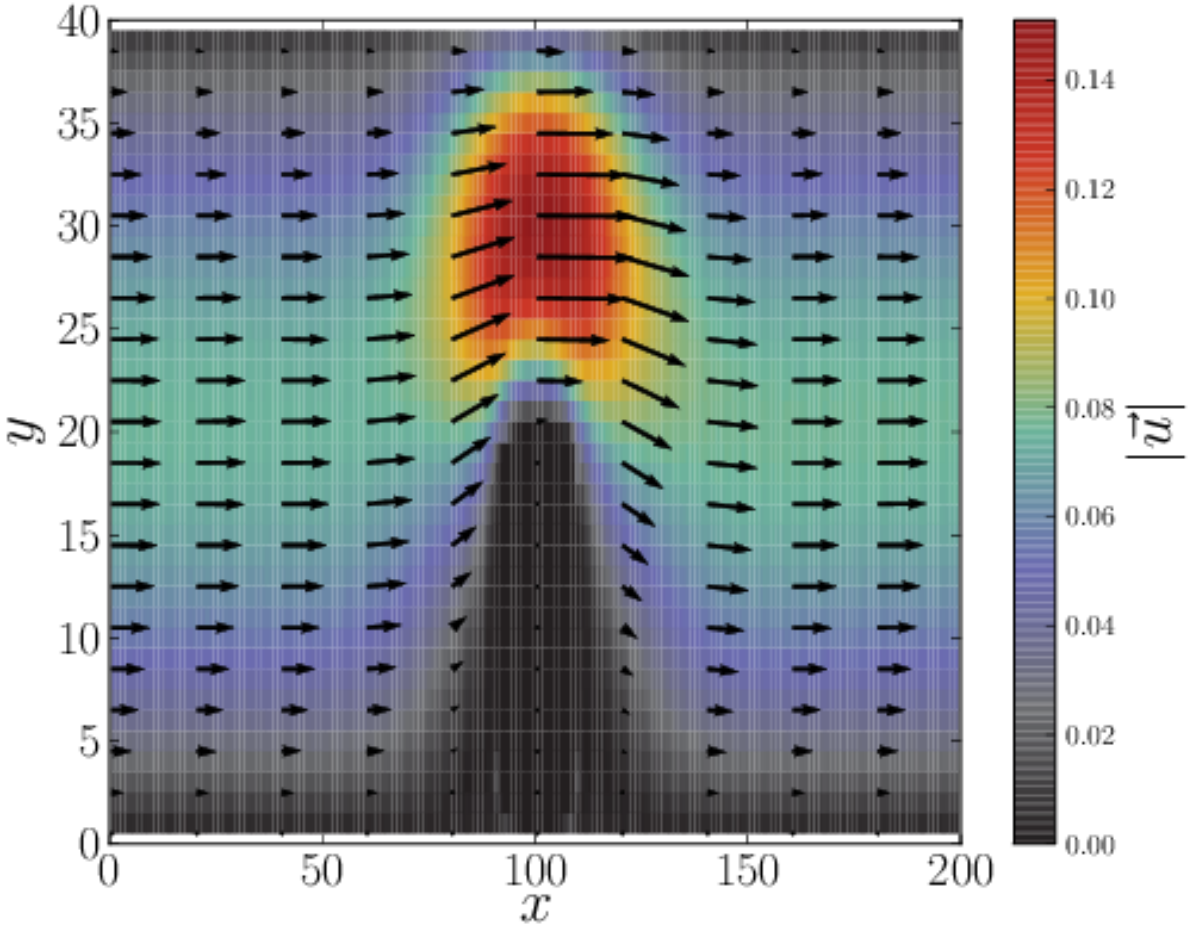

Figure : Squircle placed as a barrier.

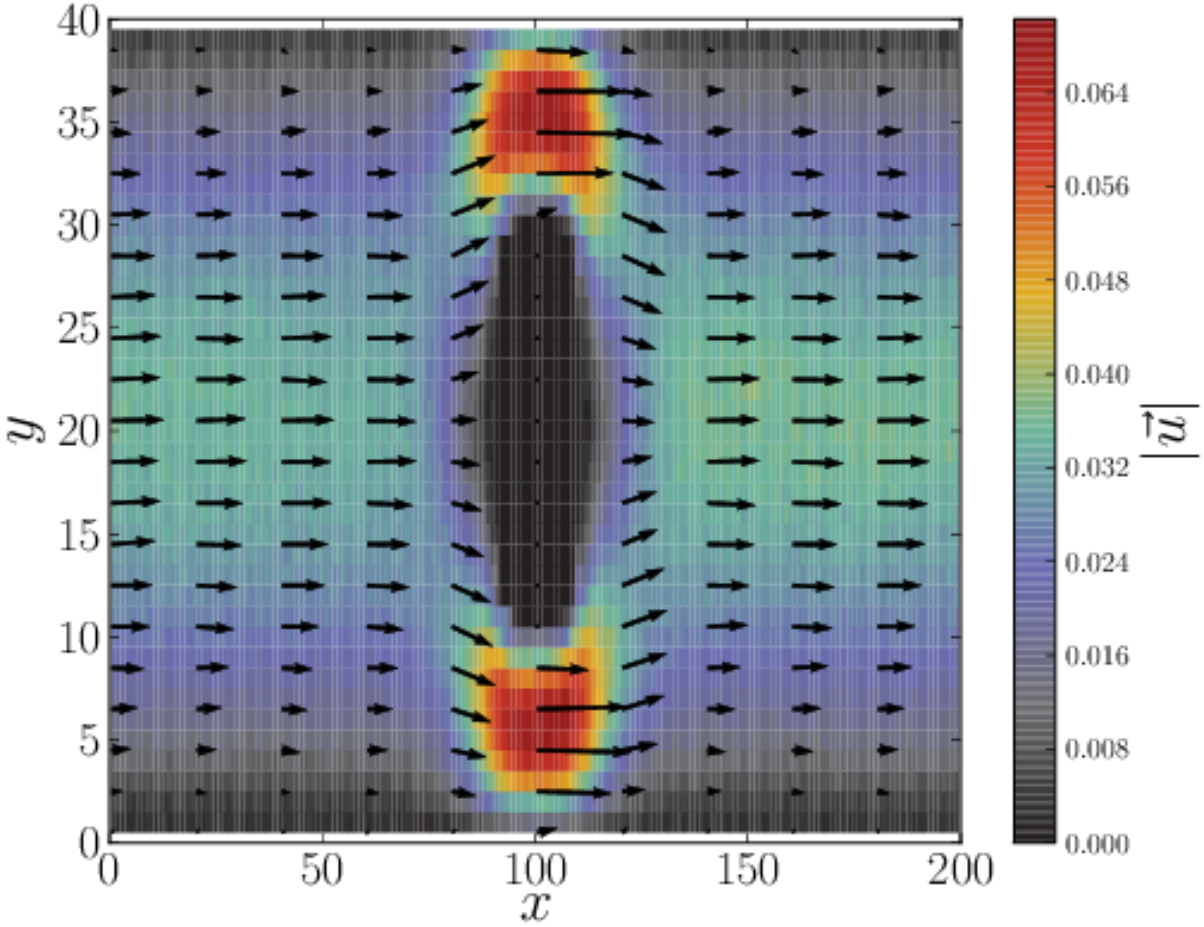

Figure : A cylinder placed as an obstacle.

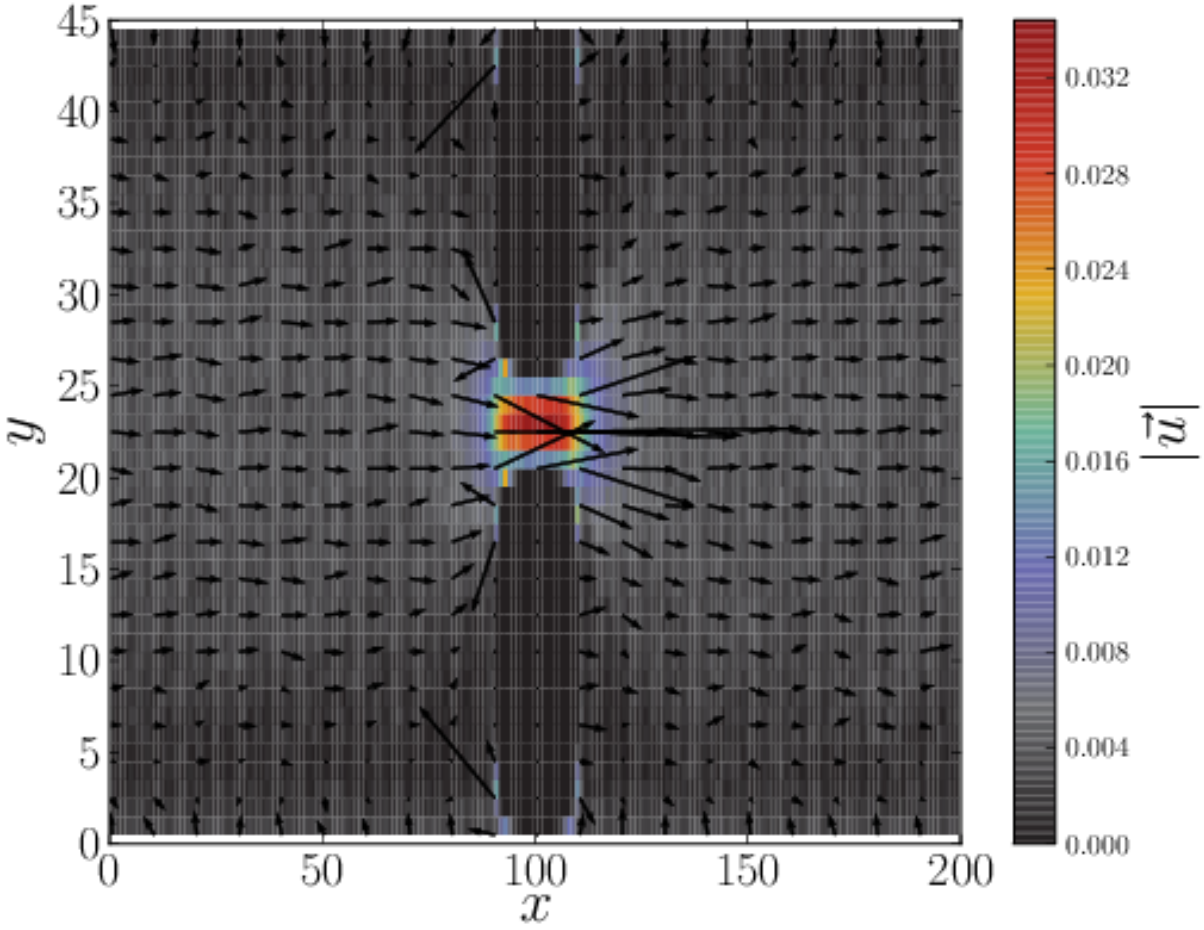

Figure : Two squircles forming a slit.

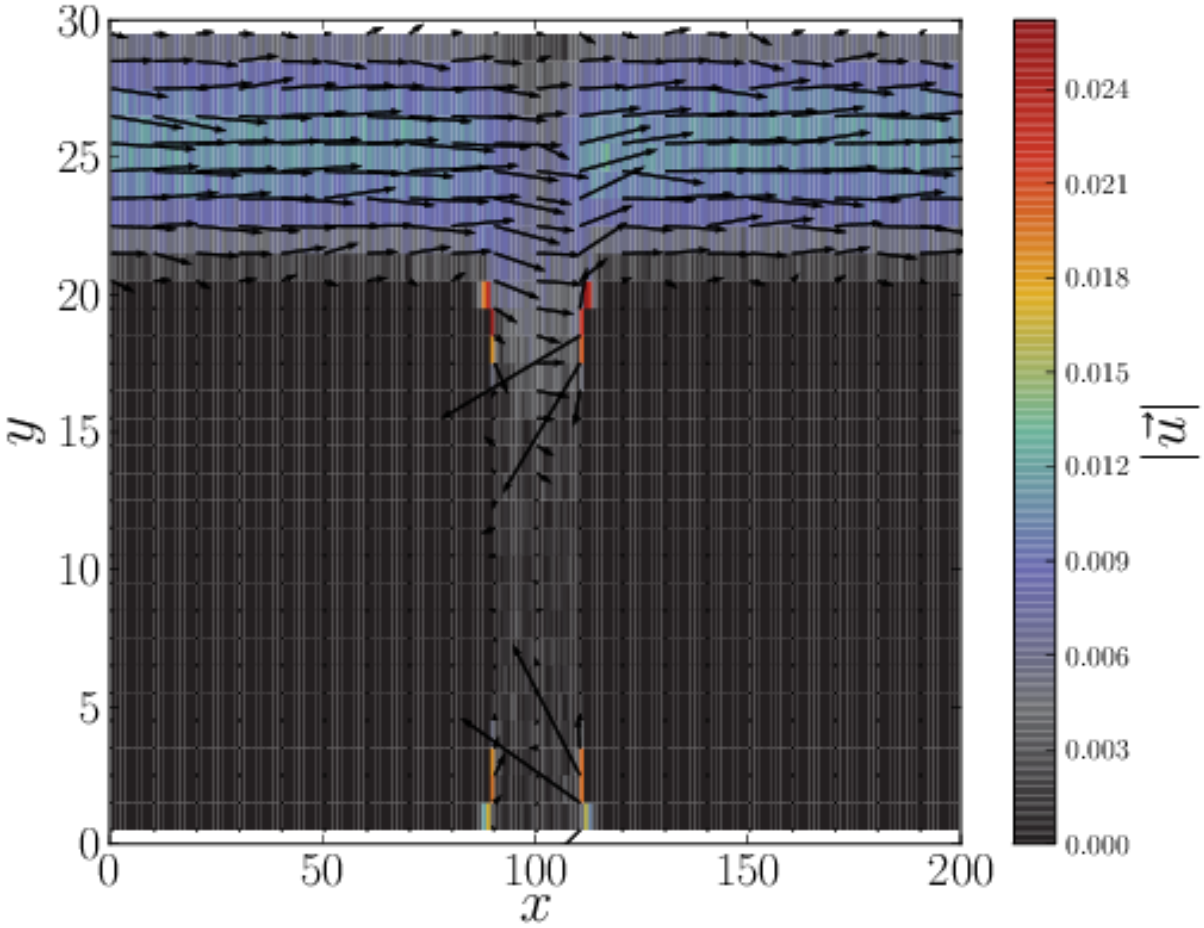

Figure : Flow through a Craighead device.

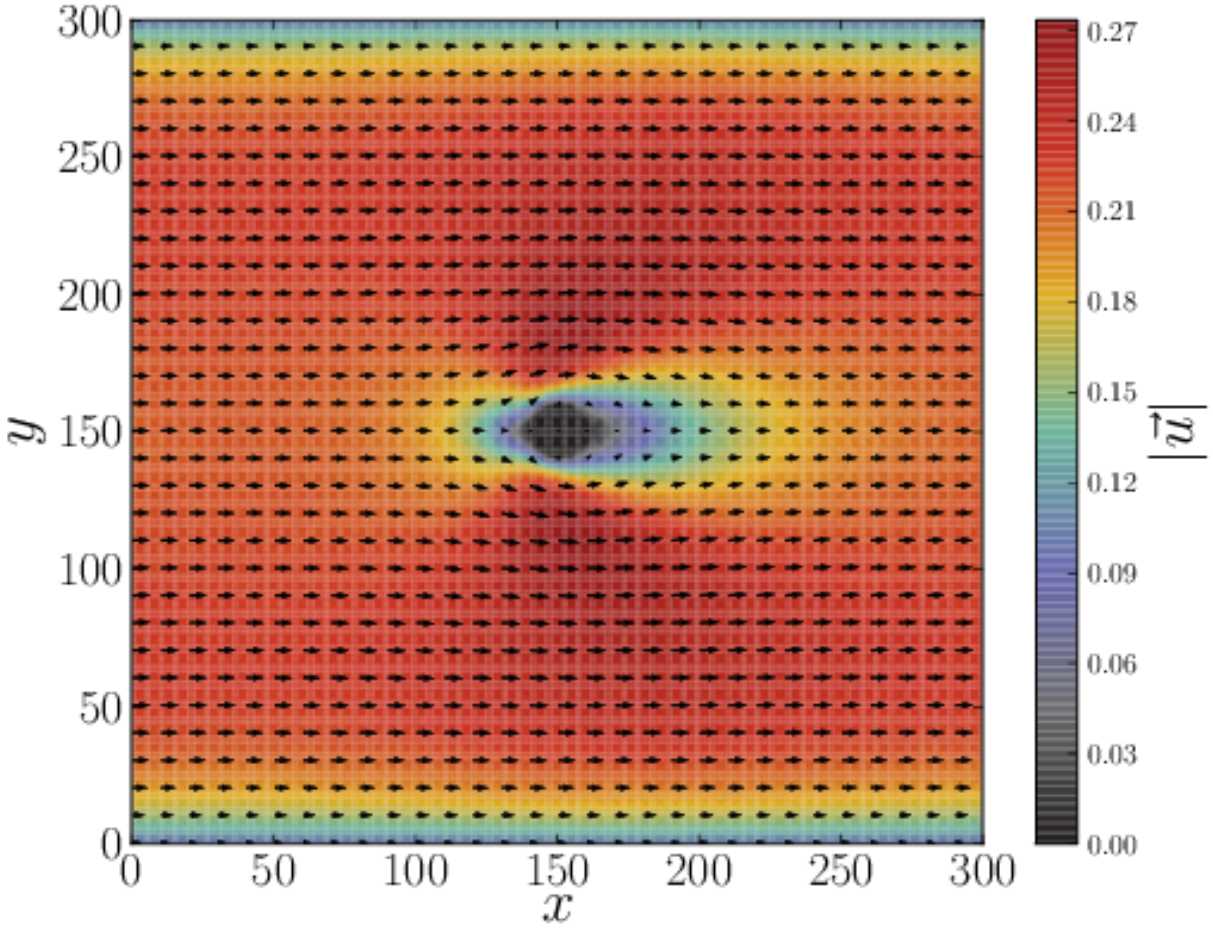

Figure : Circular obstacle.

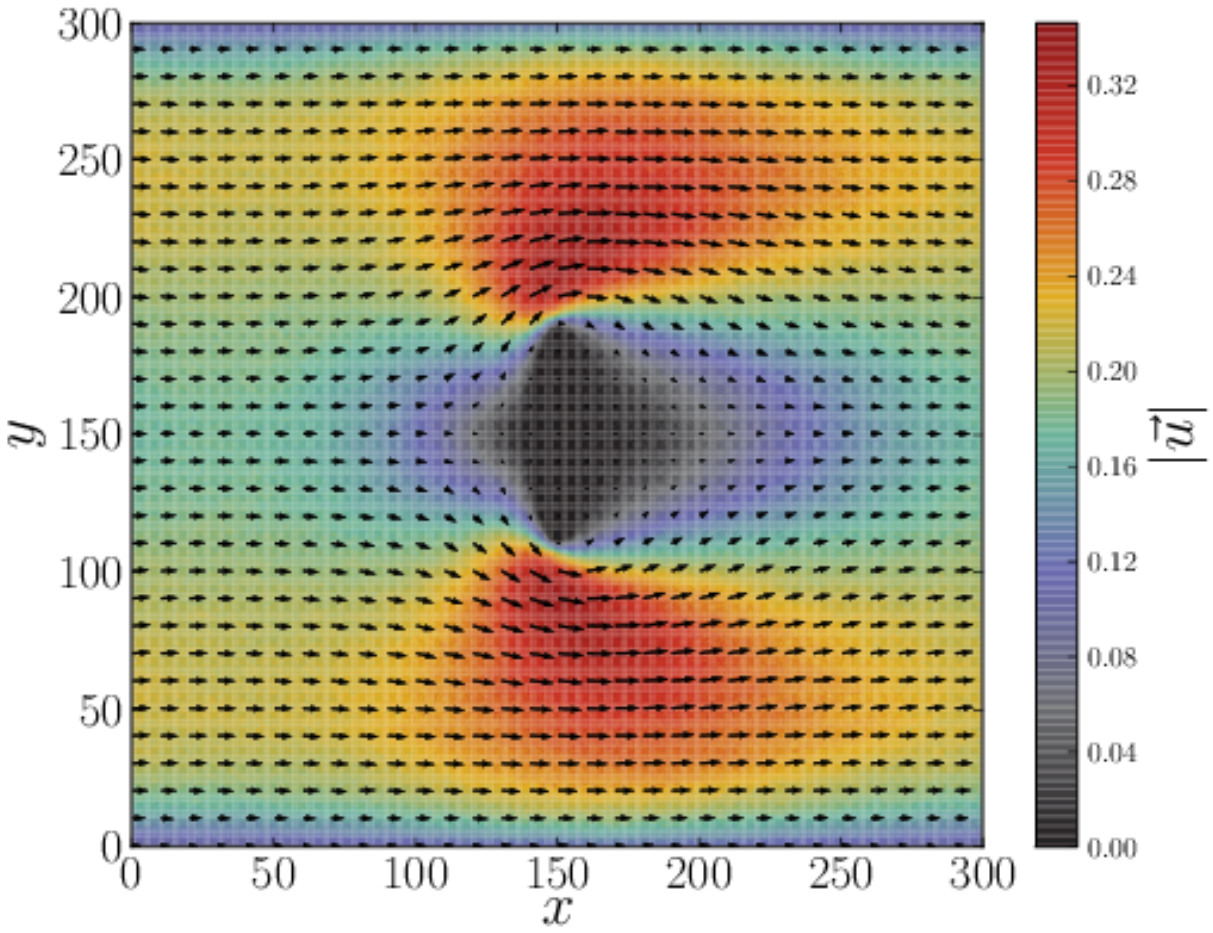

Figure : Oblate obstacle.

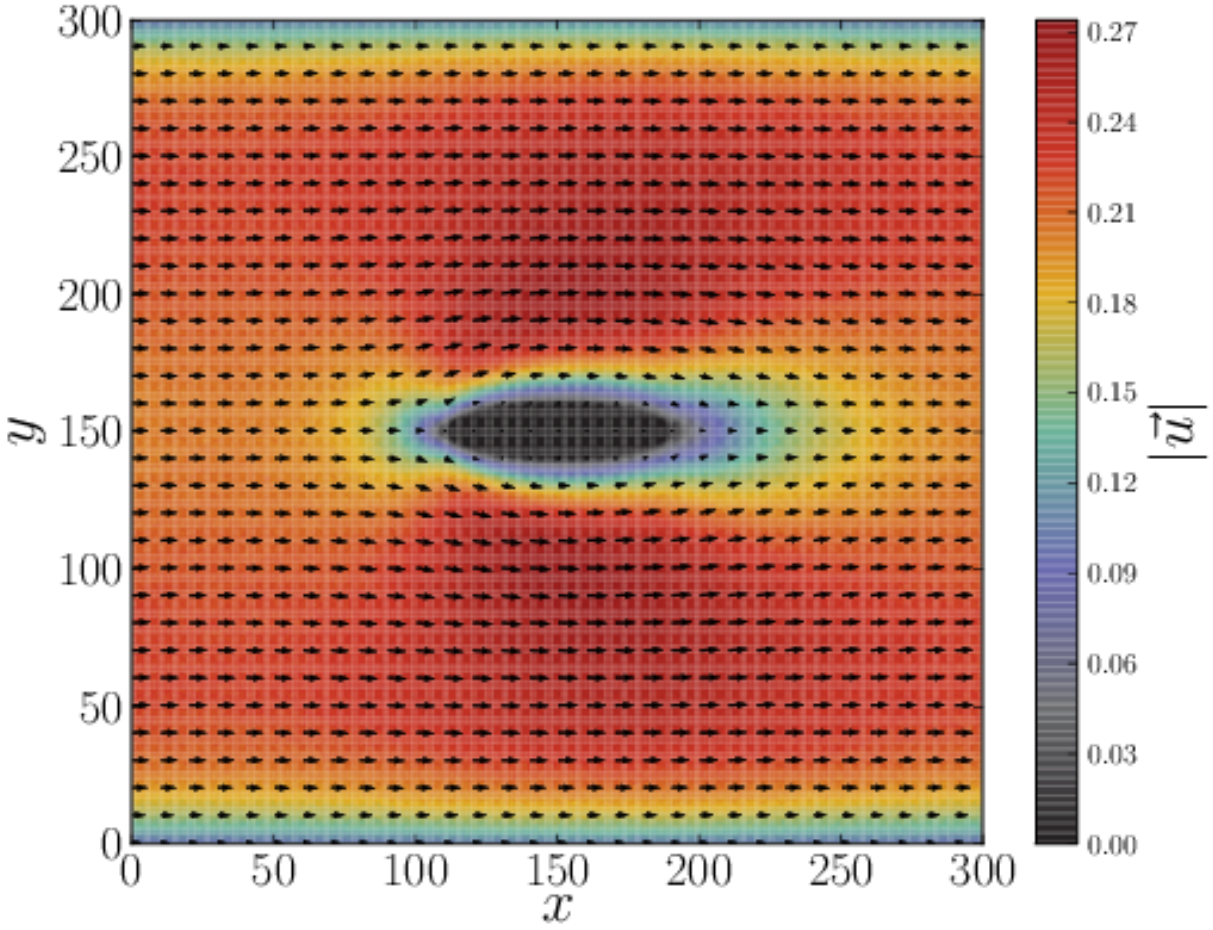

Figure : Prolate obstacle.

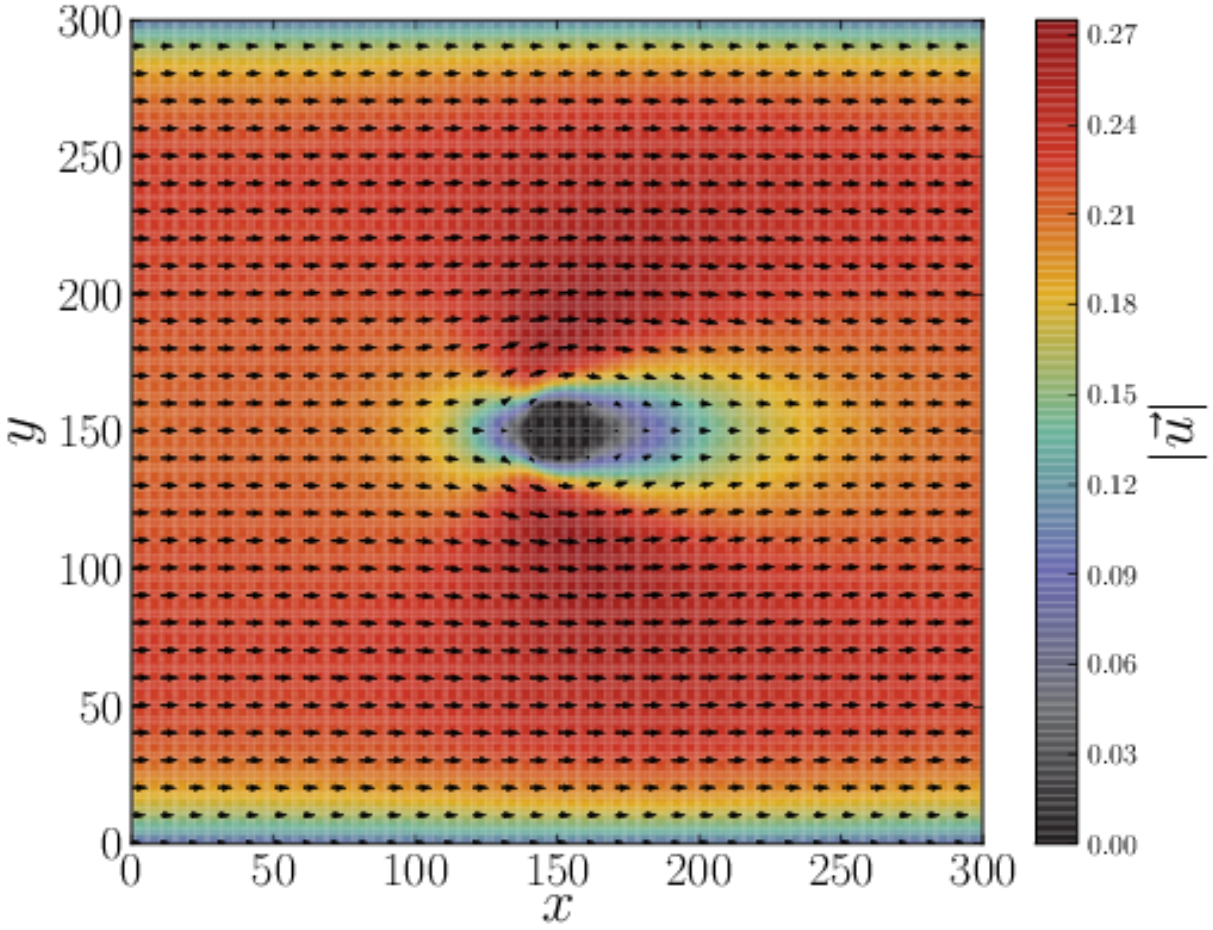

Figure : Squircle obstacle.

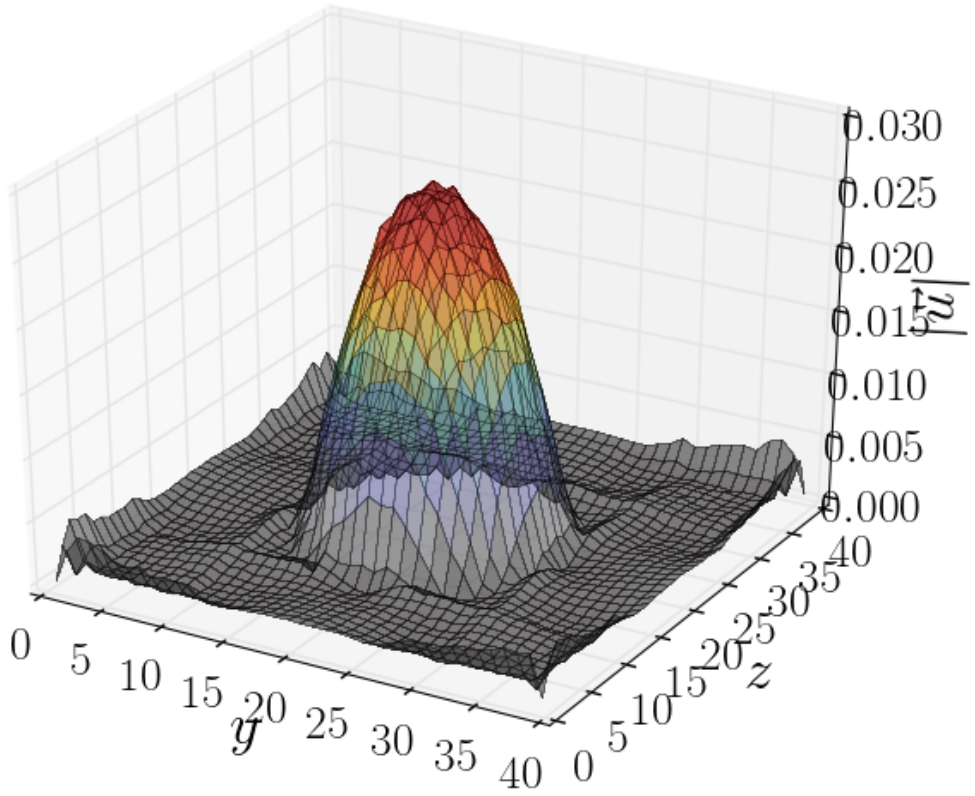

Figure : Flow within a tube.

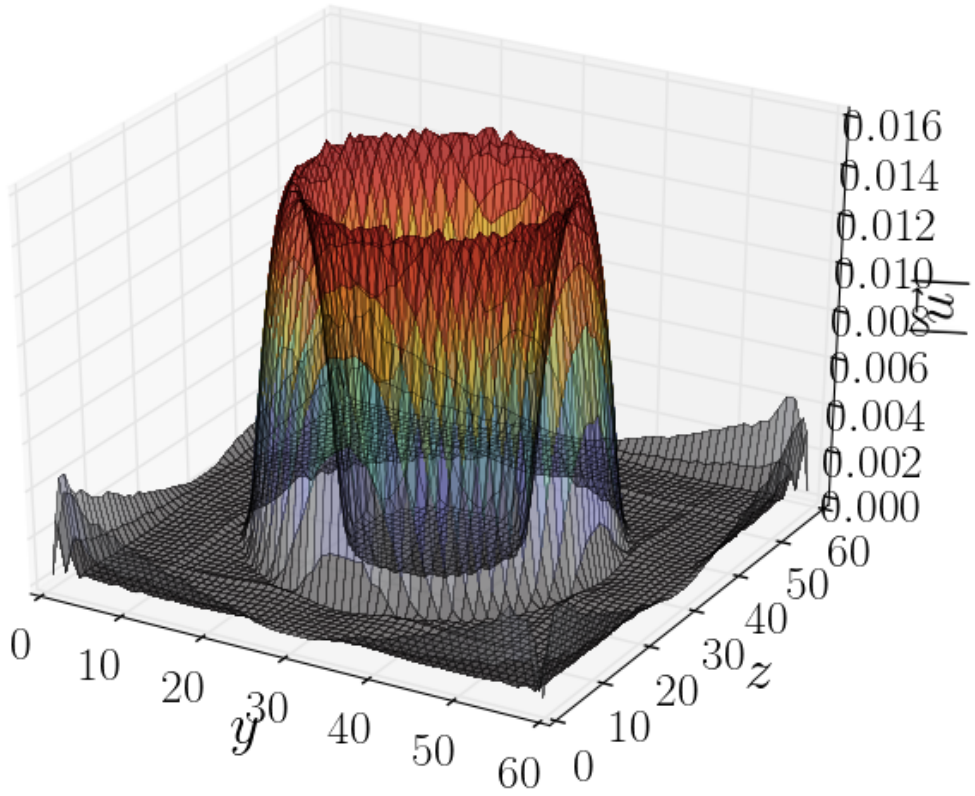

Figure : Flow within concentric tubes.

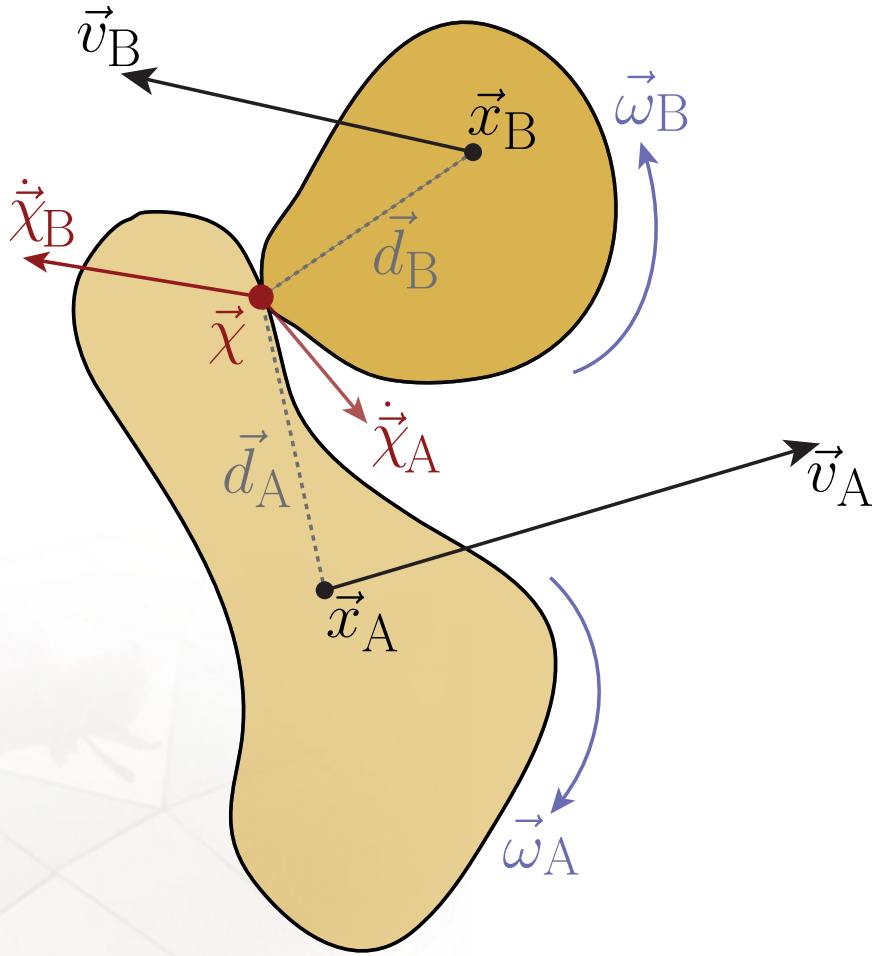

Figure : Two arbitrarily shaped bodies (with centre of mass positions $\vec{x}_A$ and $\vec{x}_B$) collide at a contact point $\vec{\chi}$. Immediately prior to the collision they have velocities $\vec{v}_A$ and $\vec{v}_B$ and angular velocities $\vec{\omega}_A$ and $\vec{\omega}_B$. At the contact point, the velocity of the surface of one body was $\dot{\vec{\chi}}_A$, while the other was $\dot{\vec{\chi}}_B$.

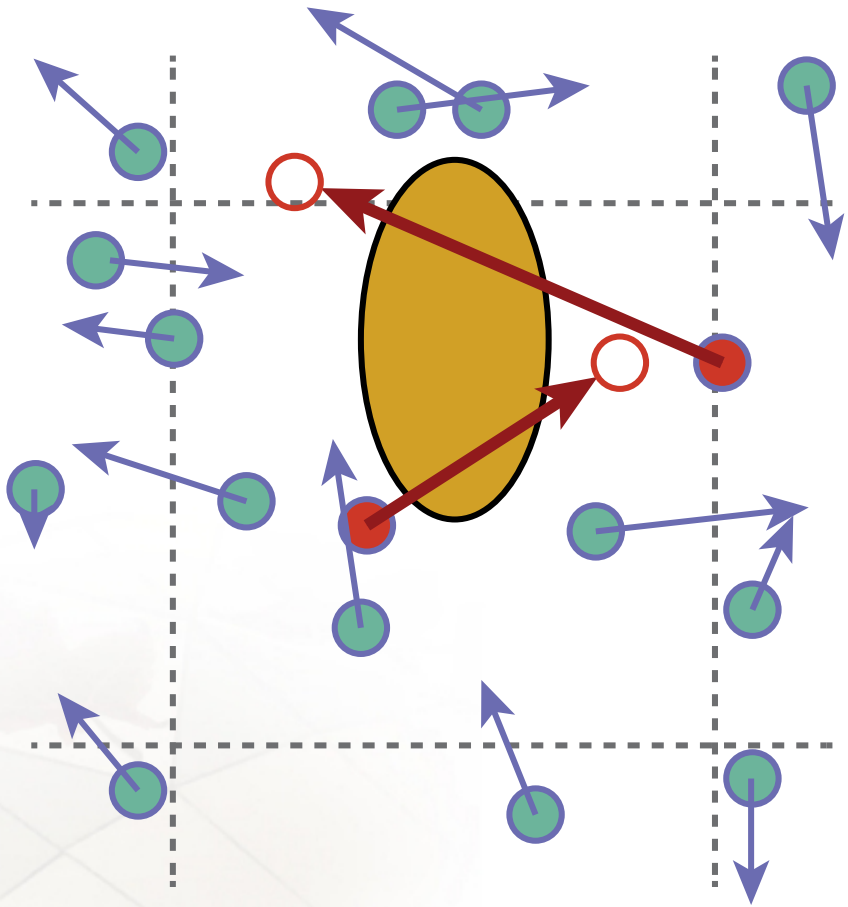

Figure : If a BC-solute is much smaller than the mean-free path of MPCD fluid particles then particles may commonly pass through the body without undergoing a collision event.

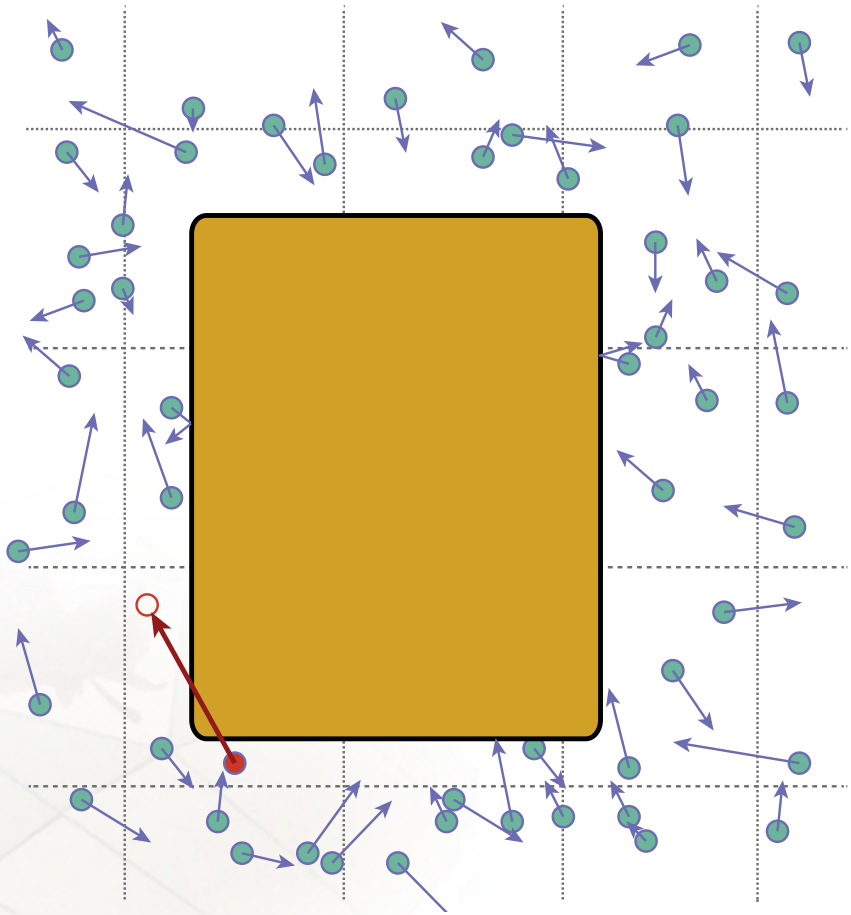

Figure : MPCD fluid particles may pass through the edges of sharp bodies without colliding.

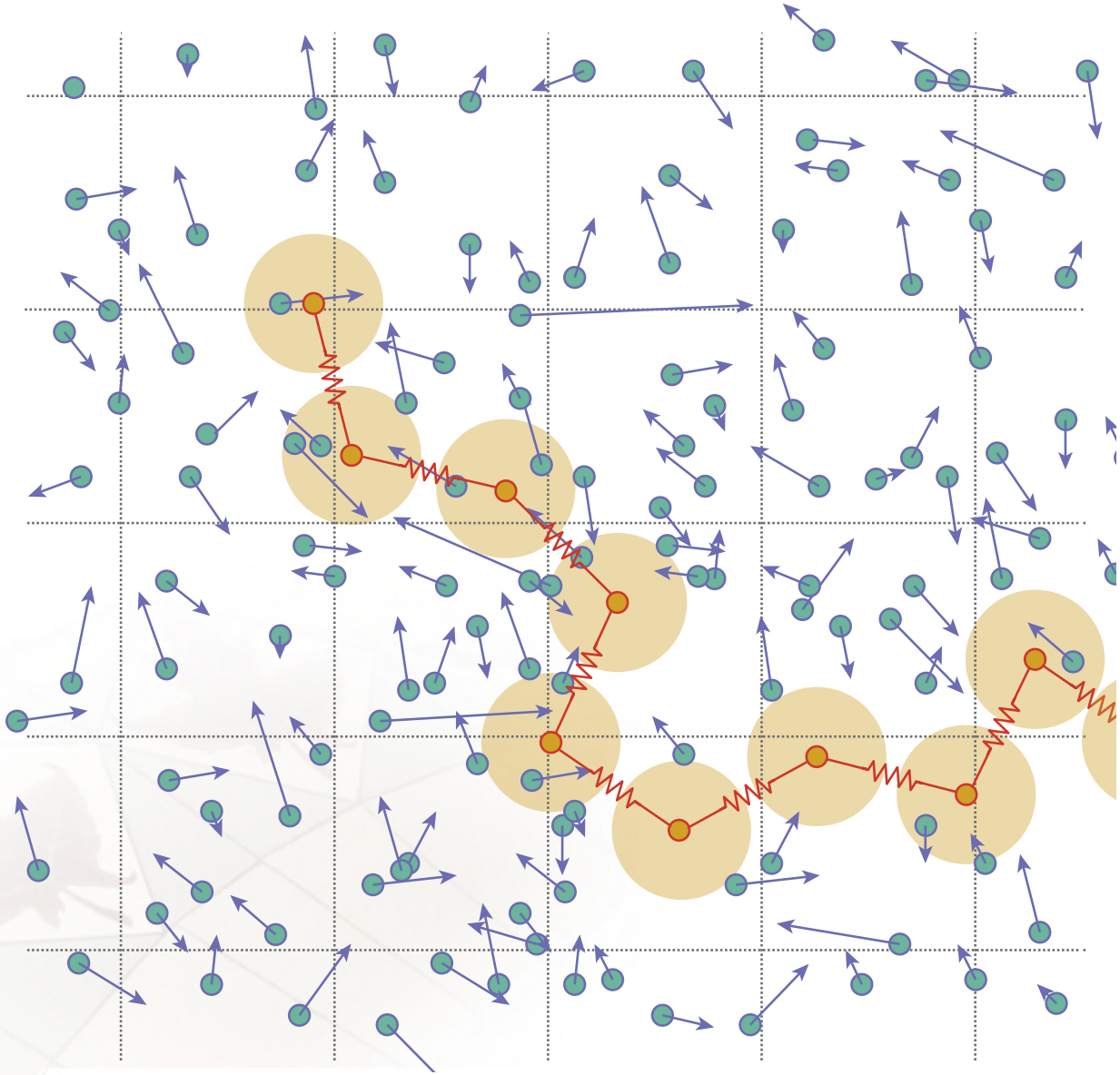

Figure : The MD-in-MPCD coupling scheme calculates MD-MD interactions, while including MD monomers as point particles in MPCD collision steps.

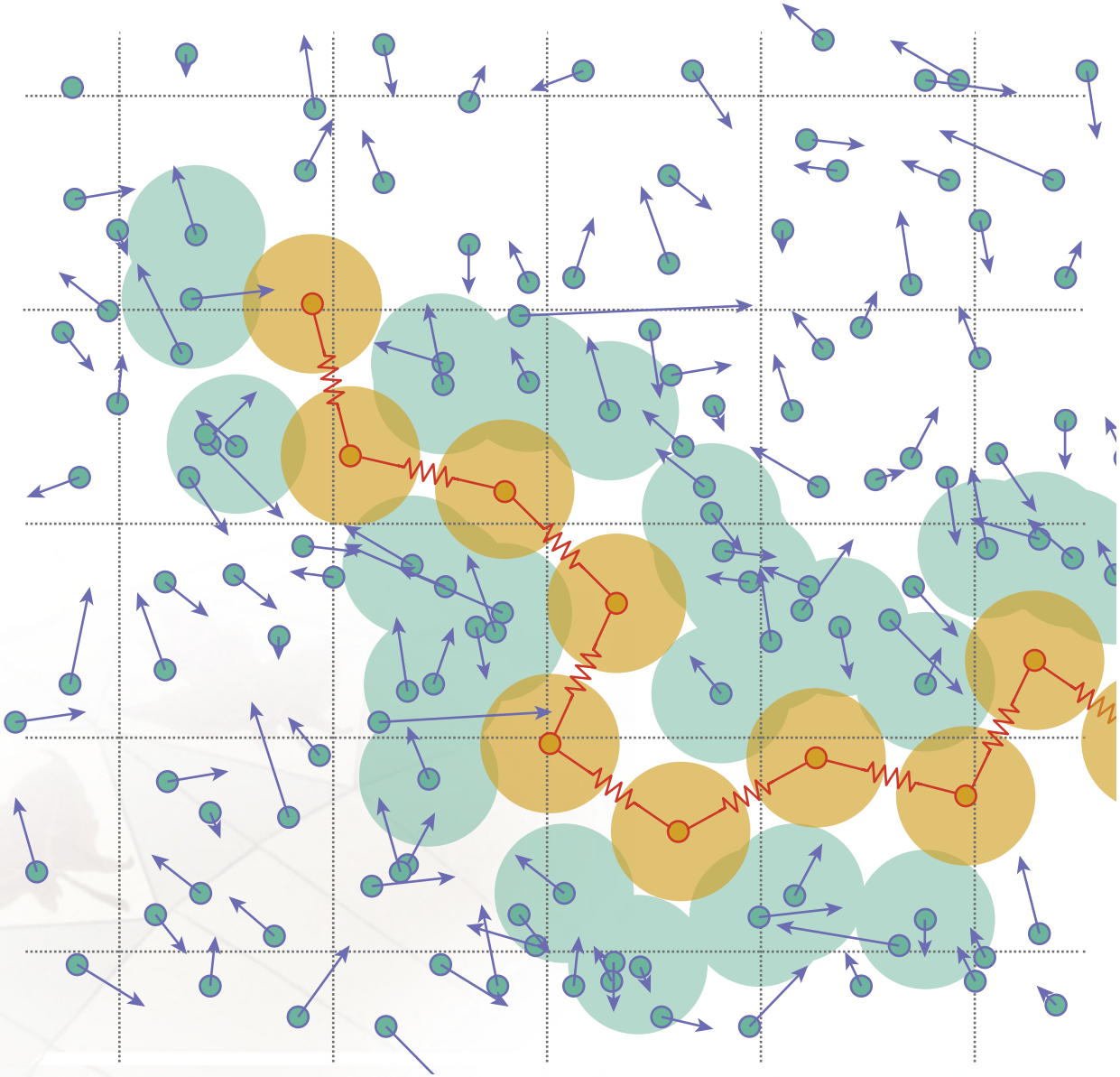

Figure : The MPCD-in-MD coupling scheme calculates MD-MD and MD-MPCD interactions.

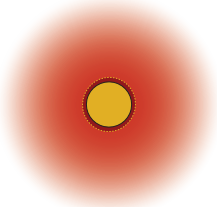

Figure :

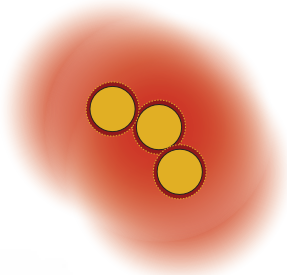

Figure : $\lambda_D \gg R_g$

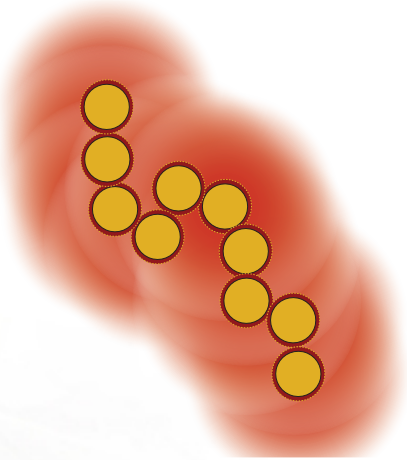

Figure :

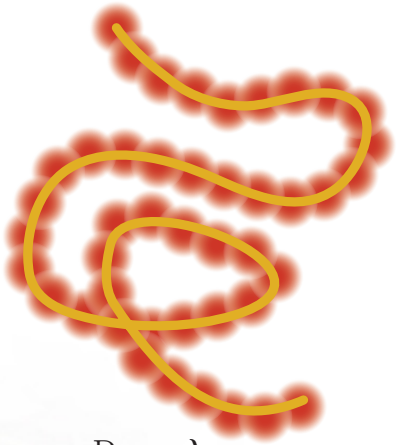

$R_g > \lambda_D$

Figure : $\lambda_D \ll R_g$

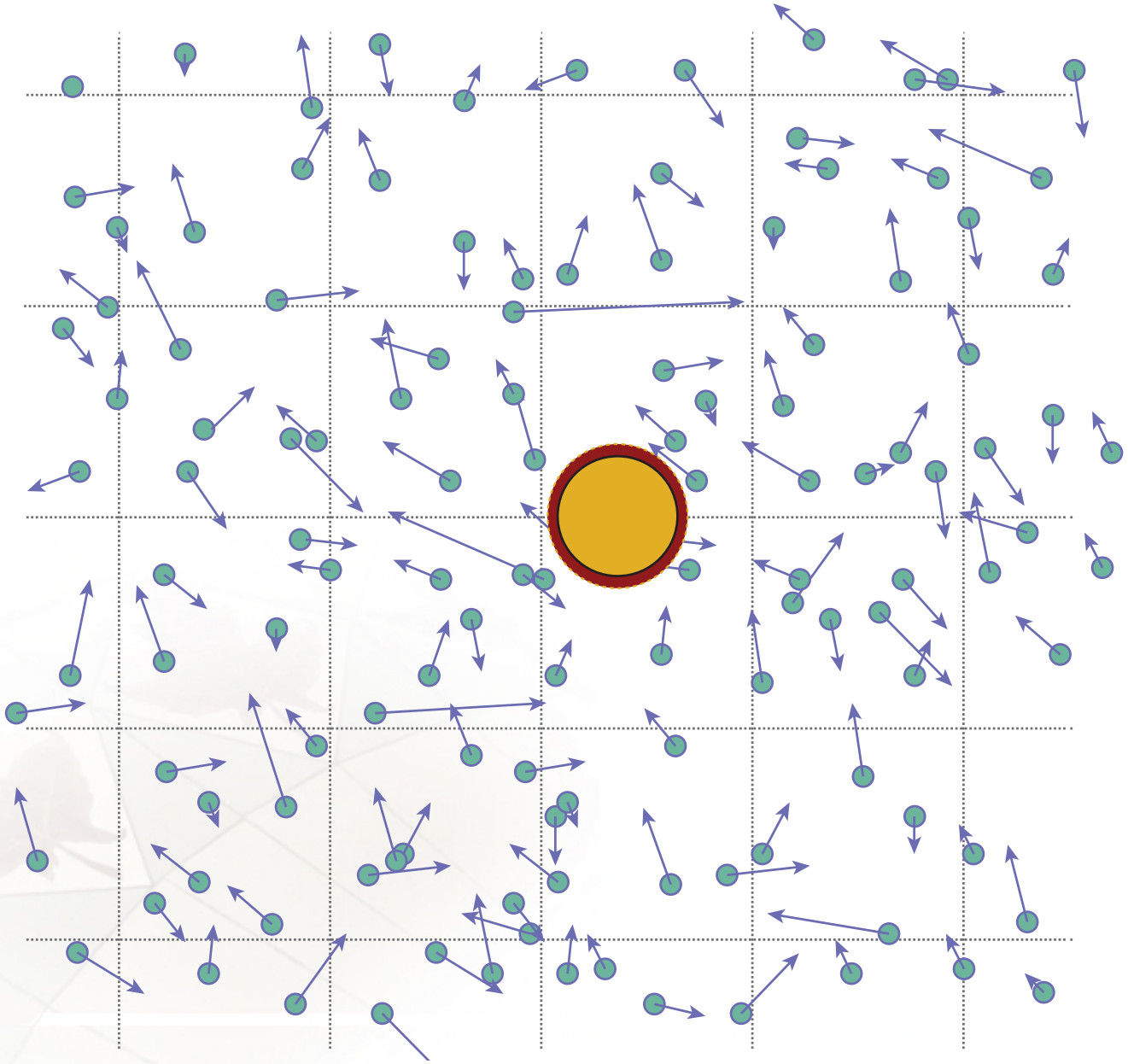

Figure :

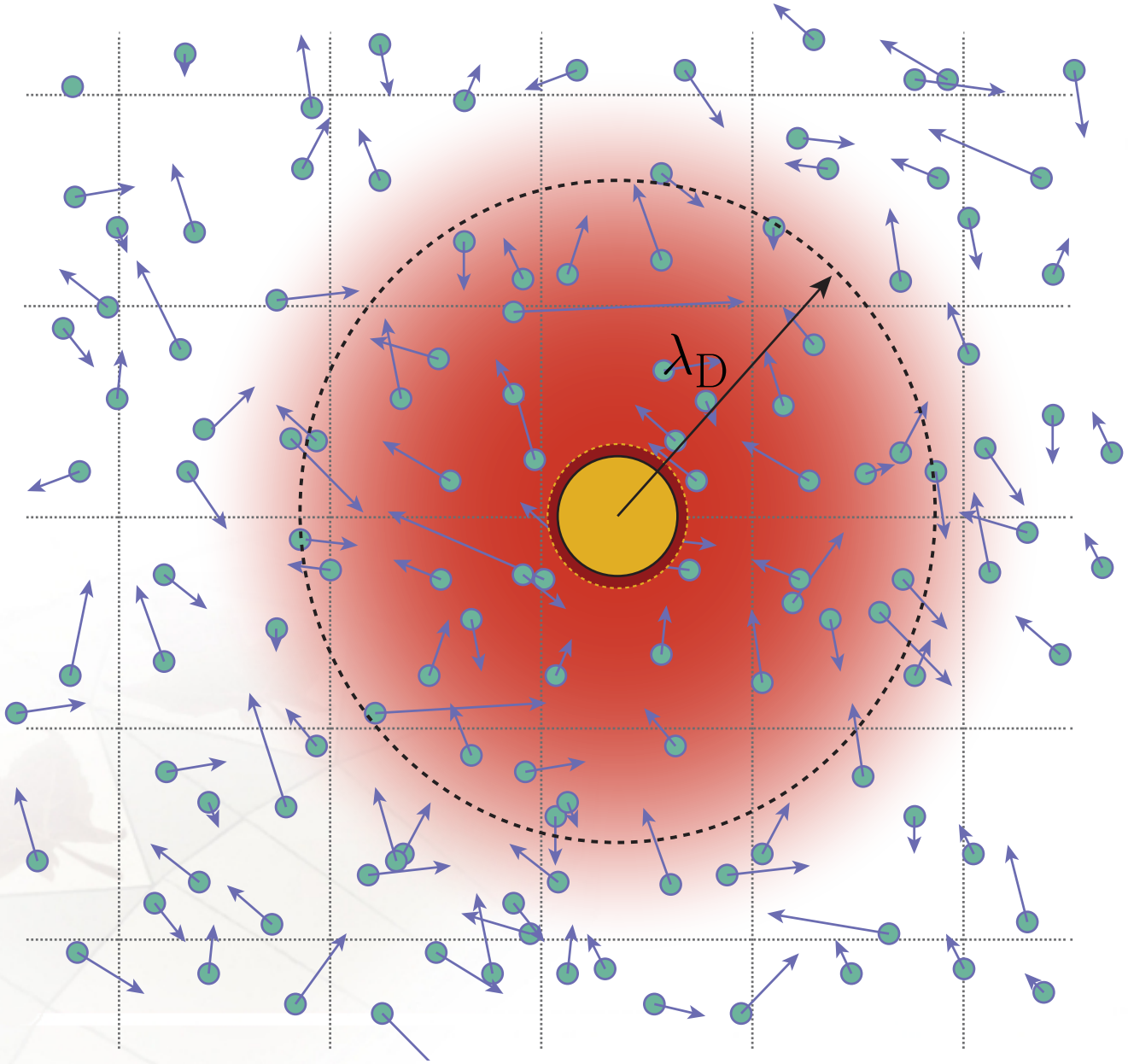

Figure :

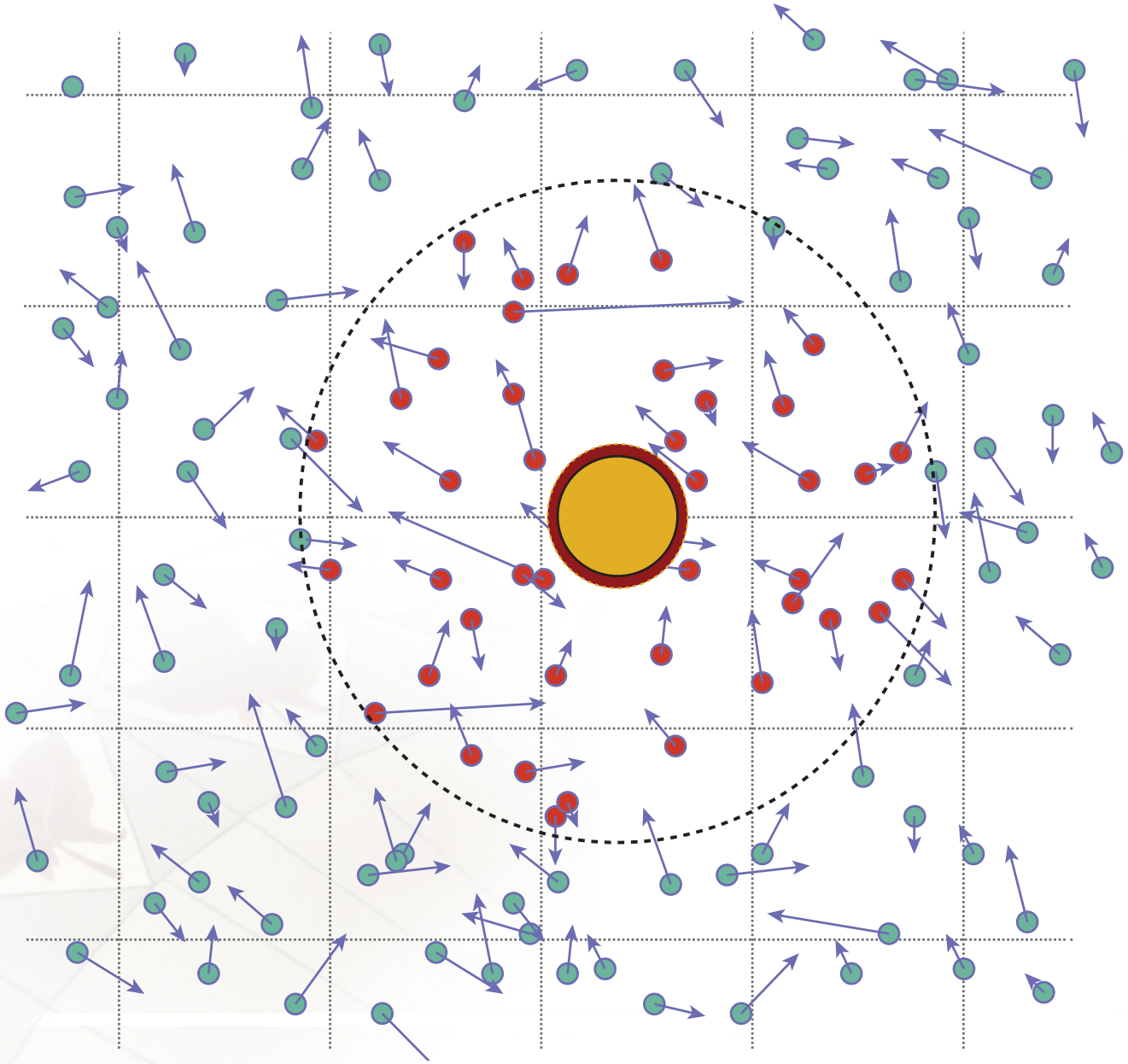

Figure :

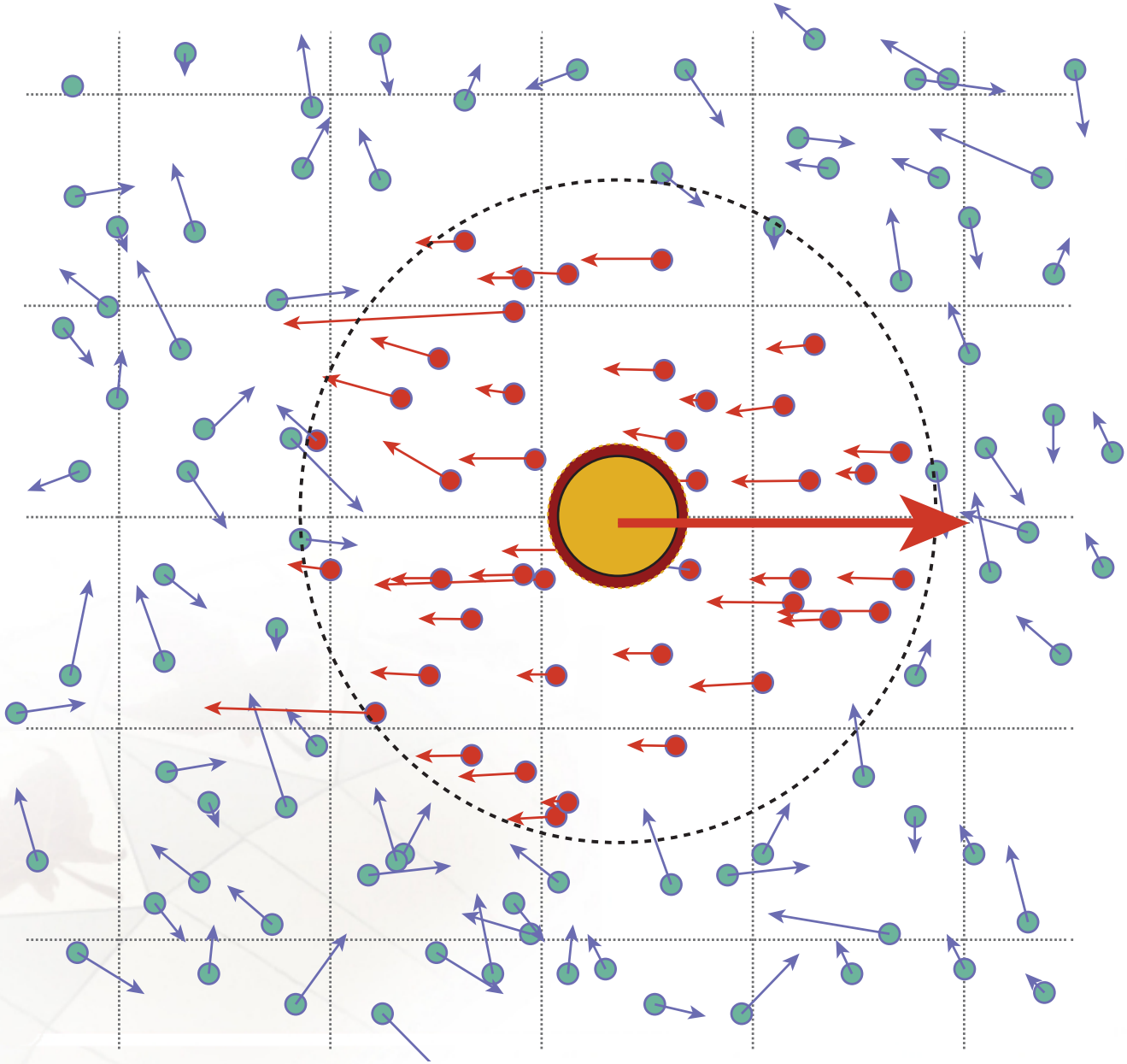

Figure : Schematic representation of the mean-field MPCD-MD Debye-Hückel algorithm. A charged MD bead is surrounded by point-like MPCD fluid particles. MPCD fluid particles are given charges based on their position. In this way, including explicit counterions is avoided. The charges assigned to each MPCD particle are proportional to the local counterion distribution that is predicted by the Debye-Hückel

uOttawa

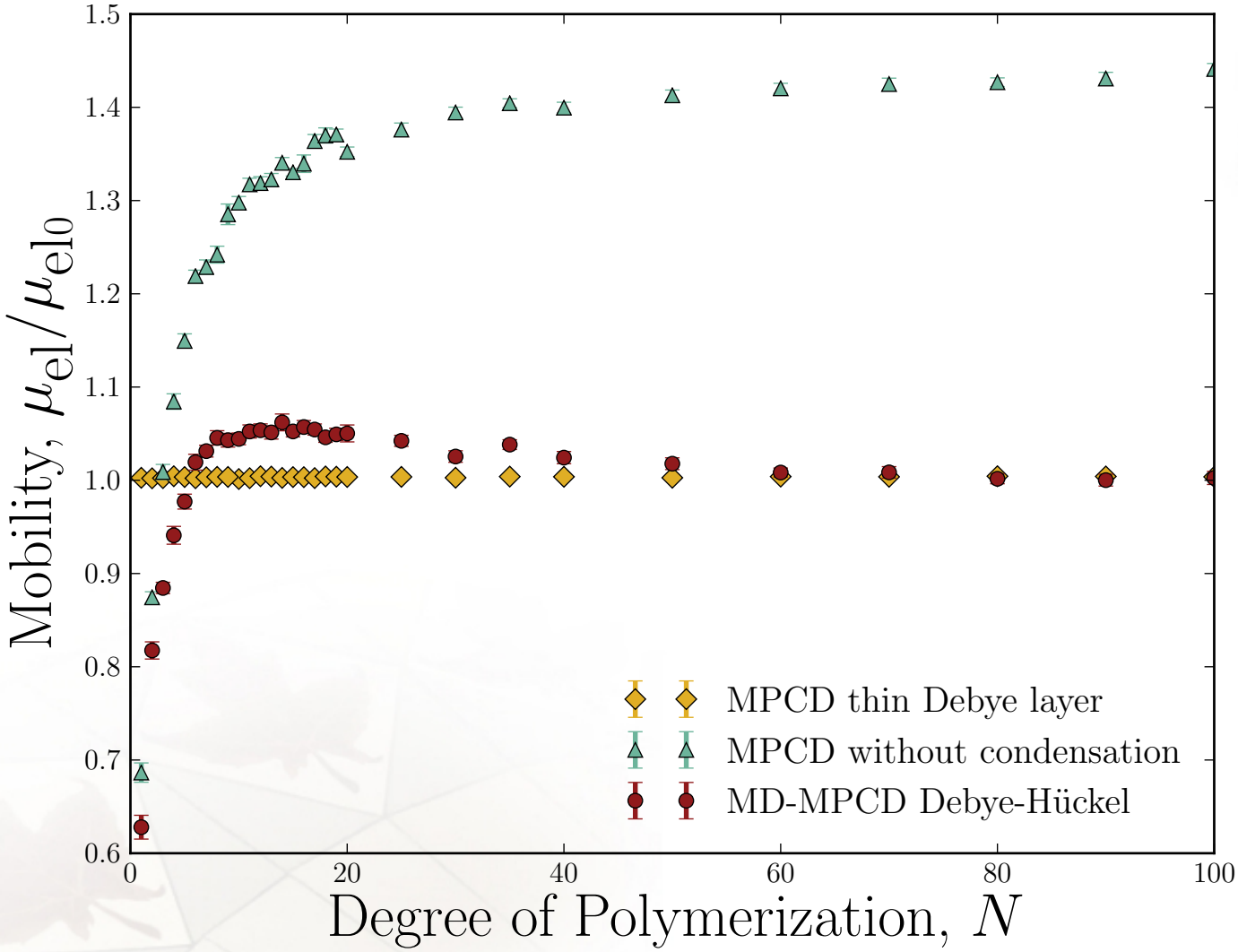

Figure : The electrophoretic mobility of polyelectrolytes as a function of the degree of polymerization N normalized by the free-draining value μ_{el0}. Thin Debye layer simulations (diamonds) produce the free-draining mobility for all contour lengths, while MPCD-MD Debye-Hückel simulations without charge condensation (triangles) capture the rise due to hydrodynamic interactions within finite Debye layers. The full results of hybrid simulations with counterion condensation (circles) capture the non-monotonic form of the electrophoretic mobility curve.

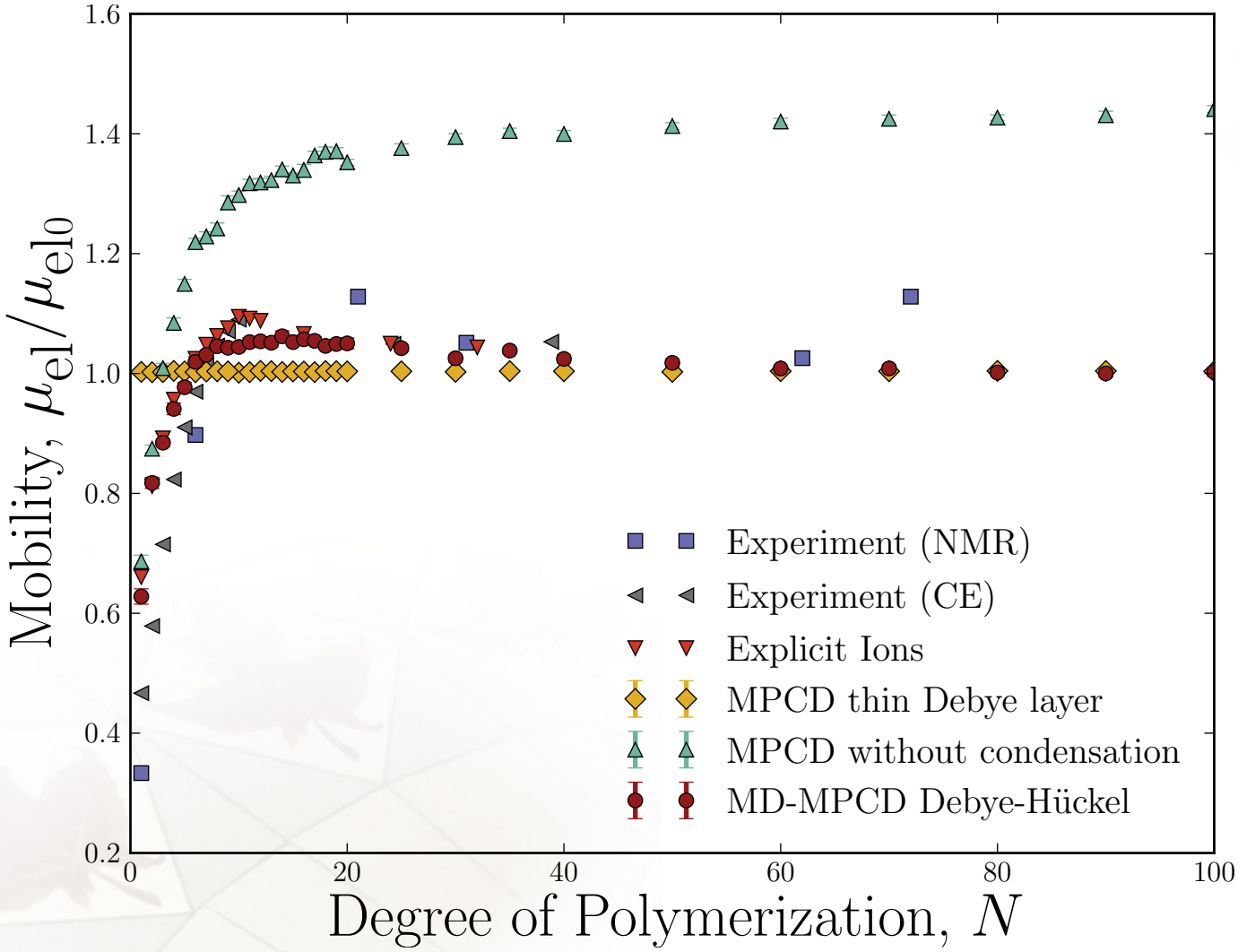

Figure : The electrophoretic mobility of polyelectrolytes as a function of the degree of polymerization N normalized by the free-draining value μ_{el0}. The results of hybrid simulations with counterion condensation (circles) compare well to both the experimental results (squares and left-facing triangles) and simulations using explicit ions (upward triangles).

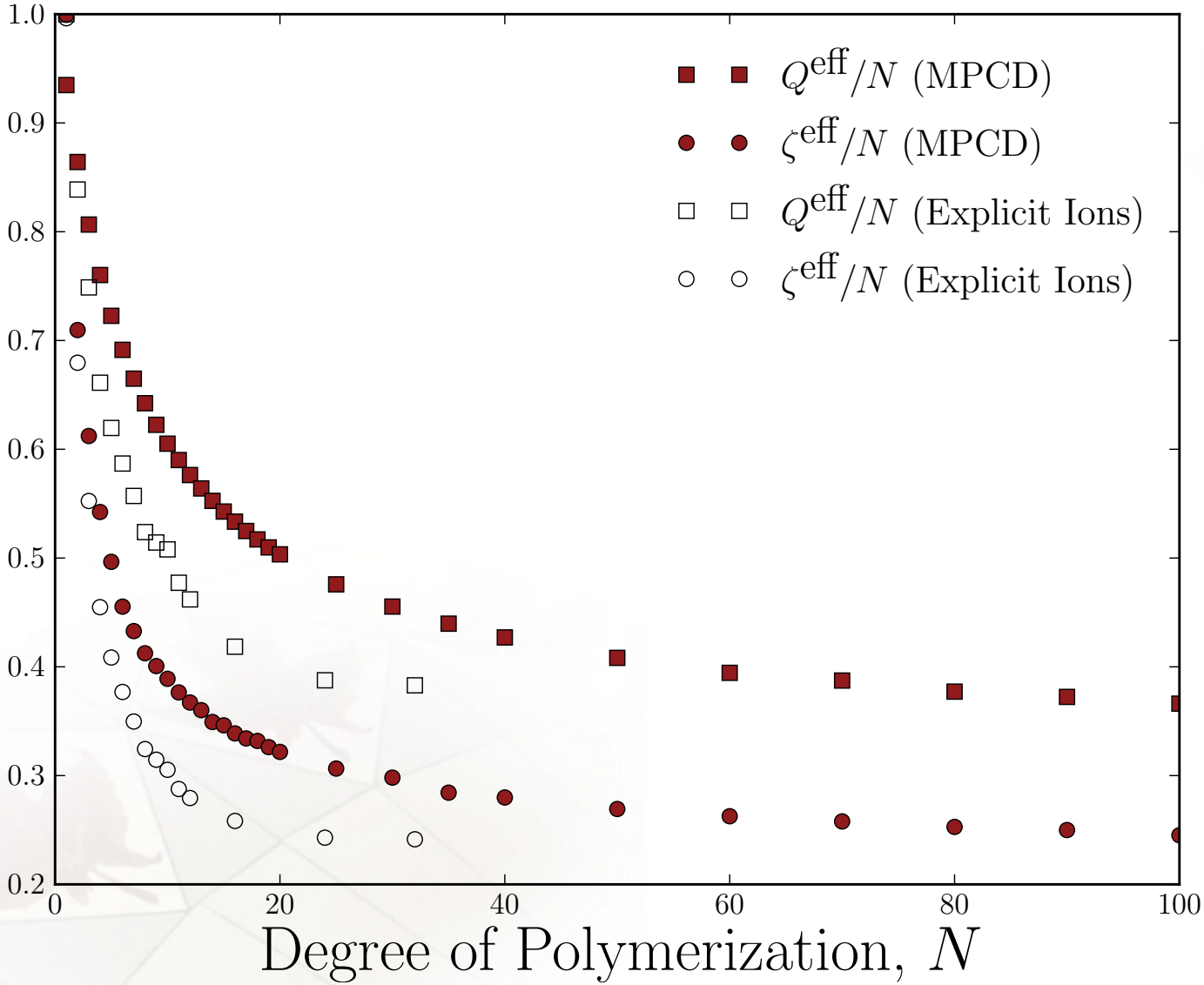

Figure : The effective friction ζ^{eff} (circles) and effective charge Q^{eff} (squares) as a function of the degree of polymerization N. The filled symbols are the hybrid simulation results, while the open symbols are simulations using explicit ions reproduced with permission. The diamonds show the effective friction when there is no charge condensation.

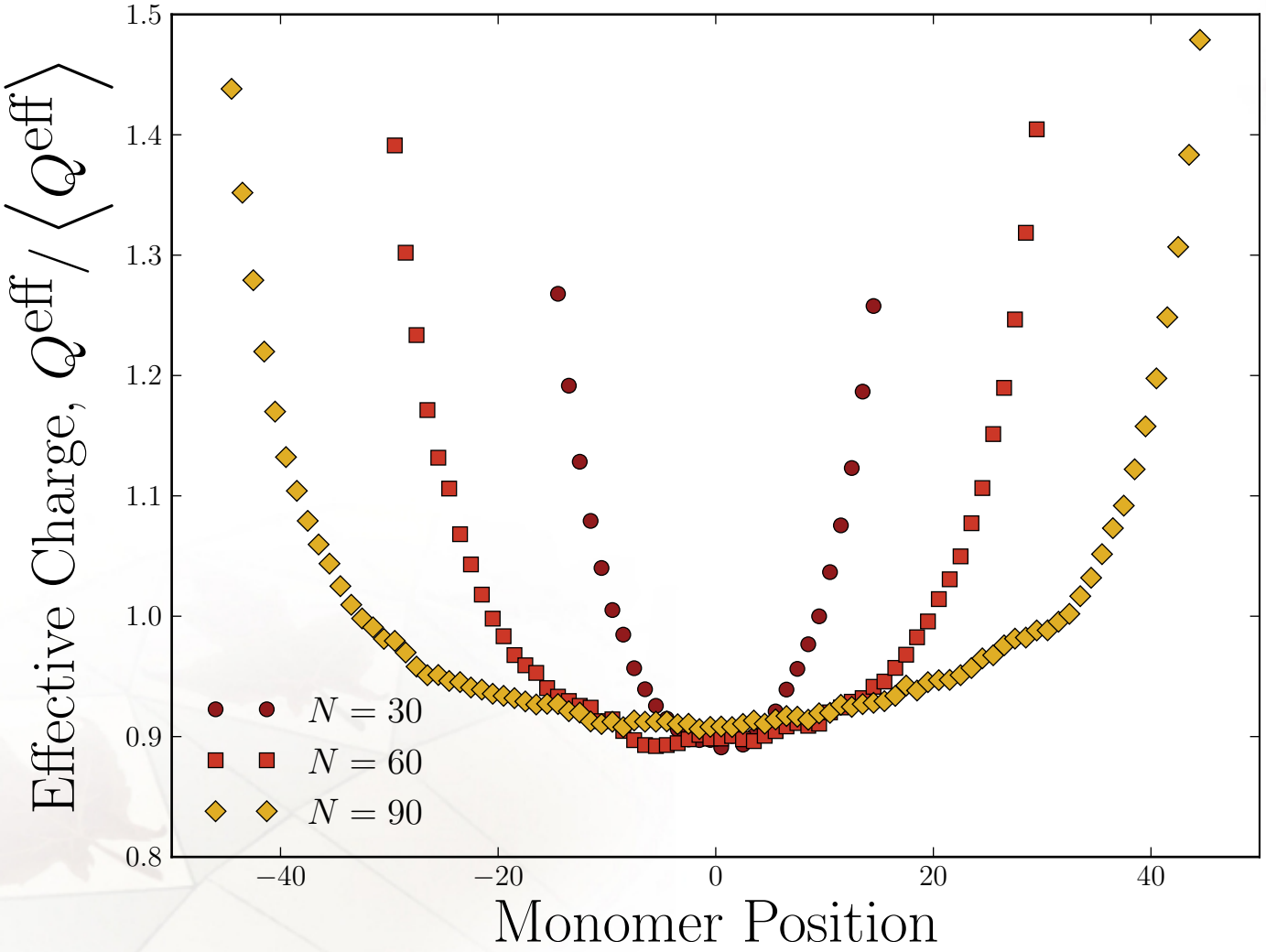

Figure : The effective charge as a function of monomer position normalized by the average effective charge on all monomers.

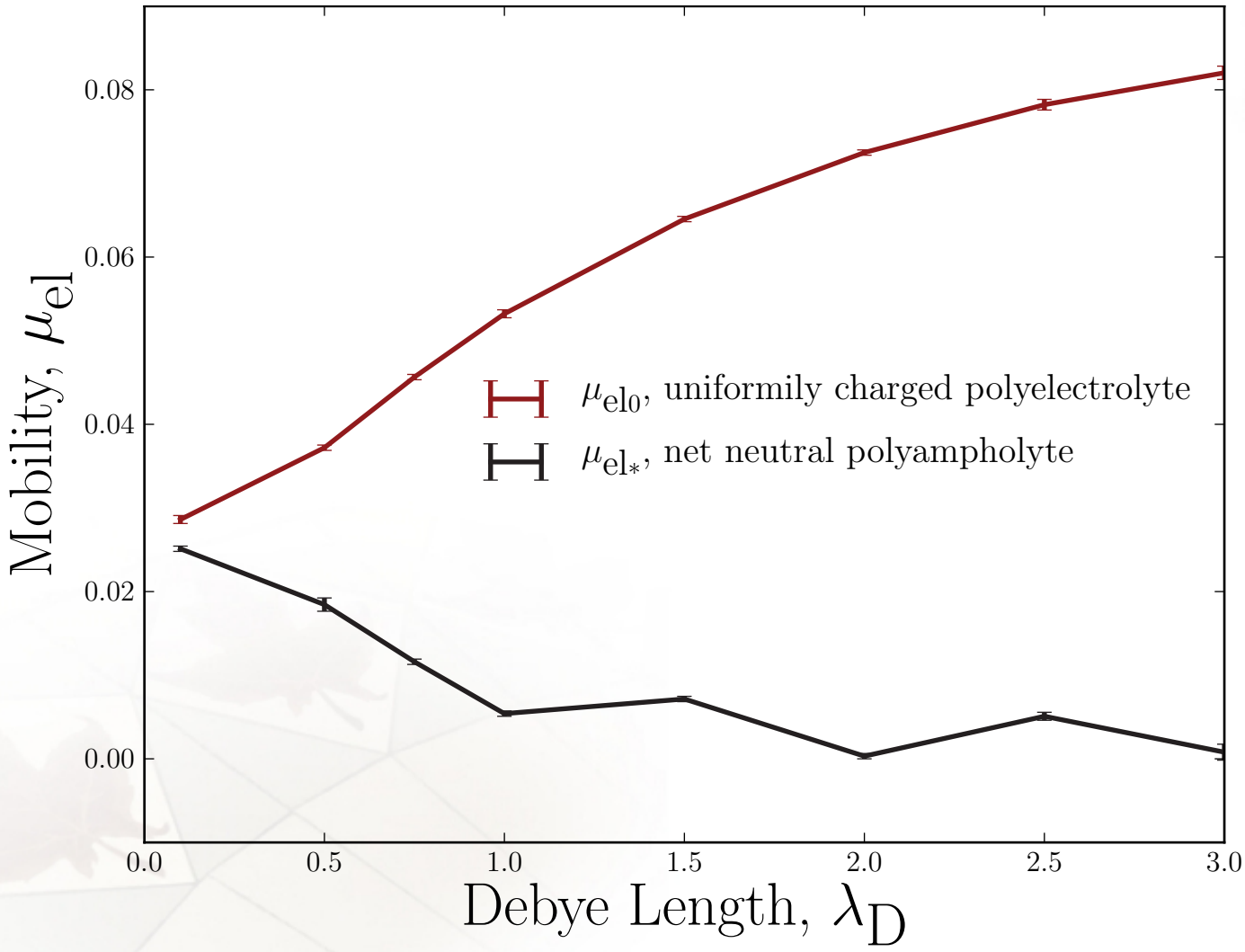

Figure : Electrophoretic mobility of a uniformly charged polymer, $\mu_{\mathrm{el}\,0}$, as a function of Debye length λ_{D}. Also mobility of a net neutral block copolymer, $\mu_{\mathrm{el}\,*}$, rescaled by a constant factor.

$$N_{\text{cut}} = 4$$

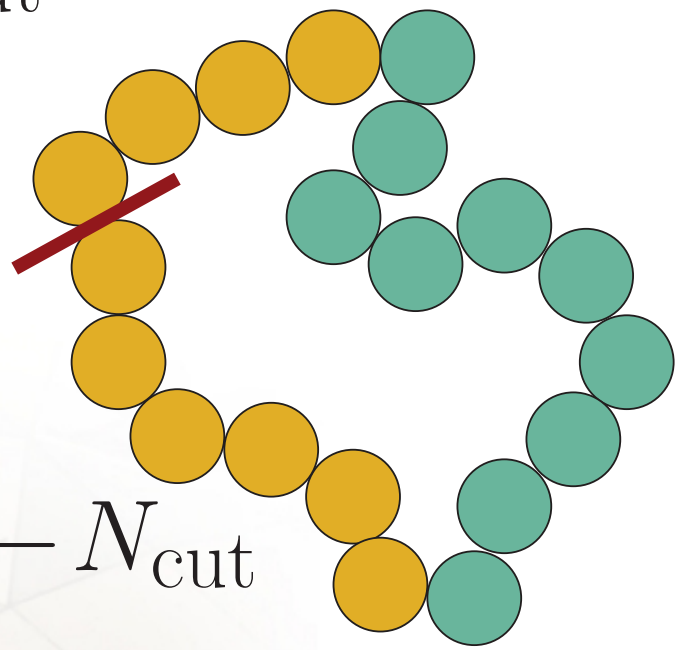

$$\frac{N}{2} - N_{\text{cut}}$$

Figure :

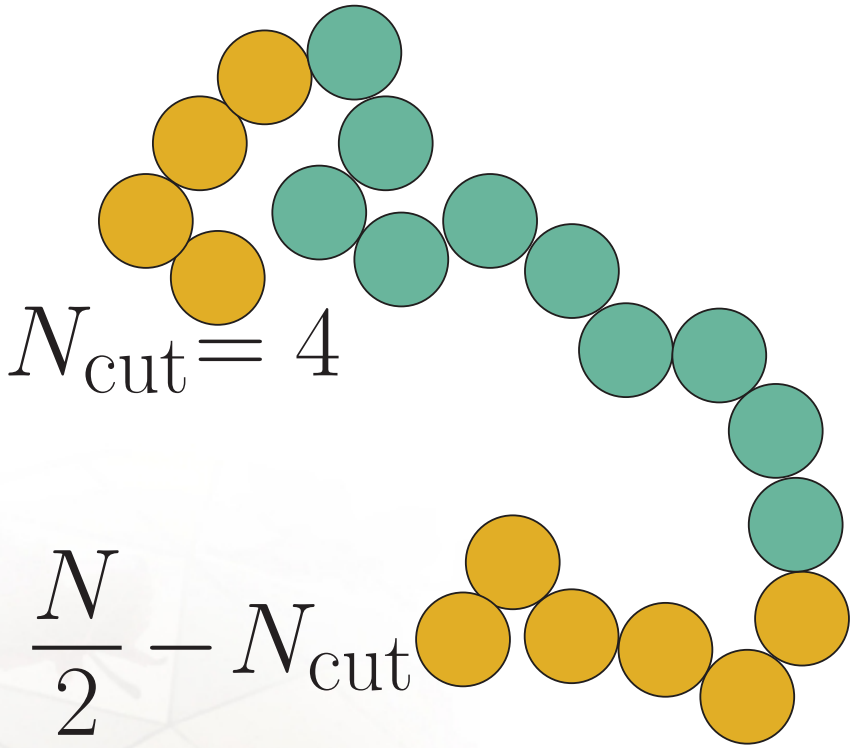

Figure : Schematic explaining the polyampholyte structure. A di-block (one positive block and one negative block) ring polymer, of net neutral charge is cut. The number of monomers away from the junction at which point the cut is made is N_{cut}. A tri-block linear polymer results that has positive ends of length N_{cut} and $N/2 - N_{\mathrm{cut}}$.

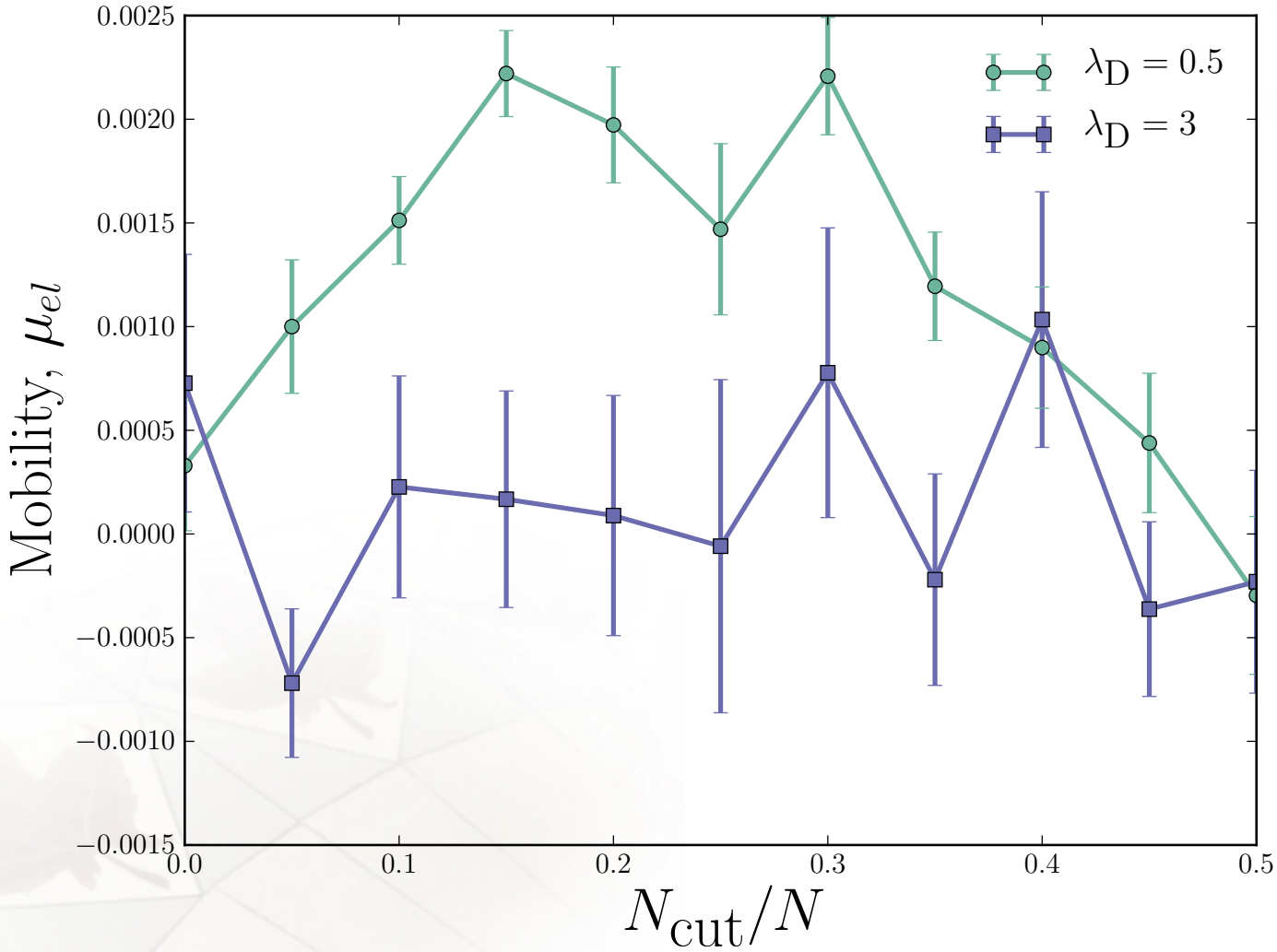

Figure : Electrophoretic mobility of a net neutral block copolymer ($N = 20$) as a function of cutting position N_{cut} for two values of λ_{D}.

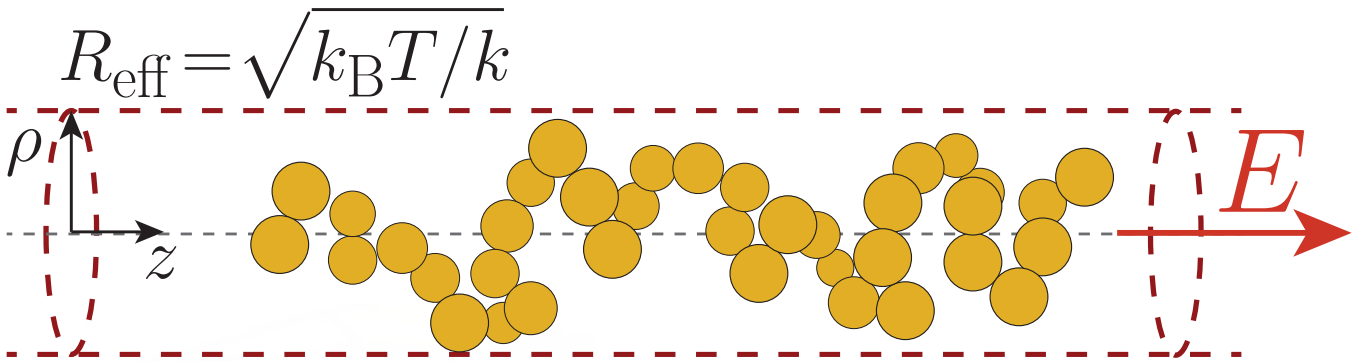

Figure : A polyelectrolyte chain of unperturbed radius of gyration R_g undergoing electrophoretic motion under the action of an electric field E. An harmonic potential with a cylindrical geometry confines the chain radially.

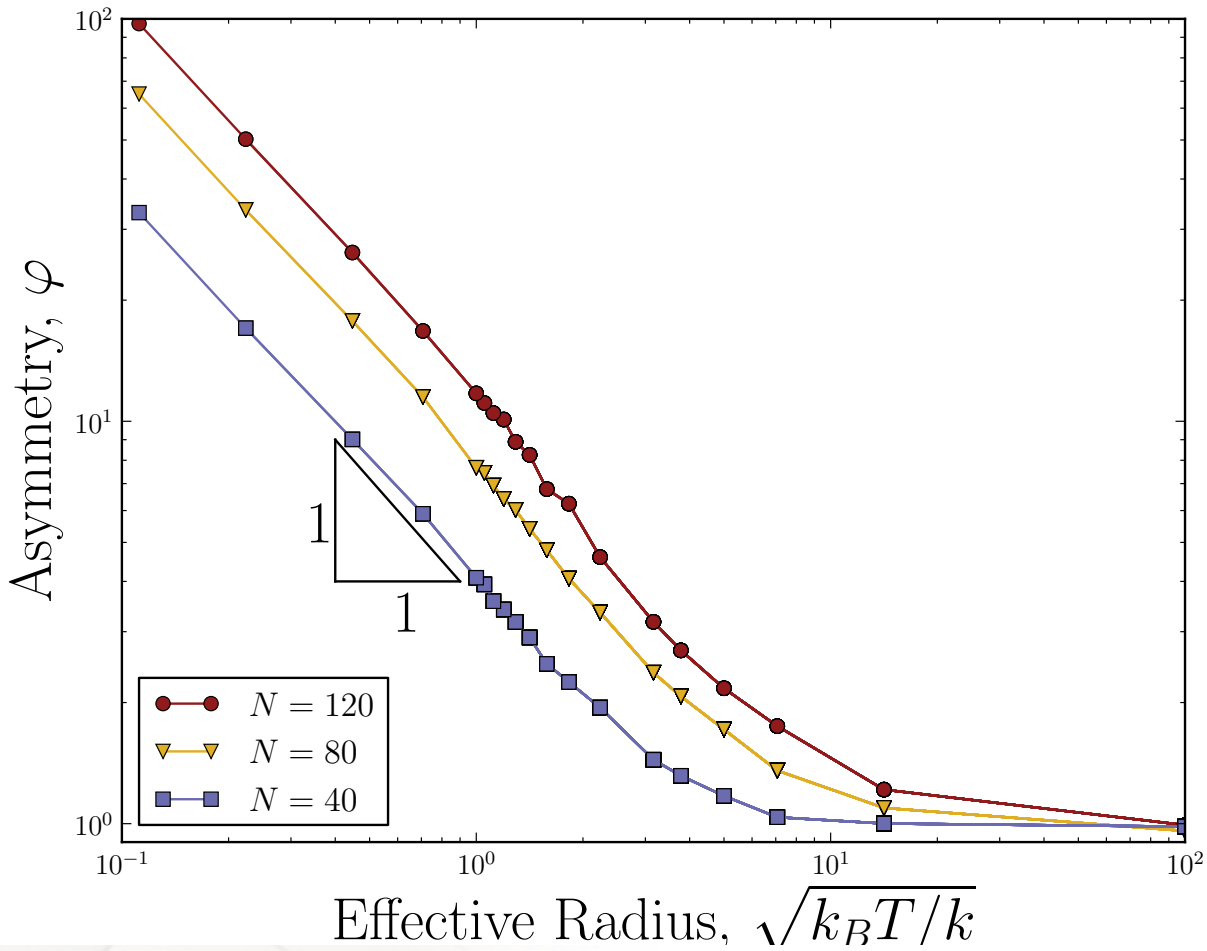

Figure : Asymmetry ratio $\varphi = R_{g,z}/R_{g,\rho}$ as a function of effective confinement radius of the harmonic well $R_{\text{eff}} = \sqrt{k_B T/k}$.

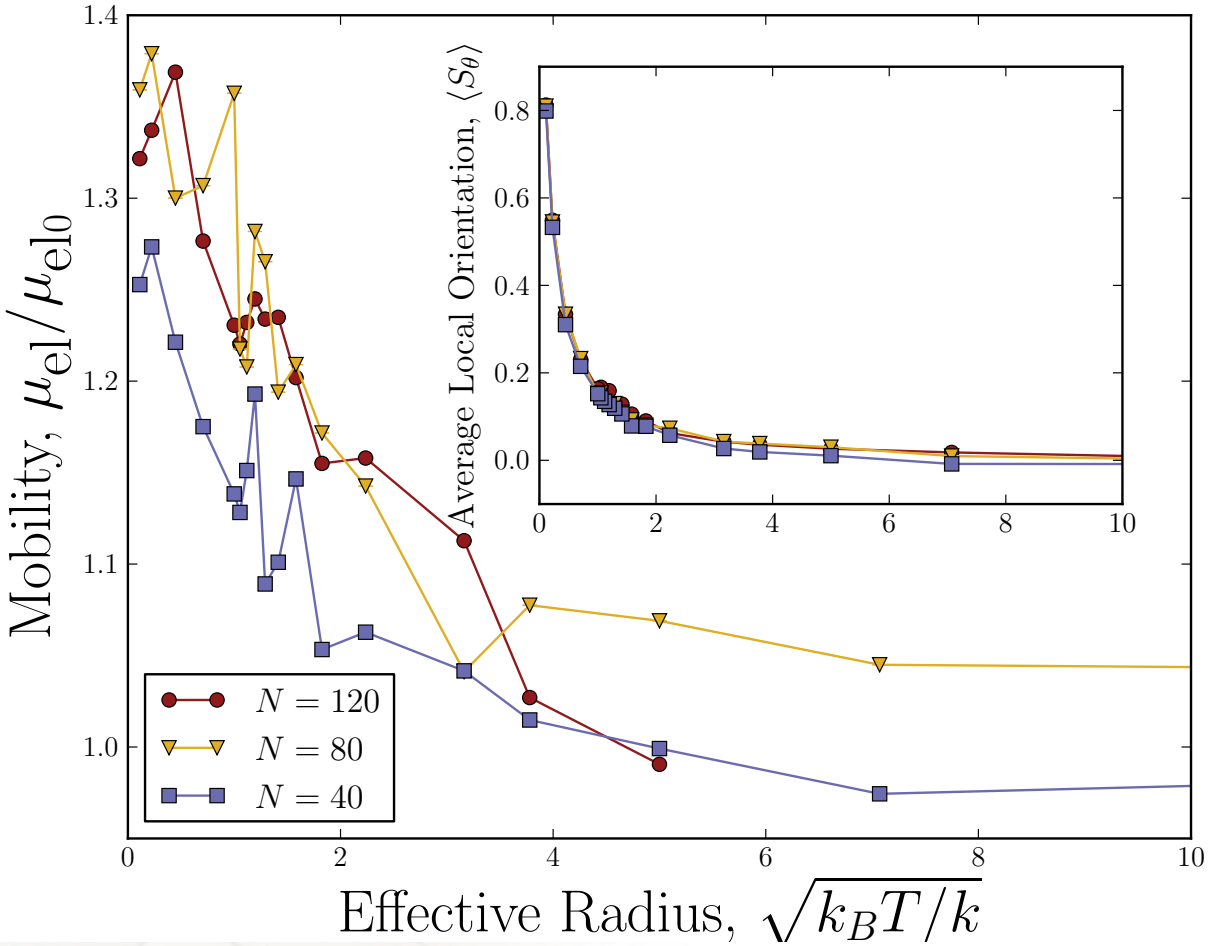

Figure : The electrophoretic mobility of confined polyelectrolytes as a function of effective confinement radius of the harmonic well $R_{\text{eff}} = \sqrt{k_B T/k}$ normalized by the free-solution value μ_{el_0} for various degrees of polymerization N. The inset shows the average local order parameter of the bonds between monomer as a function of the effective confinement radius R_{eff}.

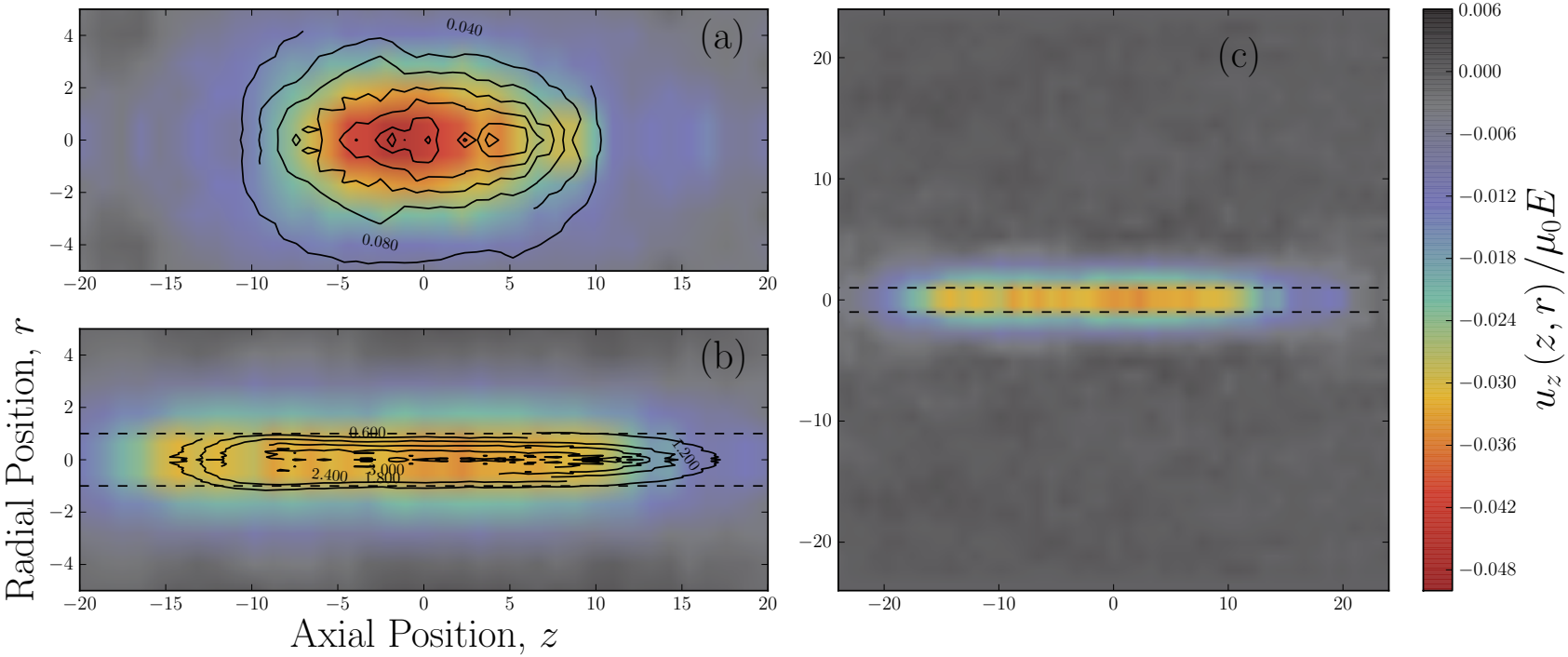

Figure : Speed of the fluid about the polyelectrolyte's centre of mass normalized by the electrophoretic speed of the chain. The degree of polymerization is $N = 200$, the electric field is $E = 2$ and the polymer is coupled to the fluid via the MPCD-in-MD scheme. (a) shows the fluid speed field generated by the electrophoresis of an unconfined, free-solution polyelectrolyte. (b) shows the field over the same range but for a charged chain that is confined by an axially symmetric harmonic potential with an effective radius of $R_{\text{eff}} = 1$. (c) presents the far-field fluid speeds for the same situation as shown (b). The speed of the surround fluid is zero immediately outside of the polymer coil.

Figure : The local order parameter is, on average, $\langle S_\theta \rangle = 0$ for an unconfined chain but if the chain is strongly confined then the bonds between monomers are more likely to be aligned.

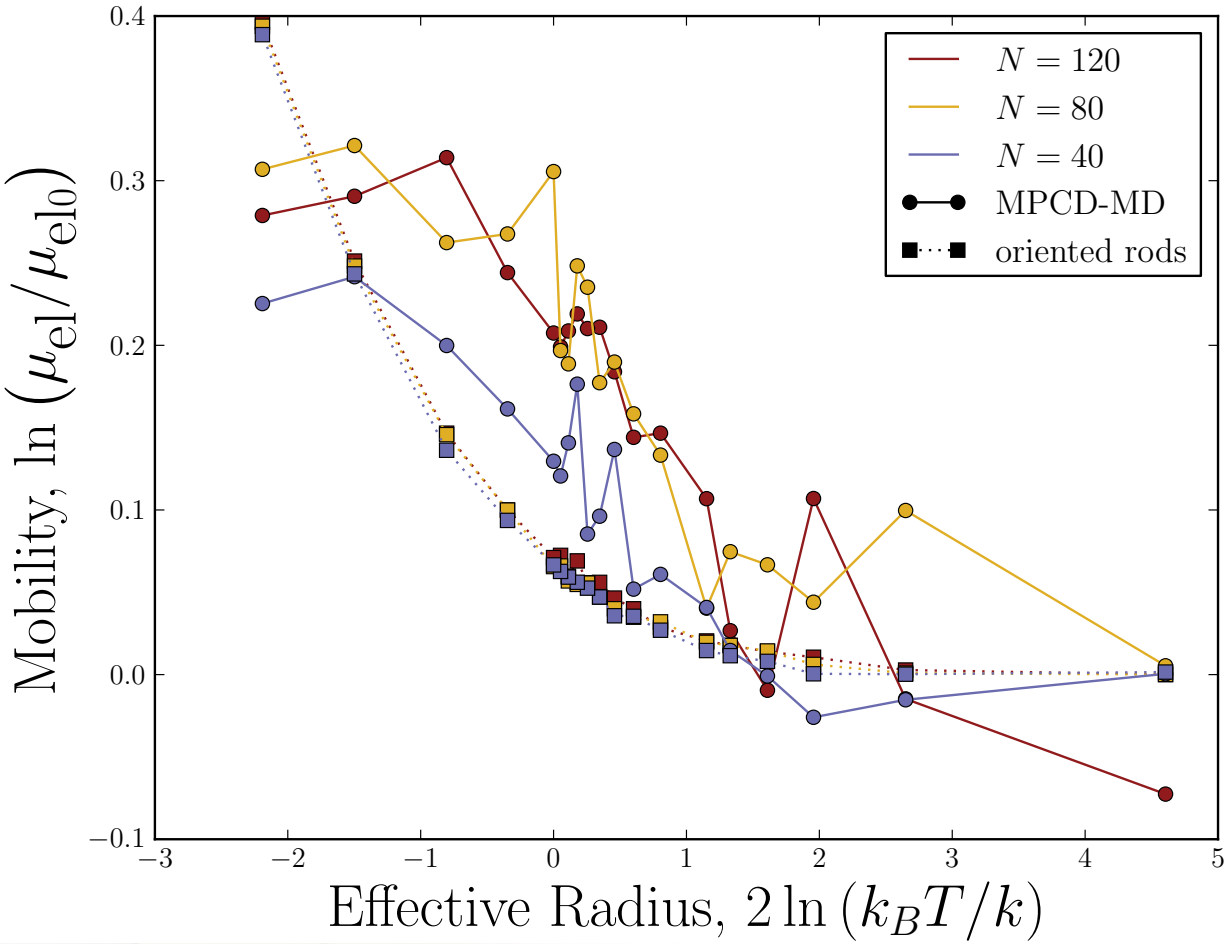

Figure : Dotted lines model the rise in mobility by approximating the mean local segment friction coefficients as oriented rods.

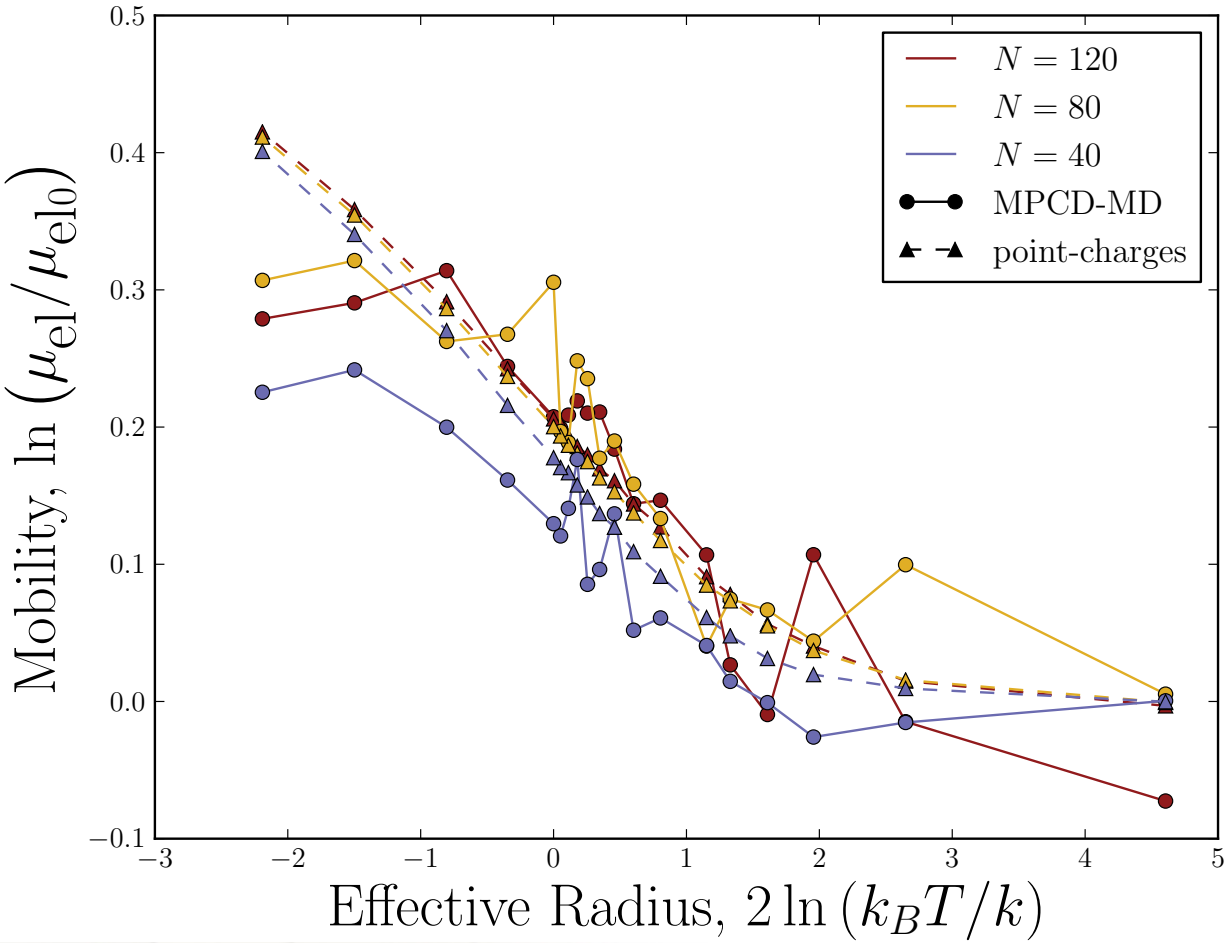

Figure : Dashed lines model the polyelectrolyte as an ensemble of charged point-forces at the instantaneous position of the monomers from simulations as calculated by the Long-Ajdari screened hydrodynamic interaction tensor.

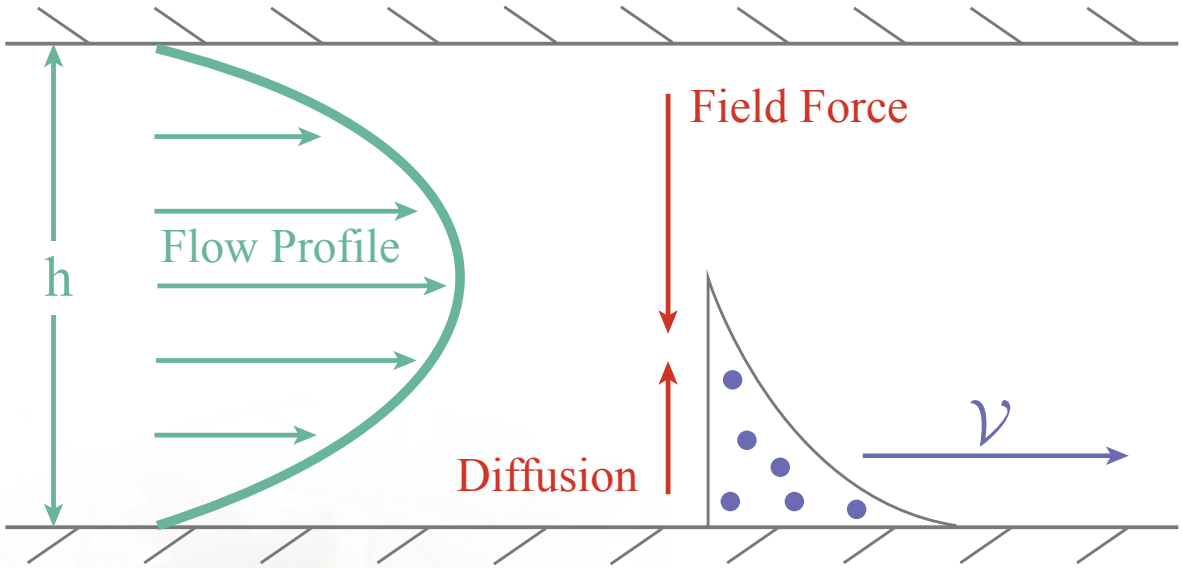

Figure : Schematic of normal-mode FFF. An external force, perpendicular to the flow profile pushes the solute against the accumulation plate. The competition between the force and the diffusivity establishes a concentration gradient. The mean velocity of the solute is a function of the solute concentration and solvent velocity profiles.

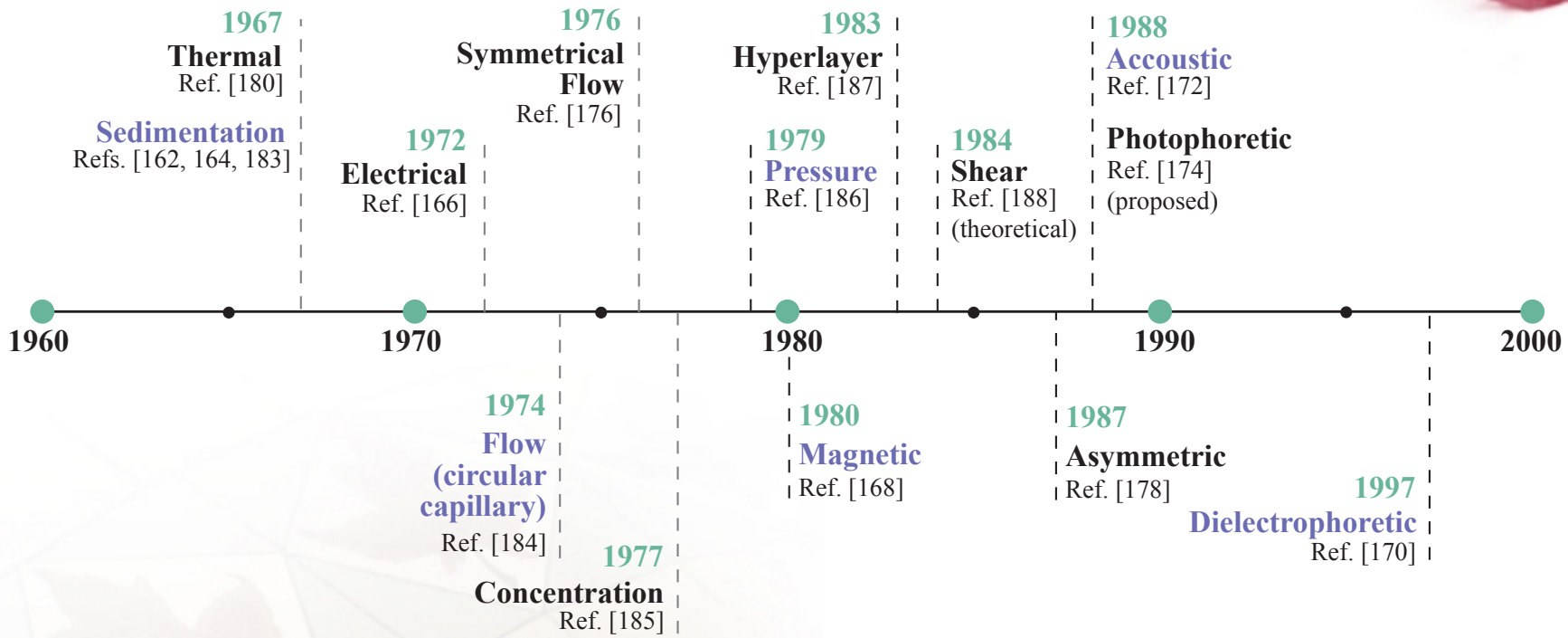

Figure : Historical development of the family of FFF sub-techniques. After Cölfen and Antonietti.

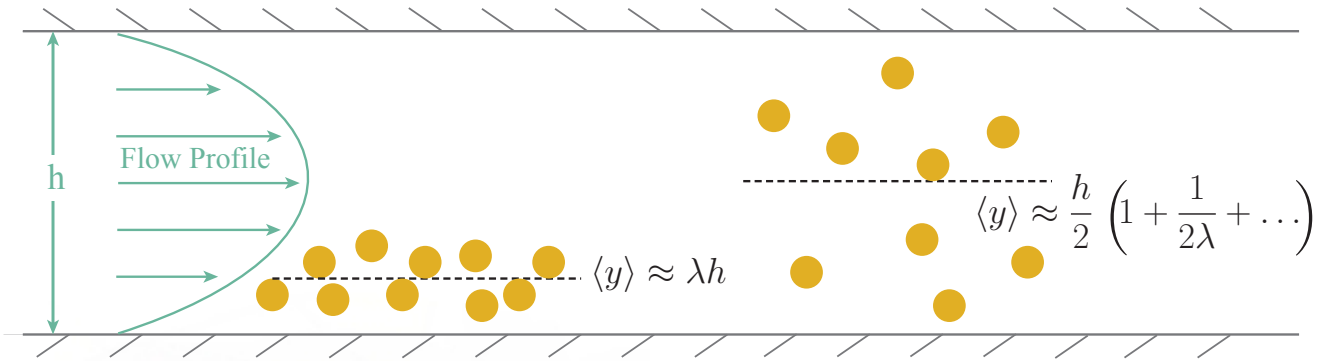

Figure : The two limiting behaviour of the concentration distribution. In strong forces, the solutes are qualitatively confined to a film of thickness $\langle y \rangle = \lambda h$. In weak fields, the distribution is perturbed from being homogeneous.

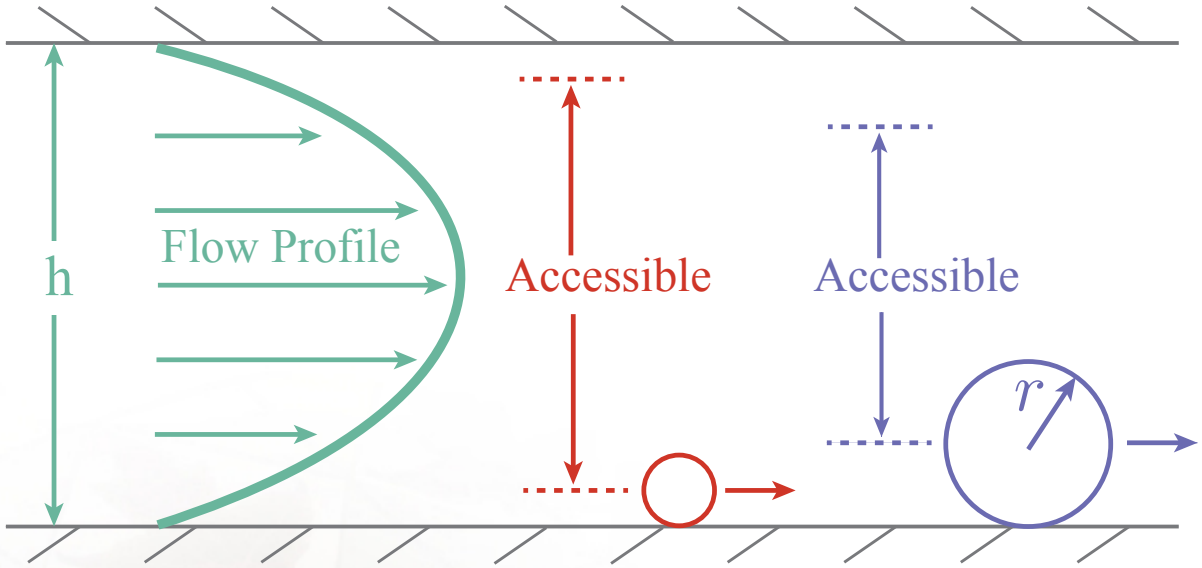

Figure : Schematic representation of steric-mode FFF. When hard, finite-sized solutes undergo elution, they are excluded from a region near the wall where the fluid velocity is low. As a result, they tend to elute earlier than smaller particles.

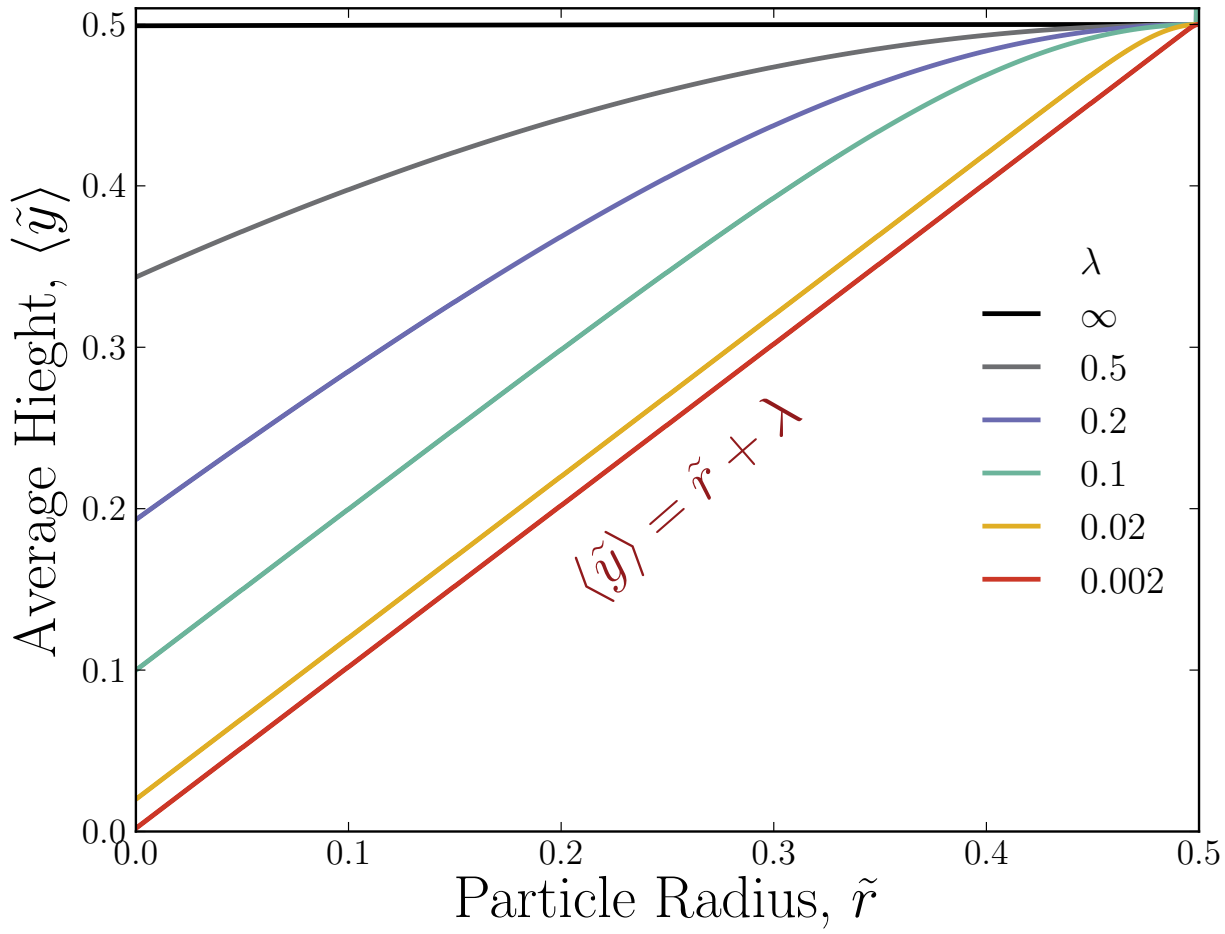

Figure : Mean concentration height for a variety of retention parameters varying from no force ($\lambda = \infty$) to a relatively large forces ($\lambda = 0.002$). The mean concentration height grows with particle size $\tilde{r}$ when $\lambda \ll 1$.

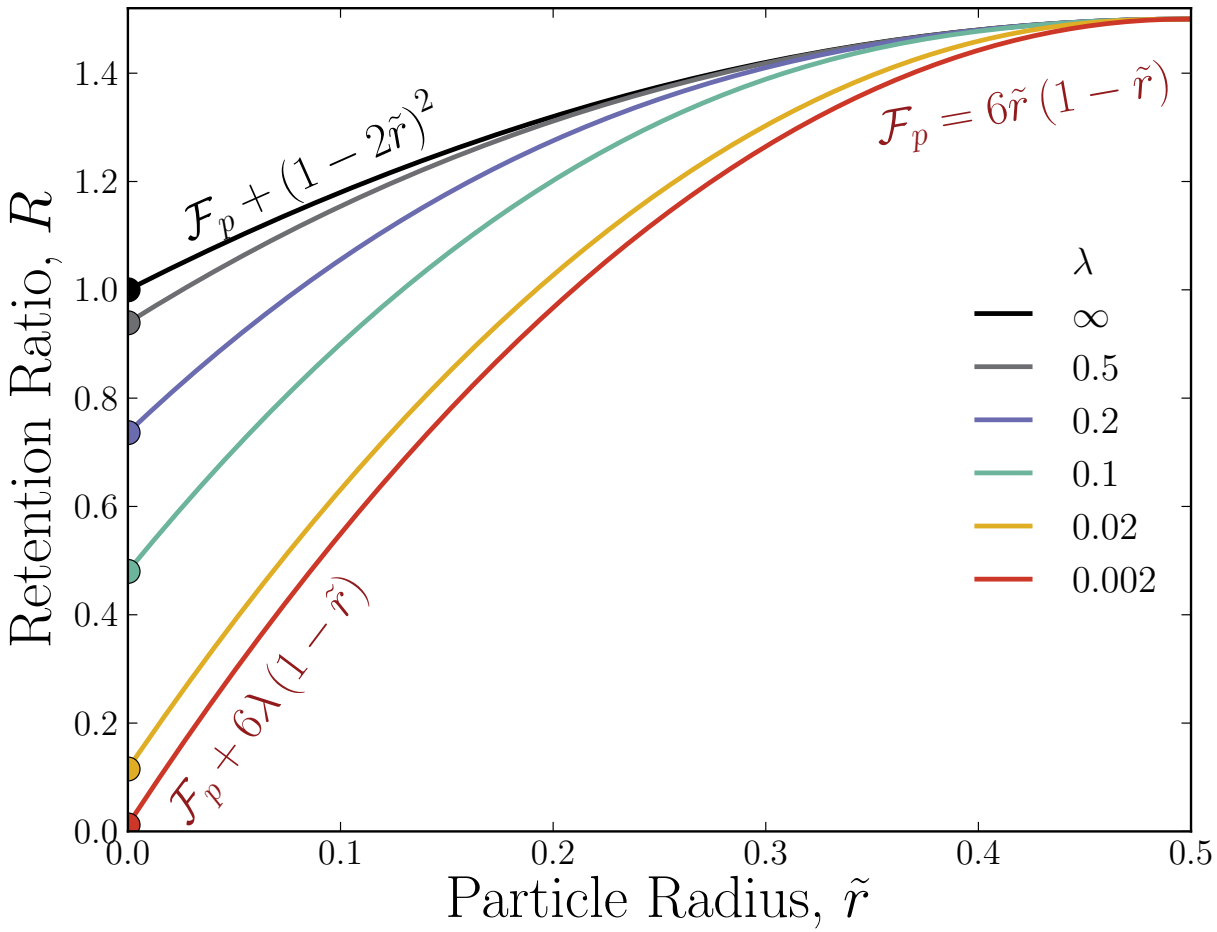

Figure : Retention ratio for a variety of retention parameters varying from no force ($\lambda = \infty$) to relatively large forces ($\lambda = 0.002$).

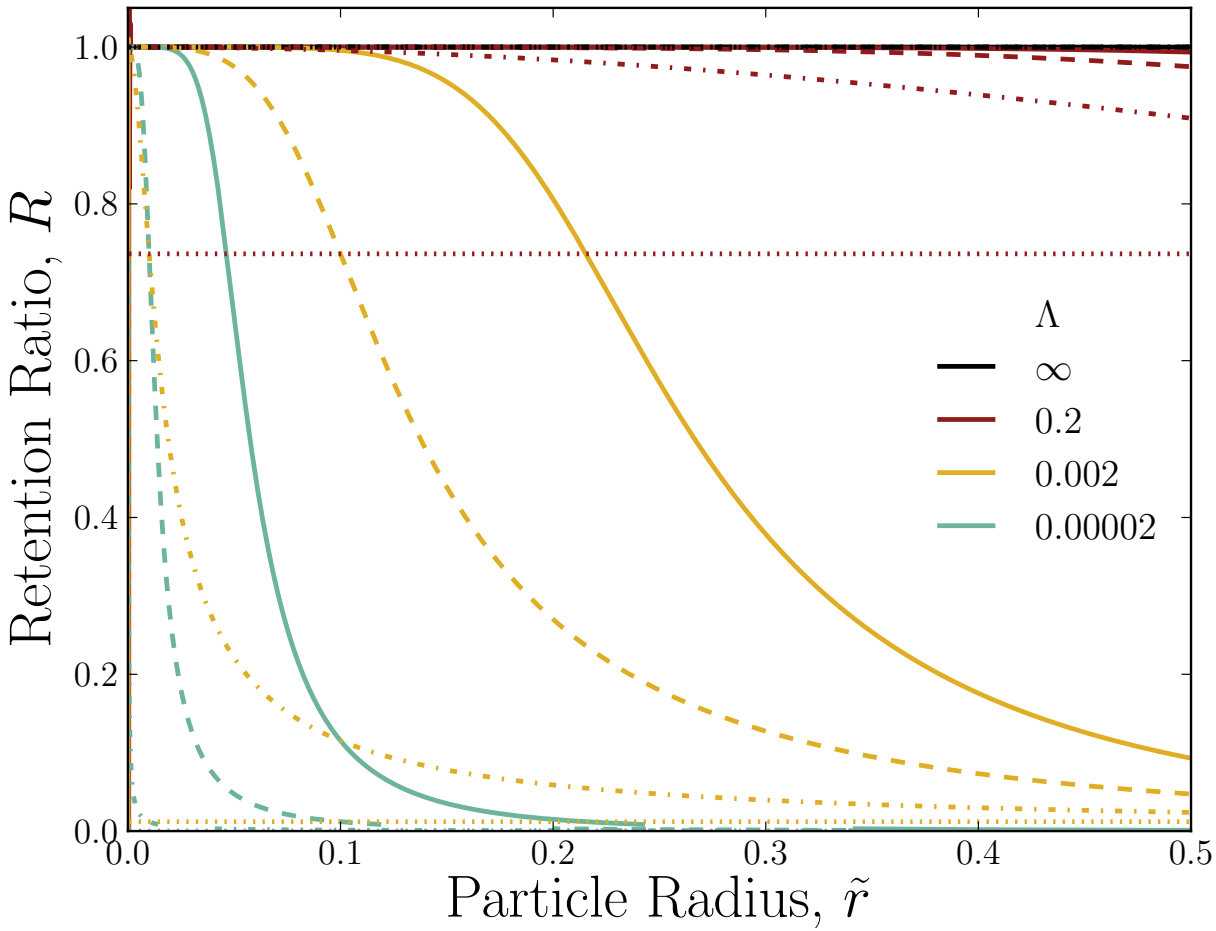

Figure : Retention ratio $R(\tilde{r})$ as predicted by the standard point-particle theory for normal-mode FFF. The retention parameter λ is assumed to vary like $\lambda = \Lambda \tilde{r}^{-\alpha}$ but the particle size is otherwise not taken into account. Solid lines denote $\alpha = 3$, dashed $\alpha = 2$, dash-dot $\alpha = 1$ and dotted lines denote $\alpha = 0$ (all of which are horizontal). Small particles elute first except when $\alpha = 0$ where retention time is not a function of particle size.

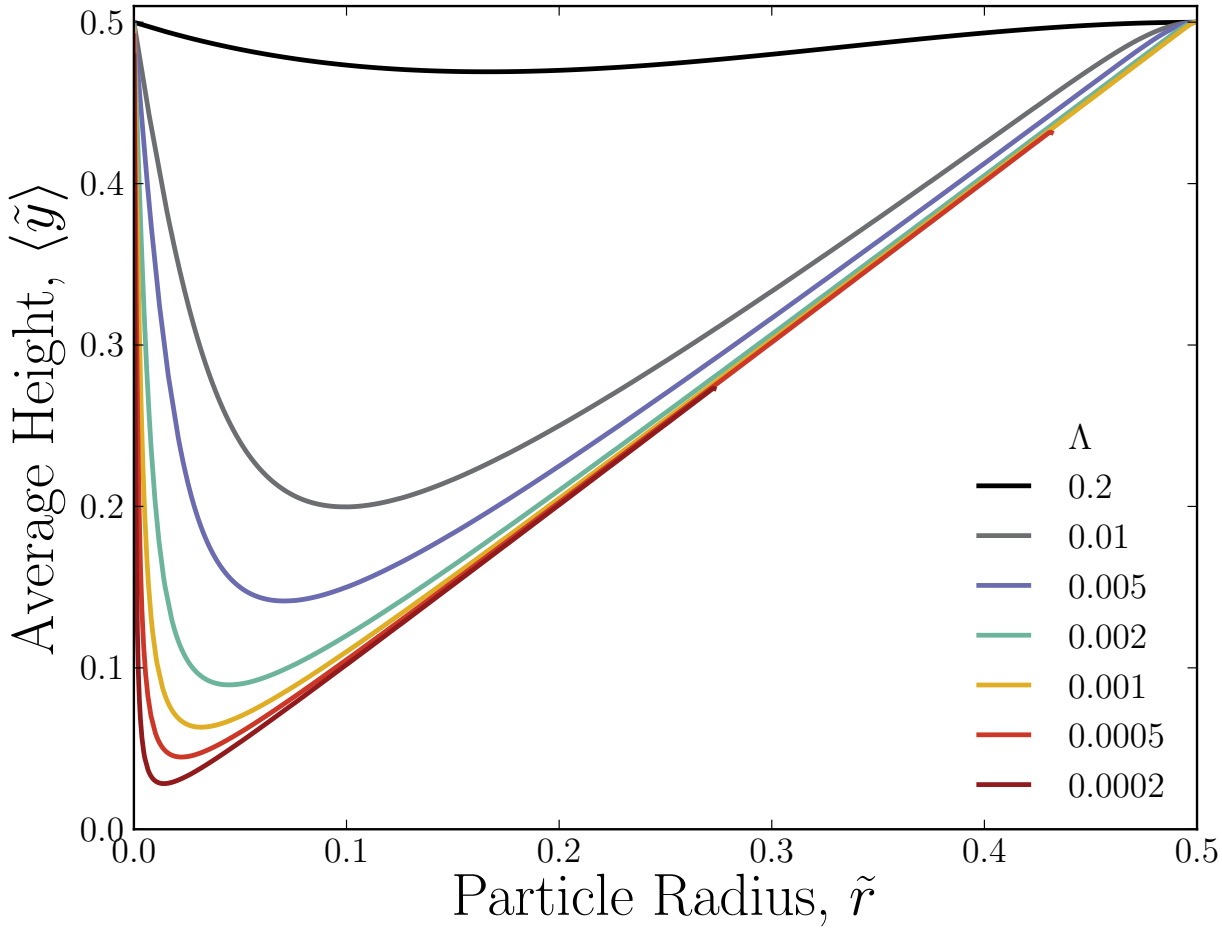

Figure : Average height of solutes from the accumulation wall for $\alpha = 1$. As Λ decreases, the mean concentration height's minima occurs at smaller and smaller particle sizes.

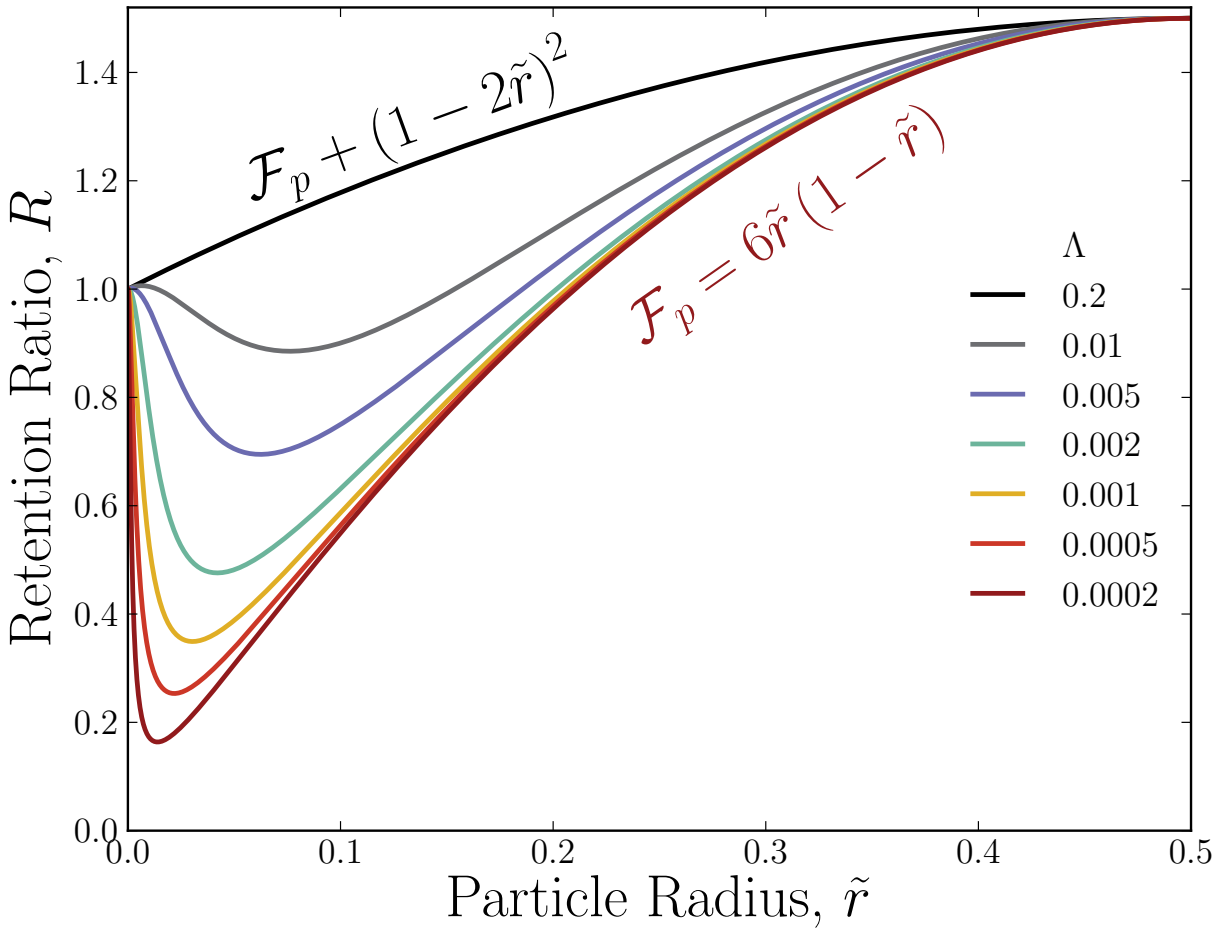

Figure : Retention ratio for $\alpha = 1$. When the force varies as $\tilde{r}^{\alpha}$, the retention ratio no longer rises in a simple monotonic manner. Below the critical device retention parameter $\Lambda_c = 1.90 \times 10^{-2}$, the retention ratio becomes non-monotonic.

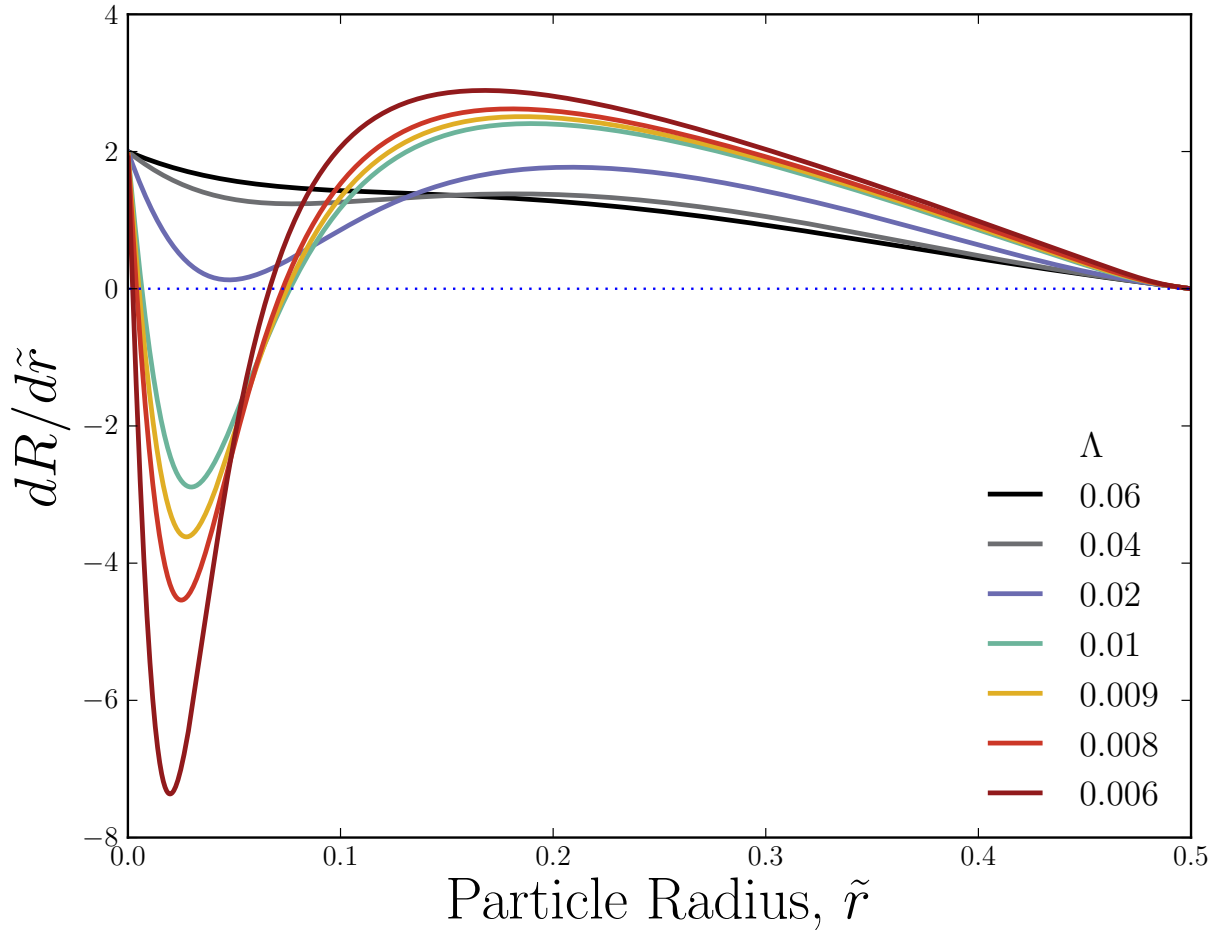

Figure : Derivative of retention ratio with respect to particle size for $\alpha = 1$.

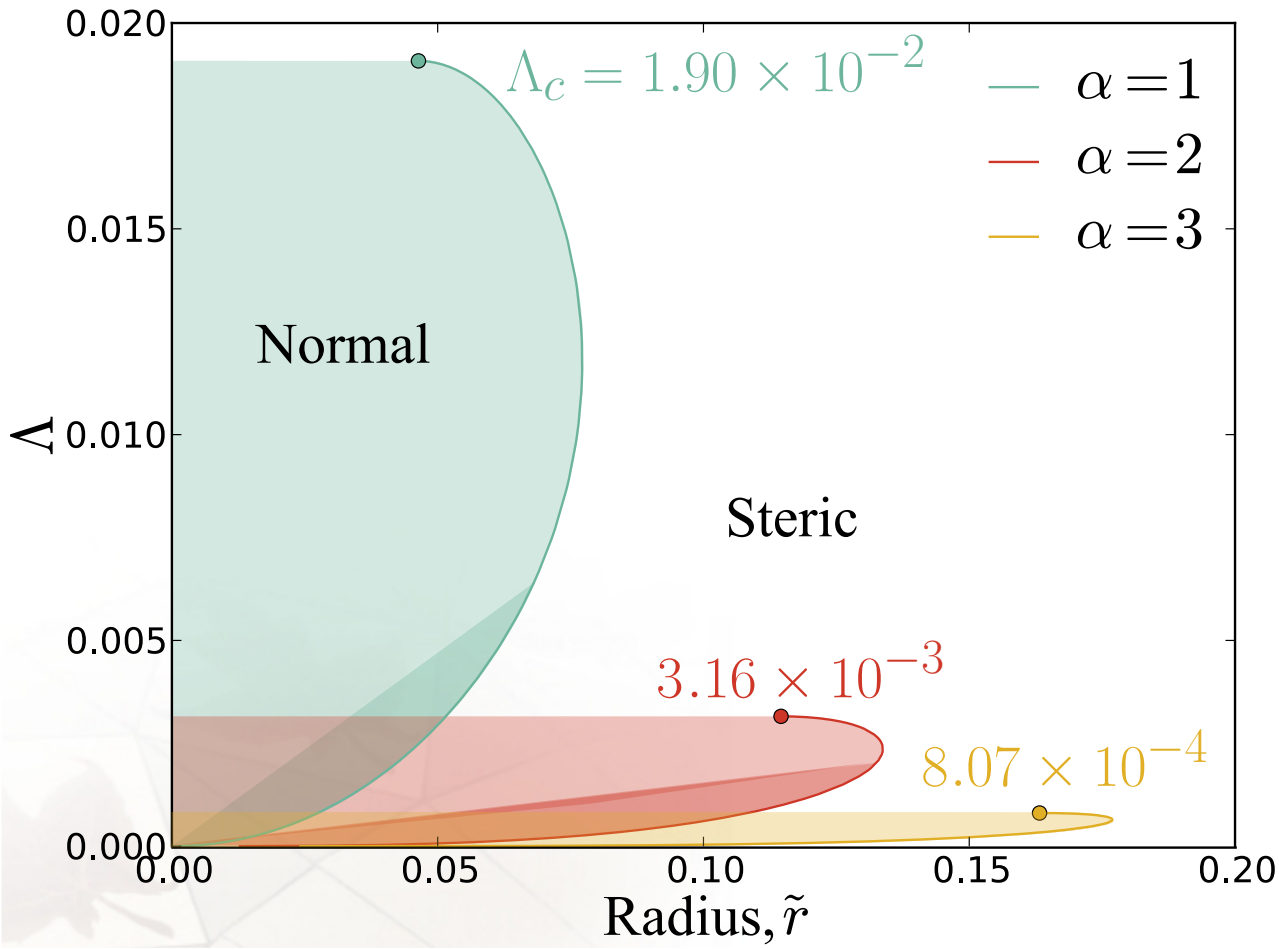

Figure : A tentative operational-mode diagram for FFF. The dividing line between normal-mode FFF and large particle steric-mode FFF is the numerically determined critical particle size $\tilde{r}_{NS}$. Normal-mode FFF is represented by the shaded regions and does not exist above a critical device retention parameter Λ_c; the critical device retention parameter values ($\Lambda_c = 1.90 \times 10^{-2}$ for $\alpha = 1$; $\Lambda_c = 3.16 \times 10^{-3}$ for $\alpha = 2$; and $\Lambda_c = 8.07 \times 10^{-4}$ for $\alpha = 3$) are marked by a closed circle.

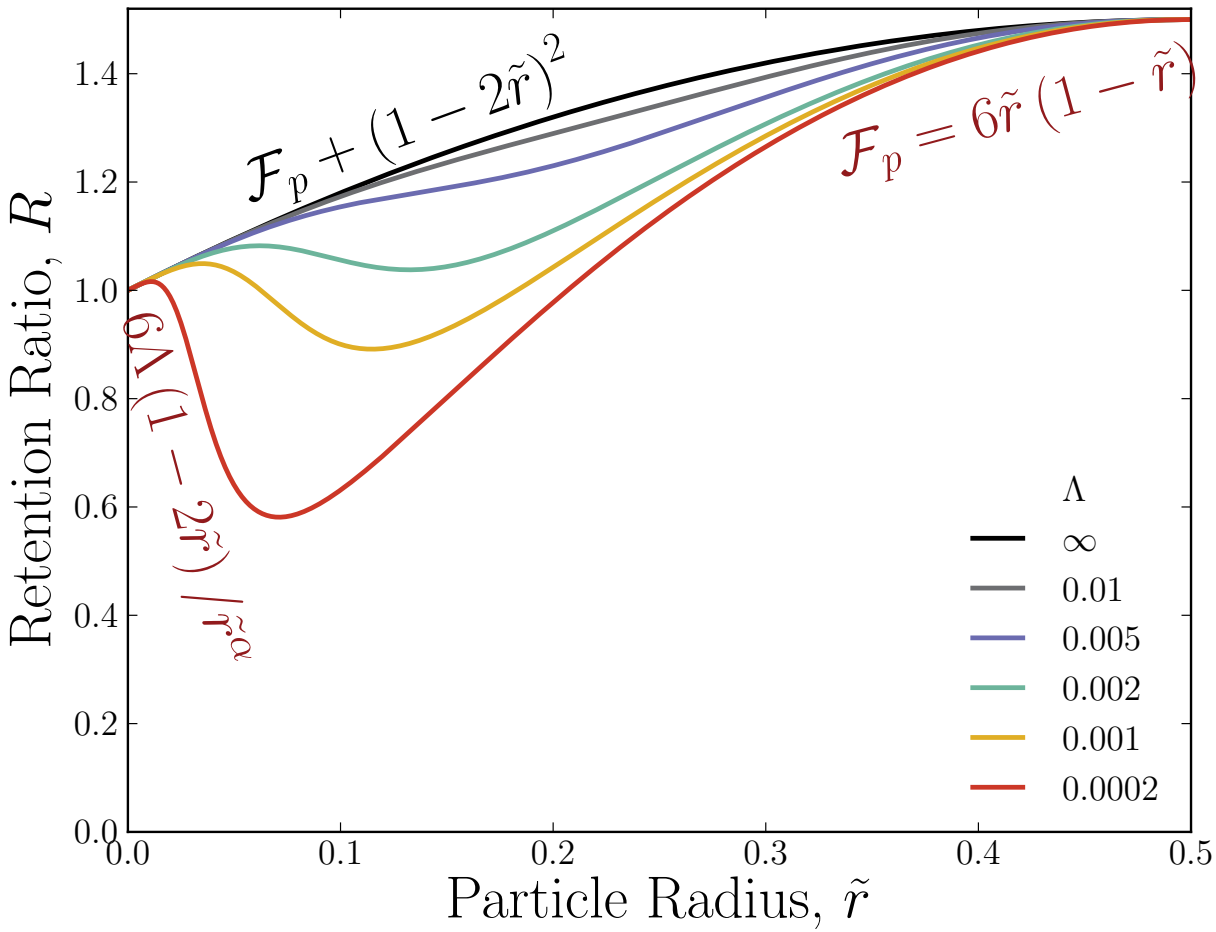

Figure : Retention ratios for $\alpha = 2$. The retention ratio is monotonic above the critical device retention parameter $\Lambda_c = 3.16 \times 10^{-3}$. As discussed in the text, there are three modes of operation when $\Lambda < \Lambda_c$: For the smallest particles the force is negligible, the slope is positive and the mode of operation is hydrodynamic chromatography. For moderately small particles the force dominates, the slope is negative and the mode of operation is normal-mode FFF. For the largest particles the effects of sterically excluded regions are most important; the slope is once again positive and the mode of operation is steric-mode FFF.

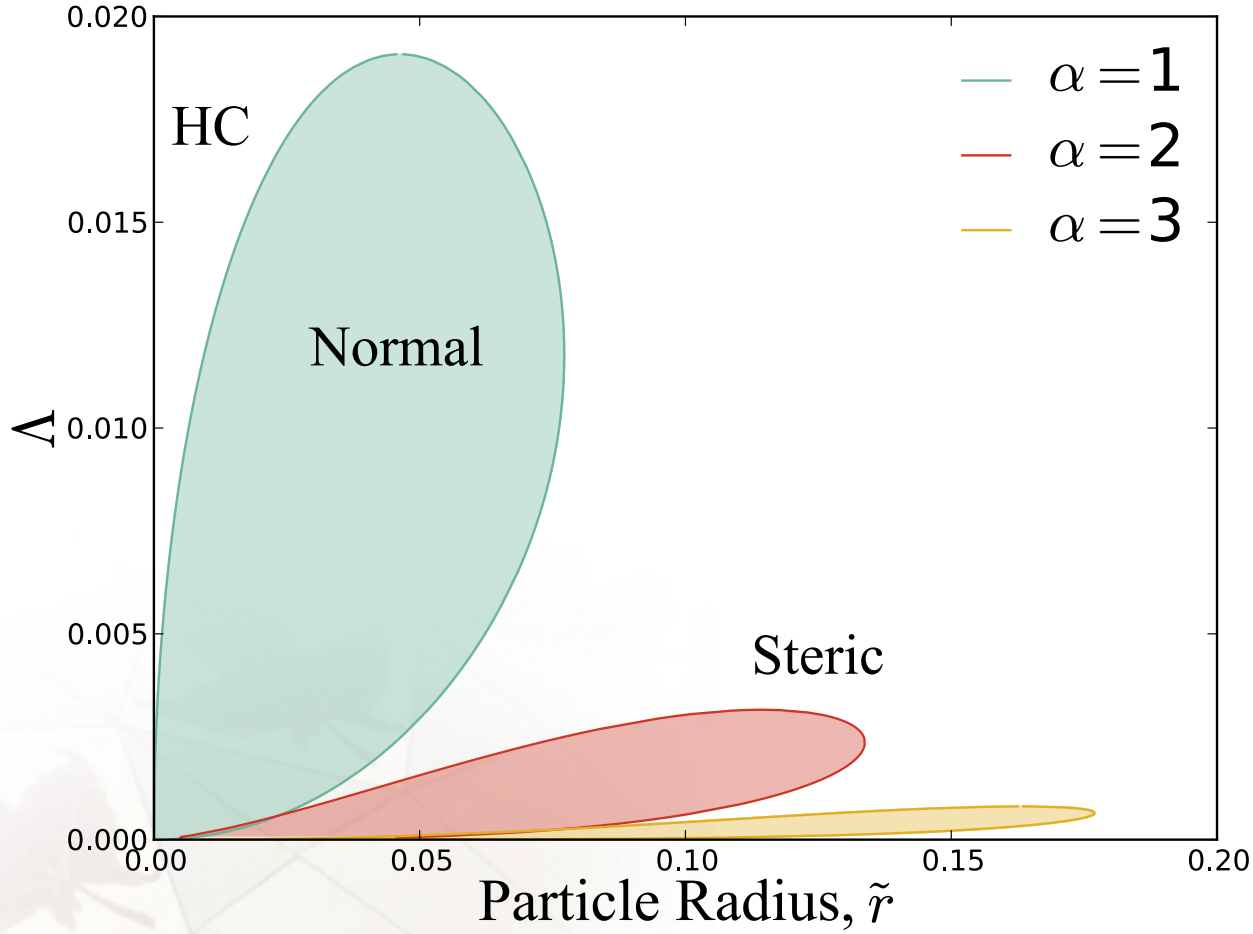

Figure : Enclosed regions are the areas of normal-mode FFF in which smaller particles elute before larger particles. Outer areas are steric-mode and hydrodynamic chromatography limit regions of operation in which larger particles elute before smaller particles. Solid lines are the numerically determined roots of $\partial R/\partial \tilde{r}$ ($\tilde{r}_{\mathrm{HN}}$ is a local maximum of R and so forms the left border while $\tilde{r}_{\mathrm{NS}}$ is a local minimum and forms the right boarder).

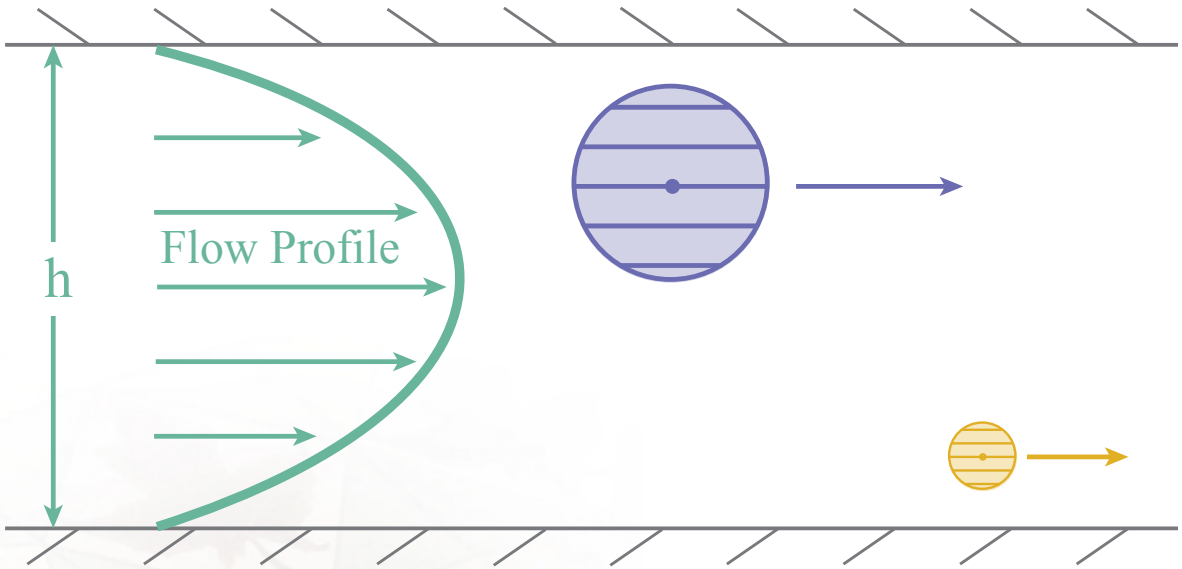

Figure : Schematic of area cross sectional integration of the particle's velocity

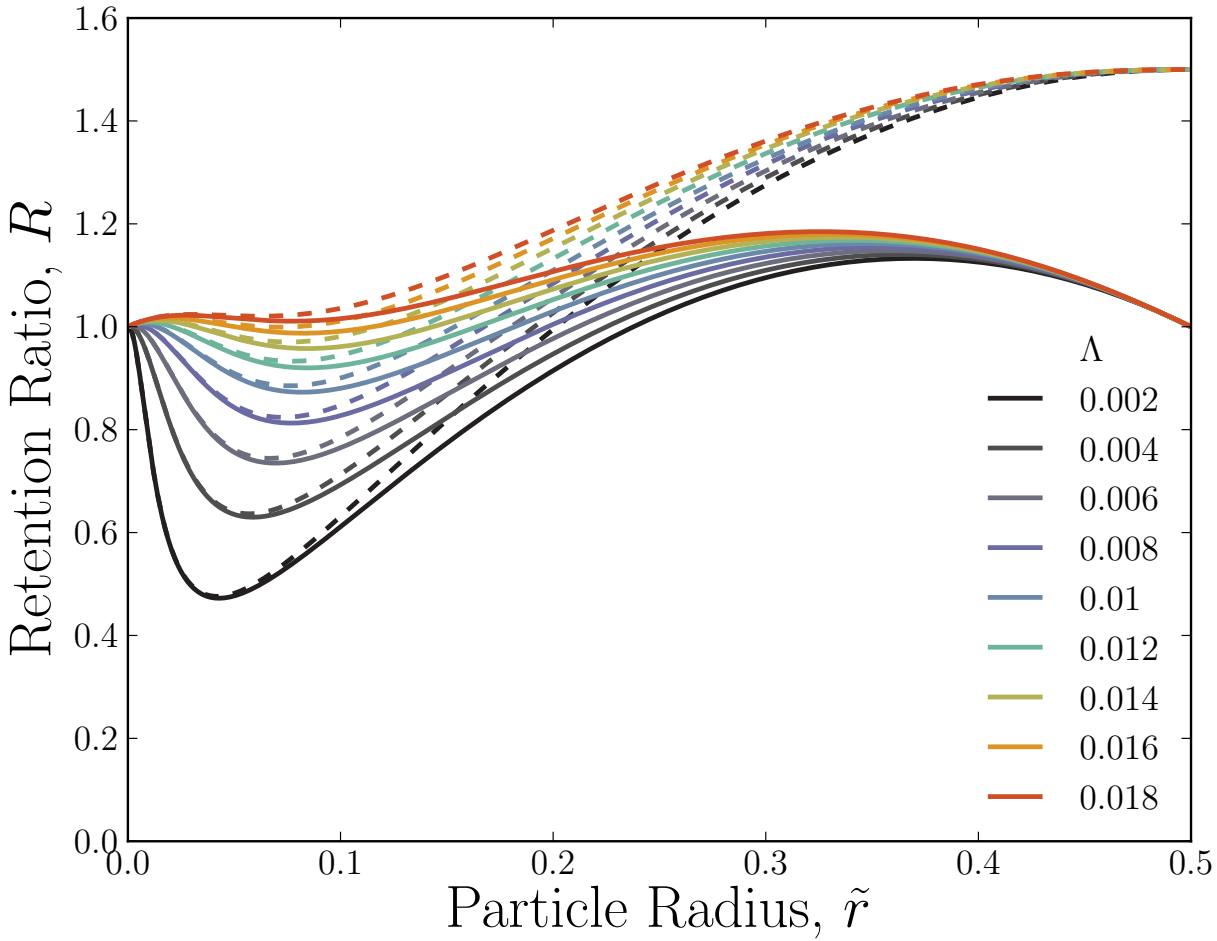

Figure : The retention ratio for $\alpha = 1$, taking into account both Faxén's Law compared to simply assuming the centre of mass velocity, as done previously.

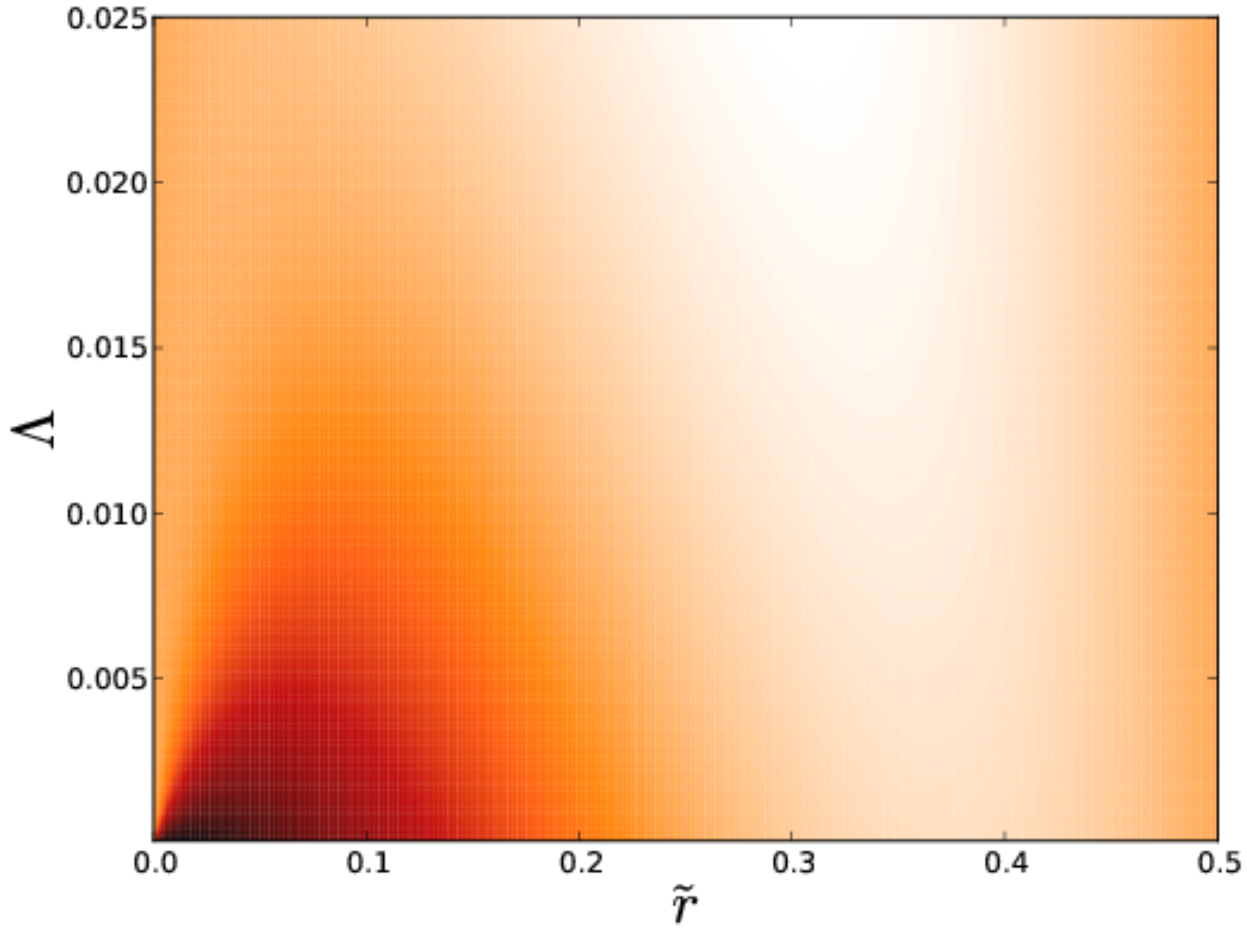

Figure : The retention ratio explicitly depends on the particle size $\tilde{r}$ and the device retention parameter Λ. The greatest magnitude is found in the strong fields/small particle size region.

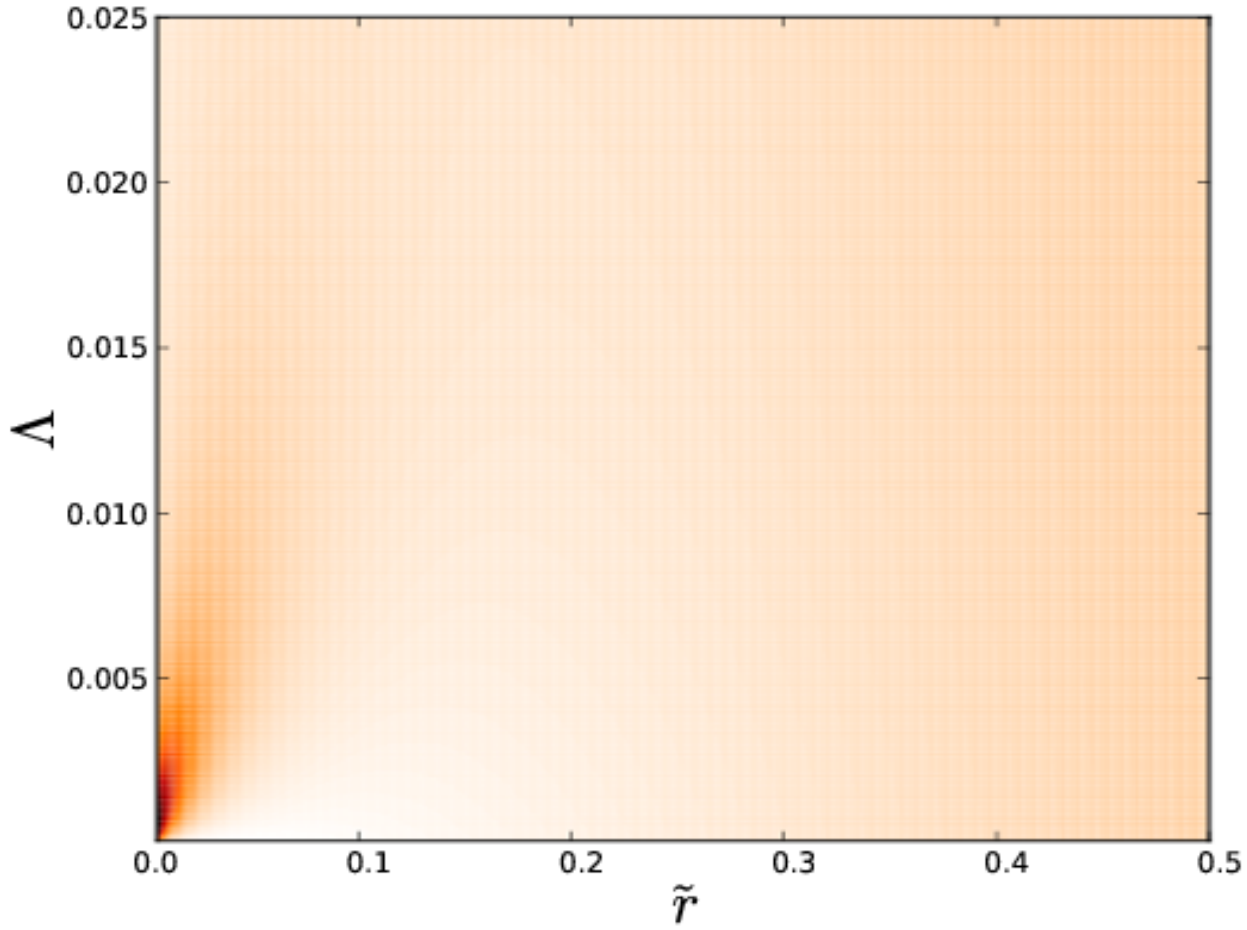

Figure : The derivative of retention ratio. It is large only in the steep normal-mode region.

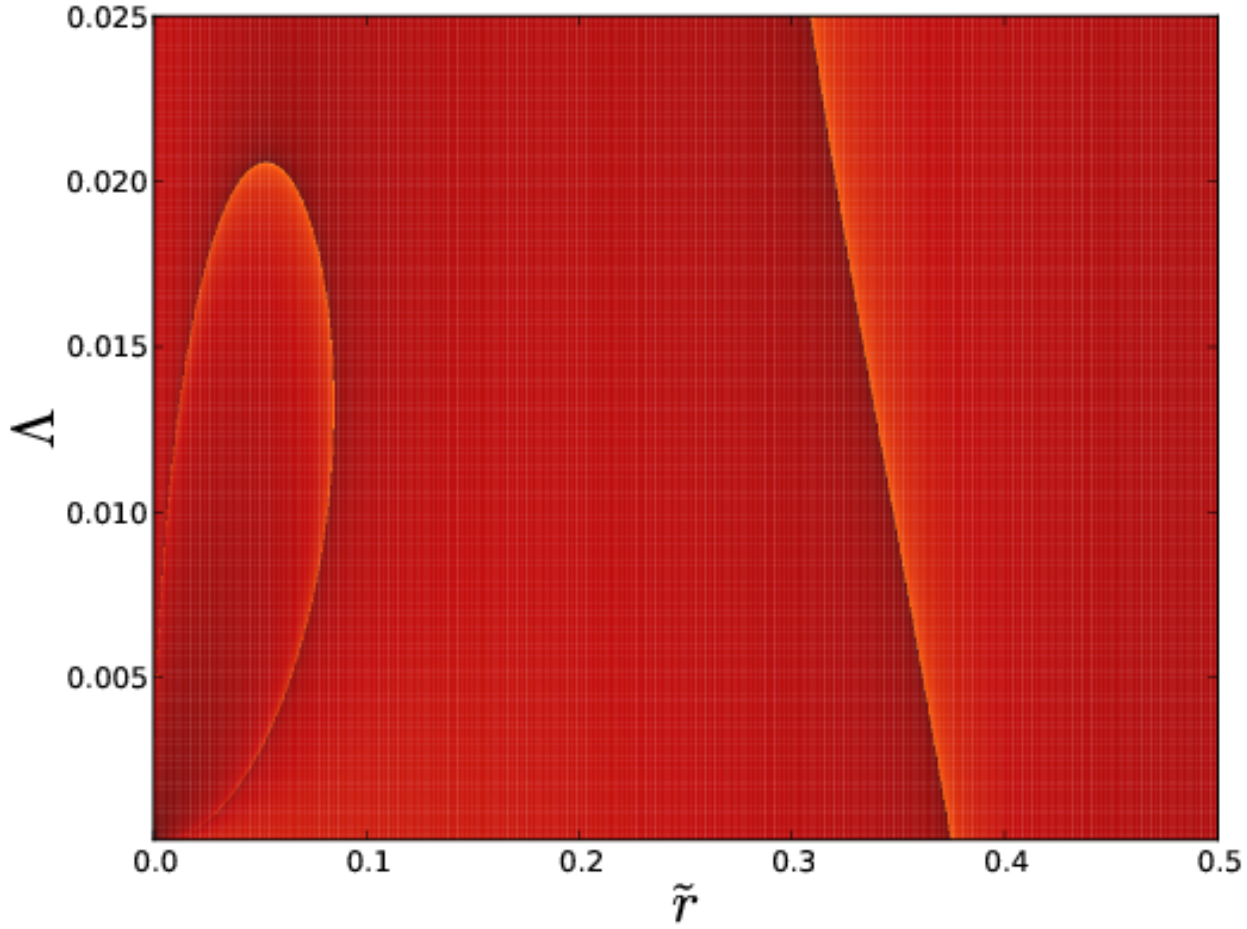

Figure : Though the roots of the derivative give the transitions between operational-modes, they were not clearly visible. In order to see them more clearly, the logarithm of the magnitude is taken.

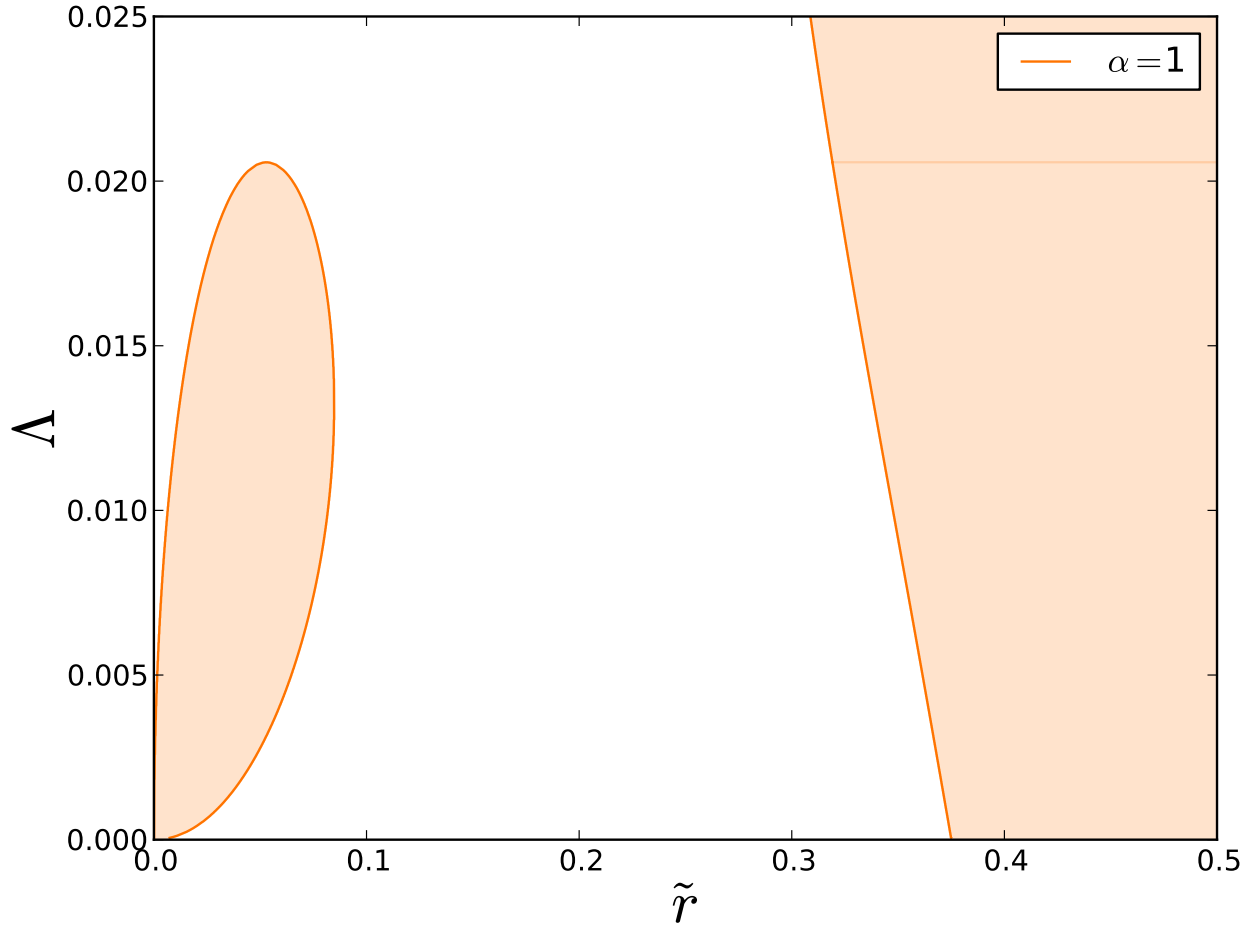

Figure : The roots of the derivative give the transitions between operational-modes for $\alpha = 1$. Enclosed regions are the areas of normal-mode and Faxén-mode FFF. Outer areas are steric-mode and hydrodynamic chromatography regions of operation.

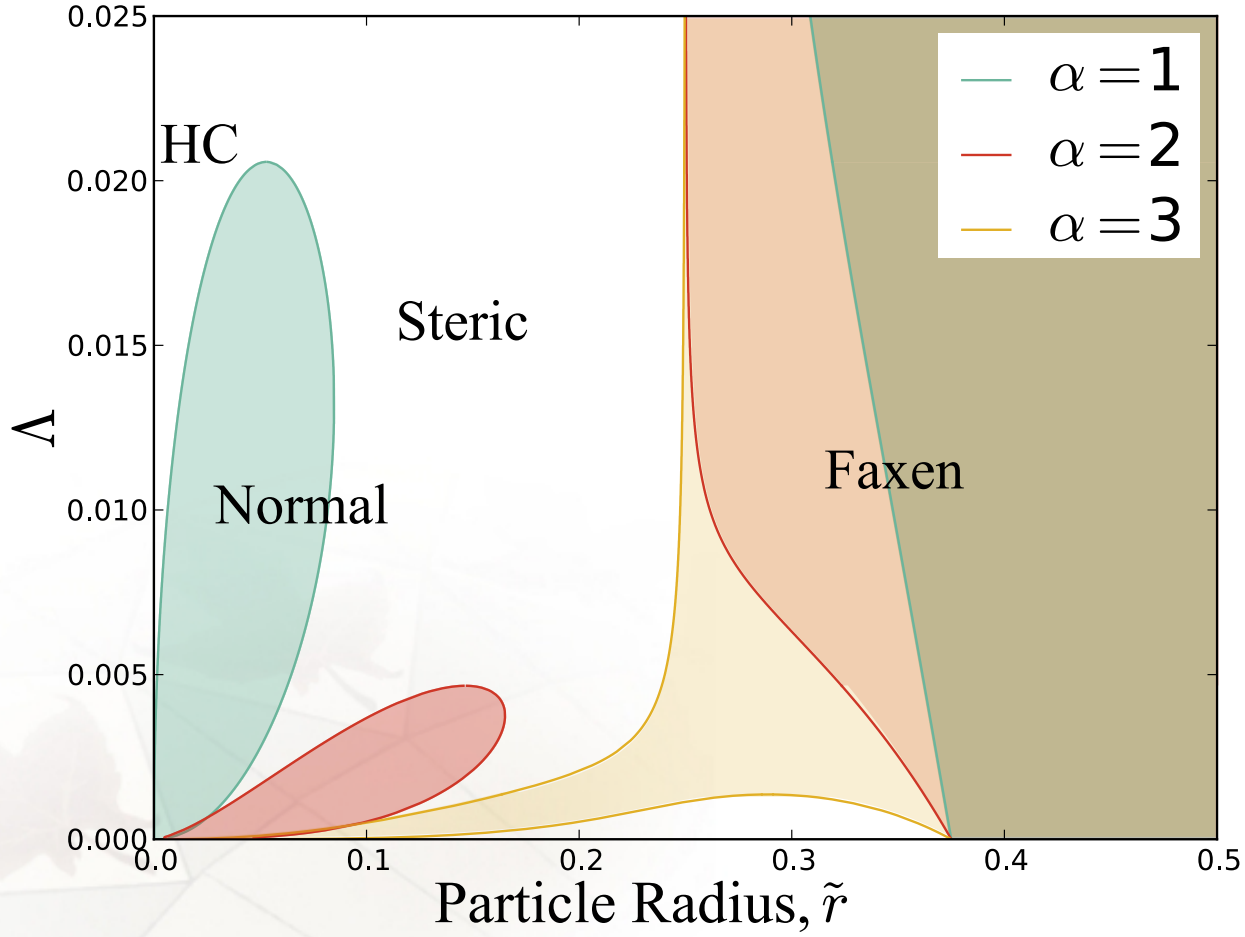

Figure : Ideal FFF-modes map. The numerically determined roots of $\partial R/\partial \tilde{r}$ give the critical sizes marking the transitions between the four different modes of operation $\tilde{r}_{HN}$, $\tilde{r}_{NS}$ and $\tilde{r}_{SF}$.

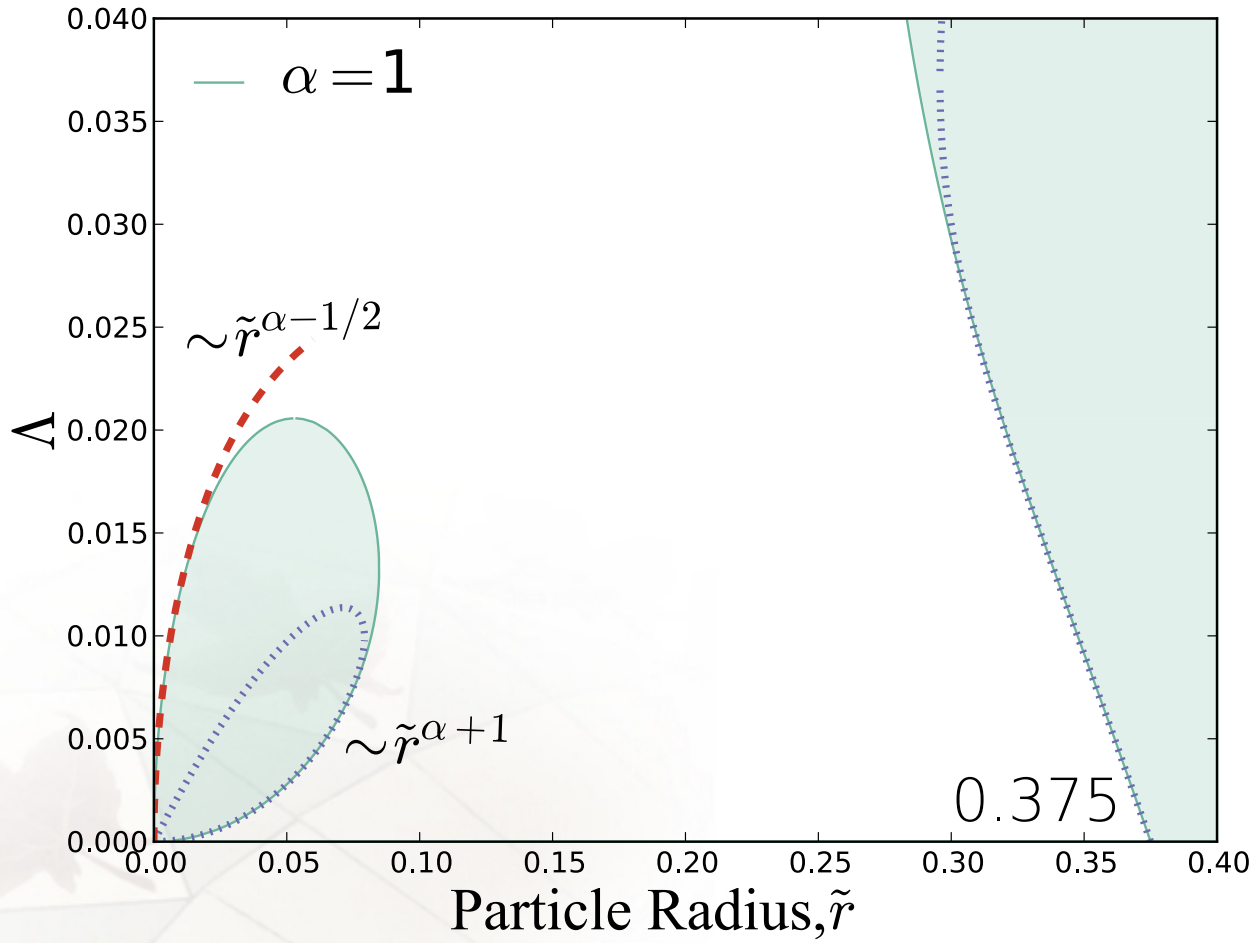

Figure : Approximations to $\tilde{r}_{SF}$ and $\tilde{r}_{NS}$ work well for small device retention parameters Λ as shown by the dotted lines for the example of $\alpha = 1$. The dashed line shows the small $\tilde{r}$ approximation for the $\tilde{r}_{HN}$ transition.

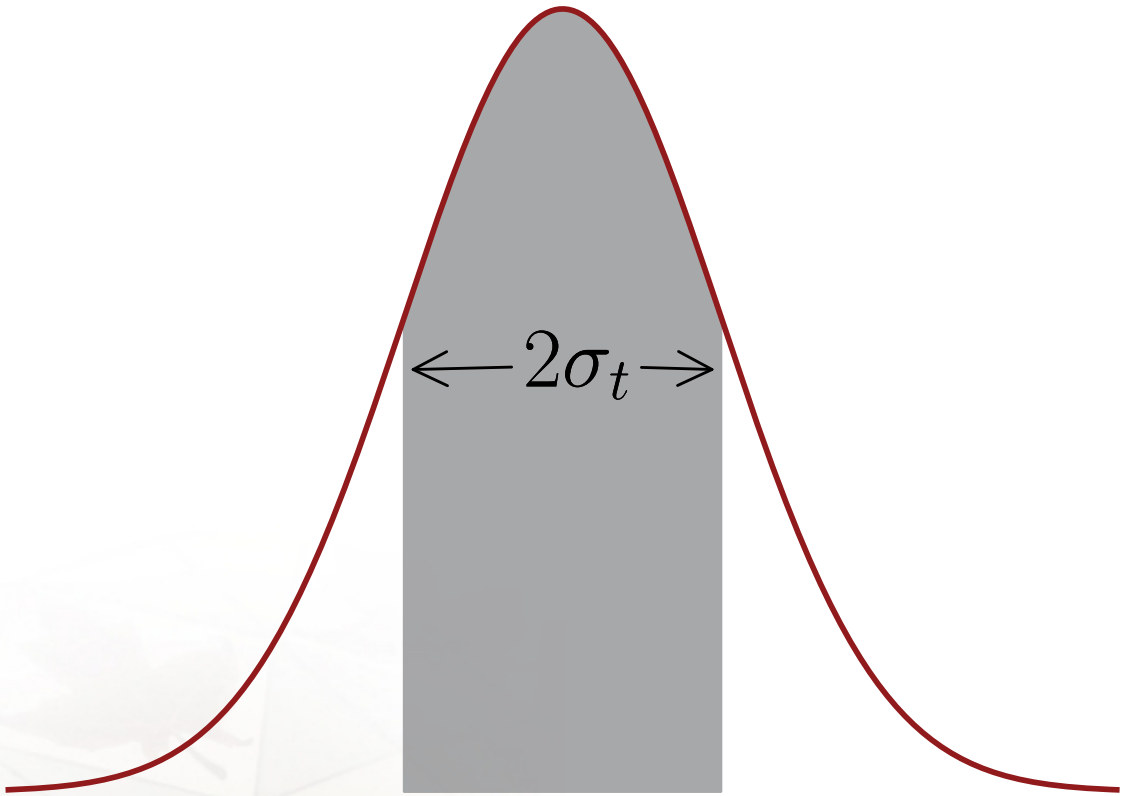

Figure : Colloquially, the width of a zone is twice the standard deviation of a Gaussian peak.

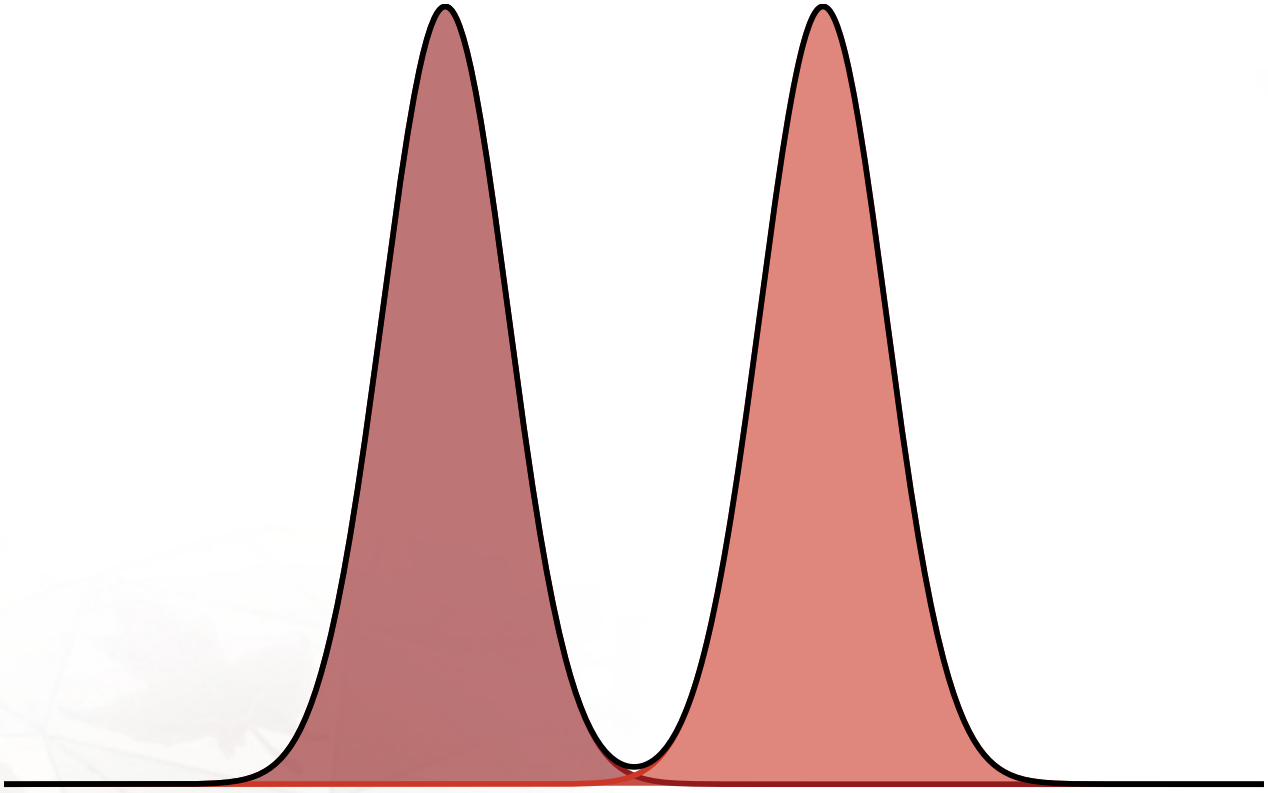

Figure : Highly resolved pair of Gaussian peaks

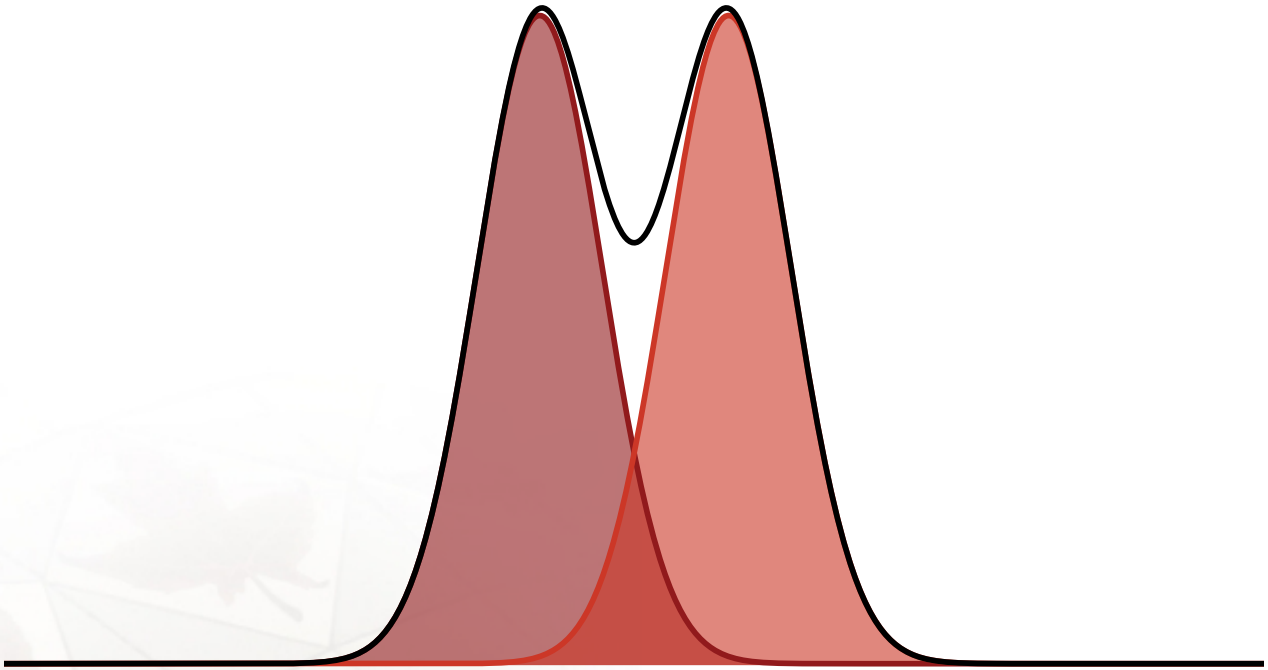

Figure : Poorly resolved pair

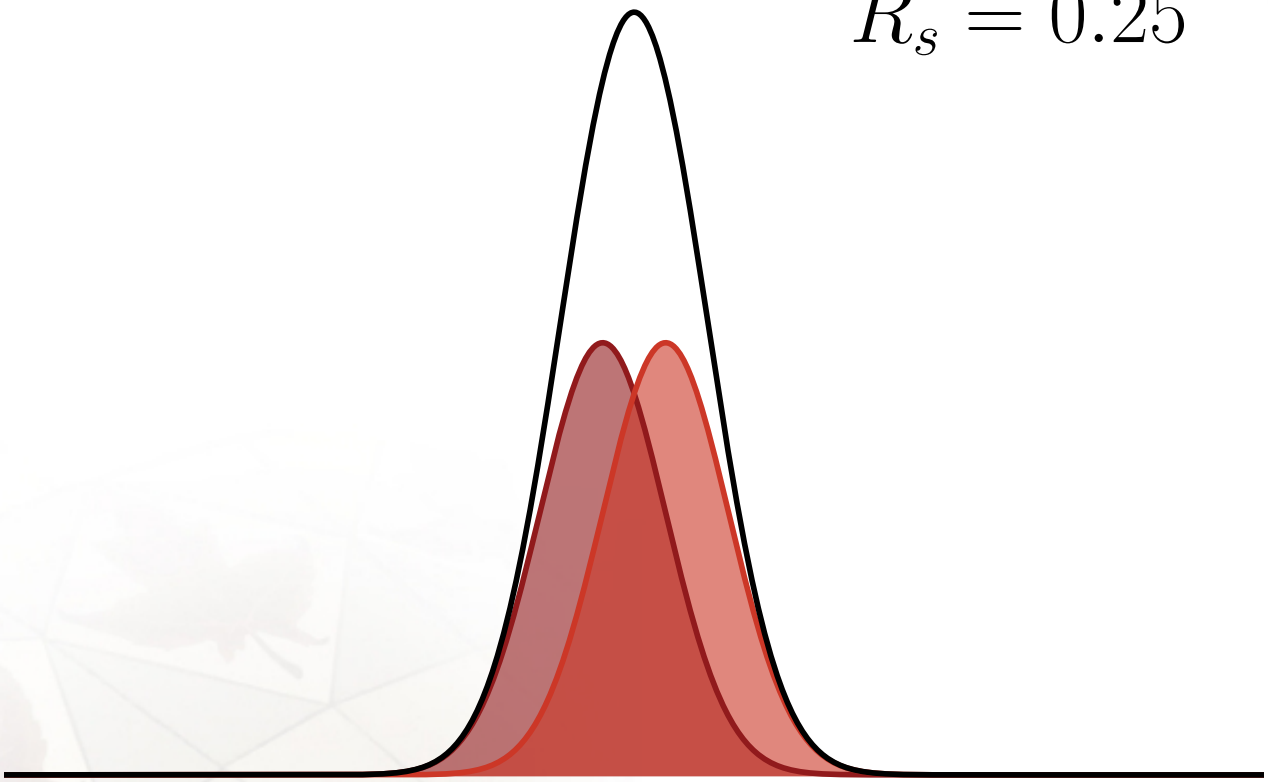

Figure : Intermediate, near-unity case

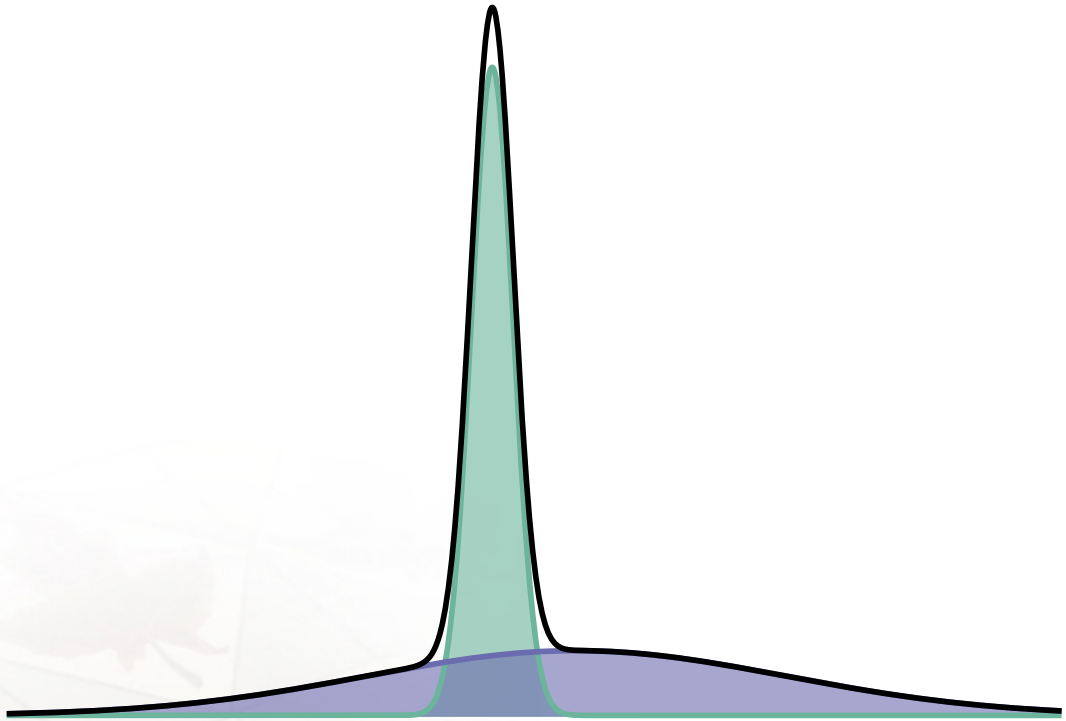

Figure : Two Gaussian peaks with very different standard deviations (2 and 20). In such cases, resolution is not an adequate metric of the ability to discern between peaks.

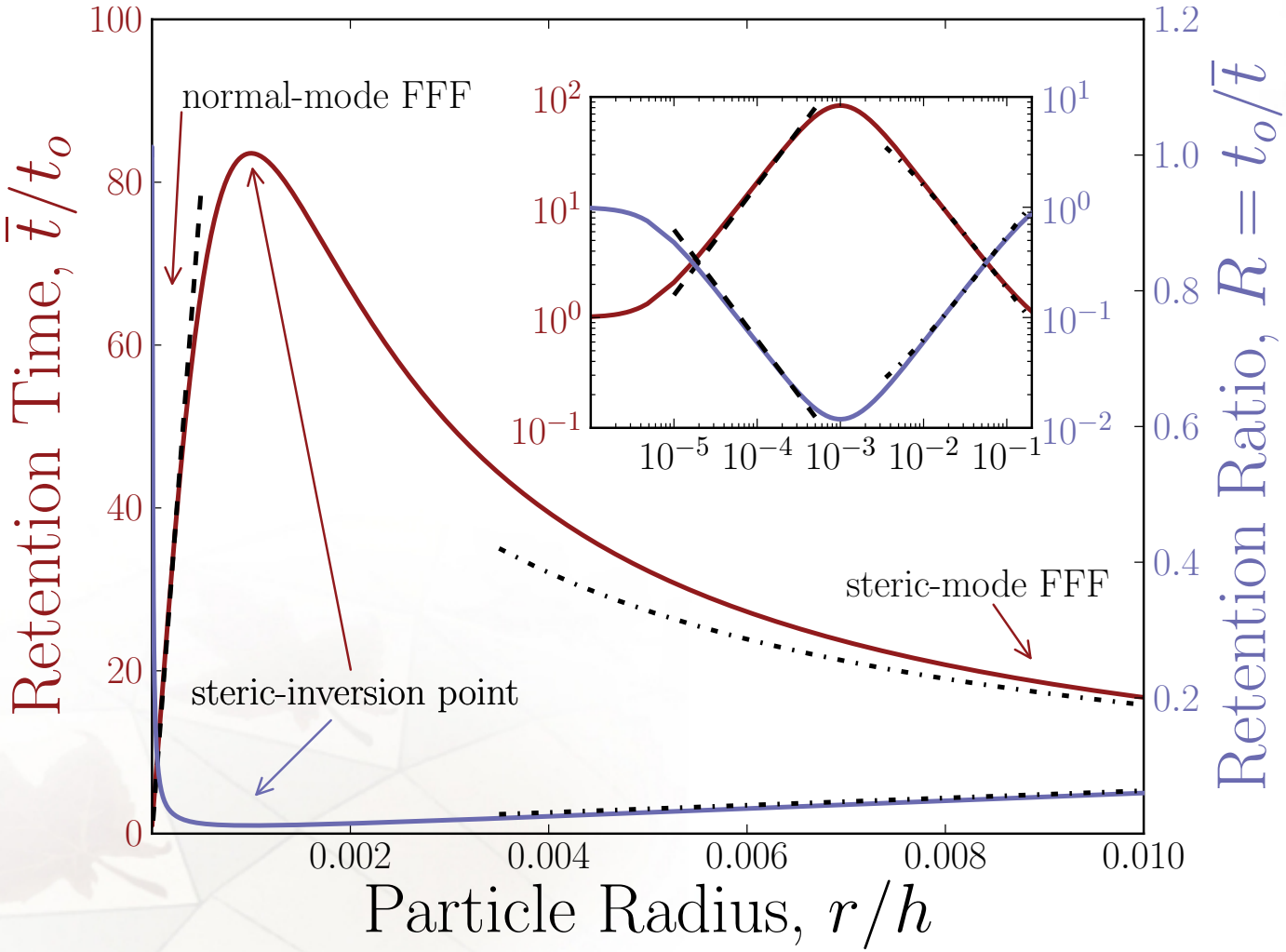

Figure : An example of a retention time (normalized by void time, t_o) and retention ratio as a function of scaled particle size $\tilde{r}$ with $\Lambda = 10^{-6}$. The inset shows the same ideal retention curve on a log-log scale.

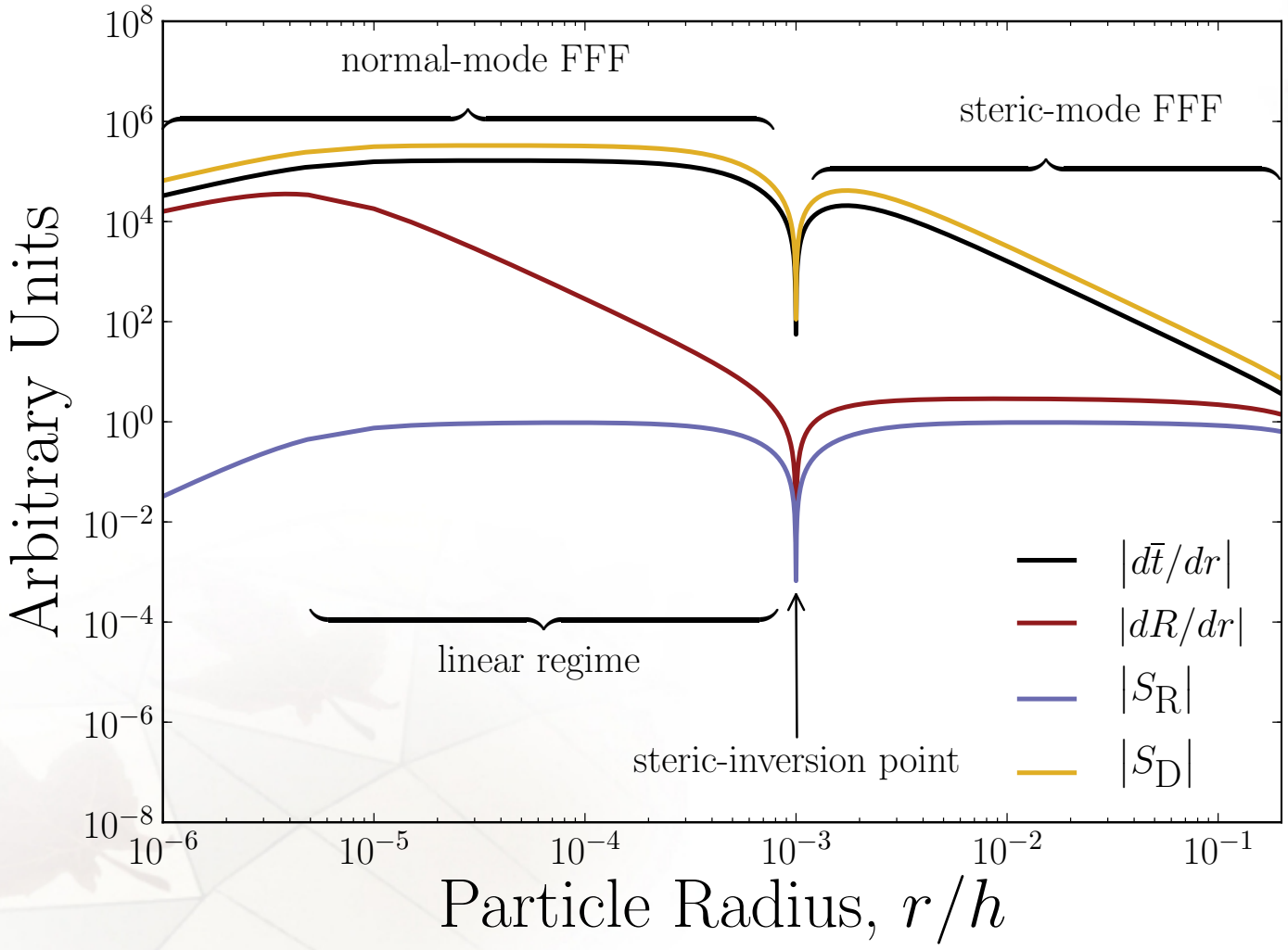

Figure : Rate of change of the retention time ($d\bar{t}/dr$), rate of change of the retention ratio (dR/dr), relative selectivity (S_R) and device selectivity (S_D) as a function of scaled particle size $\tilde{r} = r/h$.

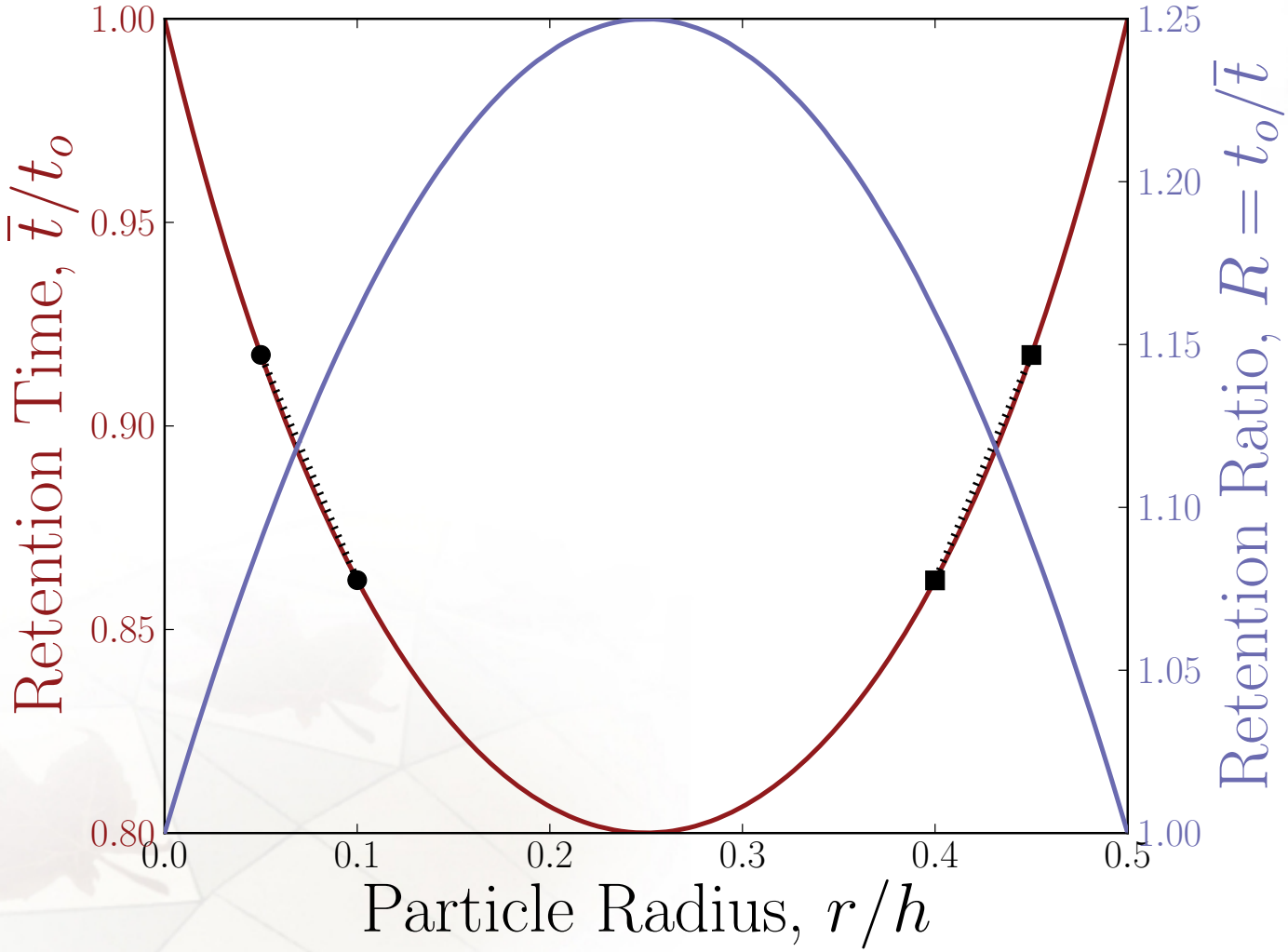

Figure : Retention time $\overline{t}$ (normalized by the void time t_o) and its inverse (the retention ratio R) as a function of scaled particle size $\tilde{r}$ in the hydrodynamic chromatography limit.

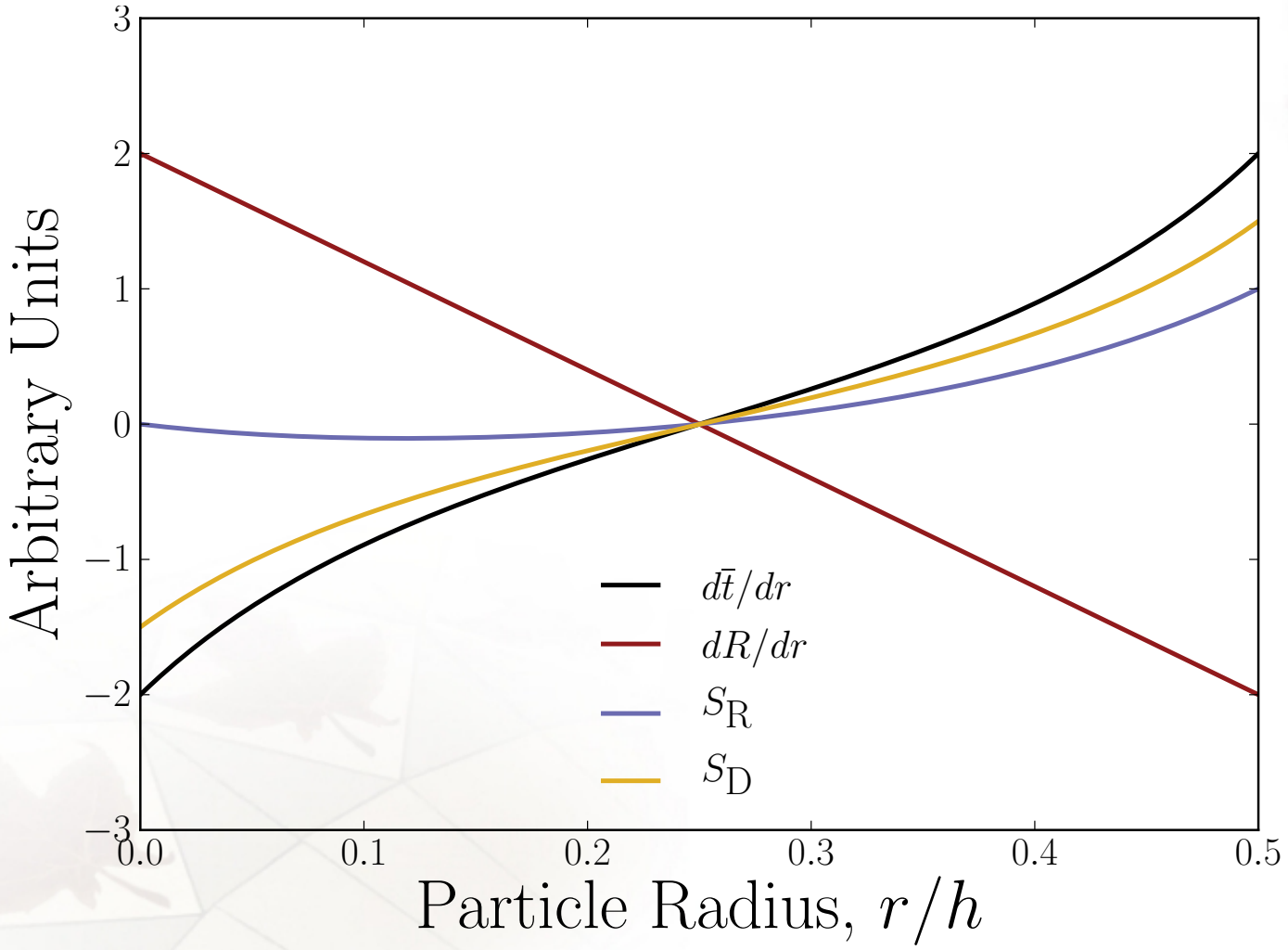

Figure : Rate of change of the retention time ($d\bar{t}/dr$), rate of change of the retention ratio (dR/dr), relative selectivity (S_R) and device selectivity (S_D) as a function of scaled particle size r/h for hydrodynamic chromatography. The traditionally defined relative selectivity S_R is highly non-symmetric.

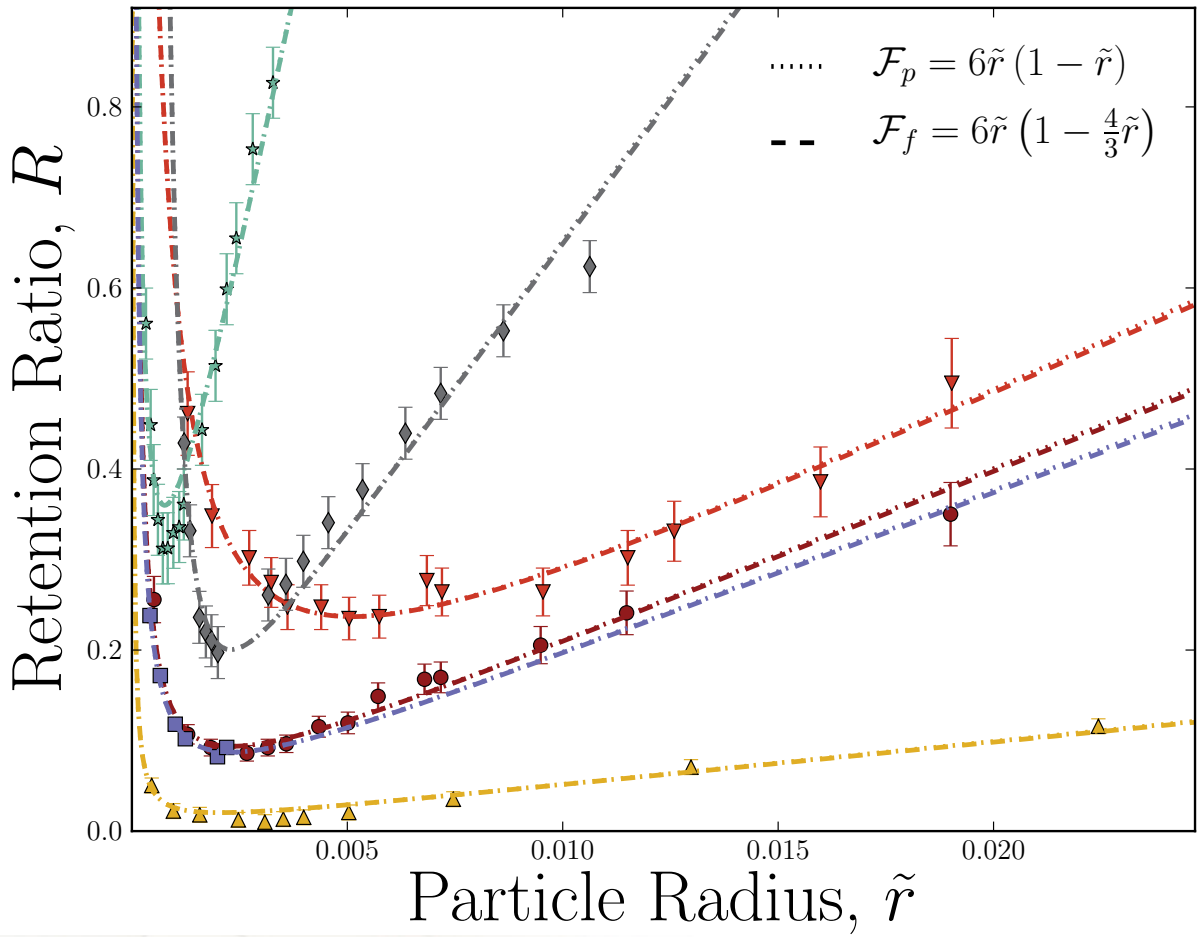

Figure : Fit to a variety of FFF systems. Dotted lines ignore Faxén's law, while dashed lines account for it. In this range, the dotted and dashed lines overlap perfectly. Thermal FFF utilizes a temperature gradient and $\alpha = 1$. The data are for $\Delta T = 40$ K and $\Delta T = 5$ K. Symmetric, asymmetric, and hollow-fiber FFF use a cross flow and have $\alpha = 1$. For GrFFF, $\alpha = 3$.

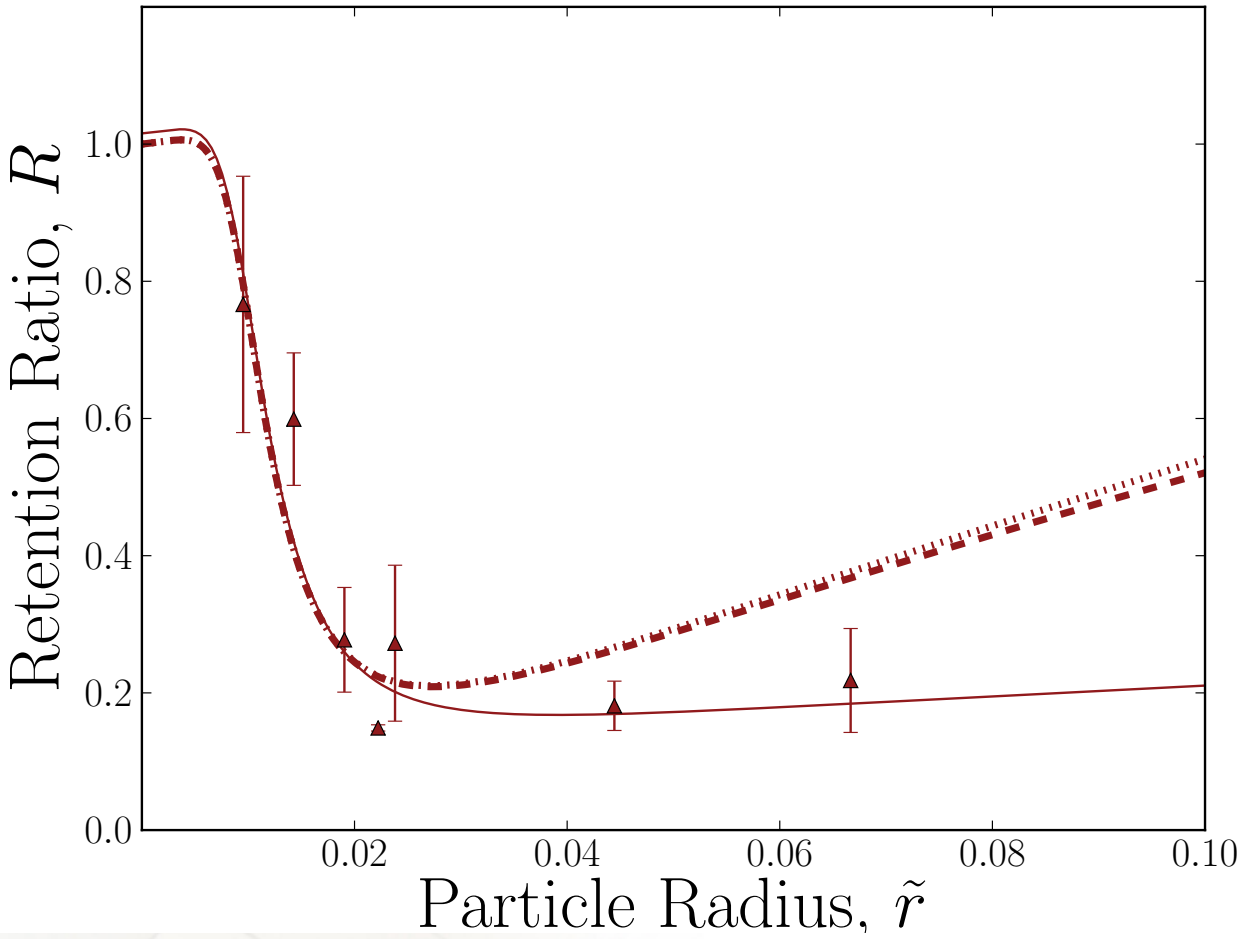

Figure : MPCD simulation results for $\alpha = 3$ and $\Lambda = 1.87 \times 10^{-7}$. This is a relatively strong external field. The dotted lines show the retention curve that neglects Faxén's law, while the dashed line shows the unified ideal retention theory that accounts for Faxén's law. Solid lines show the theory that accounts for increased drag.

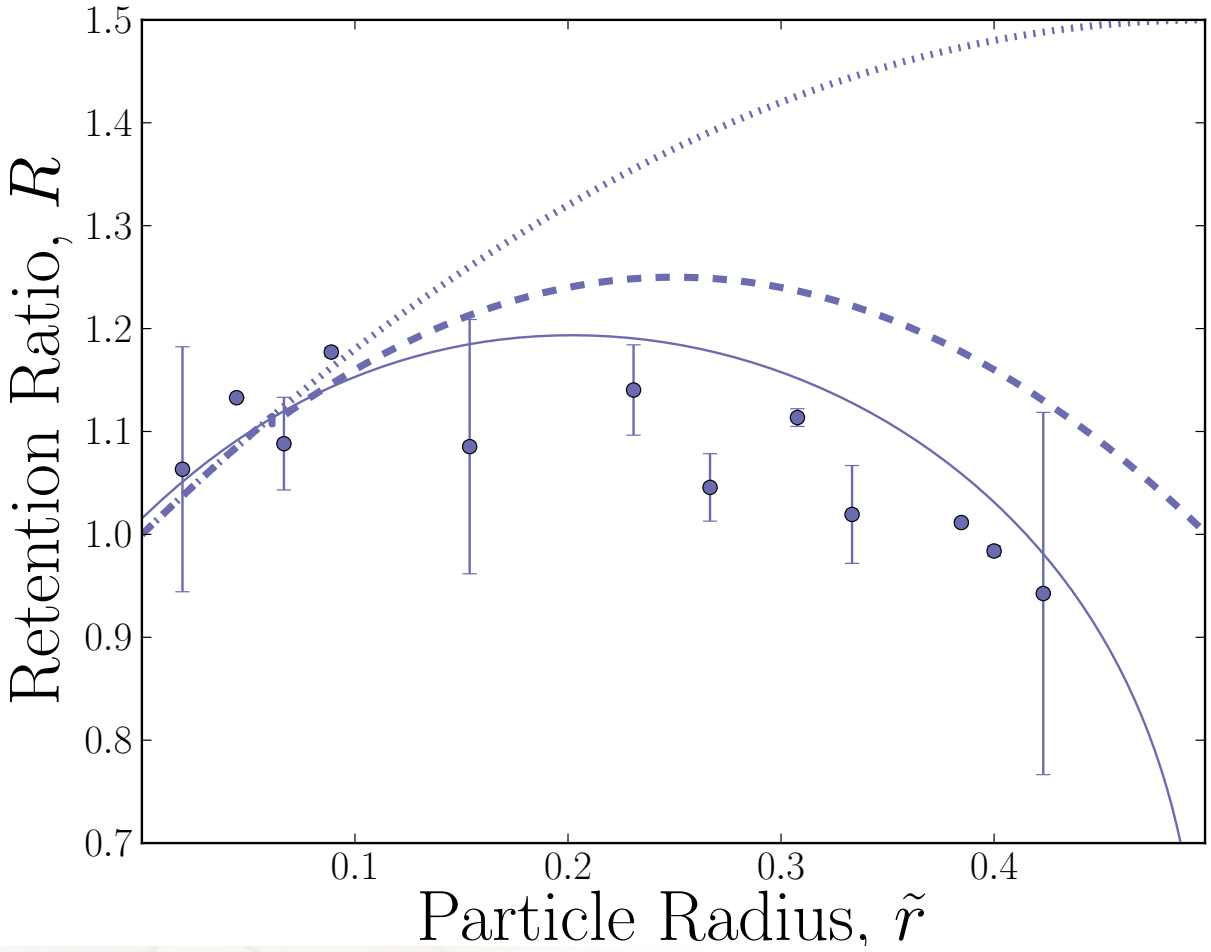

Figure : MPCD simulation results for $\alpha = 3$ and $\Lambda = 0$. This is the HC limit with no external field. The dotted lines show the retention curve that neglects Faxén's law, while the dashed line shows the unified ideal retention theory that accounts for Faxén's law. Solid lines show the theory that accounts for increased drag.

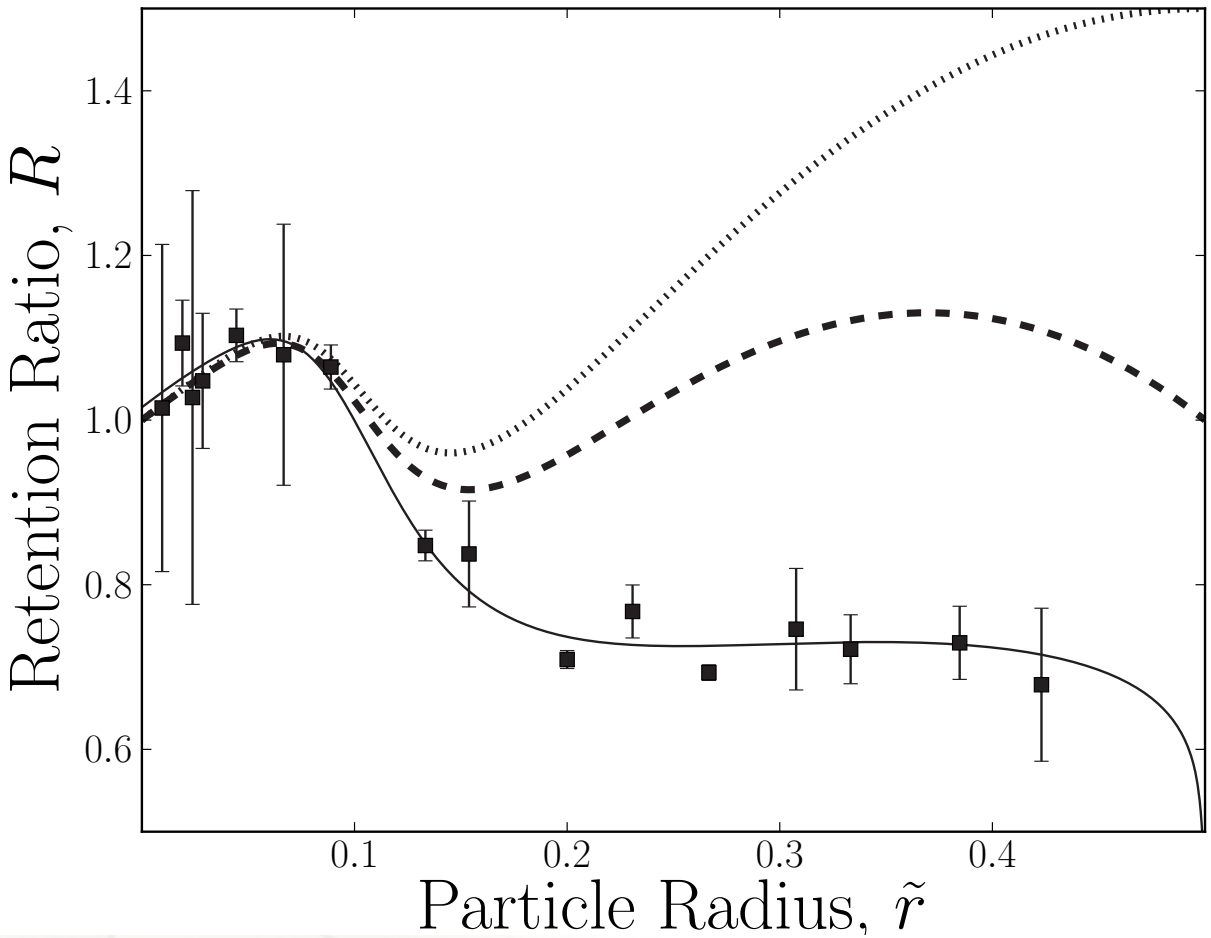

Figure : MPCD simulation results for $\alpha = 3$ and a weak external field ($\Lambda = 1.87 \times 10^{-4}$).

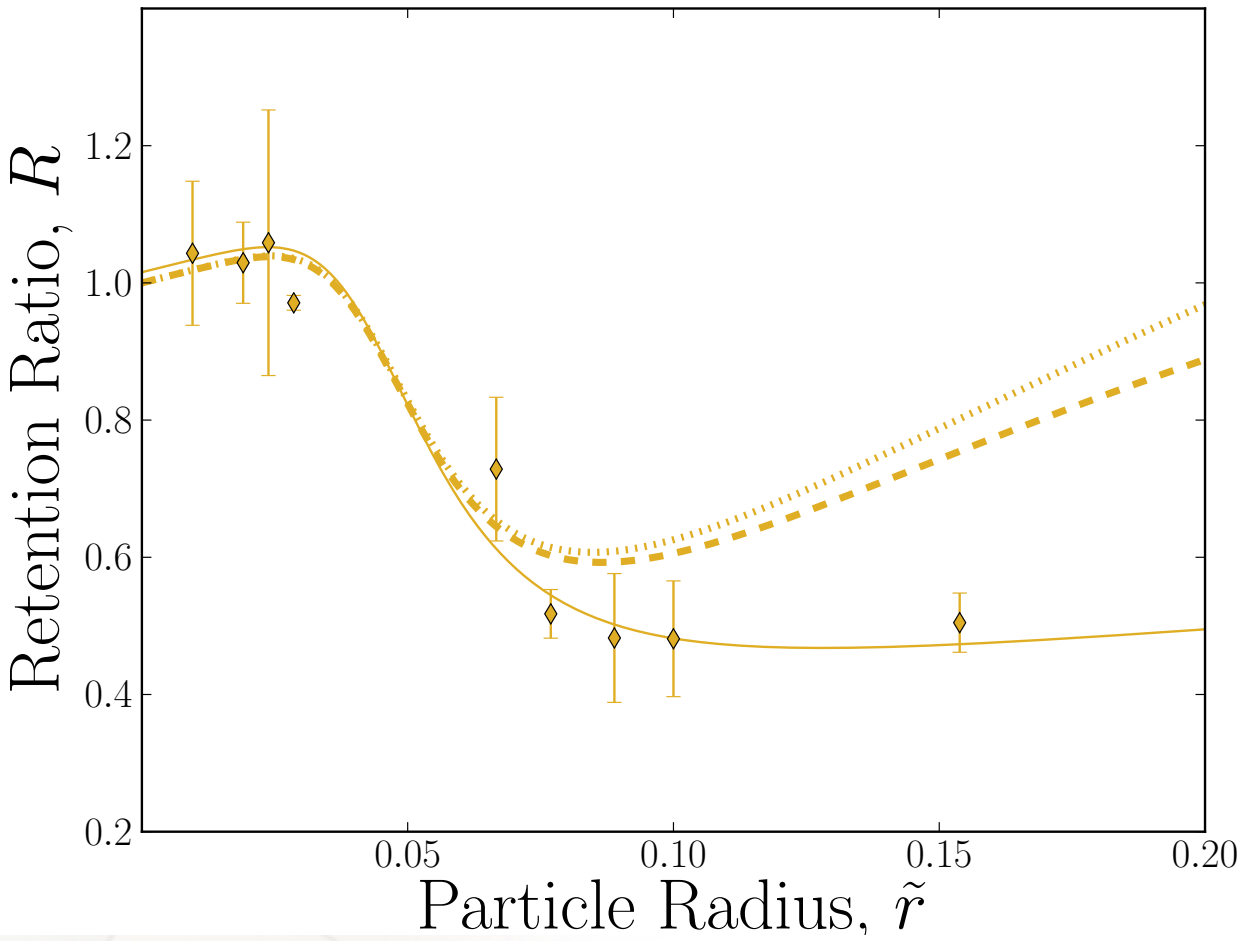

Figure : MPCD simulation results for $\alpha = 3$ and an intermediate external field ($\Lambda = 1.87 \times 10^{-5}$).

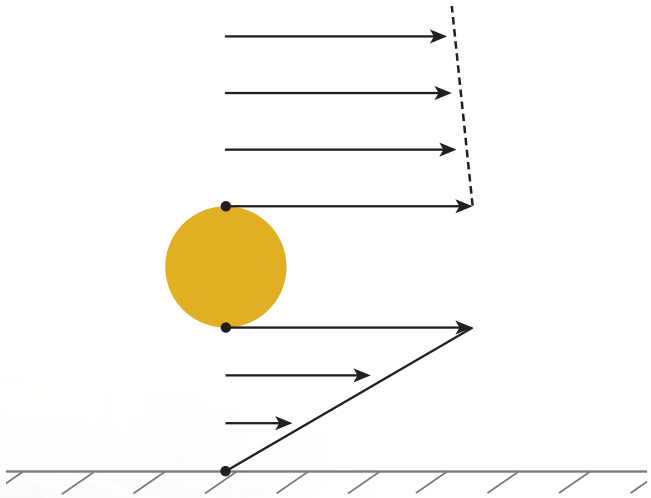

Figure : Schematic illustrating that no-slip boundary conditions at the solute surface and the channel walls demands higher shears than in free-solution. This leads to larger drag forces and so a larger effective drag coefficient.

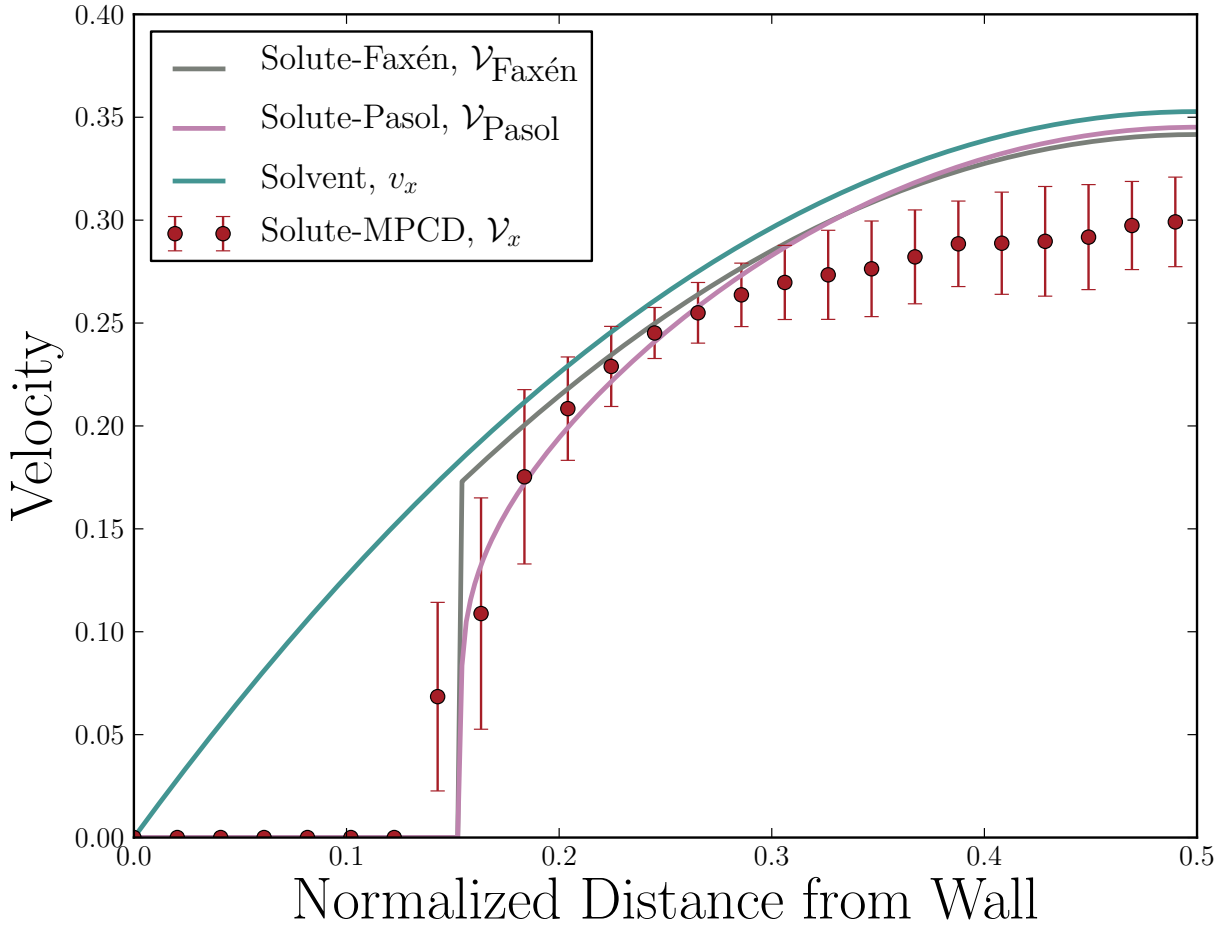

Figure : Particle $r = 4a$ in channel $h = 26a$.

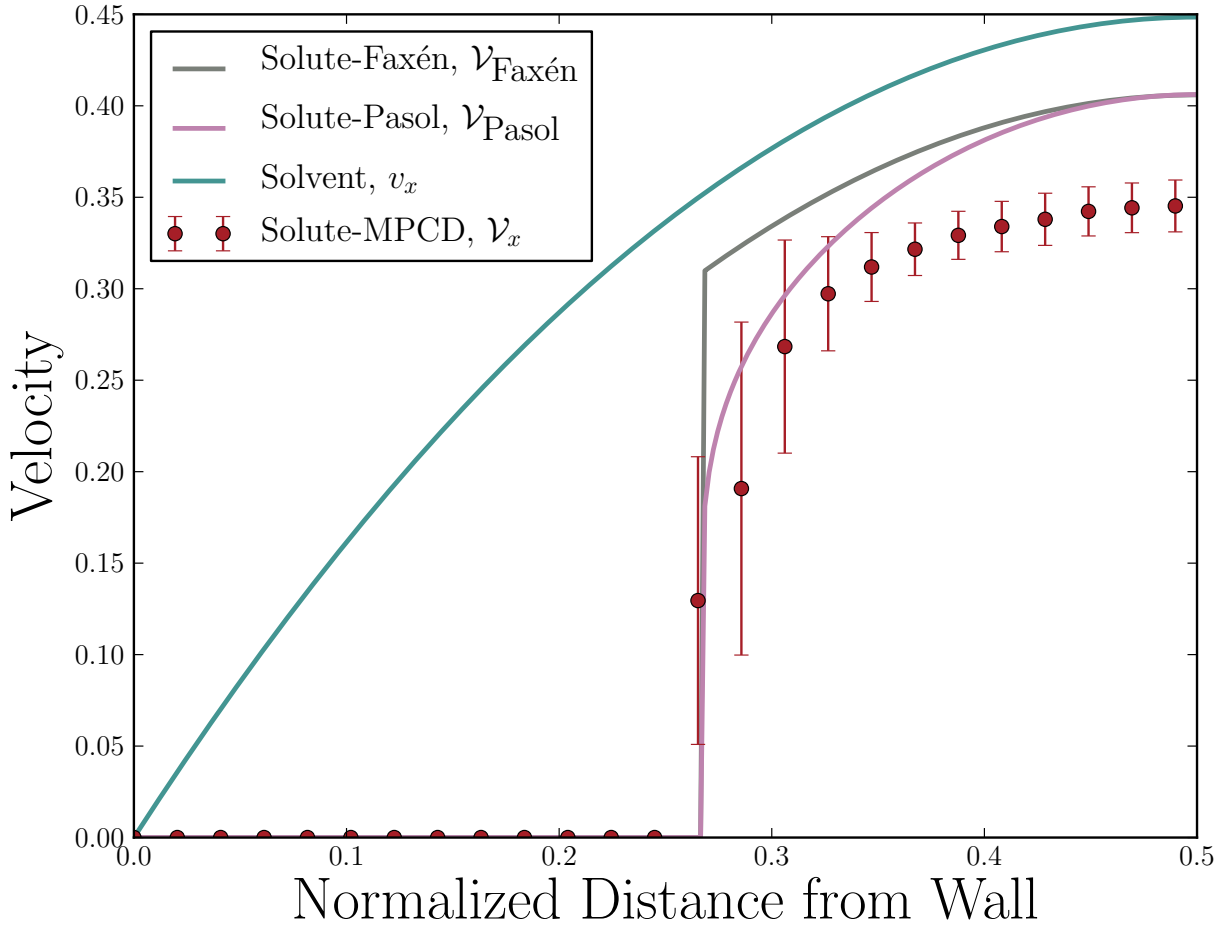

Figure : Particle $r = 4a$ in channel $h = 15a$.

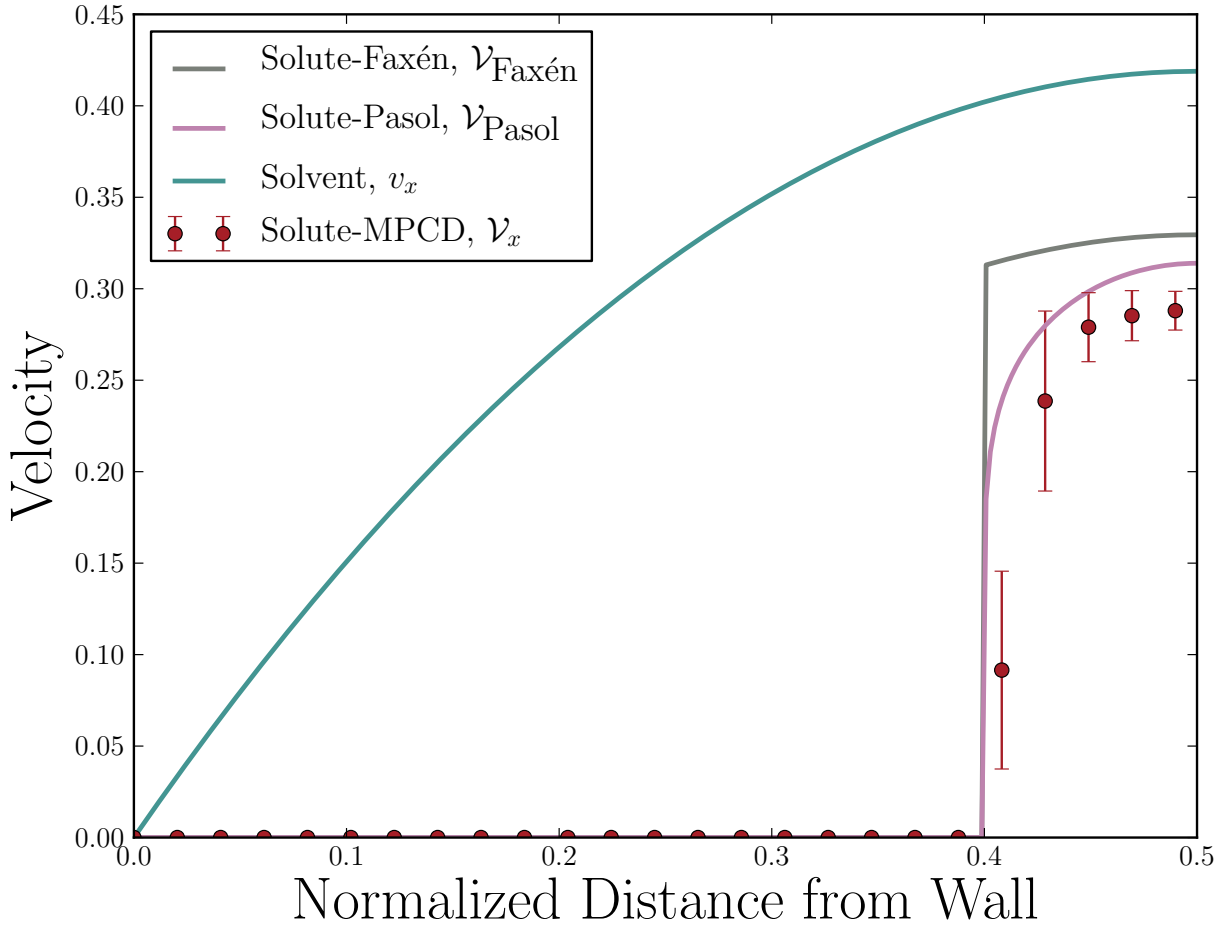

Figure : Particle $r = 6a$ in channel $h = 15a$.

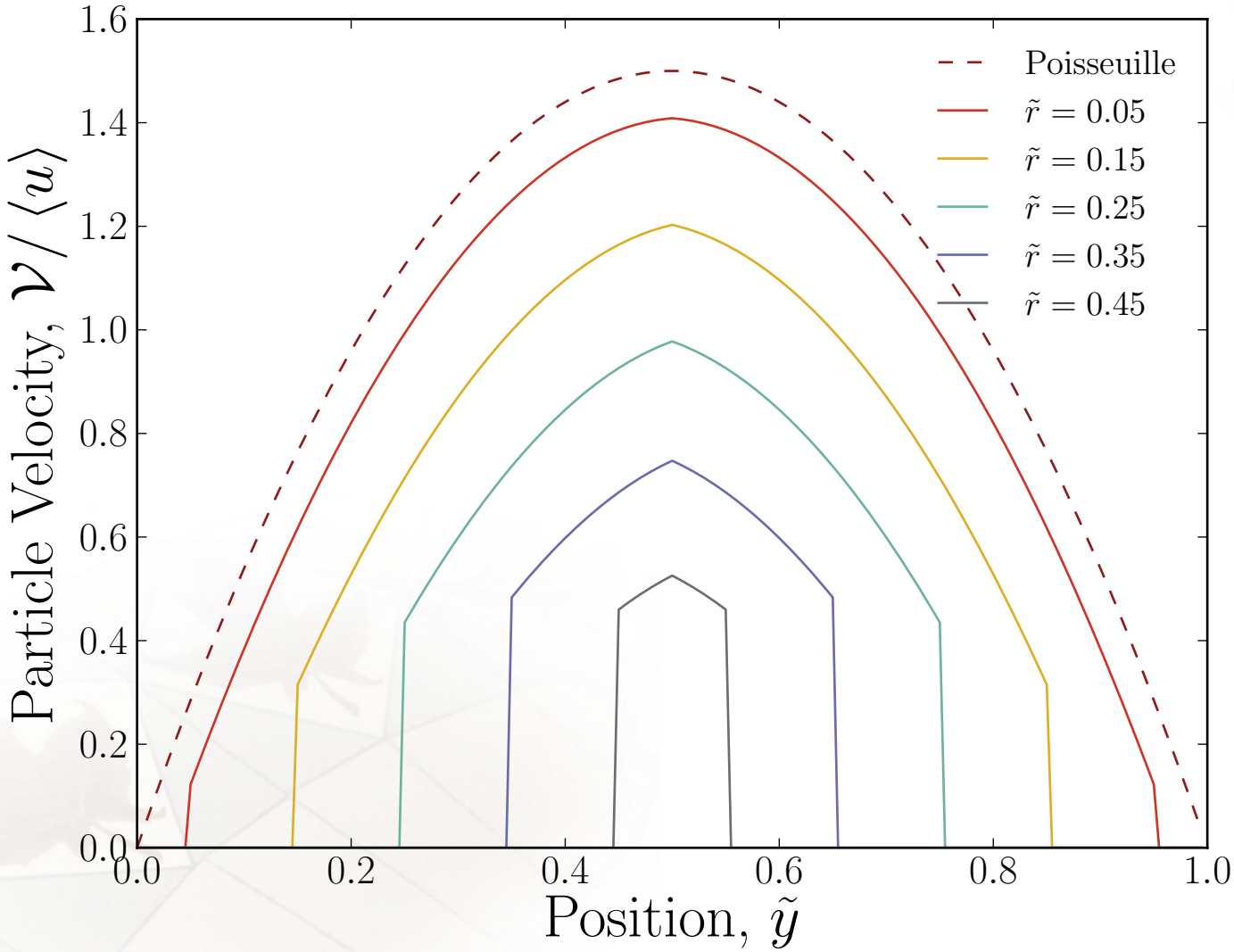

Figure : Faxén expansion.

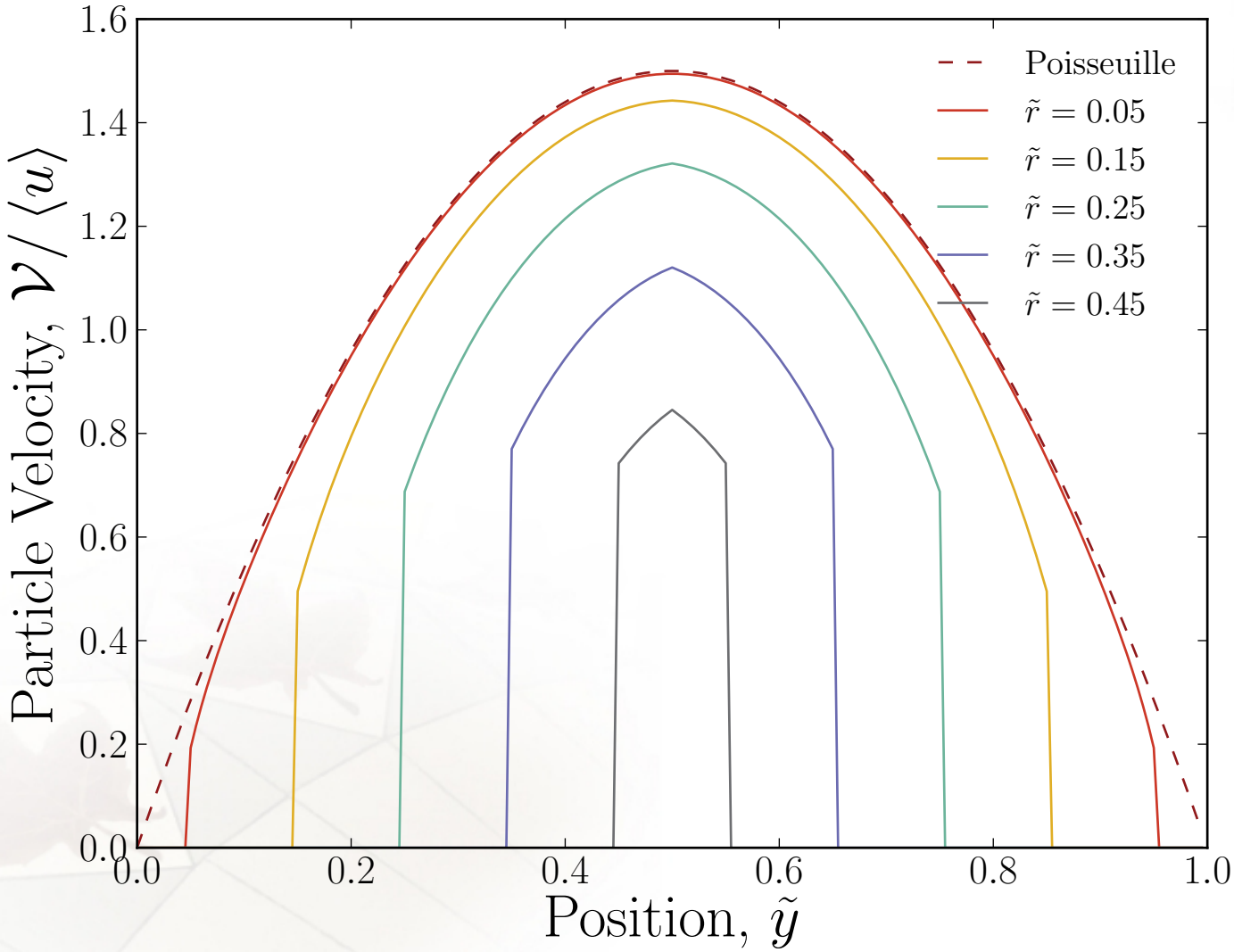

Figure : Far-wall approximation.

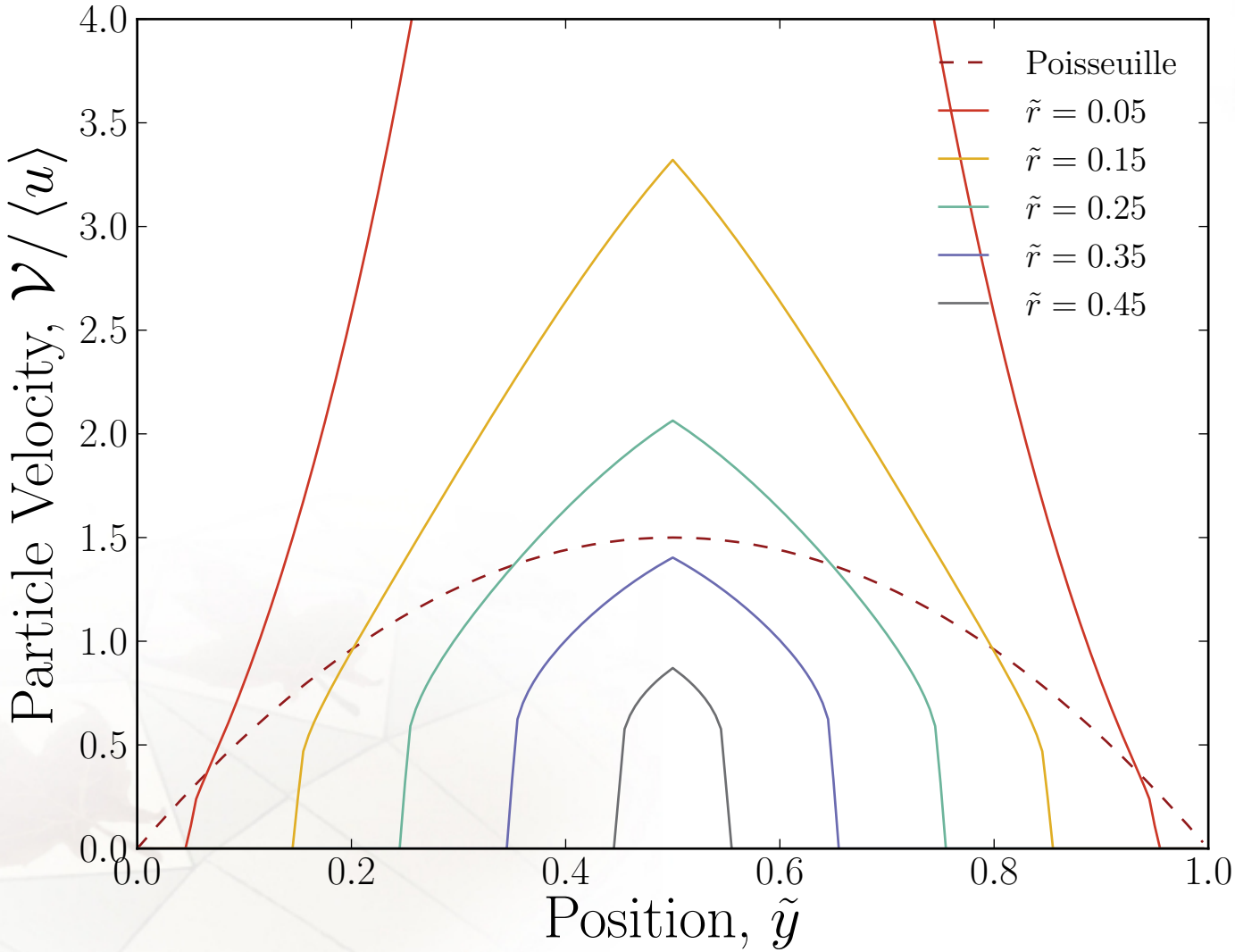

Figure : Near-wall approximation.

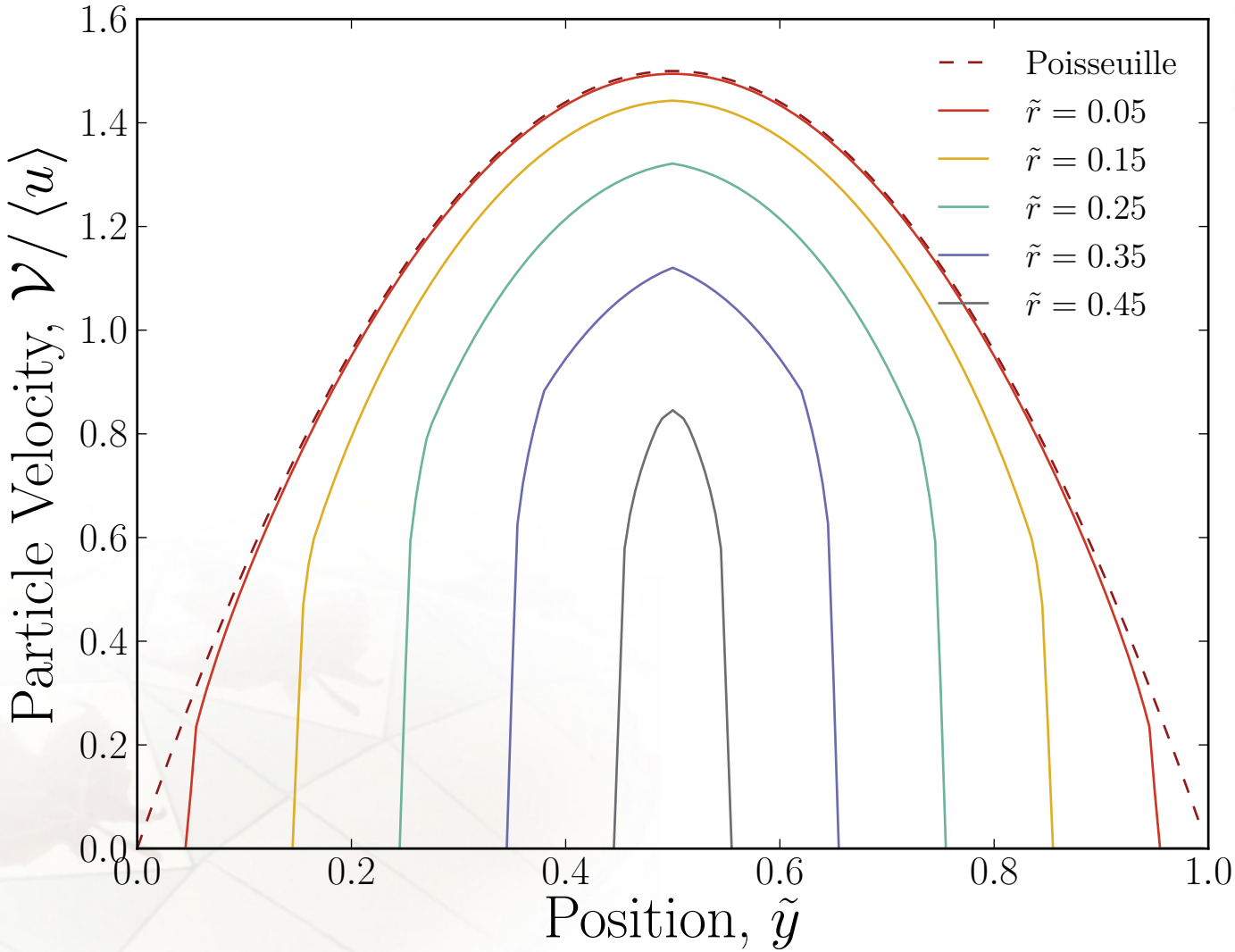

Figure : Piece-wise combination of near- and far-wall approximations.

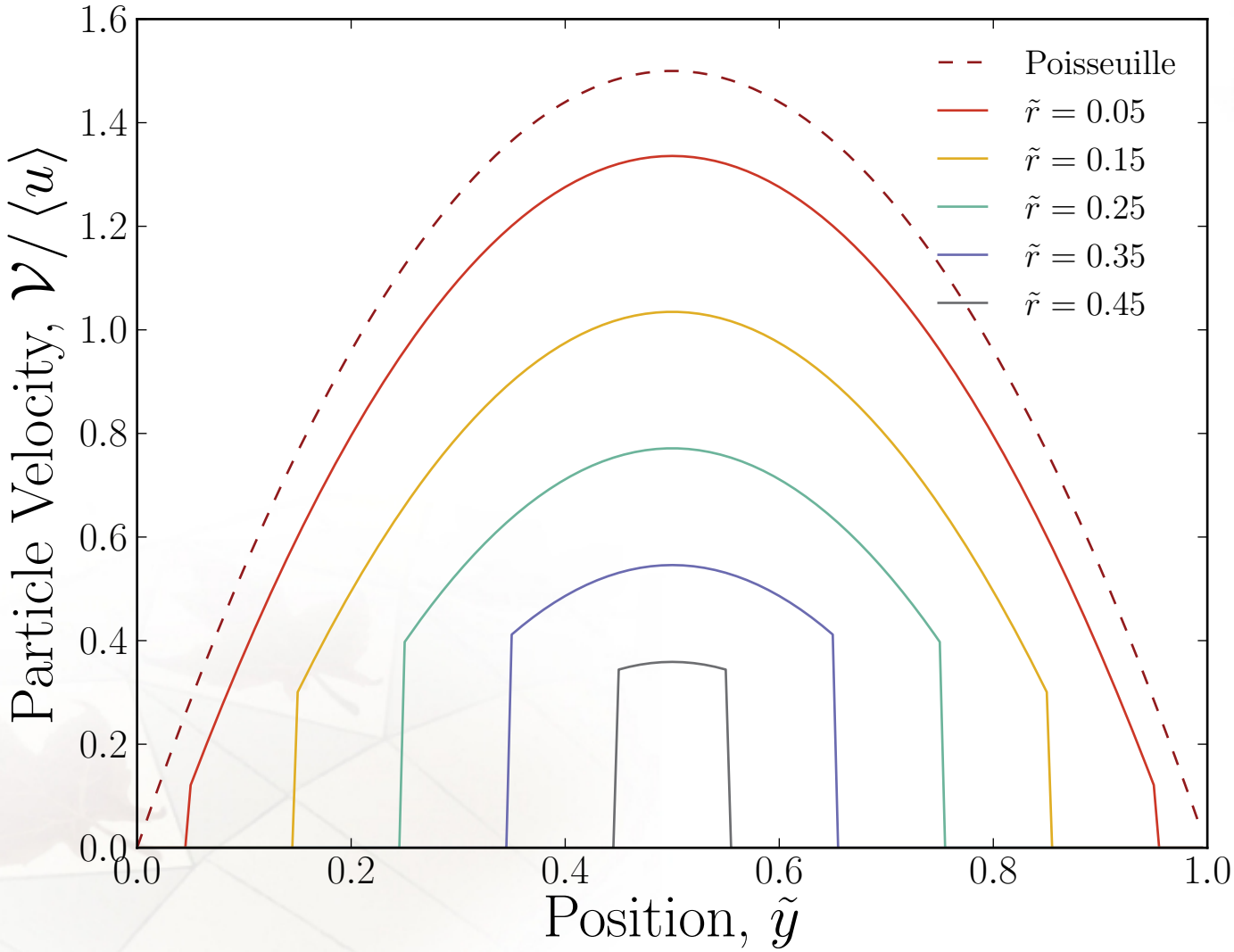

Figure : Faxén expansion.

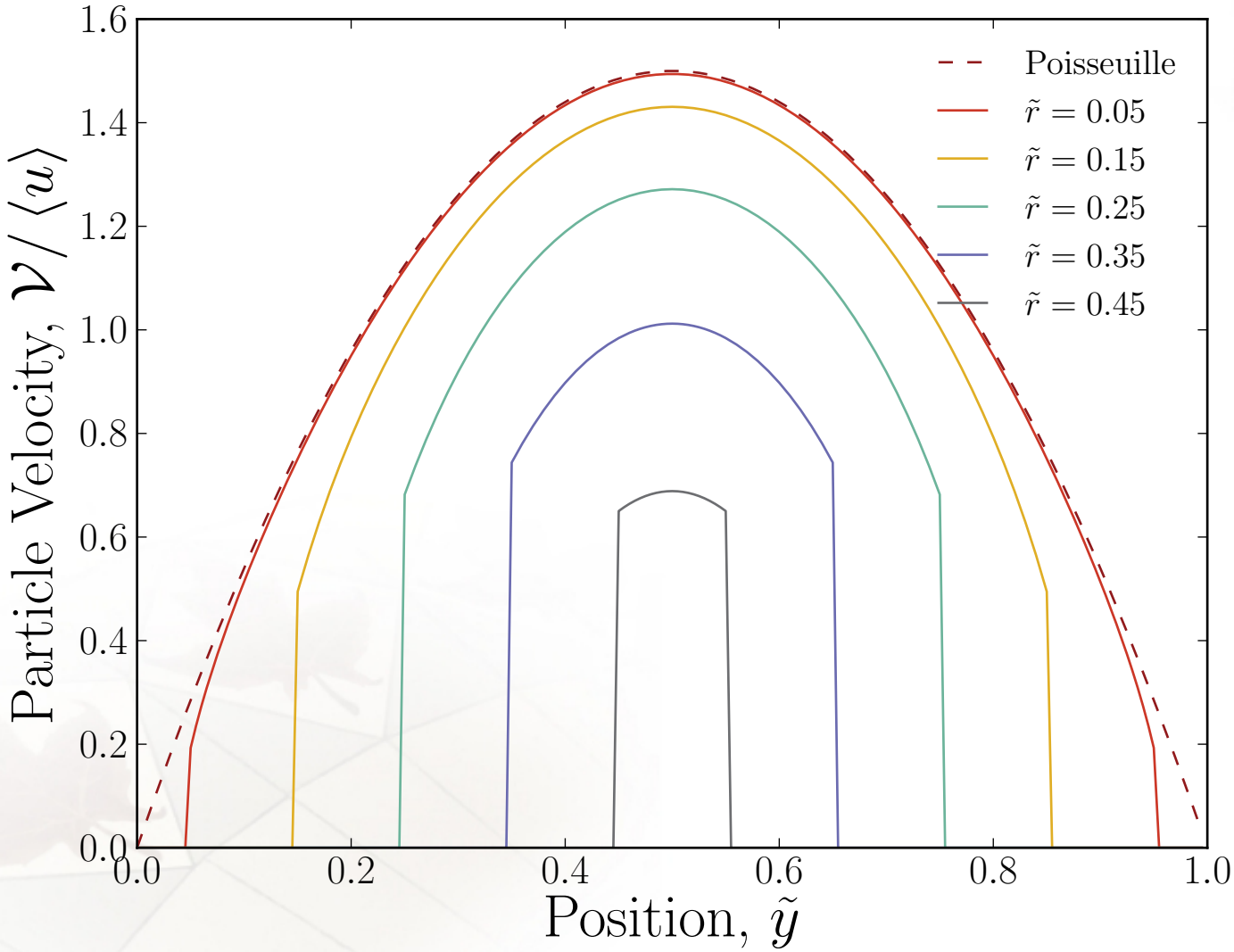

Figure : Far-wall approximation. .

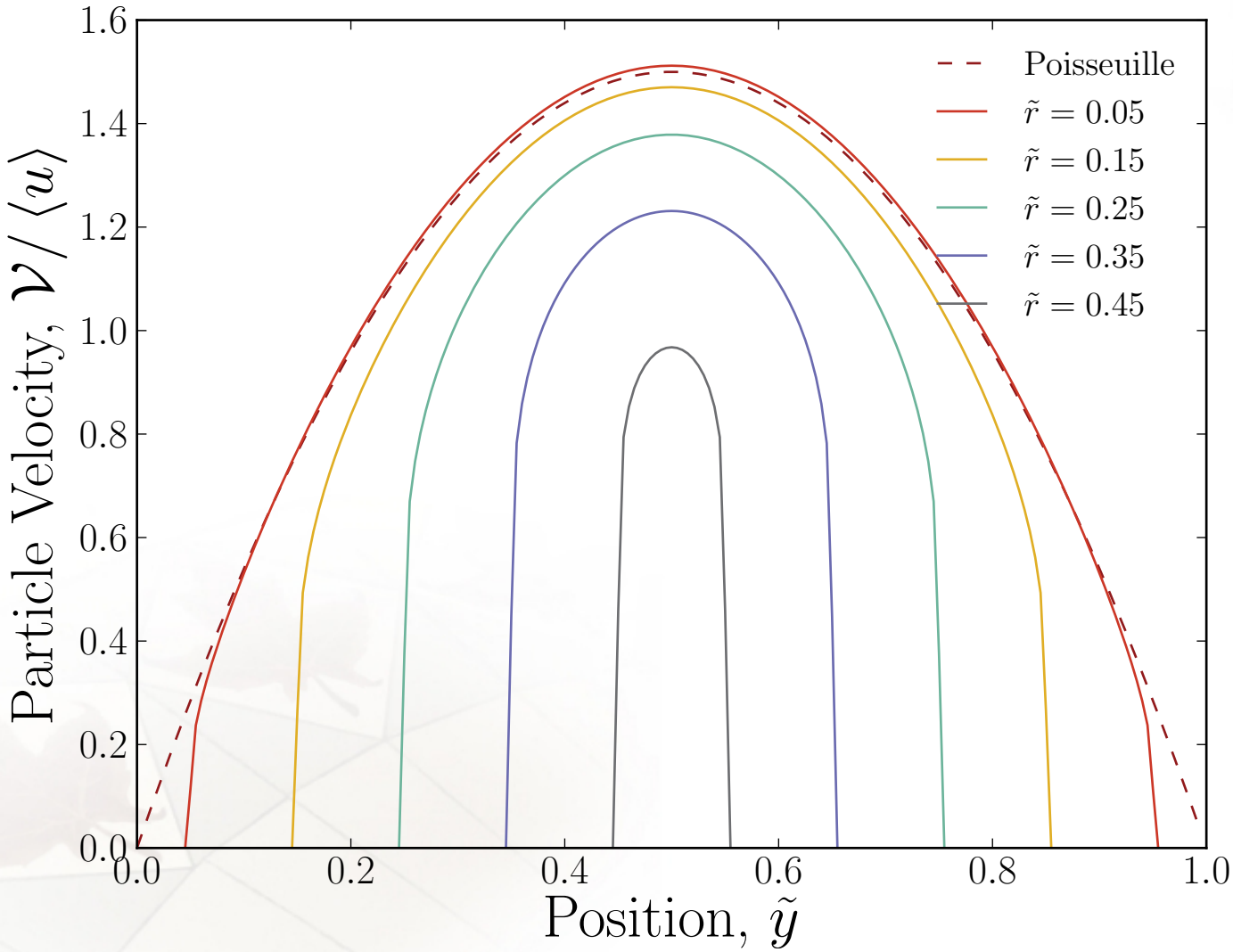

Figure : Example profiles for solutes of size $\tilde{r} = \{0.05, 0.15, 0.25, 0.35, 0.45\}$.

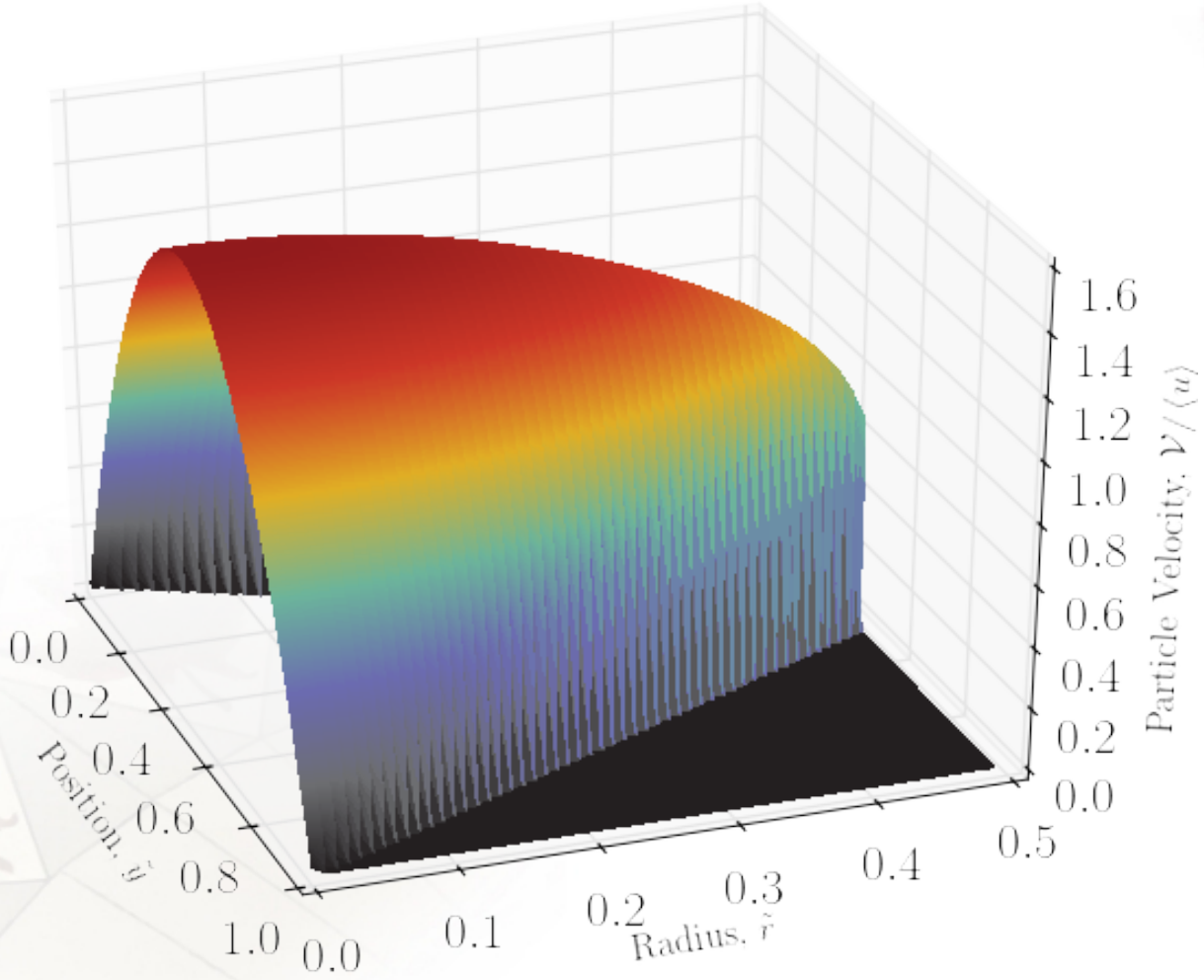

Figure : Solute velocity as a function of position and solute size.

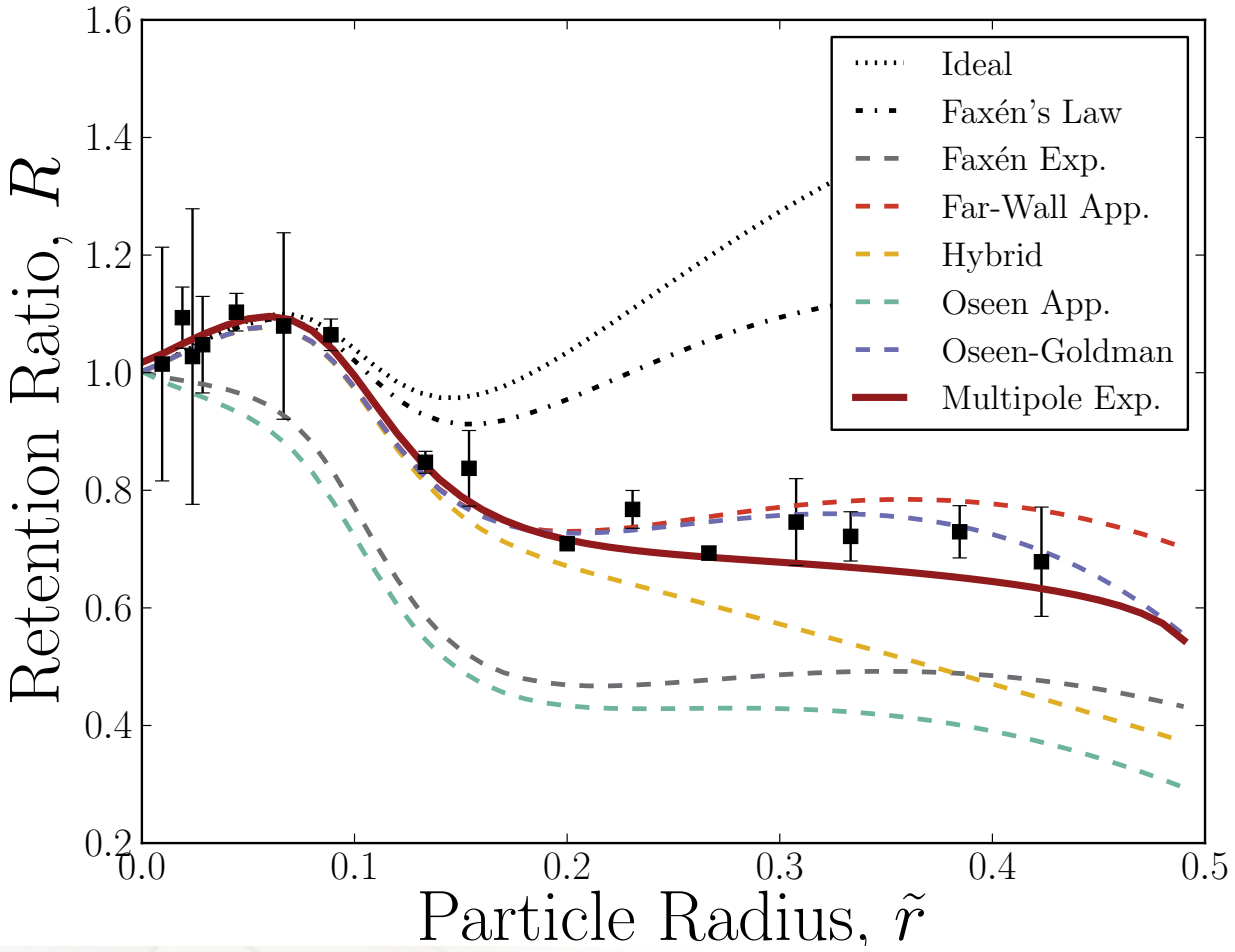

Figure : MPCD simulation results for $\alpha = 3$ and $\Lambda = 1.87 \times 10^{-4}$ (black squares) are compared to the various approximations discussed in the text. The solid red line shows the predicted retention curve that numerically takes into account Faxén's law and, more significantly, hydrodynamic interactions with both channel walls via the form given by the multipole expansion method.

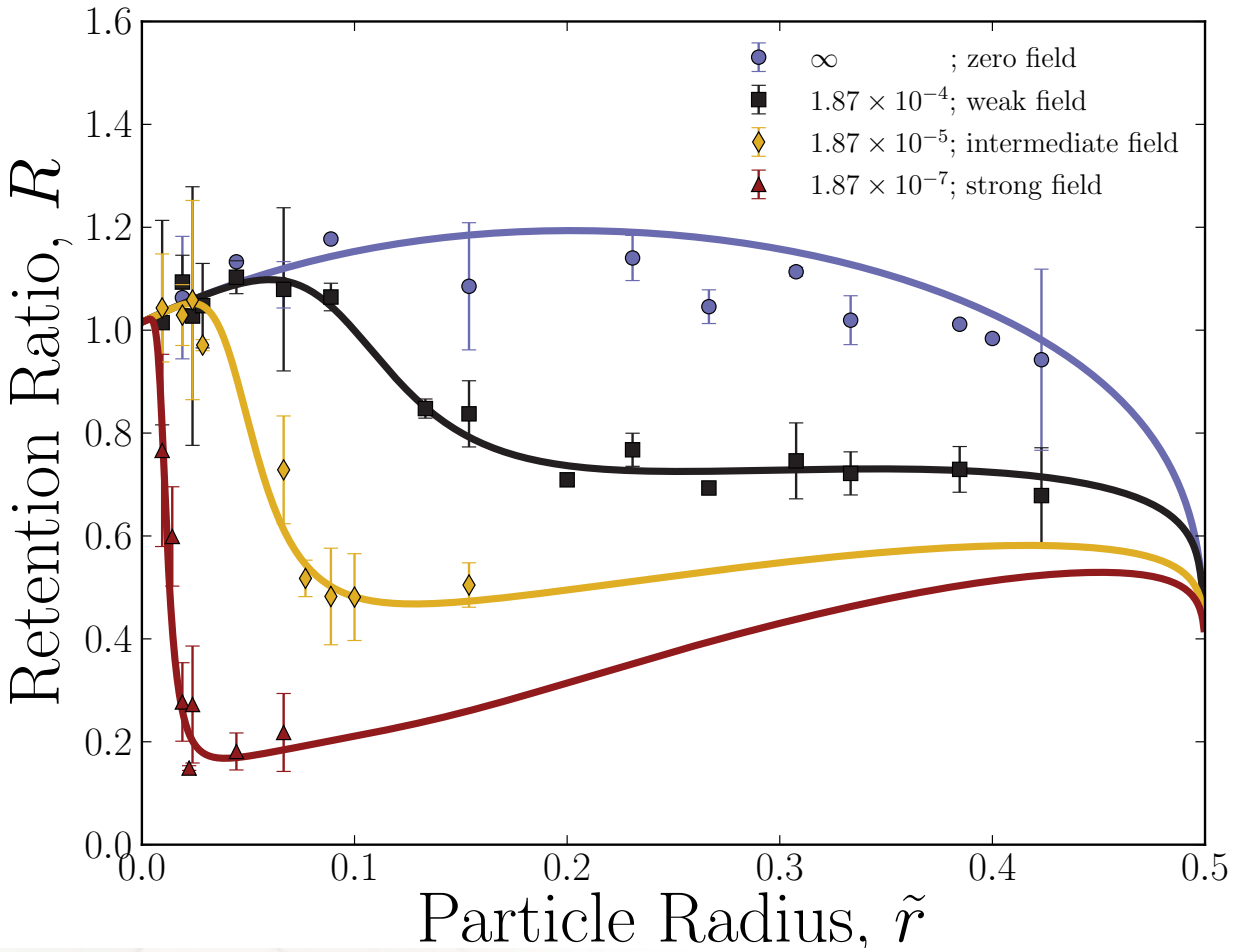

Figure : MPCD simulation results for $\alpha = 3$ are shown as blue circles, black squares, yellow diamonds and red triangles, respectively. The solid lines show the predicted retention curve for each Λ, numerically taking into account Faxén's law and more significantly hydrodynamic interactions with both channel walls.

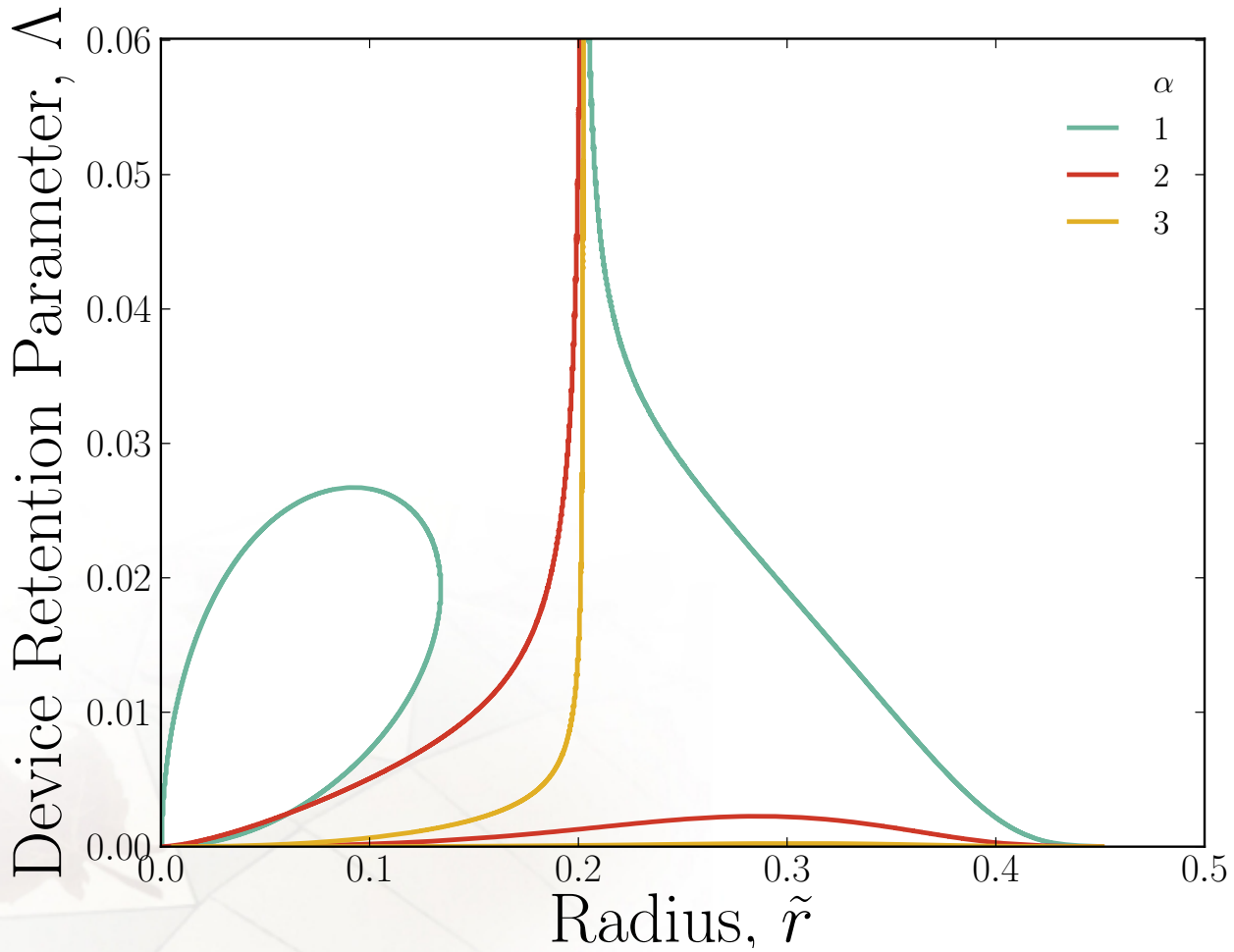

Figure : FFF-modes map. The roots of the retention ratio that numerically accounts for increased drag coefficients through the multipole expansion method results are shown. The roots represent the transitions between the four different modes of operation $\tilde{r}_{\mathrm{HN}}$, $\tilde{r}_{\mathrm{NS}}$ and $\tilde{r}_{\mathrm{SF}}$.

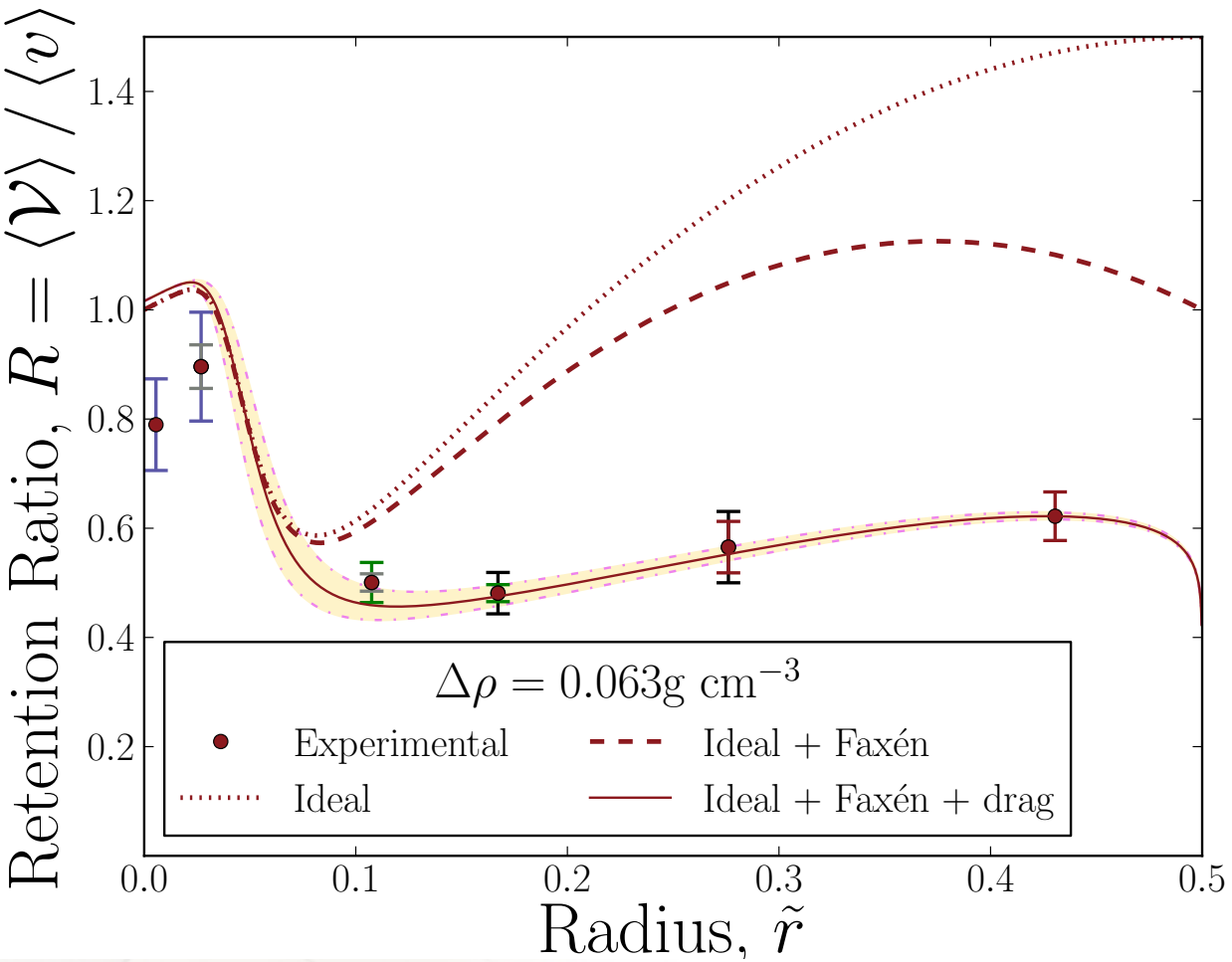

Figure : The density difference between colloids and the carrier fluid is $\Delta\varrho 0.063$ g cm^{-3}, which is equivalent to a device retention parameter of $\Lambda = 1.6 \times 10^{-5}$.

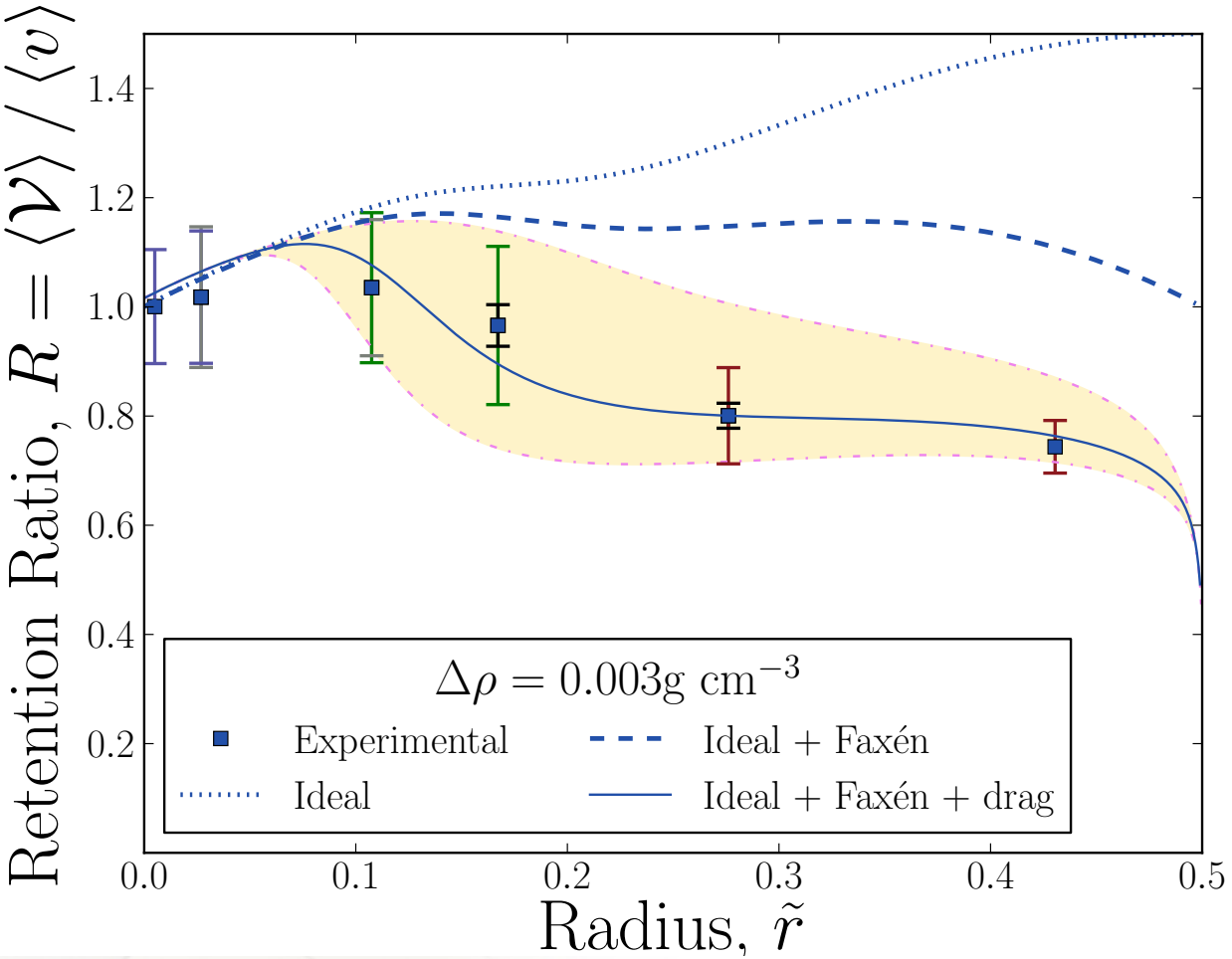

Figure : The density difference between colloids and the carrier fluid is $\Delta\varrho 0.003$ g cm^{-3}, which is equivalent to a device retention parameter of $\Lambda = 10^{-3}$.

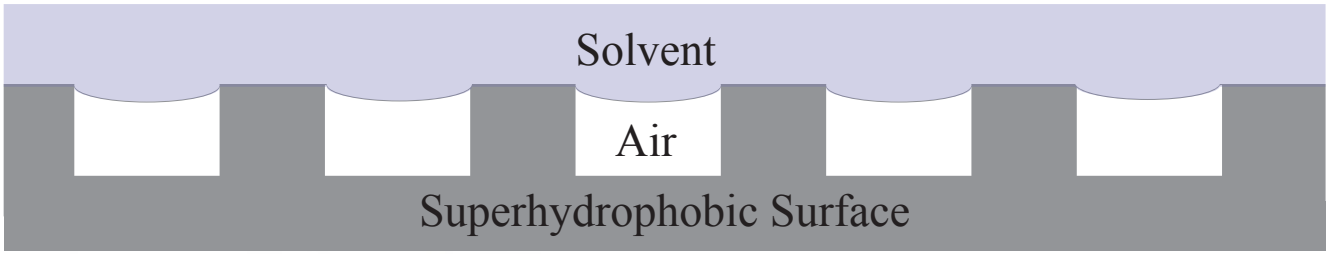

Figure : Schematic of a nano-structured, superhydrophobic surface at which a large slip length could be found.

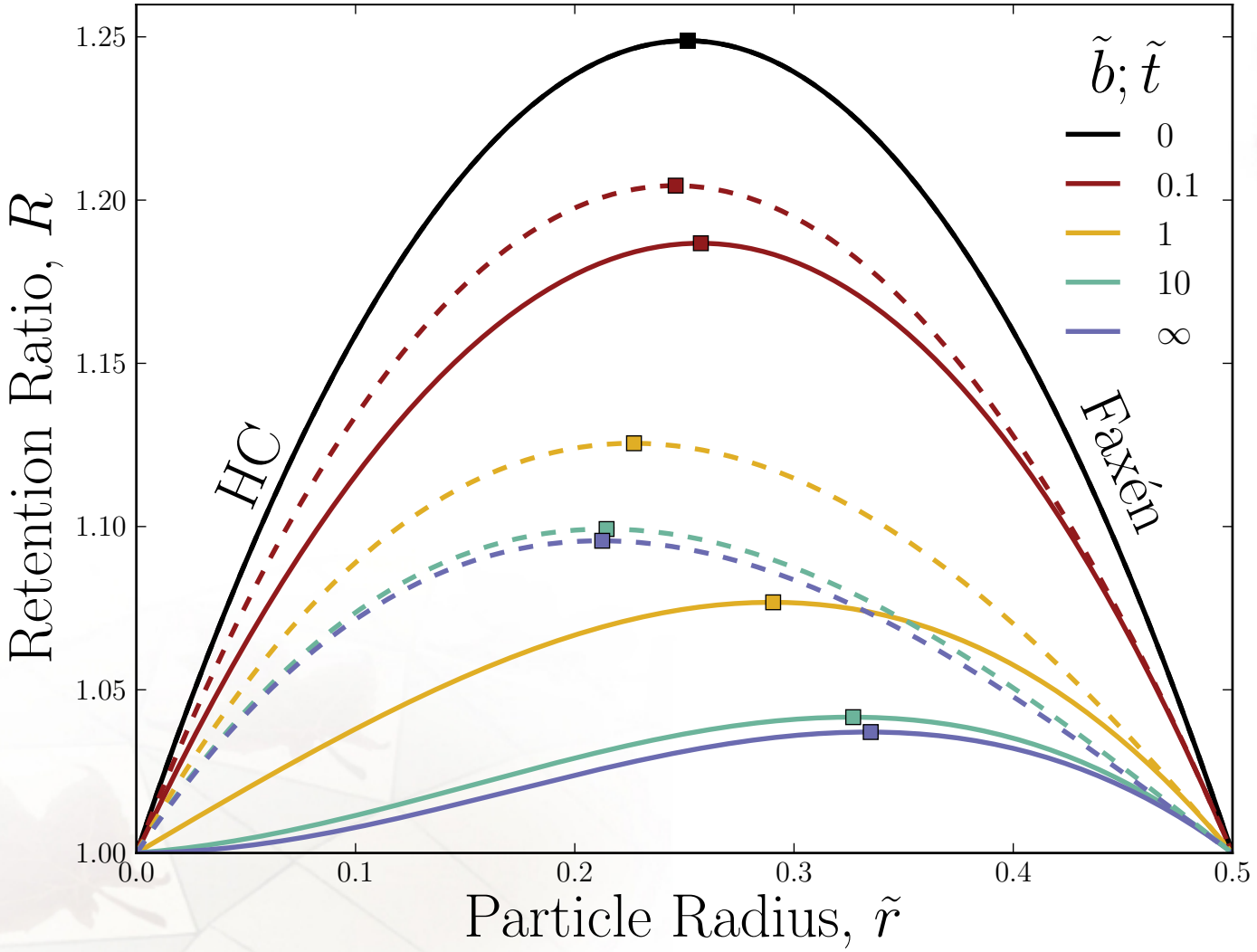

Figure : The retention ratio of FFF with a large but finite device retention parameter $\Lambda = 0.25$. Only hydrodynamic chromatography (HC) and Faxén-mode FFF exist. The transition between the two is marked. No-slip FFF is a black (top curve) solid line. The other solid lines show slip at the depletion wall while the dashed lines show slip at the accumulation wall; the colour code for the various slip lengths $\tilde{t}$ and $\tilde{b}$ is given in the legend.

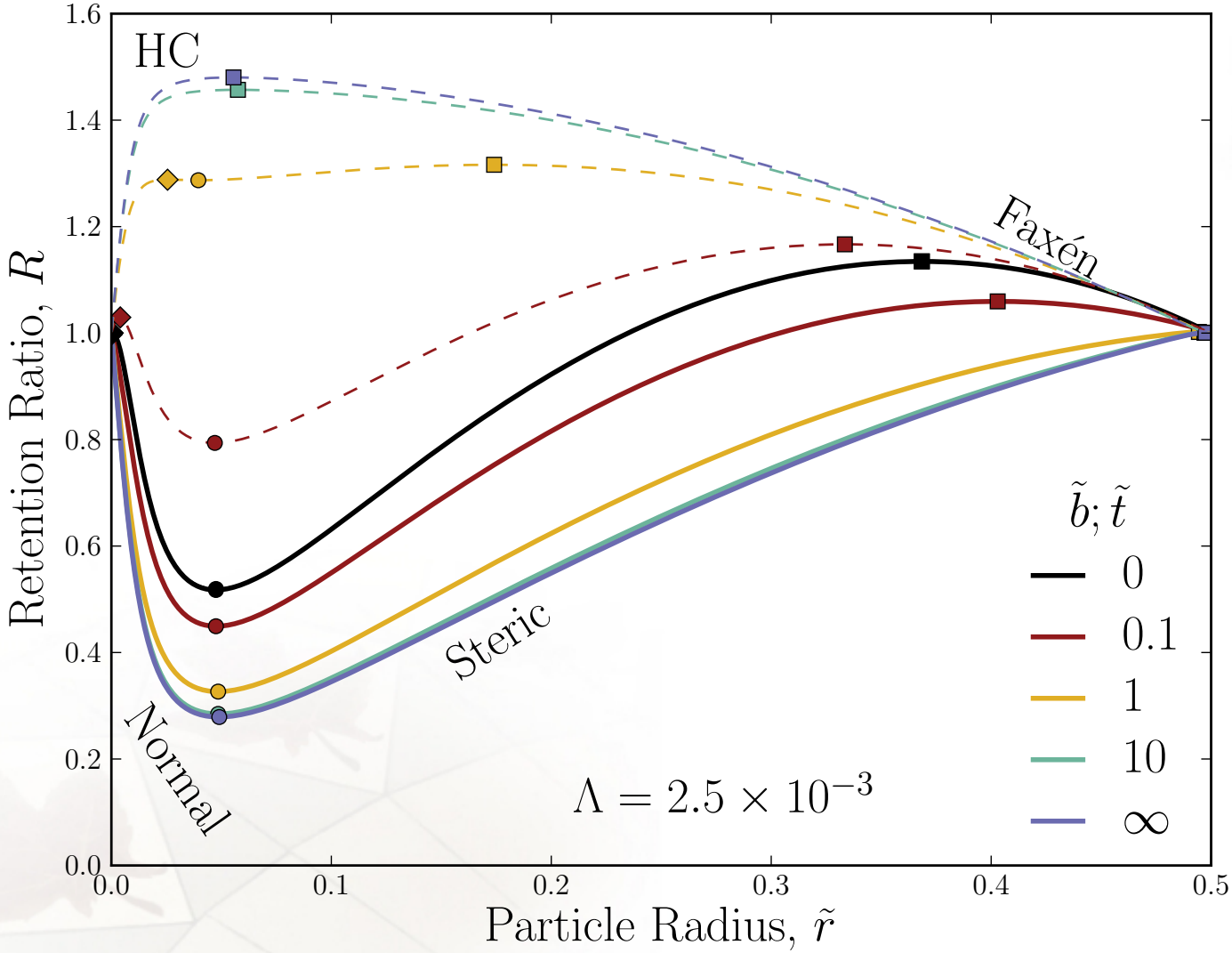

Figure : Retention ratio as a function of particle size for $\Lambda = 2.5 \times 10^{-3}$. Retention ratio as a function of particle size for slip at the depletion wall (solid lines) and slip at the accumulation wall (dashed lines). The no-slip solution is given by the solid black line. Diamonds denote the transition from hydrodynamic chromatography (HC) to normal-mode FFF, circles mark the normal- to steric-mode transition and squares label the transition to Faxén-Mode FFF.

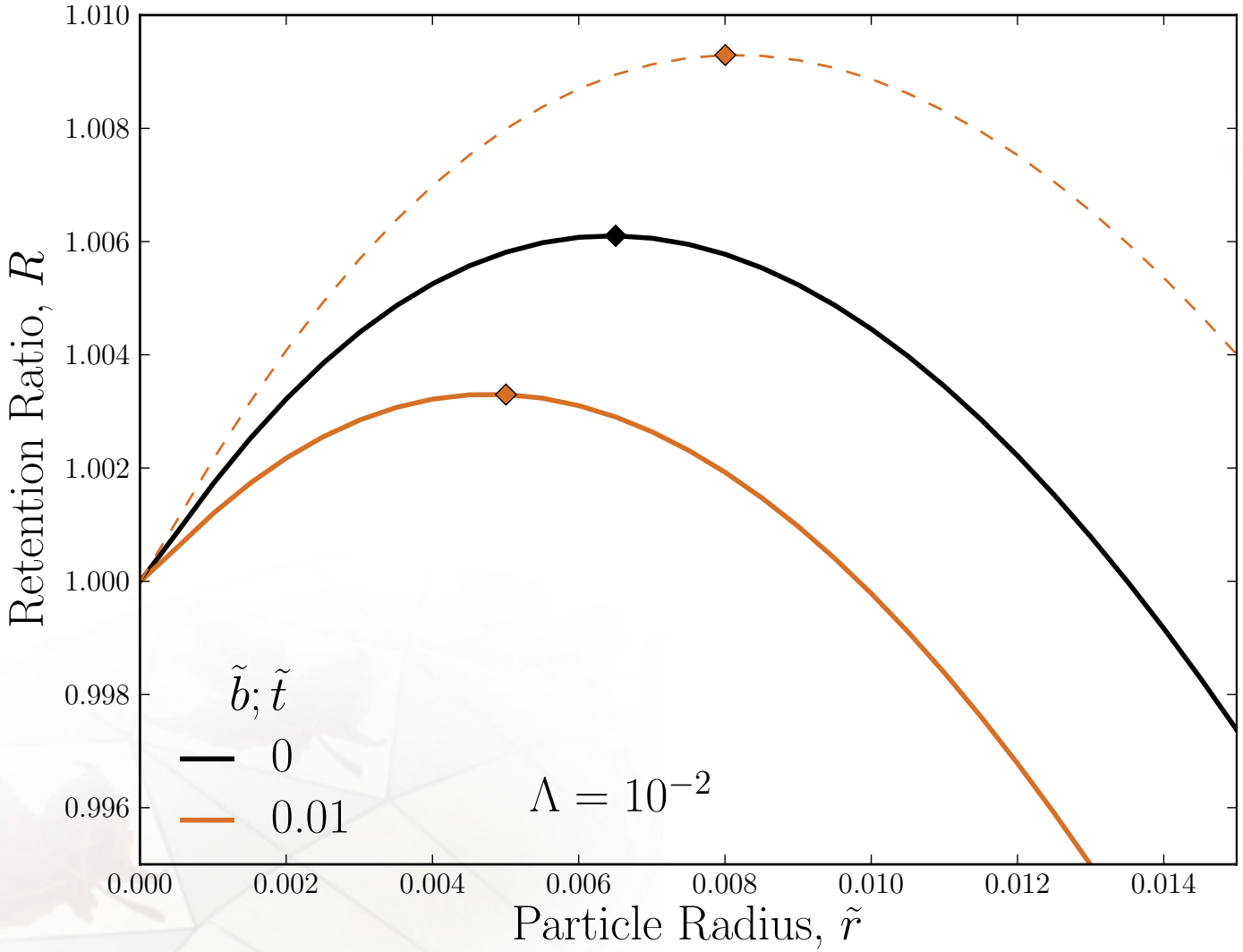

Figure : Retention ratio of small particle sizes for $\Lambda = 10^{-2}$ showing HC and the beginning of normal-mode FFF. Retention ratio as a function of particle size for slip at the depletion wall (solid lines) and slip at the accumulation wall (dashed lines). The no-slip solution is given by the solid black line. Diamonds denote the transition from hydrodynamic chromatography (HC) to normal-mode FFF, circles mark the normal- to steric-mode transition and squares label the transition to Faxén-Mode FFF.

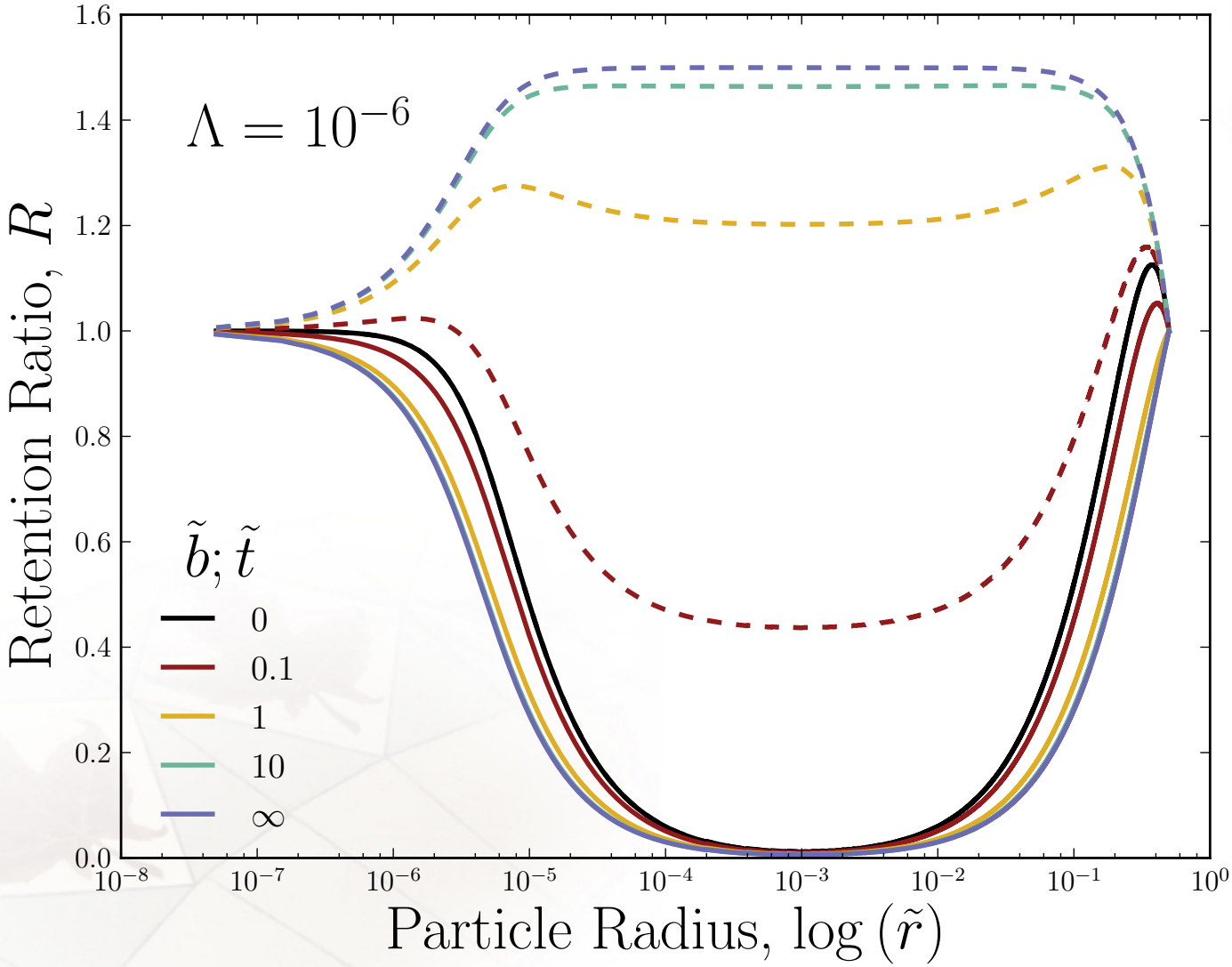

Figure : Retention ratio for a device retention parameter $\Lambda = 10^{-6}$ for slip at the depletion wall (solid lines) and slip at the accumulation wall (dashed lines). The no-slip solution is given by the solid black line.

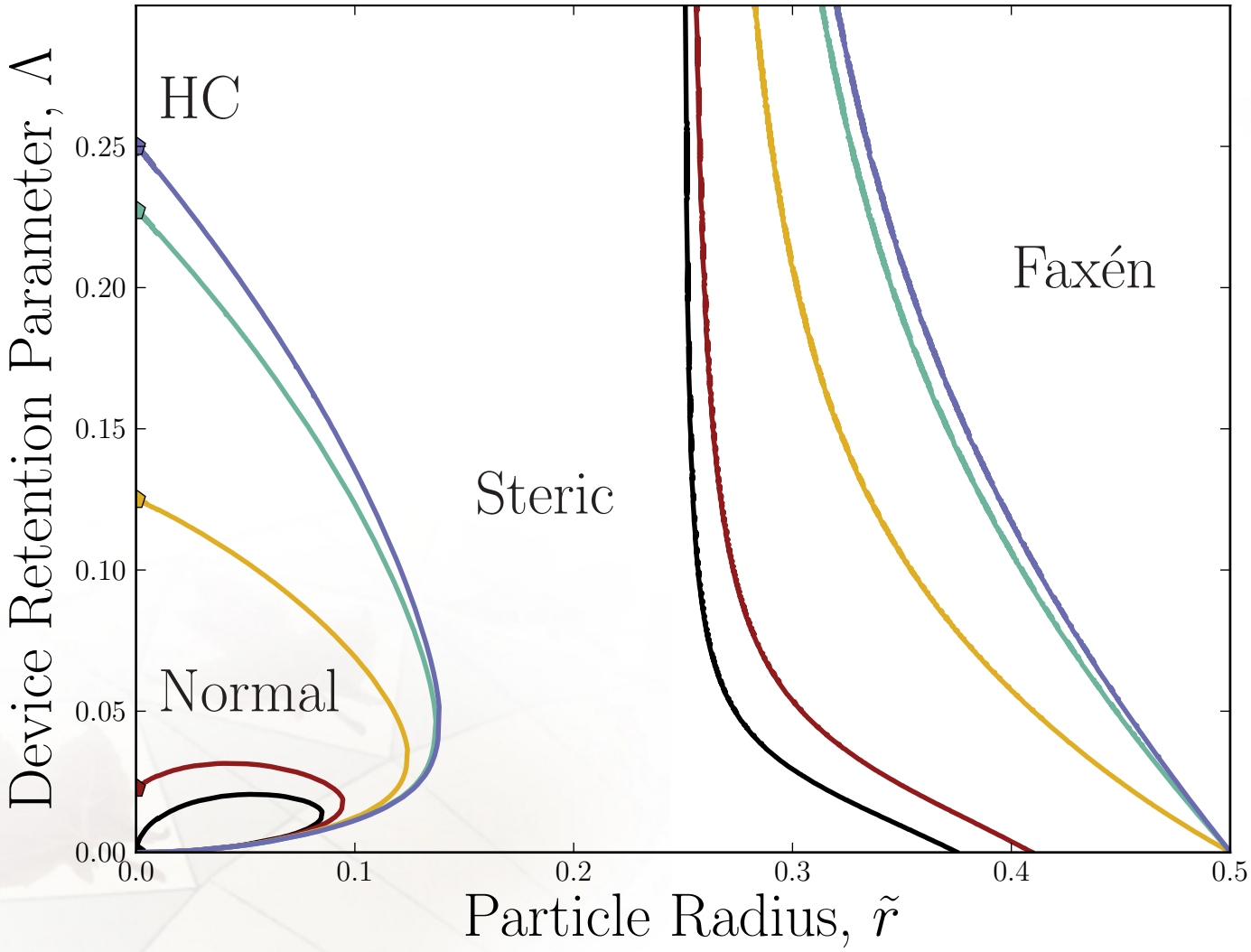

Figure : Operational-mode diagrams for various slip lengths at the depletion wall (and no-slip at the accumulation wall *i.e.* $\tilde{t} > 0$ with $\tilde{b} = 0$). The intercepts are all at the origin.

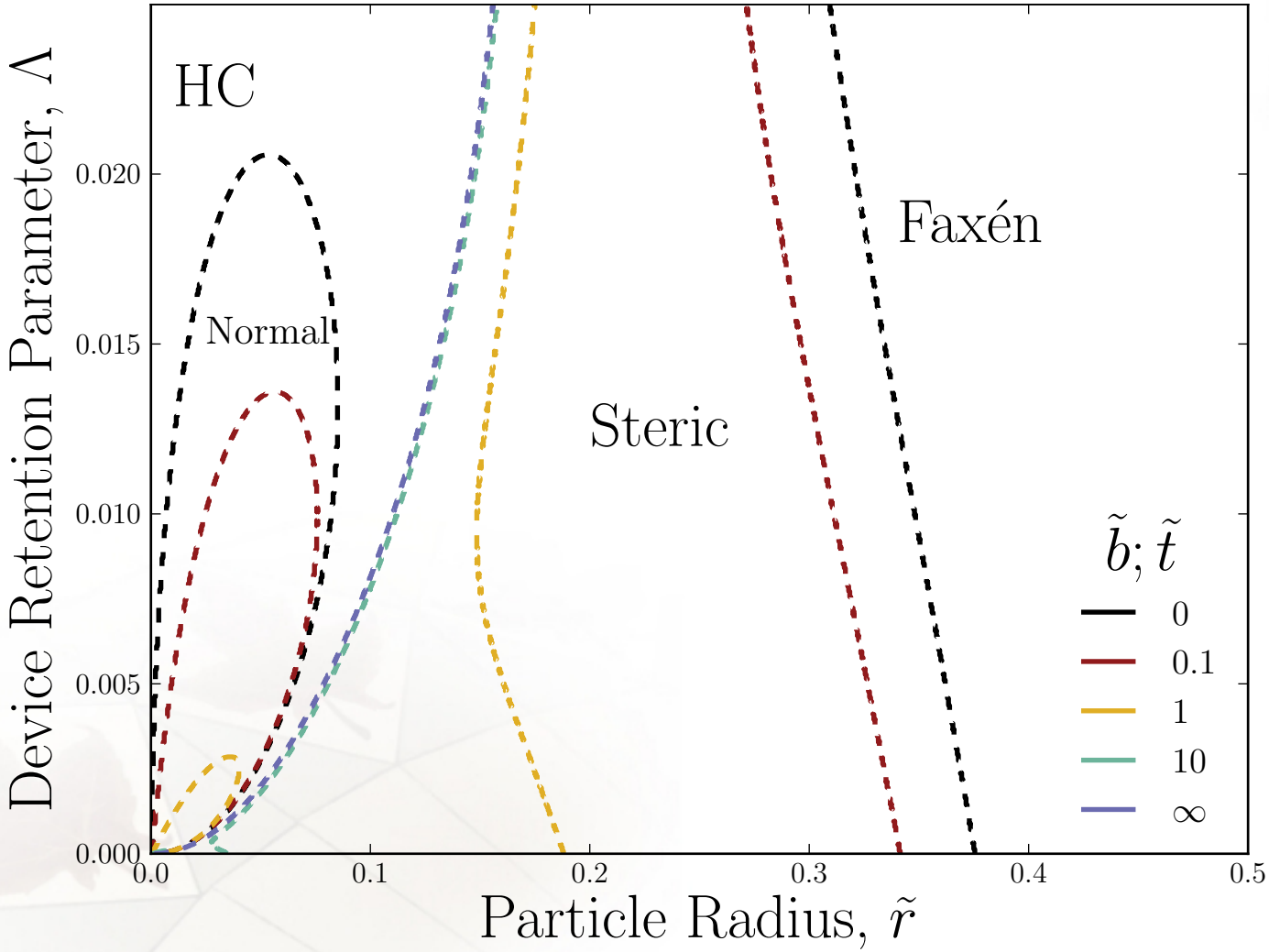

Figure : Operational-mode diagrams for various slip lengths at the accumulation wall (and no-slip at the depletion wall *i.e.* $\tilde{b} > 0$ with $\tilde{t} = 0$).

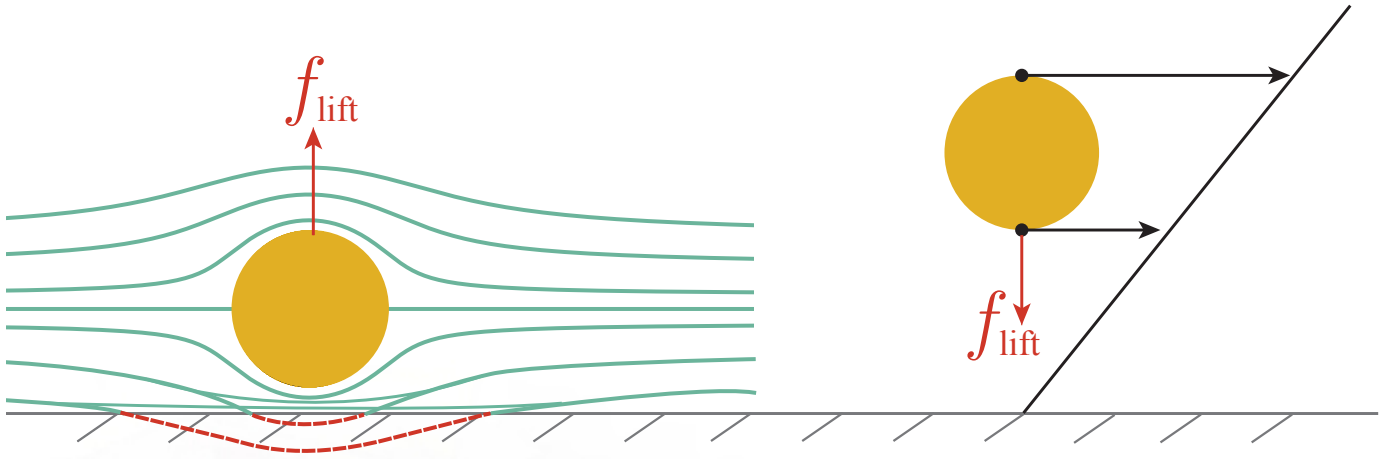

Figure : Inertial forces arise from two different mechanisms in microfluidic devices. The wall-caused lift breaks the symmetry of the flow and compresses streamlines between the particle and the wall generating a pressure away from the wall, while shear-gradient inertial forces tend to act in the opposite direction since they push solutes down shear-gradients.

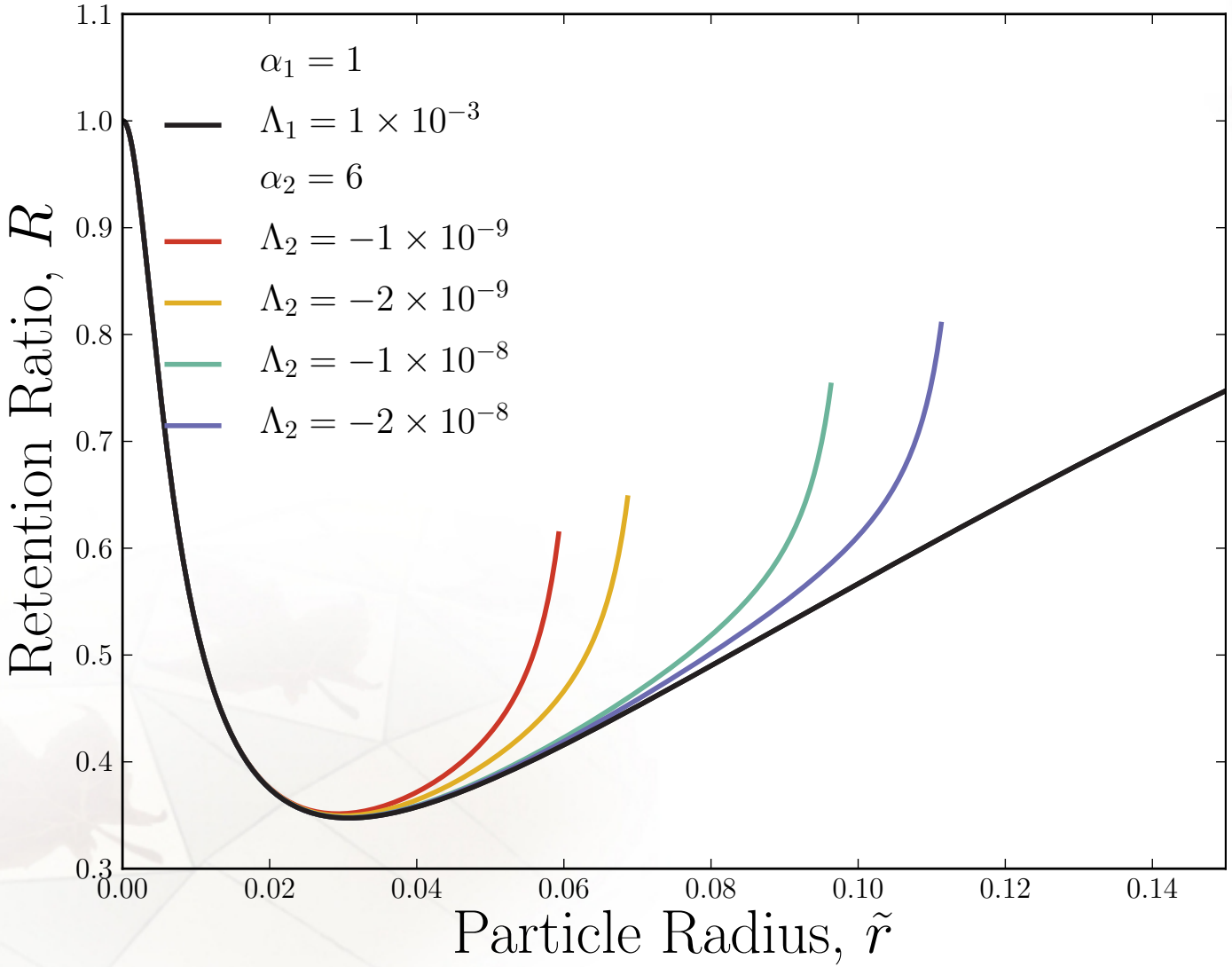

Figure : Lift force assumed to scale as $\alpha_2 = 6$.

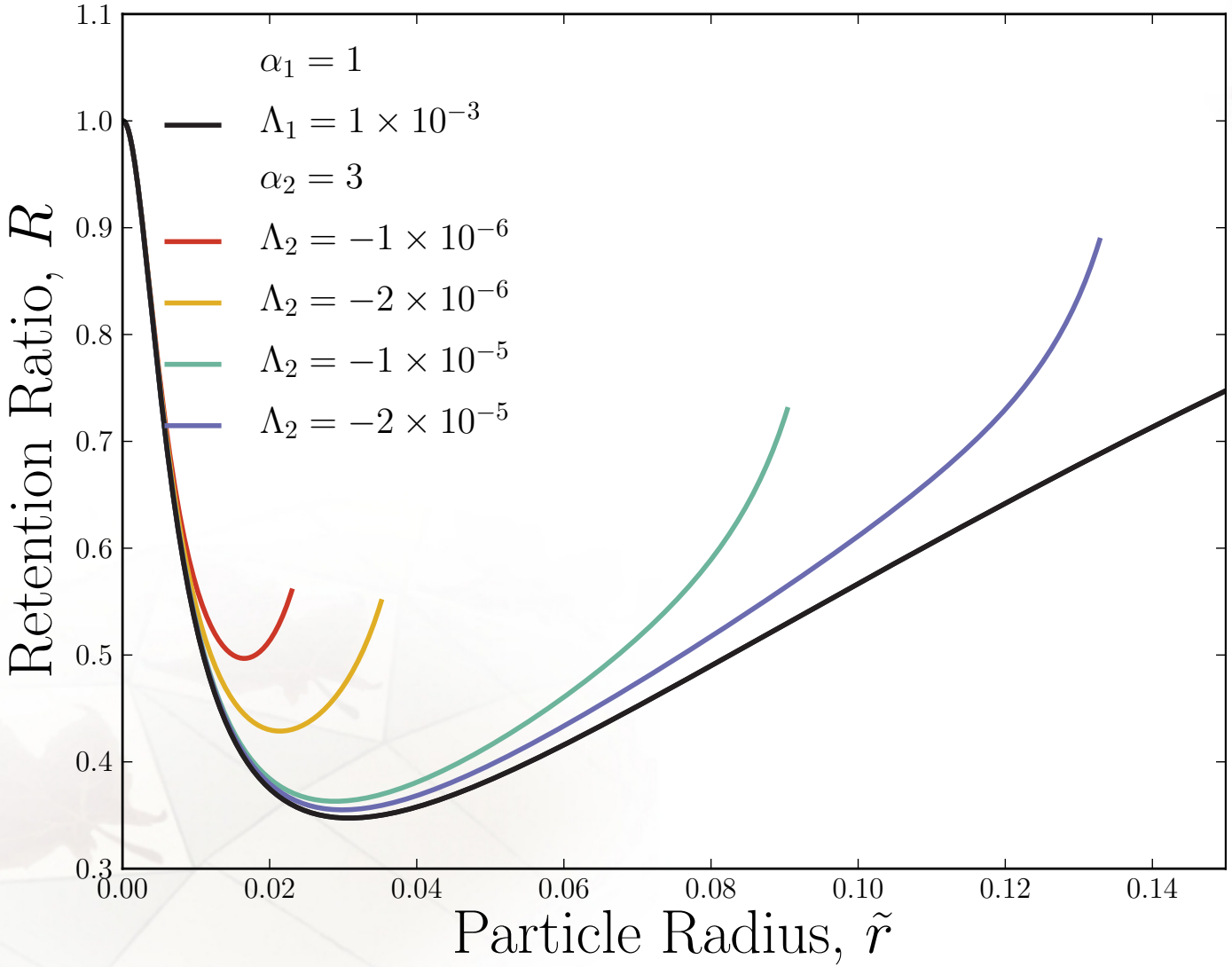

Figure : Lift force assumed to scale as $\alpha_2 = 3$.

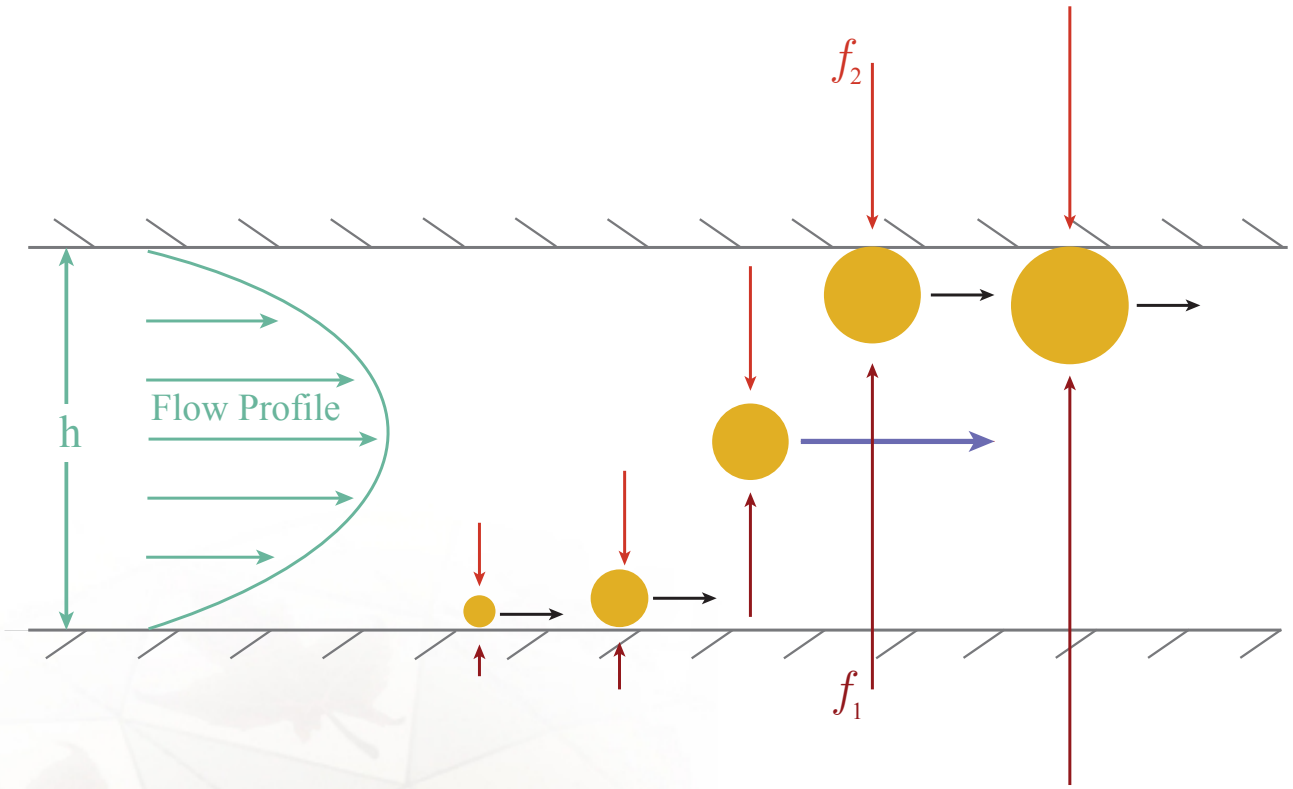

Figure : Schematic of the concept behind adverse-mode FFF. Two strong forces (f_1 and f_2), which scale differently with particle size, oppose one another. At small sizes, the force with the smaller scaling (say α_1) dominates and the solute undergoes steric-mode at the accumulation wall. At the specific size $\tilde{r}_L$ the two forces are equal and the solute is effectively buoyant. At larger, sizes the adverse force dominates and the solute once again is pushed against the channel wall, only now it is what was previously the depletion wall.

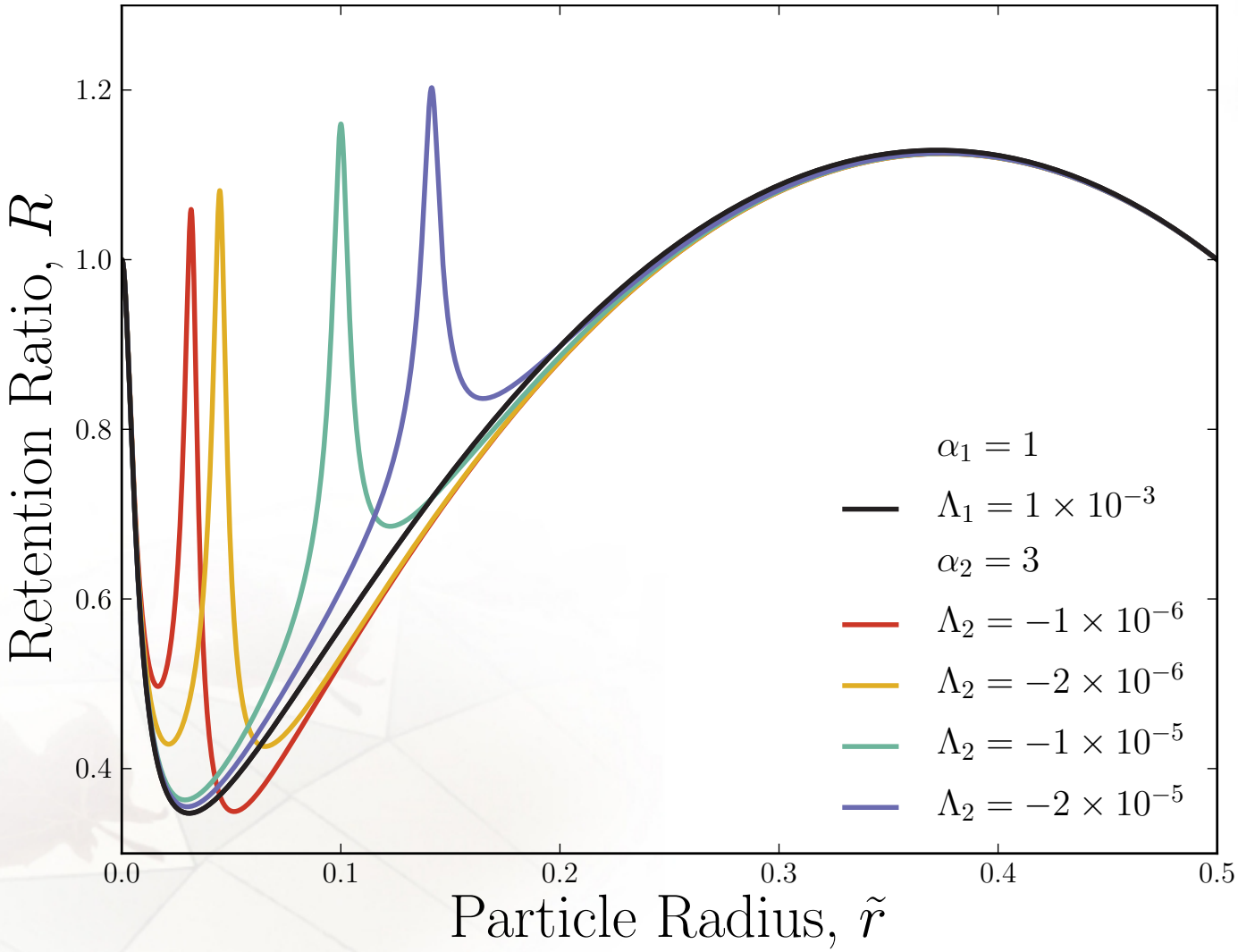

Figure : Adverse-mode FFF for$\alpha_1 = 1$ and $\alpha_2 = 3$ **moderate** competing fields.

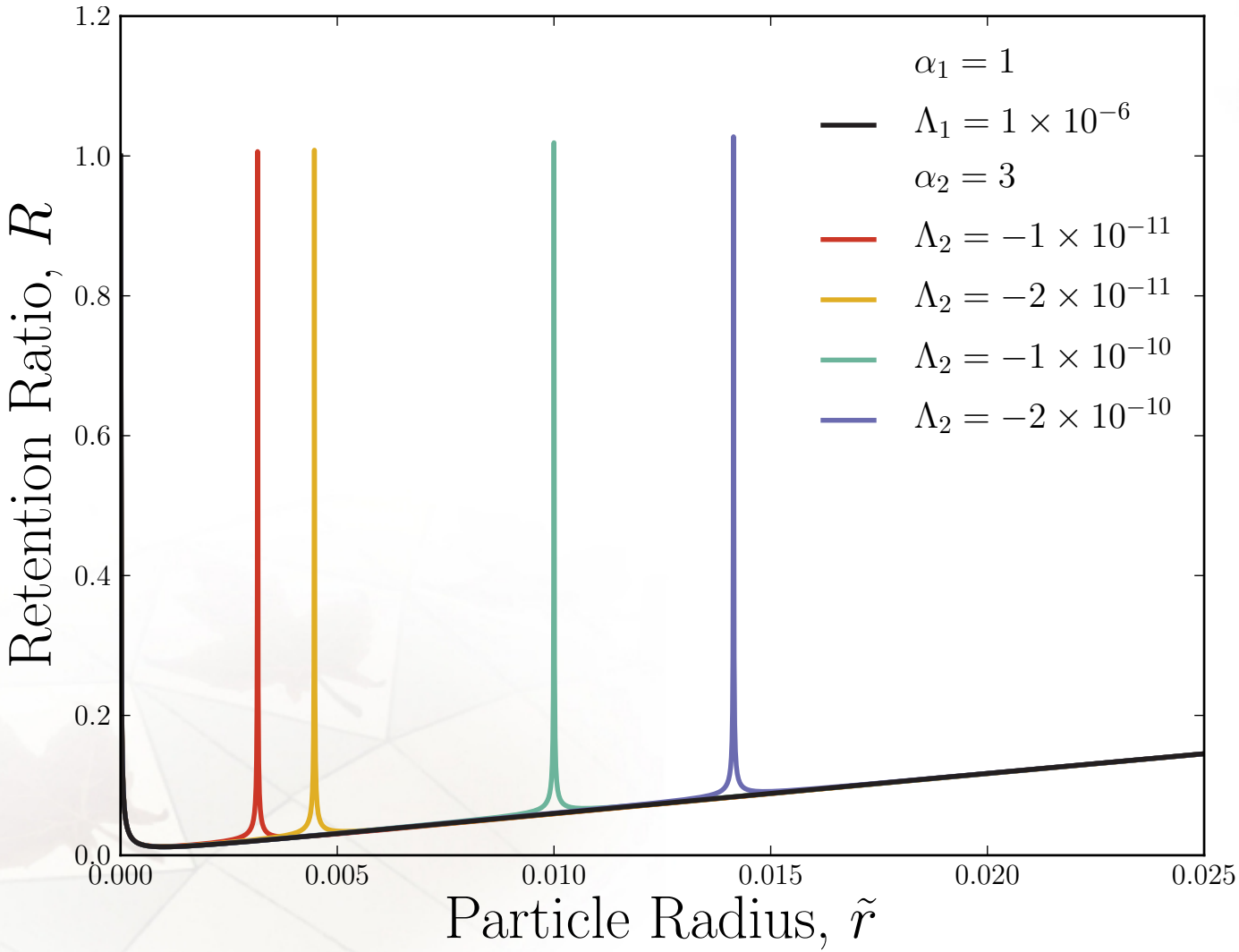

Figure : Adverse-mode FFF for$\alpha_1 = 1$ and $\alpha_2 = 3$ **strong** competing fields.

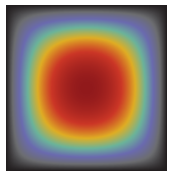

Figure : Square-duct; $\tilde{w} = 1$

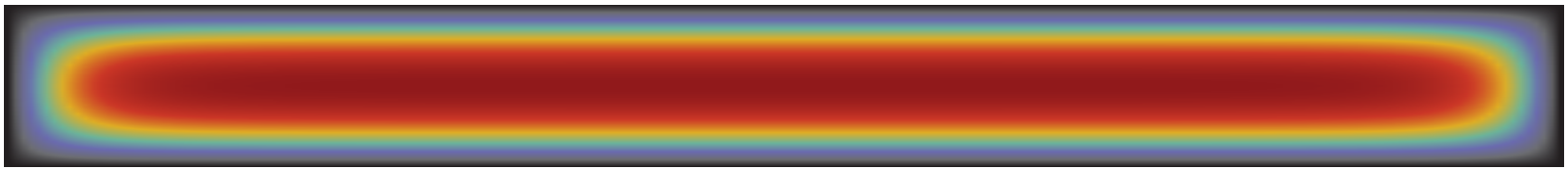

Figure : Aspect ratio of $\tilde{w} = 10$

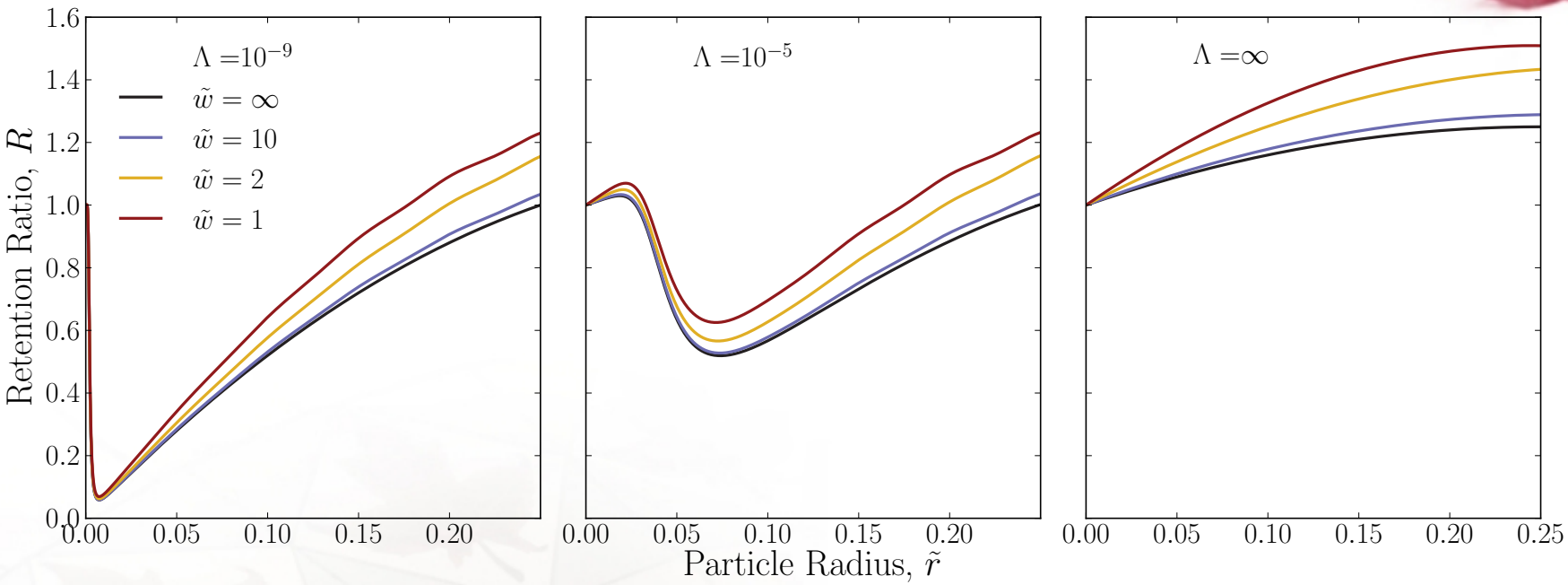

Figure : The retention ratio as a function of solute size $\tilde{r}$ for $\alpha = 3$ and various external field strengths. Solutions truncated at ten terms.

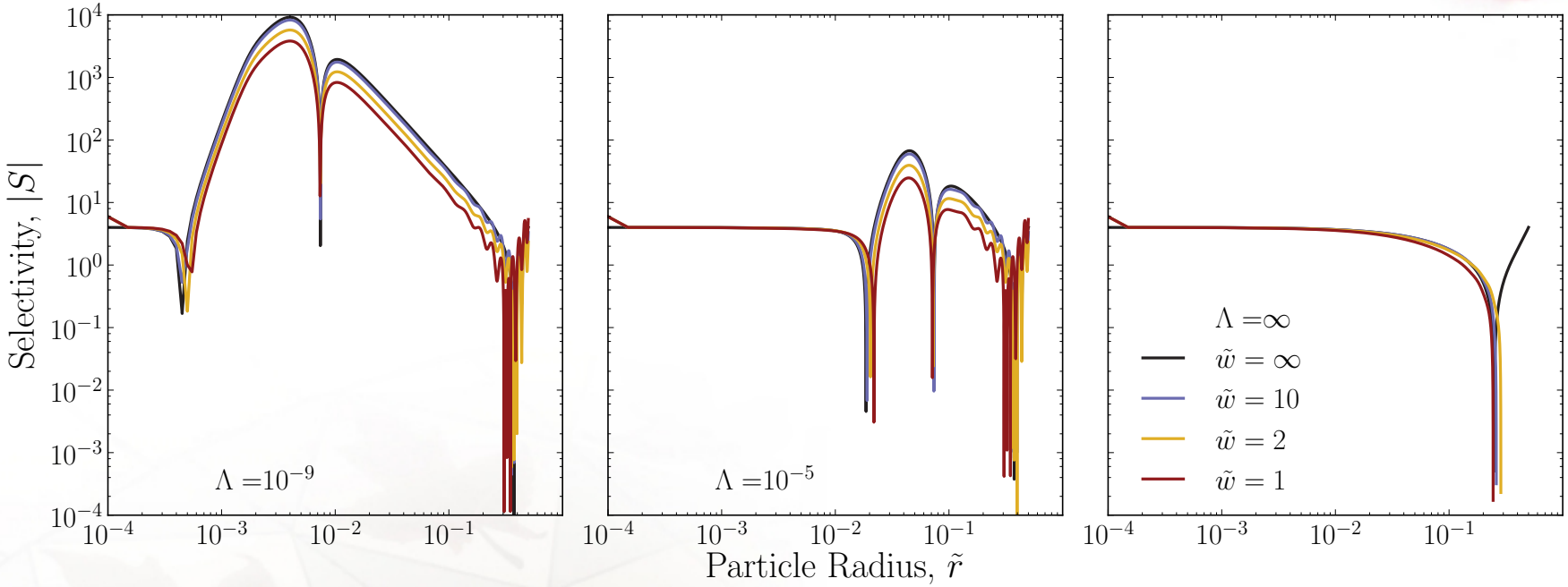

Figure : The device selectivity corresponding to each retention curve.

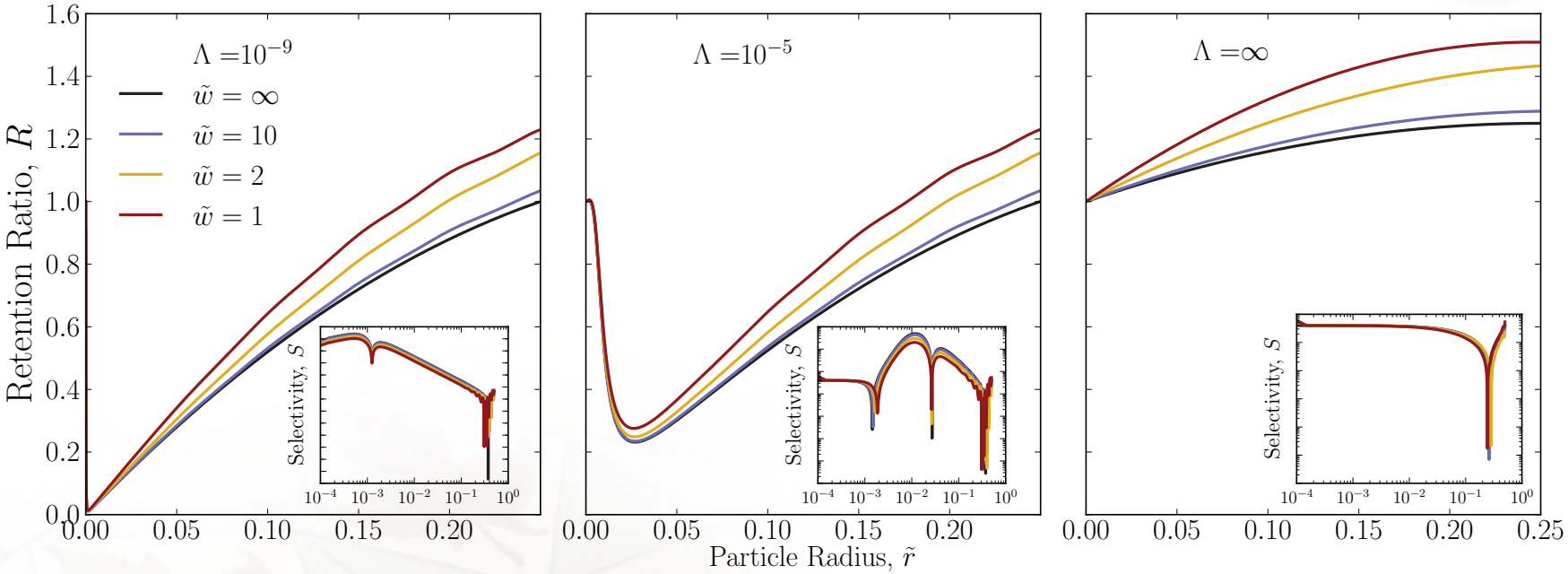

Figure : $\alpha = 2$.

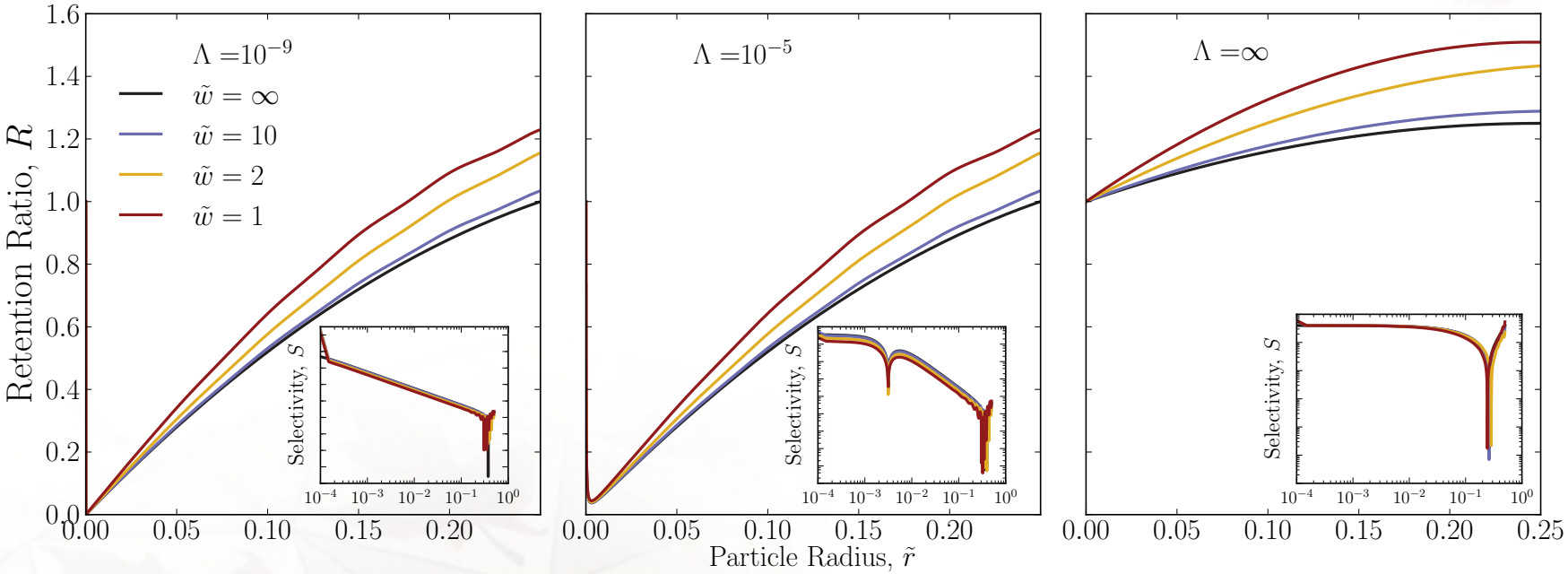

Figure : $\alpha = 1$

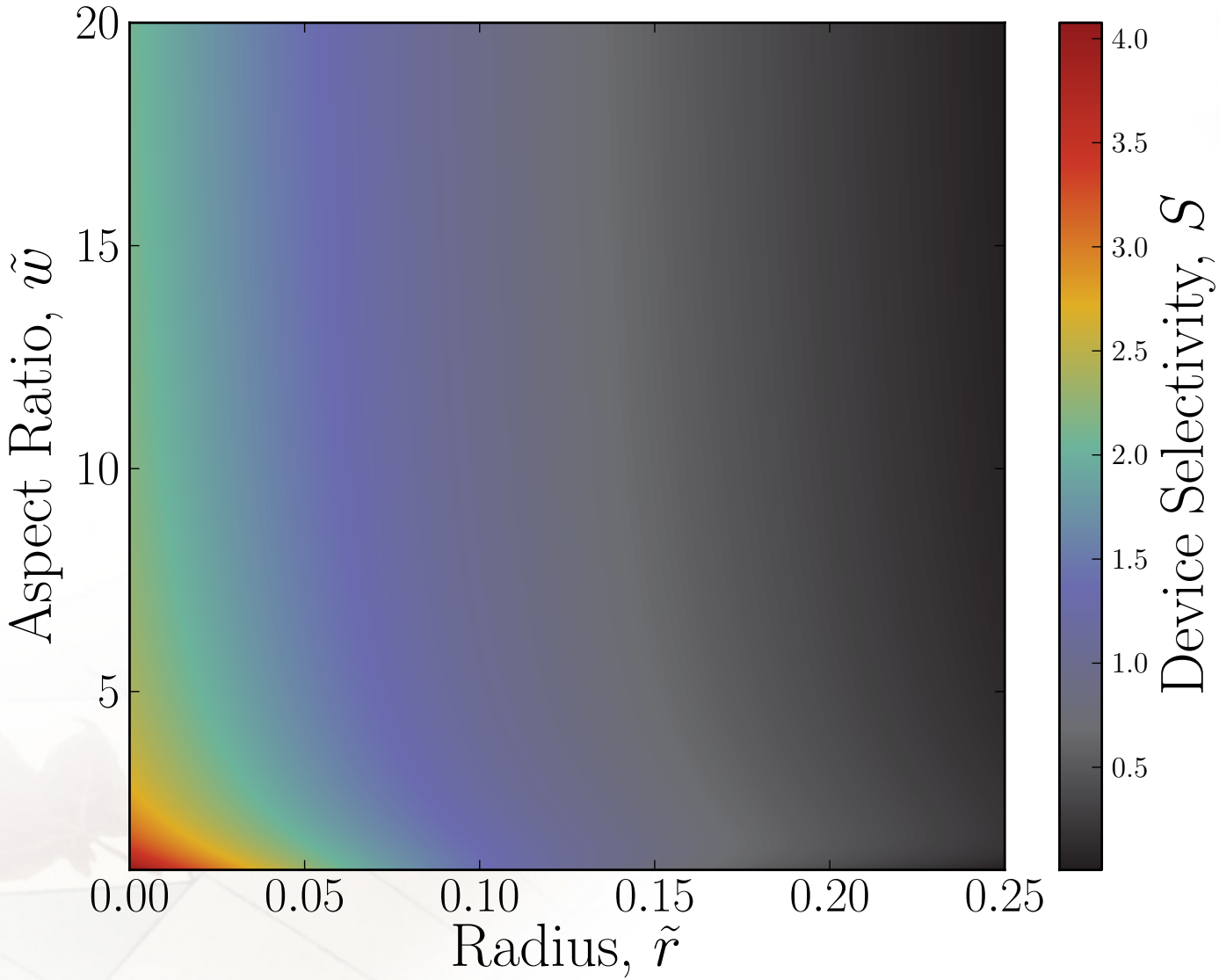

Figure : Device selectivity for HC in a rectangular channel as a function of normalized solute size and normalized width.

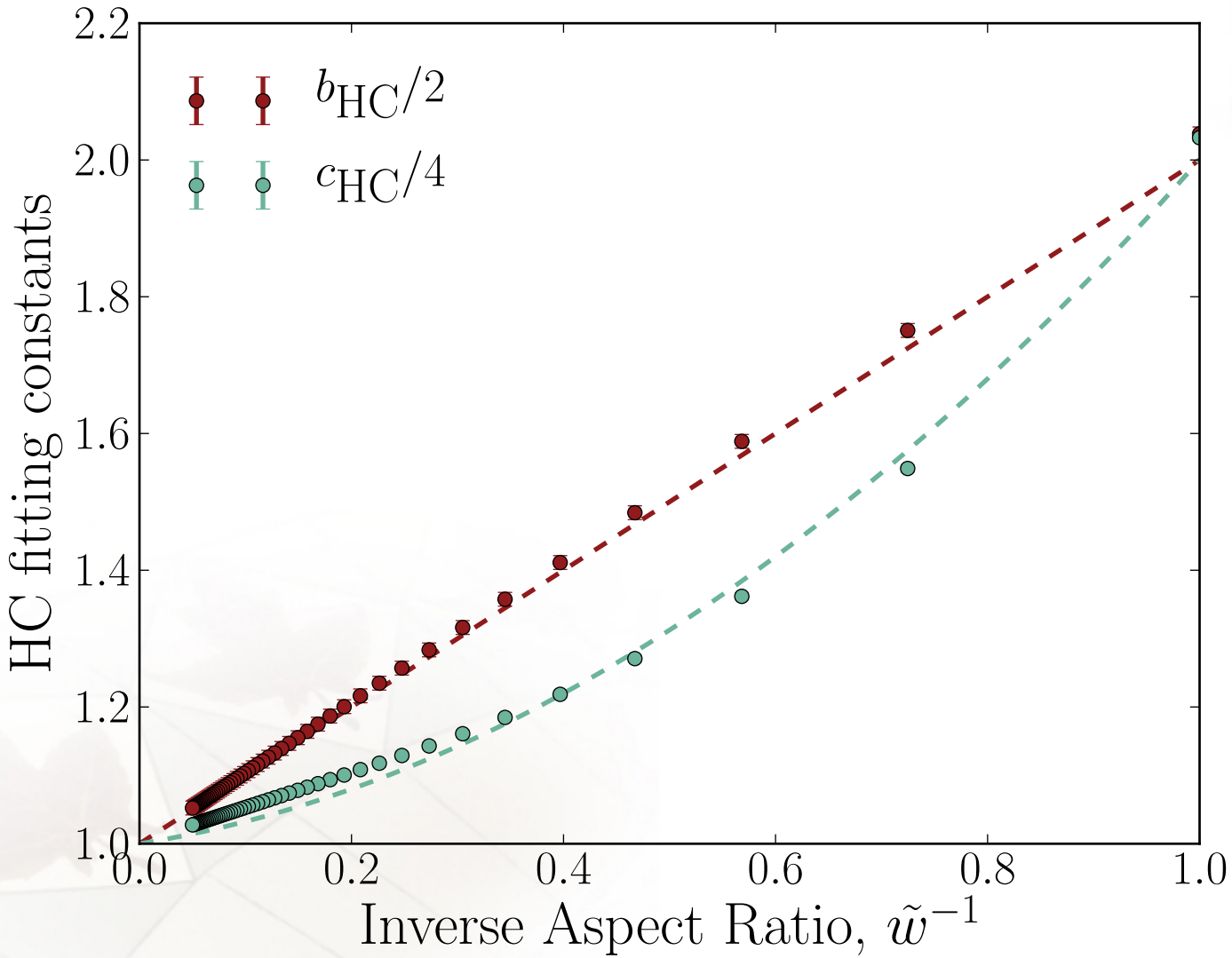

Figure : The parabolic fitting constants for hydrodynamic chromatography as functions of the aspect ratio $\tilde{w}$, normalized by their parallel-plate values. Errorbars represent uncertainty on the fit parameters.

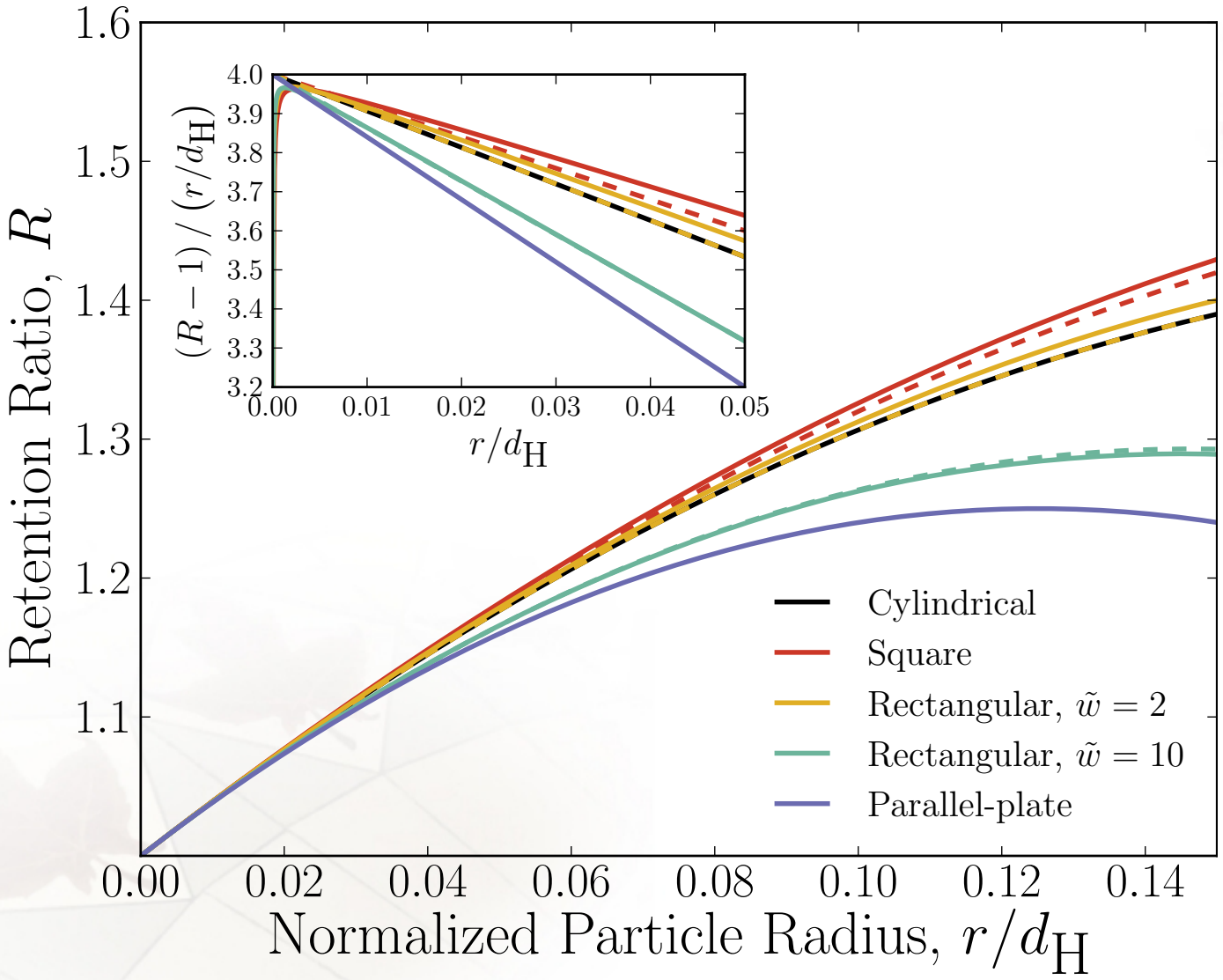

Figure : Hydrodynamic chromatography retention ratio as a function of particle radius normalized by hydraulic diameter for a number of geometries (solid lines). Dashed lines show the parabolic approximation. The inset focuses on the small particle size behaviour.

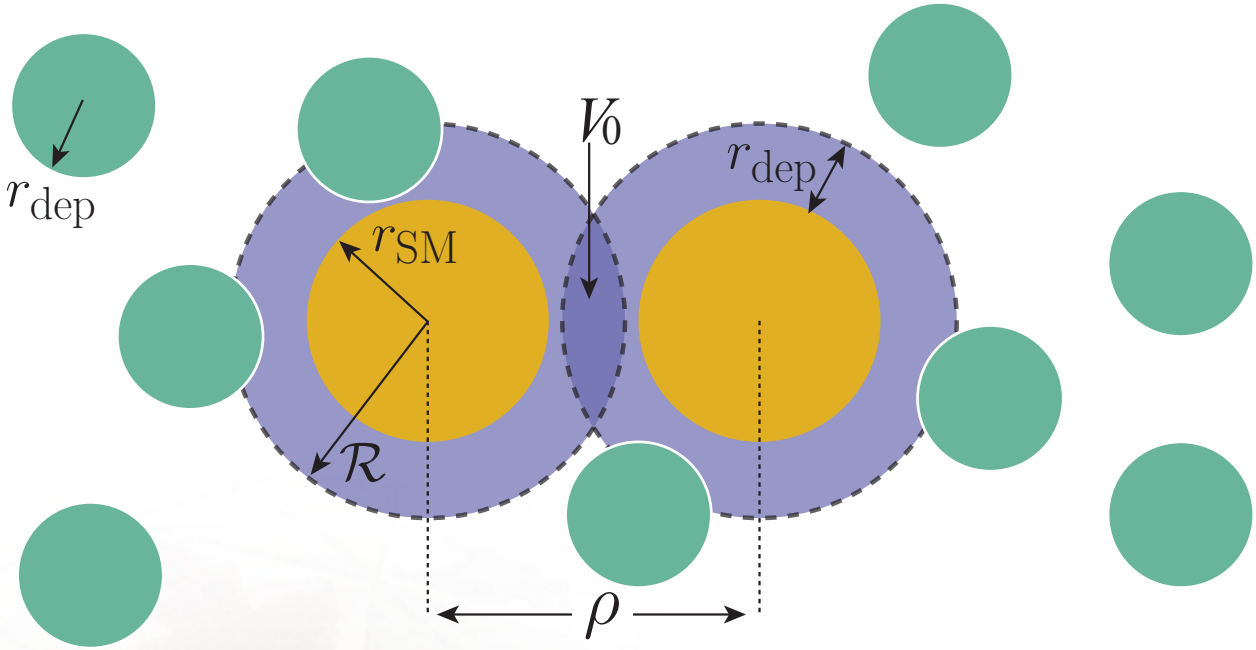

Figure : Two relatively large, spherical and disconnected DNA structural monomers (of radius r_{SM}) in a solution of depletants ($r_{\mathrm{dep}} < r_{\mathrm{SM}}$) each possess a depletant-related excluded volume (of radius $\mathcal{R} = r_{\mathrm{SM}} + r_{\mathrm{dep}}$). When the structural monomers are near ($2r_{\mathrm{SM}} < \rho < 2\mathcal{R}$) an overlap volume V_o exists, causing the number of states available to the population of depletants to be greater than when the monomers are separate ($\rho \geq 2\mathcal{R}$). This leads to an effective force that favours bringing the two structural monomers closer together.

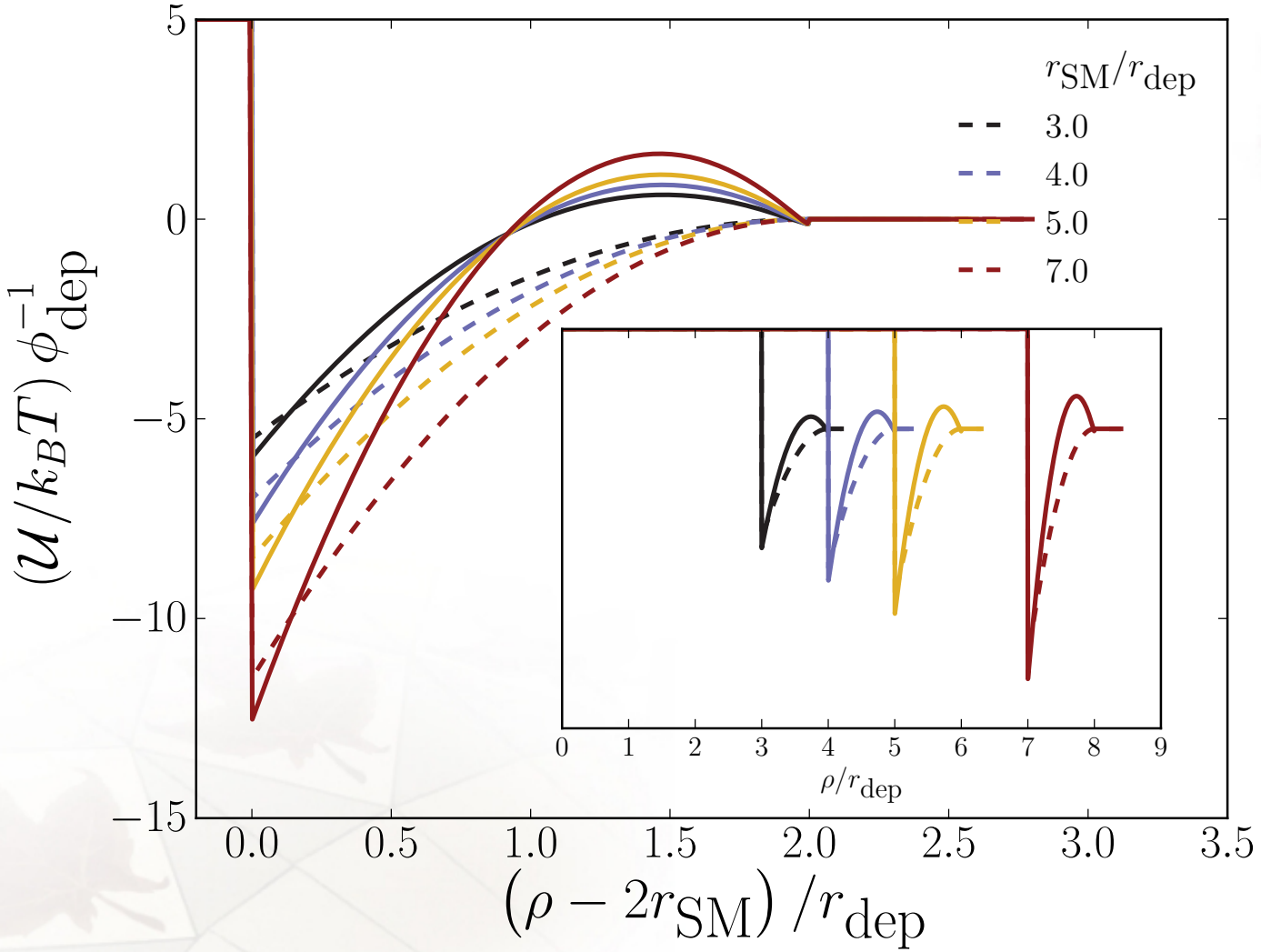

Figure : Depletion-induced attractive pair-potential between two structural monomers for a variety of monomer-depletant ratios. The abscissa is a shifted and normalized centre-to-centre separation that emphasizes differences in well-depths. The Asakura and Oosawa model is shown as dashed lines, while the MT-RF predictions are shown as solid lines. Scaling the pair-potential removes ϕ_{dep} in the AO model but not in the MT model. The MT-RF pair-potentials are for the example volume fraction of $\phi_{dep} = 0.2$.

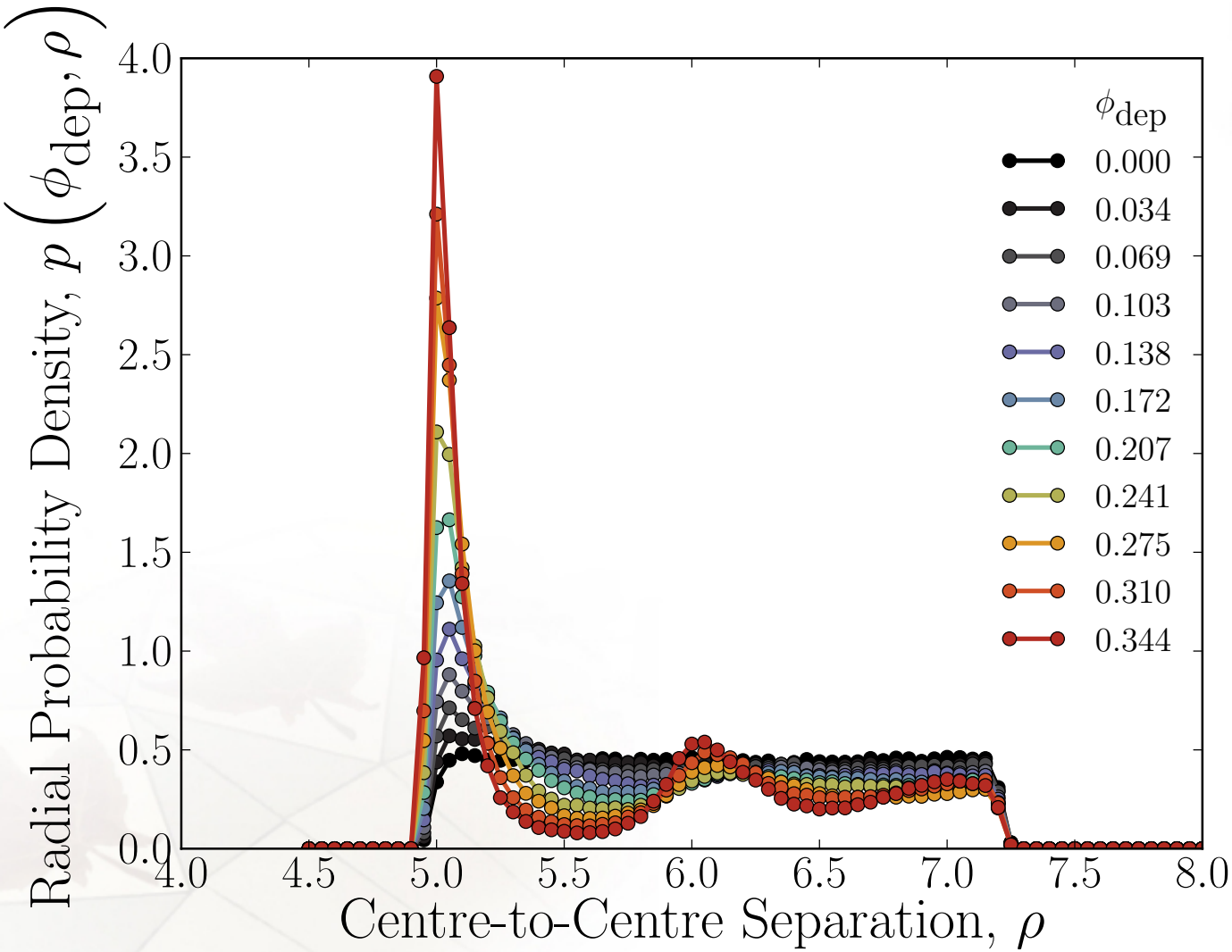

Figure : Radial probability density p of finding two free shifted-WCA structural monomers at a given separation. The structural monomers are of size $r_{\text{SM}} = 2.5\sigma$ in baths of various volume fractions of shifted-WCA depletants of size $r_{\text{dep}} = 0.5\sigma$.

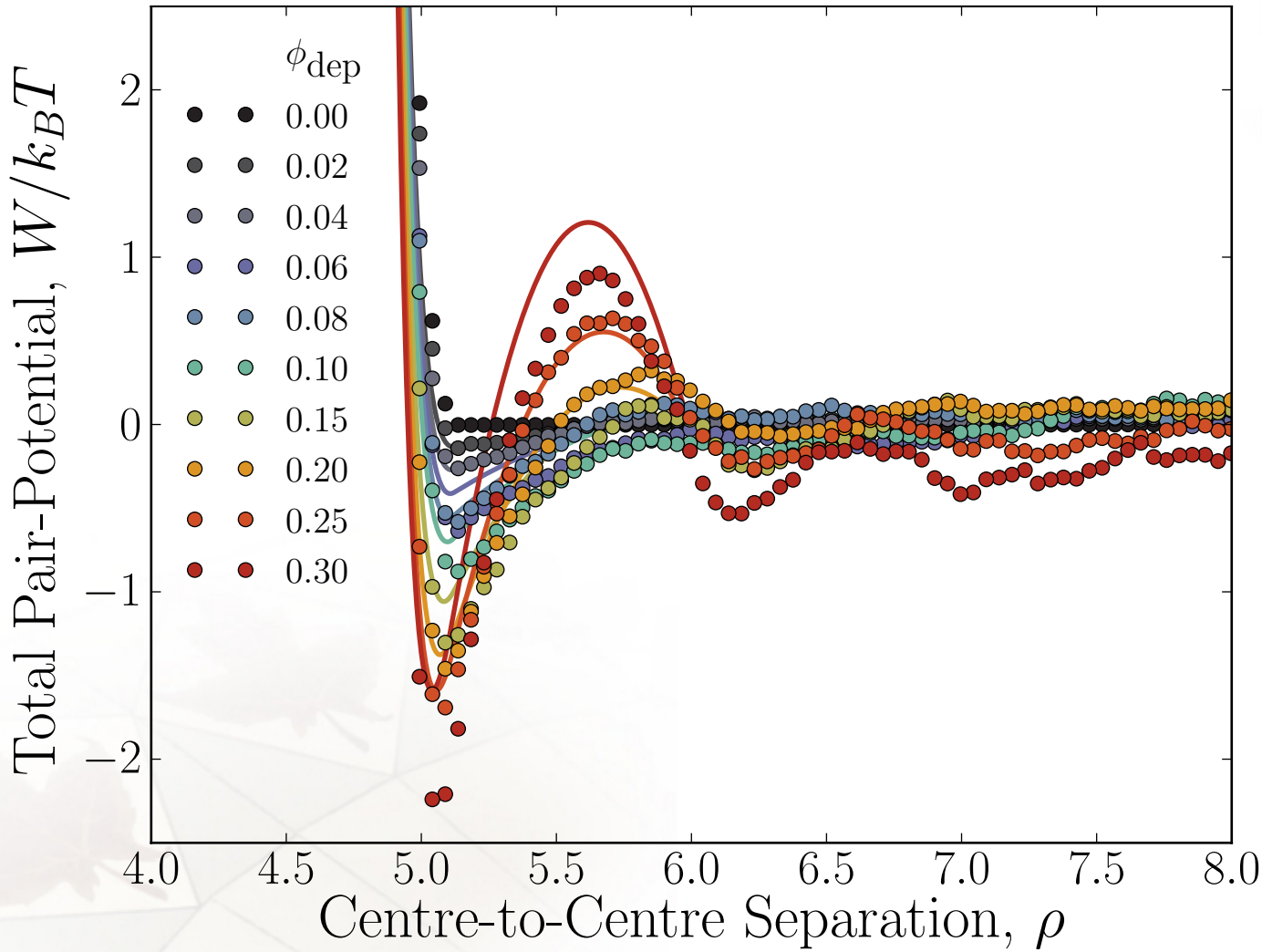

Figure : Simulated total pair-potentials W_{sWCA} from force measurements of shifted-WCA monomers of size $r_{\mathrm{SM}} = 2.5\sigma$ in baths of various volume fractions of shifted-WCA depletants of size $r_{\mathrm{dep}} = 0.5\sigma$ (•). Solid lines are the sum of the attraction predicted by the MT model and the shifted-WCA repulsion.

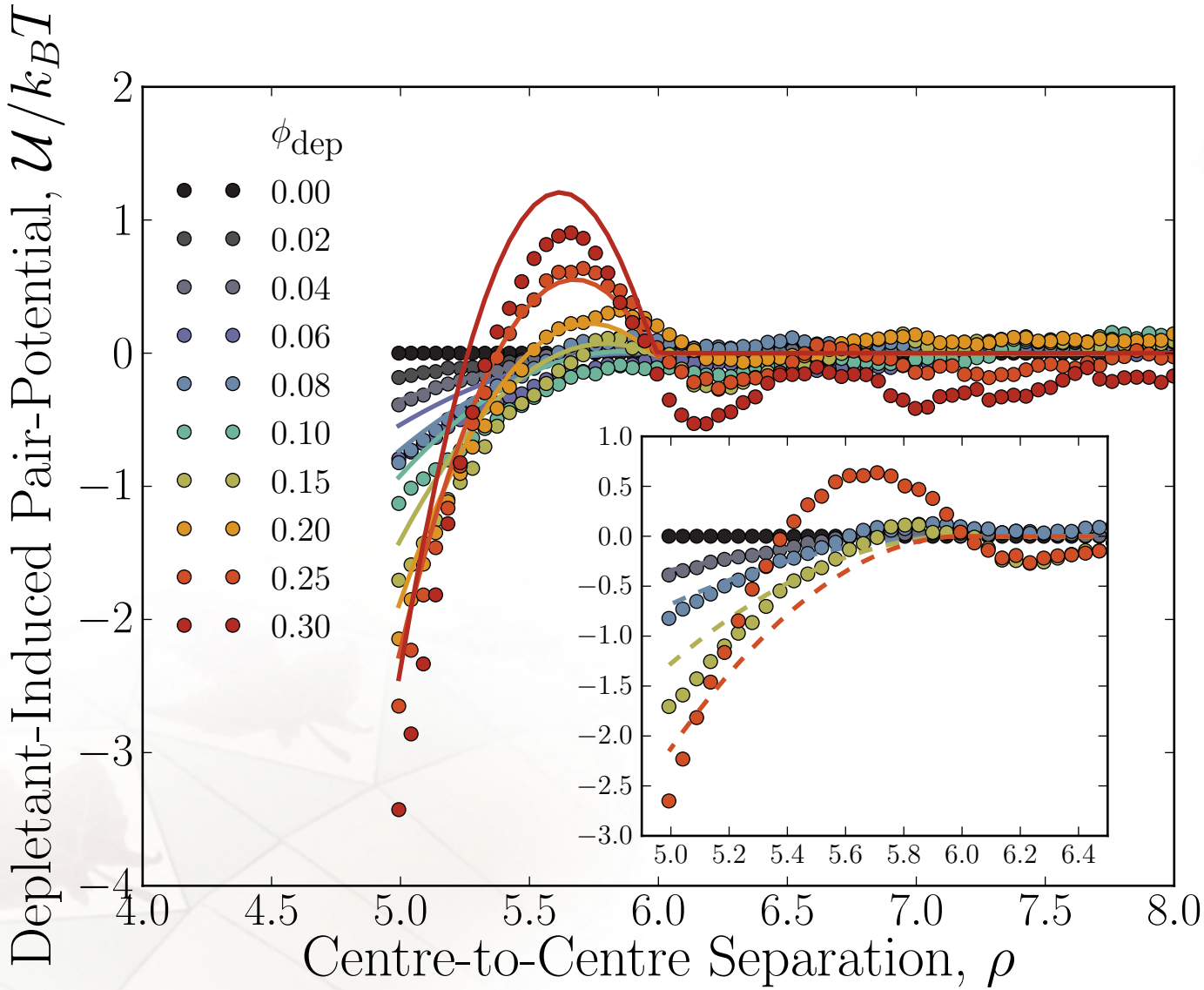

Figure : Simulated depletion-induced pair-potentials $\mathcal{U}_{\text{sWCA}}$ as a function of centre-to-centre separation for $r_{\text{SM}}/r_{\text{dep}} = 5$ (•). Values obtained from force measurements of shifted-WCA monomers of size $r_{\text{SM}} = 2.5$ and $r_{\text{dep}} = 0.5$. Solid lines show the induced pair-potentials predicted by the MT model, while dashed lines in the inset show the AO model.

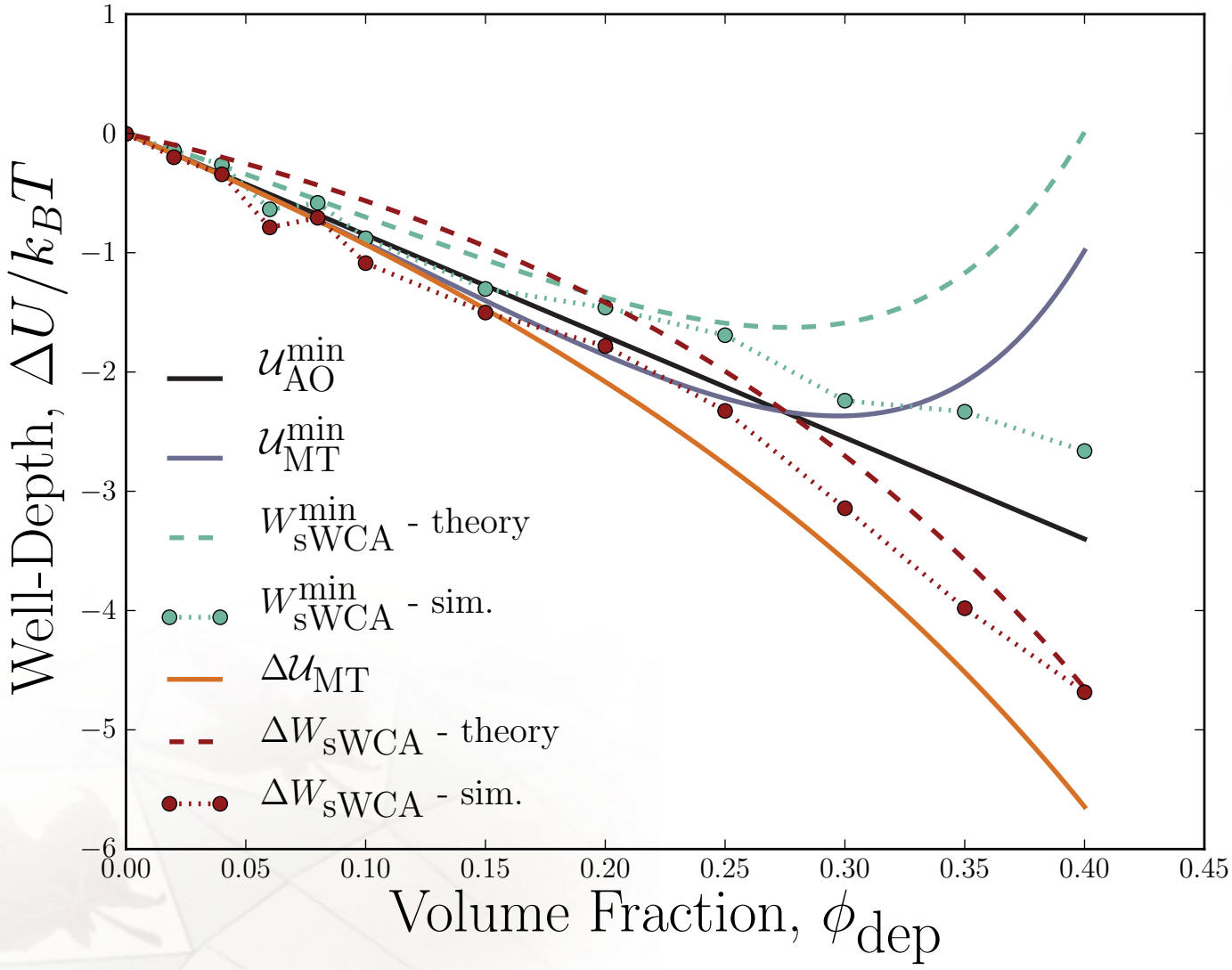

Figure : The minimum value of the pair-potential as a function of depletant volume fraction for shifted-WCA structural monomers of size $r_{\text{SM}} = 2.5\sigma$ and depletants of size $r_{\text{dep}} = 0.5\sigma$. The minimum from simulations ($W^{\text{min}}_{\text{sWCA}}$; green circles) is compared to the AO model ($\mathcal{U}^{\text{min}}_{\text{AO}}$; black solid line) and MT model ($\mathcal{U}^{\text{min}}_{\text{MT}}$; blue solid line). The green dashed line shows theoretical minima of the MT model plus the shifted-WCA potential ($W^{\text{min}}_{\text{sWCA}}$). The corresponding effective well-depth (minimum minus maximum) from the simulations and the models are shown as well. The theoretical effective well-depth for the MT model ($\Delta\mathcal{U}_{\text{MT}}$; yellow solid line) is deeper than either the simulations (ΔW_{sWCA}; red circles) or theoretical sum of

uOttawa

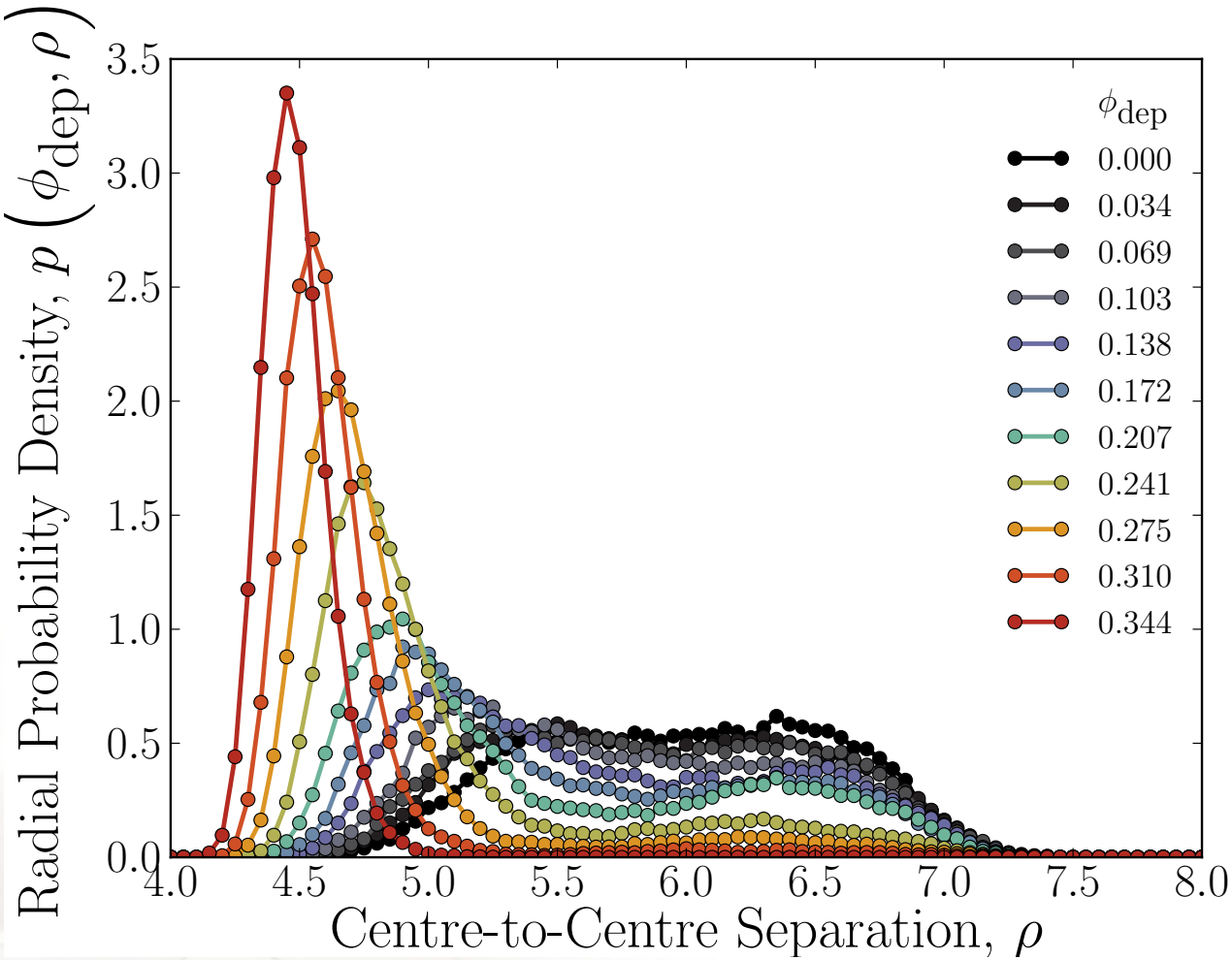

Figure : Radial probability density p of finding two free combinatorial-WCA structural monomers at a given separation. The structural monomers are of size $r_{\text{SM}} = 2.5\sigma$ in baths of various volume fractions of combinatorial-WCA depletants of size $r_{\text{dep}} = 0.5\sigma$. There is a significant probability of overlap, which results in a deep attractive well with a minimum within $r_{min} < 2r_{\text{SM}}$.

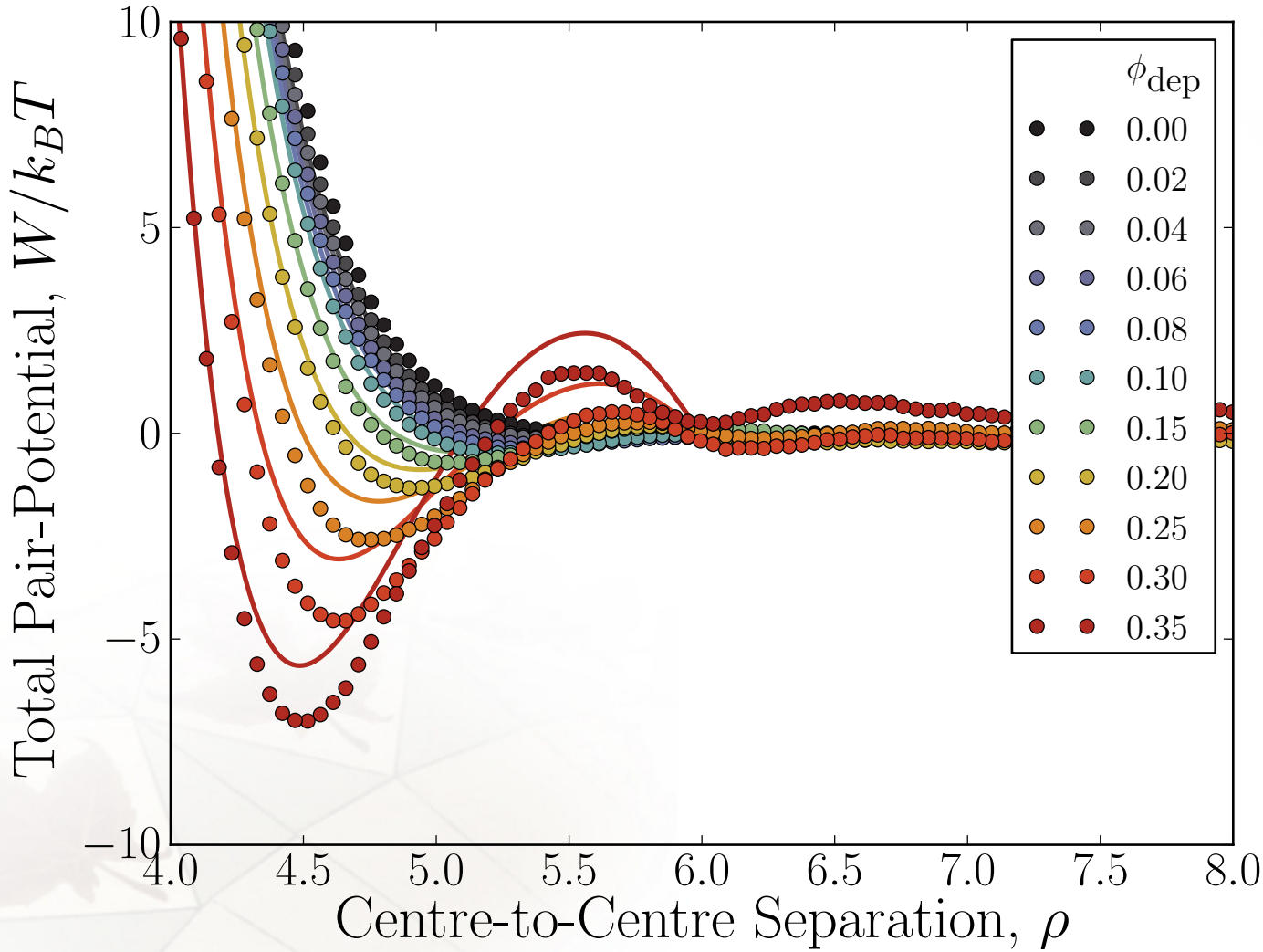

Figure : Simulated total pair-potentials W_{cWCA} from force measurements of combinatorial-WCA monomers of size $r_{\text{SM}} = 2.5\sigma$ in baths of various volume fractions of shifted-WCA depletants of size $r_{\text{dep}} = 0.5\sigma$ (•). Solid lines are the sum of the attraction predicted by the MT model and the combinatorial-WCA repulsion.

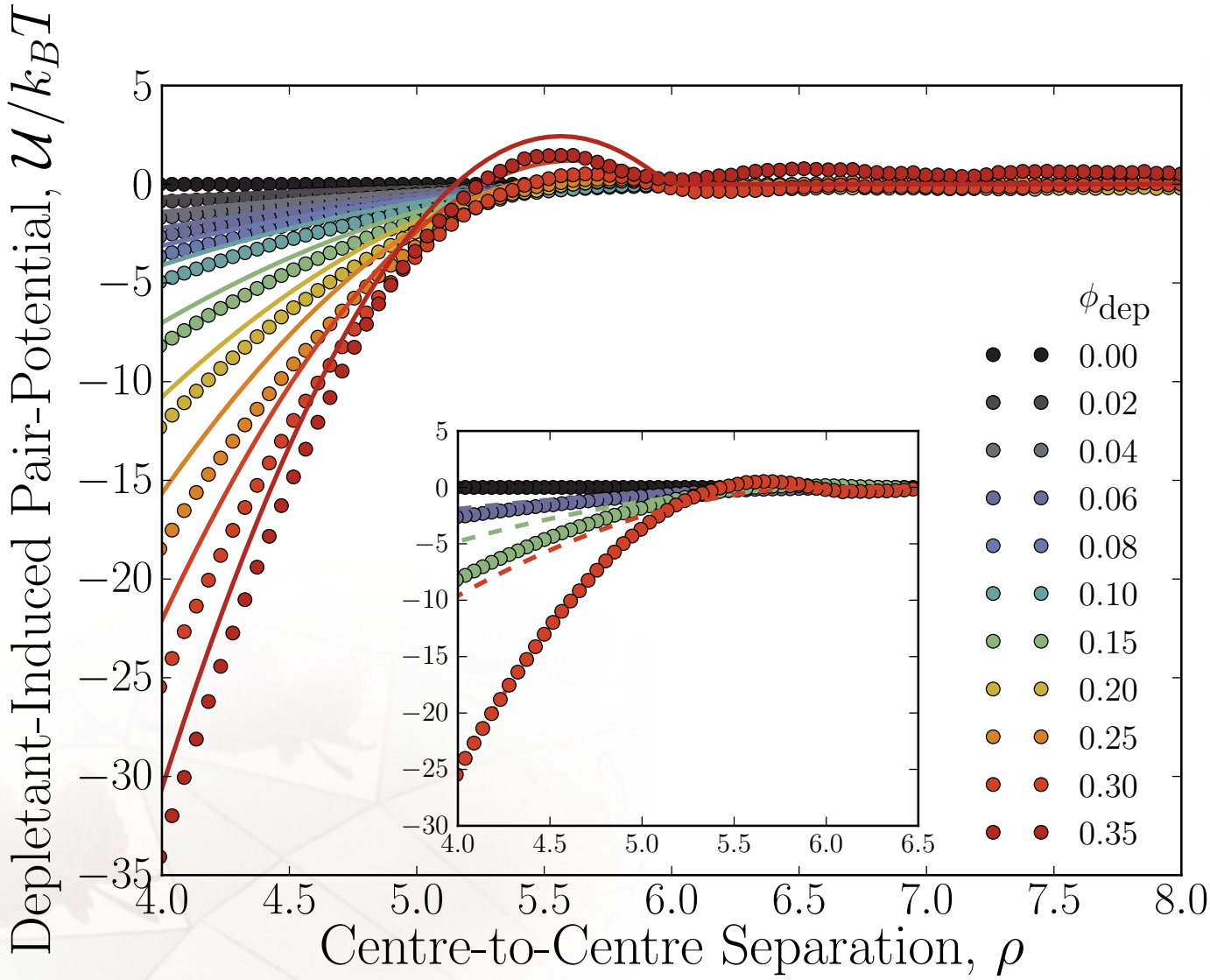

Figure : Simulated depletion-induced pair-potentials $\mathcal{U}_{\text{cWCA}}$ as a function of centre-to-centre separation for $r_{\text{SM}}/r_{\text{dep}} = 5$ (•). Values obtained from force measurements of combinatorial-WCA monomers of size $r_{\text{SM}} = 2.5\sigma$ and $r_{\text{dep}} = 0.5\sigma$. Solid lines show the induced pair-potentials predicted by the MT model, while dashed lines in the inset show the AO model. The AO model fails to accurately predict the entropic attraction when $\rho < 2r_{\text{SM}}$.

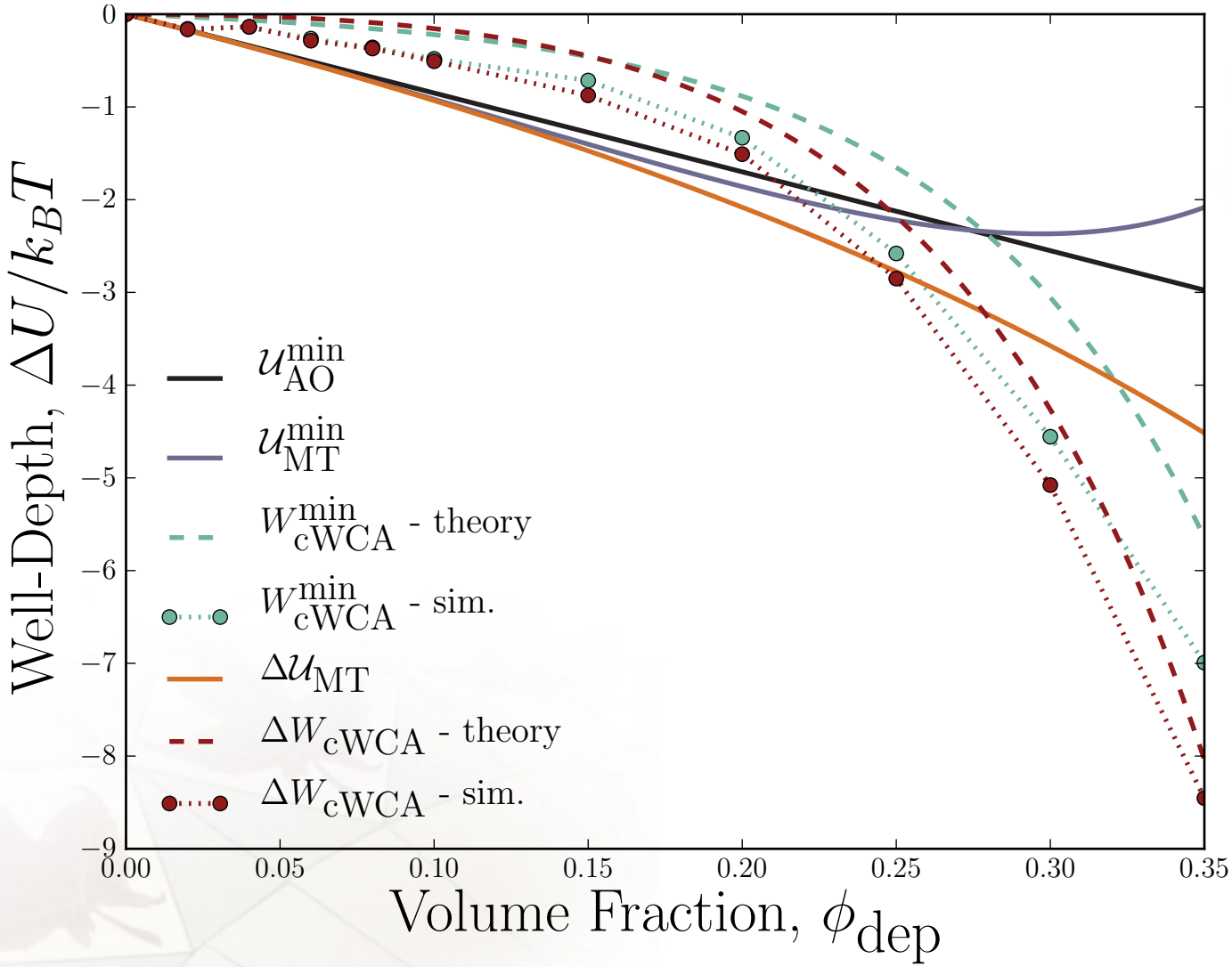

Figure : For the combinatorial-WCA simulation model. Unlike the shifted-WCA case, neither the minimum of the AO nor MT models well-approximates the value from simulations. The theoretical effective well-depth from the MT model ($\Delta\mathcal{U}_{\text{MT}}$; yellow solid line) is deeper than the simulations (ΔW_{cWCA}; red circles) and theoretical sum of the MT model plus the combinatorial-WCA potential (ΔW_{cWCA}; red dashed line) at small volume fractions of depletants, while it is more shallow at high volume fractions. Notably, the simulations (red circles) and theory (red dashed line) for ΔW_{cWCA} are significantly deeper in the combinatorial-WCA model than in the shifted-WCA model.

uOttawa

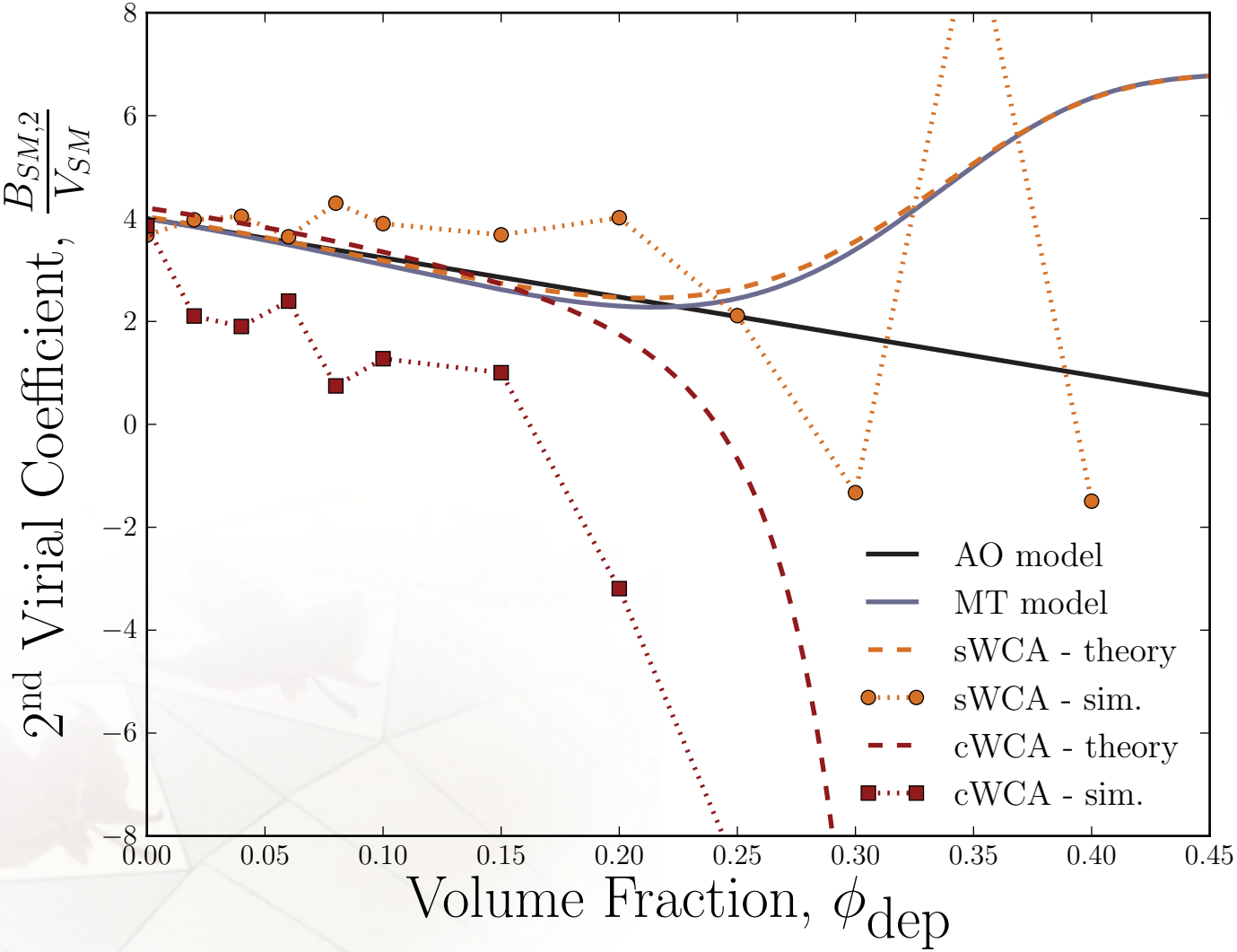

Figure : Second virial coefficient for shifted-WCA monomers with $r_{\text{SM}}/r_{\text{dep}} = 5$ as a function of ϕ_{dep}.

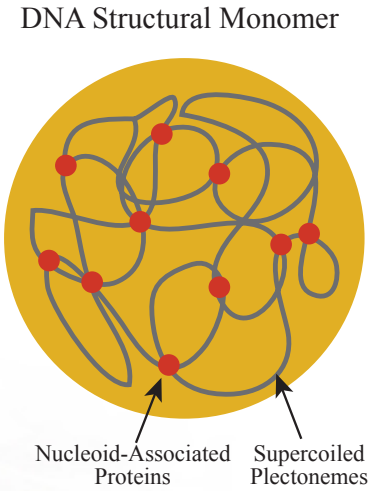

Figure : Structural monomers of supercoiled plectonemes are locally stabilized to form a crosslinked gel by various nucleoid-associated proteins.

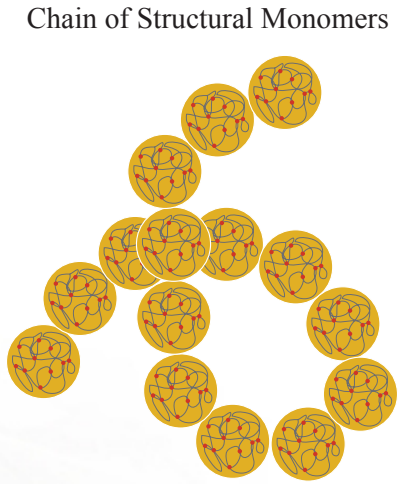

Figure : The DNA is considered to be a linear chain of structural monomers.

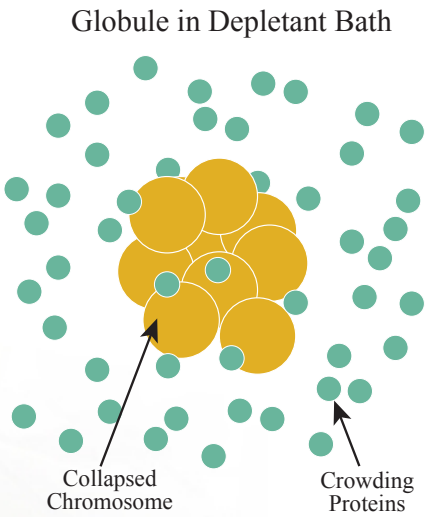

Figure : Surrounding proteins act as molecular crowding agents that can lead to collapse.

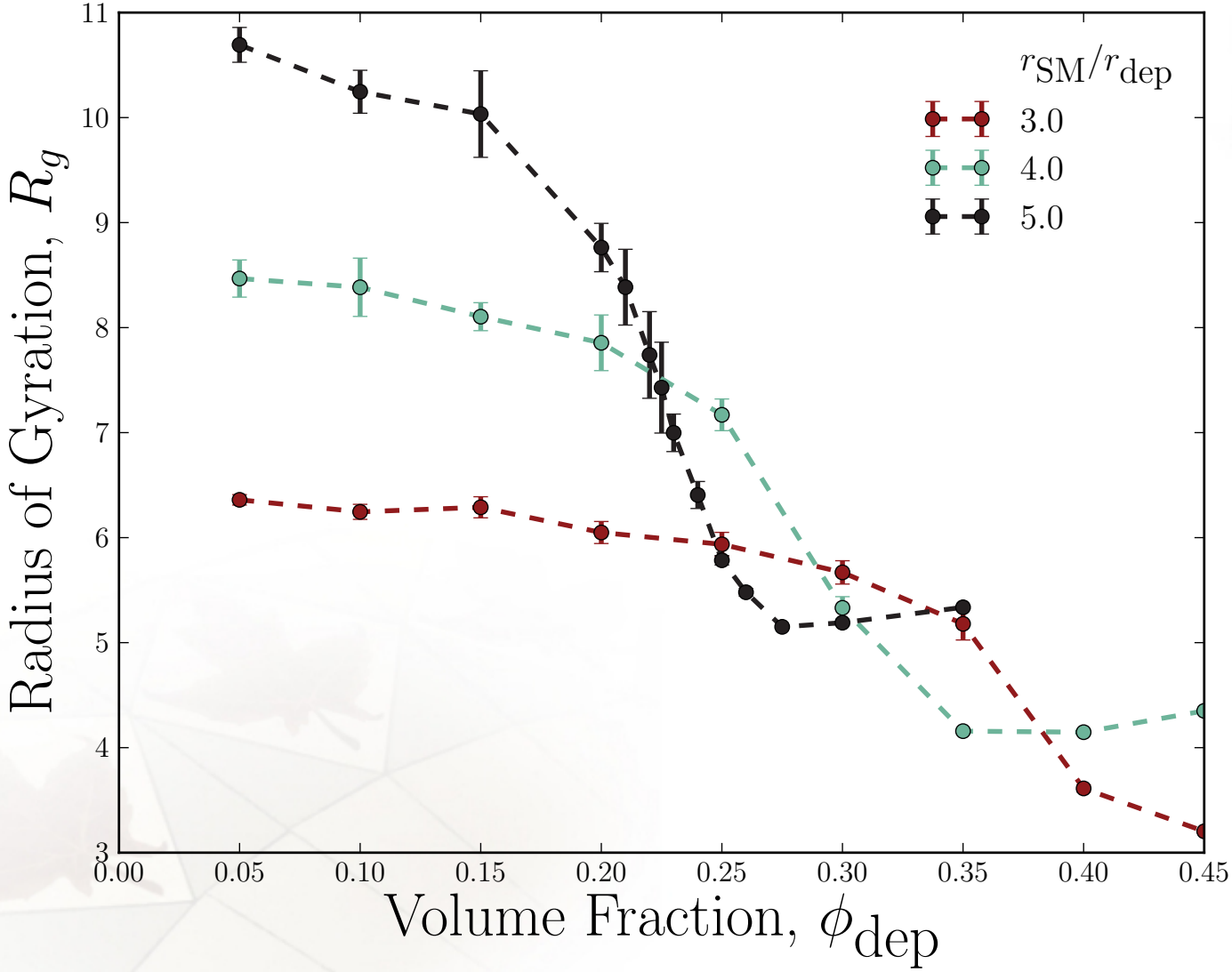

Figure : The radii of gyration of $N_{\mathrm{SM}} = 15$ chains of combinatorial-WCA structural monomers as a function of depletant volume fraction, ϕ_{dep}. The observed transition to a collapsed state varies as a function of the size ratio $r_{\mathrm{SM}}/r_{\mathrm{dep}}$.

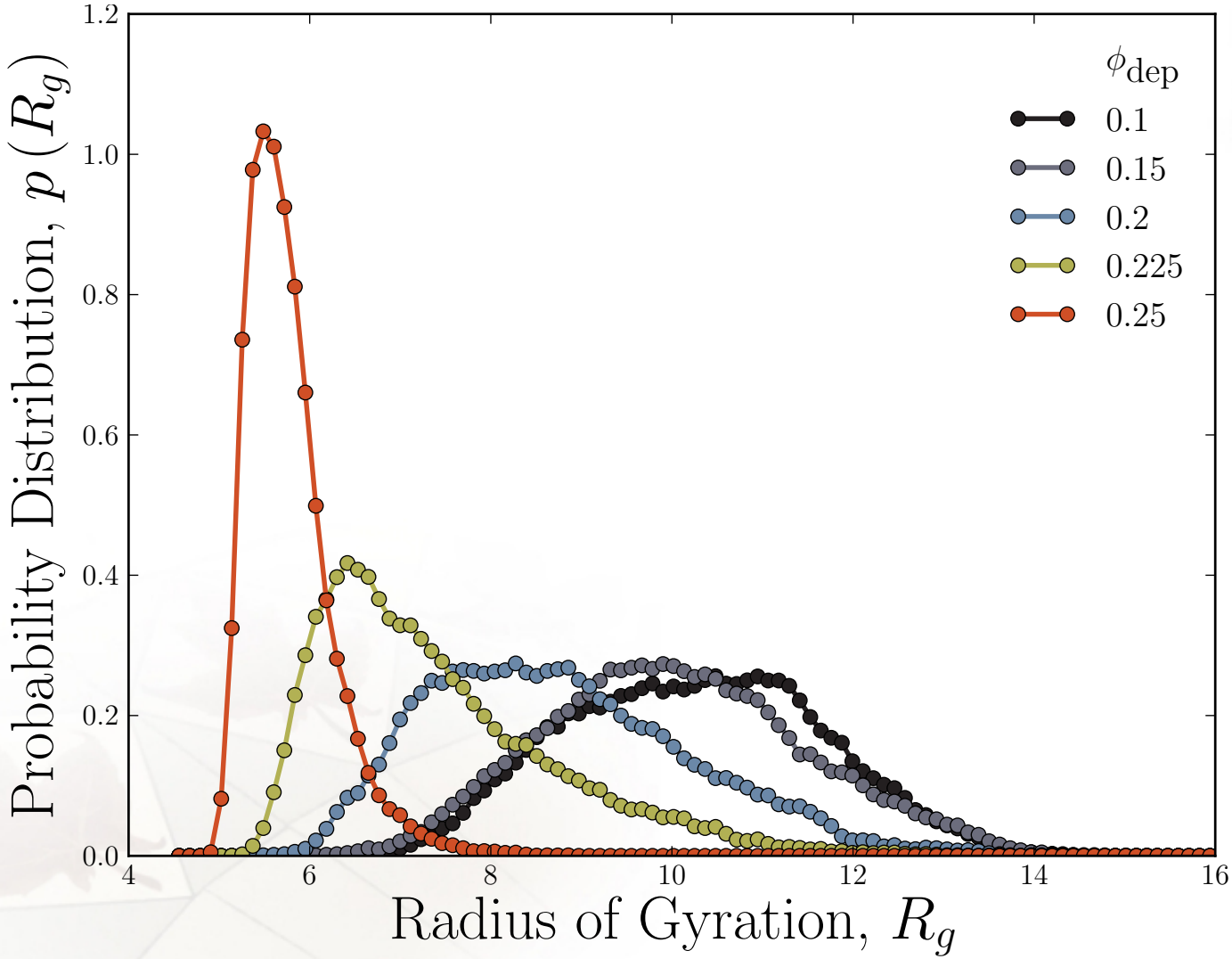

Figure : Probablity distributions of R_g for the size ratio of $r_{SM}/r_{dep} = 5$ and various volume fractions. The volume fractions shown are in the transition region, near the critical volume fraction of depletants ϕ^*_{dep} but remain unimodal. There appears to be no coexistence of both swollen and collapsed coils.

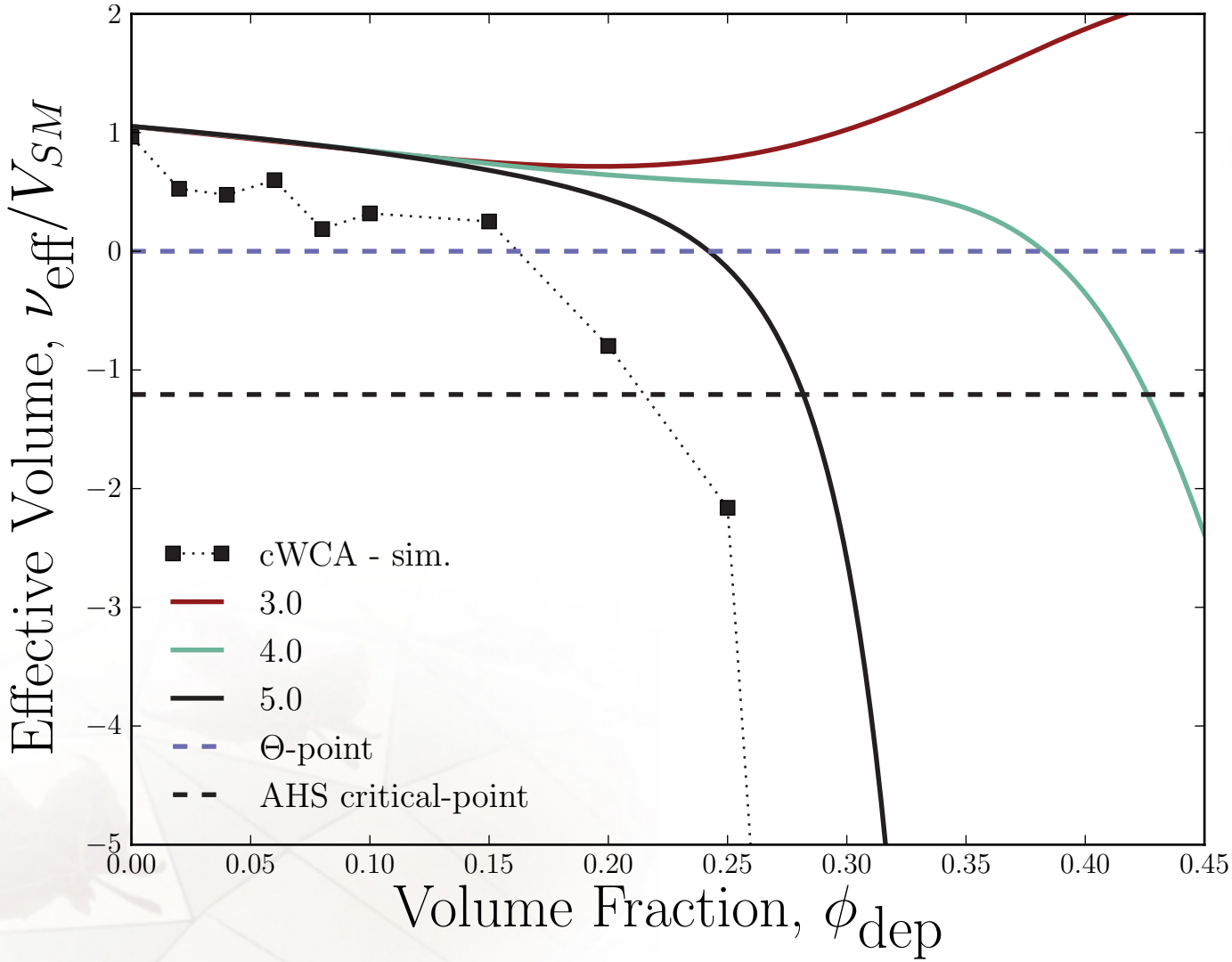

Figure : The effective volume of structural monomers interacting via depletion-induced pair-potentials. When no depletants are present the effective volume is the physical volume V_{SM}. The effective volume remains near V_{SM} at low volume fractions but drops rapidly above the Θ-point. For $r_{\text{SM}}/r_{\text{dep}} = 5$, the Θ-point is $\phi^{\Theta}_{\text{dep}} = 0.16$ and the AHS prediction of the critical-point is $\phi^{*\text{AHS}}_{\text{dep}} = 0.21$.

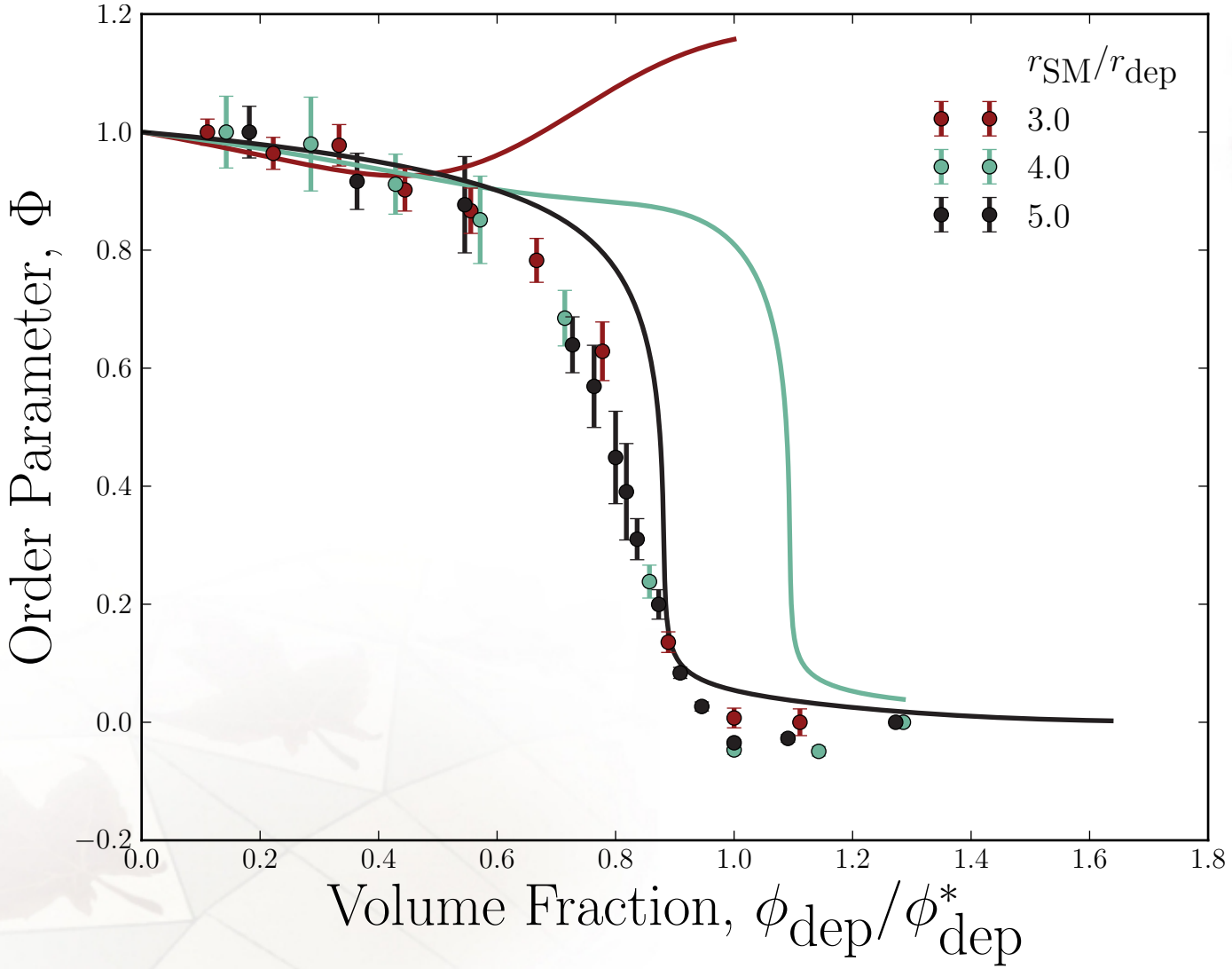

Figure : The order parameter $\Phi \equiv (R_g - R_{g,\mathrm{glob}})\,(R_{g,\mathrm{athermal}} - R_{g,\mathrm{glob}})$ reduces the radius of gyration axis. When plotted against the rescaled volume fraction $\phi_{\mathrm{dep}}/\phi^{*\mathrm{cWCA}}_{\mathrm{dep}}$ the simulation curves for $r_{\mathrm{SM}}/r_{\mathrm{dep}} = \{3, 4, 5\}$ collapse to a single curve. The theory results from substituting the effective volume into the Flory theory.

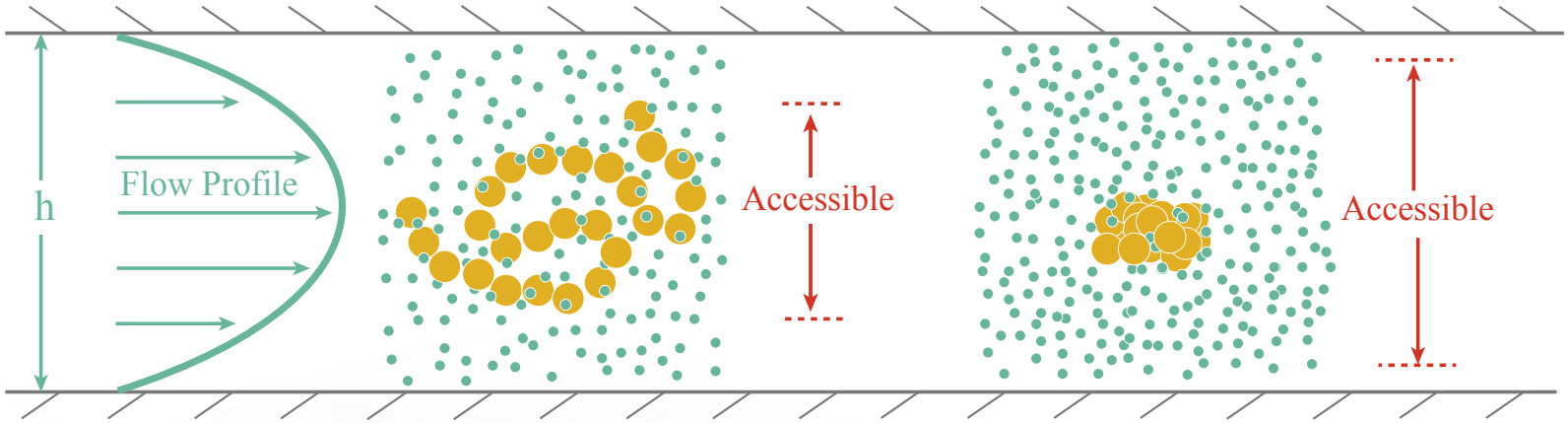

Figure : When performing hydrodynamic chromatography, a swollen chain has a hydrodynamic radius of approximately R_g and so R_g defines the near-wall excluded region. Adding a volume fraction of depletants ($\phi_{dep} > \phi^*_{dep}$) causes the coil to phase transition to a globular state, which has a much smaller effective radius. A large change in the accessible region of the channel is predicted to correspond to a large change in retention ratio.

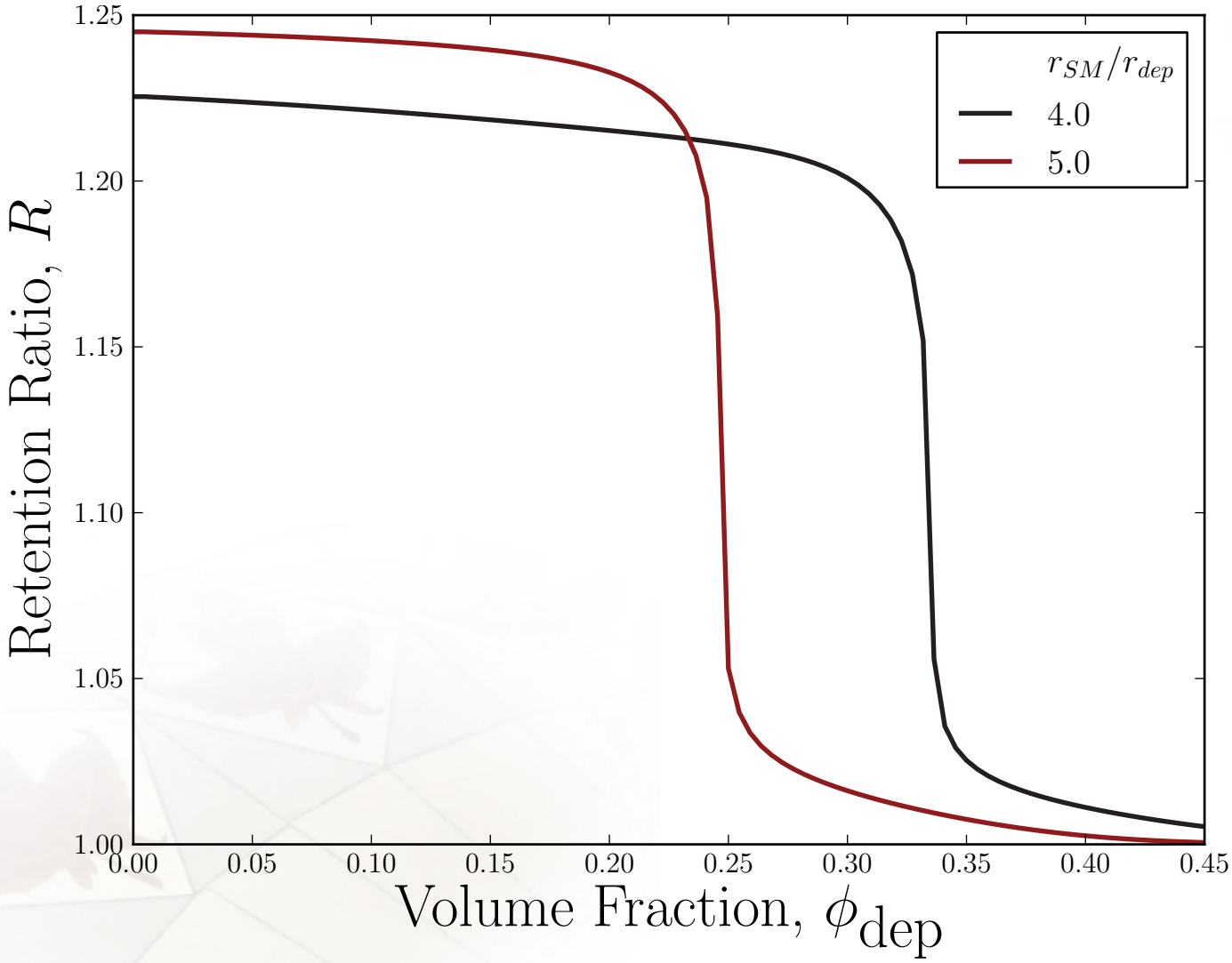

Figure : Retention ratio of a chain of structural monomers in a bath of depletants as a function of volume fraction of depletants. The critical volume fraction is clearly visible for the two sizes of structural monomers.